

# TECHNISCHE UNIVERSITÄT MÜNCHEN

Lehrstuhl für Biotechnologie

## Biomineralization of silicon dioxide on protein templates - Entrapment of proteins in silica particles

Francis Adigbli

Vollständiger Abdruck der von der Fakultät für Chemie der Technischen Universität München zur Erlangung des akademischen Grades eines Doktors der Naturwissenschaften (Dr. rer. nat.) genehmigten Dissertation.

Vorsitzender: Univ.-Prof. Dr. Dr. h.c. B. Rieger

Prüfer der Dissertation:

1. Univ.-Prof. Dr. J. Buchner
2. Univ.-Prof. Dr. S. Weinkauf

Die Dissertation wurde am 12.01.2012 bei der Technischen Universität München eingereicht und durch die Fakultät für Chemie am 27.02.2012 angenommen.



## Table of contents

<b>1</b>	<b>Summary</b> .....	<b>1</b>
<b>Part 1: Biomineralization of SiO<sub>2</sub> on protein templates</b> .....		<b>3</b>
<b>2</b>	<b>Introduction</b> .....	<b>3</b>
2.1	Biomineralization of SiO <sub>2</sub> in nature .....	3
2.2	Globular chaperones as biomineralization scaffolds .....	4
2.3	Fibrillar proteins as chaperone substrates for the directed biomineralization .....	5
2.4	Aim of the study .....	5
<b>3</b>	<b>Results</b> .....	<b>7</b>
3.1	Biomineralization on globular protein templates .....	7
3.2	Chaperone scaffolds show biomineralization activity .....	9
3.2.1	Optimized biomineralization conditions are determined by light scattering .....	11
3.2.2	A controlled increase of particle size is observed during biomineralization .....	12
3.3	Hsp26 forms stable substrate complexes with spermidine.....	14
3.4	Hsp26 and spermidine are localized within the biomineral.....	15
3.5	Scaffold induced biomineralization activity is too high for retention of nano-structure .....	18
3.6	Hsp26 does not form complexes with Silaffin or PEI.....	18
3.7	Biomineralization activity is observed for all protein scaffolds.....	20
3.7.1	The chaperone GroEL/ES scaffold induces biomineralization .....	20
3.7.2	Different fibrillar scaffolds show biomineralization activity.....	22
3.7.3	Scaffolds from microorganisms show biomineralization activity .....	23
<b>4</b>	<b>Discussion</b> .....	<b>25</b>
<b>Part 2: Entrapment of enzymes and antibodies in silica particles</b> .....		<b>29</b>
<b>5</b>	<b>Introduction</b> .....	<b>29</b>
5.1	Directed entrapment as a bioinspired immobilization technique.....	29
5.2	Immobilization of enzymes into mesoporous silica is highly protein-specific.....	29
5.3	Sol-gel entrapment is a mild and versatile method for enzyme immobilization.....	30
5.4	Immobilized enzymes present numerous advantages and applications.....	31
5.5	Aim of the study .....	31
<b>6</b>	<b>Results</b> .....	<b>32</b>
6.1	PEI-induced silica particle formation is controlled by the reaction conditions.....	32
6.1.1	Light scattering is used to determine silica particle formation kinetics .....	32
6.1.2	Dependence of PEI MW on particle formation .....	33
6.1.3	The silica particle morphology is controlled by the entrapment conditions .....	36

---

6.1.4	The porosimetric properties are optimized for protein entrapment .....	45
6.1.5	Morphologies with highest surface area also show the highest fluidity in suspension .....	48
6.1.6	Conclusions and outlook .....	50
6.2	The model protein eGFP is stably entrapped in silica particles .....	51
6.2.1	EGPF shows specific fluorescence in silica particles .....	52
6.2.2	The model protein eGFP is used for the optimization of the entrapment conditions .....	53
6.2.3	EGFP entrapment kinetics are time-linear .....	56
6.2.4	Entrapped eGFP is stabilized against heat stress .....	57
6.2.5	Entrapped eGFP is stabilized against proteolytic digest .....	58
6.2.6	Entrapped eGFP is stabilized against denaturation by chaotropes .....	59
6.2.7	Entrapped eGFP is stabilized against dehydration stress .....	59
6.2.8	Entrapped eGFP can be recovered from the silica particles by leaching .....	60
6.2.9	Conclusions .....	62
6.3	Enzymes are functionally entrapped in silica particles .....	62
6.3.1	The entrapment efficiency is increased by recycling the supernatant .....	65
6.3.2	Protein concentration and activity are equivalent in the case of entrapped lipase .....	66
6.3.3	Entrapped enzymes are stabilized against proteolytic digest .....	71
6.3.4	Entrapped enzymes are stabilized against denaturation by chaotropes .....	71
6.3.5	Entrapped enzymes are stabilized against dehydration stress .....	72
6.3.6	Entrapped enzymes can be used repeatedly .....	73
6.3.7	Entrapped enzymes can be recovered from the silica particles by leaching .....	74
6.3.8	Conclusions .....	82
6.4	Antibodies retain their specific activity after entrapment in silica particles .....	83
6.4.1	A fluorescent labeled antibody shows specific fluorescence in silica particles .....	84
6.4.2	Entrapped MAK33 is active in the ELISA .....	85
6.4.3	MAK33 is stabilized against heat stress and proteolytic digest .....	86
6.4.4	Entrapped antibodies can be recovered from the silica particles under leaching conditions .....	87
6.4.5	Conclusions and outlook .....	87
<b>7</b>	<b>Discussion .....</b>	<b>89</b>
7.1	Entrapment is independent of the pI of the immobilized protein .....	89
7.2	Increasing protein size decreases entrapment efficiency .....	90
7.3	Luciferase is destabilized by high silicic acid concentrations during entrapment .....	90

---

7.4	Electrostatic interactions between silica particles and proteins cause stable protein entrapment .....	90
7.5	Leaching of entrapped proteins is influenced by the entrapment conditions .....	92
7.6	Entrapped proteins are highly interesting for medical applications and as biocatalysts.....	93
<b>8</b>	<b>Materials and Methods.....</b>	<b>94</b>
8.1	Materials .....	94
8.1.1	Proteins and chemicals .....	94
8.1.2	Technical Equipment.....	95
8.1.3	HPLC system .....	96
8.1.4	Microscopes.....	96
8.1.5	Software.....	97
8.2	Biom mineralization.....	98
8.2.1	Detection of biom mineralization by light scattering .....	98
8.2.2	Biom mineralization samples.....	98
8.2.3	Calcination of biom mineralized Hsp 26, GroEL/ES and fibrillar proteins.....	99
8.3	Protein entrapment methods .....	99
8.3.1	Entrapment protocol.....	99
8.3.2	Characterization of silica particles from entrapment experiments .....	100
8.3.3	Leaching of entrapped proteins .....	101
8.4	Protein chemistry methods .....	102
8.4.1	Purification of Hsp26 .....	102
8.4.2	GroEL/ES complex formation .....	102
8.4.3	NBD-labeling of Spd and PEI (MW 1800).....	102
8.4.4	Size Exclusion HPLC .....	103
8.4.5	Protein determination via Bradford assay .....	103
8.4.6	Protein activity assays.....	104
8.4.7	Antibody activity assays .....	105
8.4.8	Determination of protein stabilization.....	106
8.5	Spectroscopic methods .....	107
8.5.1	Dynamic Light Scattering .....	107
8.5.2	Aggregation measurements .....	108
8.5.3	Fluorescence anisotropy .....	109
8.6	Microscopic methods.....	109
8.6.1	Fluorescence microscopy.....	109
8.6.2	Electron microscopy: SEM .....	110

---

8.6.3	Electron microscopy: TEM.....	111
8.6.4	Electron microscopy: High resolution SEM and STEM .....	111
<b>9</b>	<b>Abbreviations .....</b>	<b>113</b>
<b>10</b>	<b>Literature.....</b>	<b>117</b>
	<b>Acknowledgements.....</b>	<b>132</b>

## 1 Summary

The presented study first investigated the directed biomineralization on globular and fibrillar protein templates. Depending on the morphologies of the protein template, globular, non-globular and fibrillar hybrid silica structures were obtained. The control of silica morphologies at mild reaction conditions with protein templates presents a new field of applications for catalysis and nano-structures.

Second, the immobilization of functional proteins by non-directed, random entrapment in silica particles generated by biomineralization-inducing organic molecules was investigated. Random entrapment was used for protein immobilization in order to minimize the influence of different proteins on silica particle formation. The methodology presented here utilizes the silica sol-gel technique, where entrapping of an enzyme is achieved randomly throughout the chemical formation of highly porous silica under physiological temperature and pH conditions, avoiding degradation during entrapment. Using a polycationic polyamine to biomimetically form silica particles, controlling their morphologies with the reaction conditions, this study established a generalized entrapment protocol which suppresses protein-specific effects. For eGFP and the enzymes lipase, DHFR,  $\beta$ -galactosidase and luciferase, as well as for MAK33 antibodies, entrapment demonstrated protecting effects. Furthermore, leaching of the proteins from the silica network could be induced and influenced by the particle morphology generated at defined reaction conditions. The entrapment of proteins for technical applications leads to a number of advantages compared to free enzymes, such as stabilization, re-usability and rapid reaction quenching by the removal of the enzyme-containing silica particles. These properties are relevant for applications in pharmaceutical sciences, industrial catalysis and biomedical, biodegradable materials, biosensors and screening devices.

---

## Zusammenfassung

Im ersten Teil der vorgestellten Studie wurde die gerichtete Biomineralisation an globulären und fibrillaren Proteintemplaten untersucht. Abhängig von der Morphologie des Proteintemplats wurden unterschiedliche Silikat-Hybridstrukturen erhalten. Die Kontrolle der Silikatmorphologie unter milden Reaktionsbedingungen mittels Proteintemplaten eröffnet neue Anwendungsmöglichkeiten in den Gebieten der Biokatalyse und der Generierung von Nanostrukturen.

Im zweiten Teil dieser Studie wurde die Immobilisierung diverser Zielproteine mittels ungerichteter, statistischer Einlagerung zwischen Silikapartikel untersucht, welche von biomineralisationsfähigen organischen Molekülen gebildet wurden. Die statistische Einlagerung wurde verwendet, um den Einfluss der unterschiedlichen Zielproteine auf die Silikapartikelbildung zu minimieren. Die statistische Einlagerung der Enzyme wurde in dieser Studie mittels der Sol-Gel-Reaktion erreicht, welche das Enzym schonend und unter milden Temperaturen und pH Werten während der Bildung von porösen Silikaten immobilisiert. Mit Hilfe von polykationischen Polyamiden, welche biomimetisch die Partikelbildung und deren Morphologie kontrollieren, wurde in dieser Studie ein generalisiertes Einlagerungsprotokoll etabliert, welches proteinspezifische Effekte unterbindet. Die Proteineinlagerung zeigte stabilisierende Effekte für eGFP, die Enzyme Lipase, DHFR,  $\beta$ -Galactosidase und Luciferase, sowie für MAK33 Antikörper. Außerdem konnte gezeigt werden, dass eingelagerte Proteine unter bestimmten Reaktionsbedingungen wieder aus dem Silikatnetzwerk kontrolliert heraus gelöst werden können.

Die Einlagerung von Proteinen für technische Anwendungen in Biomineralen bietet zahlreiche Vorteile gegenüber dem Einsatz von Proteinlösungen, darunter die Stabilisierung und Wiederverwendbarkeit der Proteine, sowie die Möglichkeit, die enzymatischen Reaktionen rasch zu stoppen, indem die immobilisierten Enzyme der Reaktionslösung durch Sedimentation entzogen werden. Diese Eigenschaften sind für die Anwendungen in den pharmazeutischen Wissenschaften, der industriellen Katalyse und für die Herstellung von biomedizinischen, bioabbaubaren Materialien, Biosensoren und biochemischen Diagnostiksystemen.



## Part 1: Biomineralization of SiO<sub>2</sub> on protein templates

### 2 Introduction

#### 2.1 Biomineralization of SiO<sub>2</sub> in nature

Biomineralization, i.e. the formation of inorganic materials with complex morphologies, is a widespread biological phenomenon which occurs from prokaryotes (e.g., Fe<sub>3</sub>O<sub>4</sub> nanocrystals in magnetotactic bacteria) to humans (bone and teeth) (Lowenstam & Weiner, 1989; Bäuerlein *et al*, 2007; Kröger & Poulsen, 2008). Spectacular examples of biomineralization are found in unicellular eukaryotes that produce intricately structured cell walls made of CaCO<sub>3</sub> (e.g., coccolithophores) or SiO<sub>2</sub> (e.g., diatoms, radiolaria) (Kröger & Poulsen, 2008).

How the cell translates DNA sequence information into patterned three-dimensional SiO<sub>2</sub> structures has been the object of intense research for more than a century (Round *et al*, 1990). Insight into the mechanisms of silica biomineralization could inspire the development of patterned inorganic materials with complex morphologies and advanced properties (Heuer *et al*, 1992; Mann, 1993; Mann & Ozin, 1996).

Diatoms have evolved into the most species-rich group of eukaryotic algae, present in almost every water habitat. They are enormously important for the biological cycling of silicon and carbon, and are responsible for about 20% of the total photosynthetic CO<sub>2</sub> fixation, which is equivalent to the photosynthetic activity of all rain forests combined (Kröger & Poulsen, 2008; Field *et al*, 1998). Diatoms possess species-specific, precisely controlled silica morphologies (Fig. 1) (Round *et al*, 1990; Pickett-Heaps *et al*, 1990).

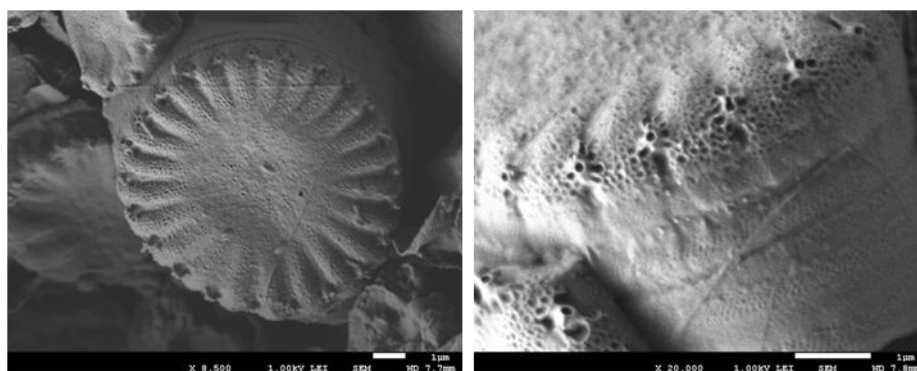


**Fig. 1:** High resolution SEM micrograph of unsputtered cell wall from *Thalassiosira pseudonana*. Micrographs have been recorded with the LEI detector at 1 kV acceleration voltage. Working distances were (left) 7.7 mm and (right) 7.8 mm. Scale bar: 1 µm. (Diatom sample preparation is described in 8.6.3.1 and microscopy was carried out as described in 8.6.4.)

Current research shows that diatom biosilica is an inorganic-organic hybrid material mainly composed of inorganic silica to which various specific organic macromolecules (diatom-

specific silaffins, long-chain polyamines (LCPA) and other proteins) are attached (Kröger & Poulsen, 2008). Silaffins and LCPA accelerate and control silica morphogenesis from silicic acid *in vitro* through phase separation processes (Kröger & Poulsen, 2008). The R5 peptide (SSKKSGSYSGSKGSKRRIL) derived from a repeat unit of the sil1 gene from *Cylindrotheca fusiformis* diatoms is one of the most popular biomimetic biomineralization “starters” for the synthesis of spherical silica nanoparticles of 200 nm to several microns via polycondensation of silicic acid in the presence of phosphate buffer (Patwardhan, 2002; Luckarift *et al*, 2004; Crookes-Goodson *et al*, 2008; Brott *et al*, 2001). Spermidine motives are found in the LCPAs of diatoms, some of which are composed of oligo-propyleneimines attached to propylamine, spermine, or spermidine (Crookes-Goodson *et al*, 2008). The influence of spermine and spermidine on silica particle formation has been shown before (Belton *et al*, 2005).

Native silaffins are covalently bound to long-chain polyamines (LCPA) and therefore branched (Kröger *et al*, 1999, 2001). Branched polyethyleneimine (PEI) is structurally comparable to polyamines isolated from *Stephanopyxis turnis* and *Cylindrotheca fusiformis* (Sumper *et al*, 2003). The polycationic PEI was shown to self-associate in the presence of phosphate ions and to be able to catalyze silica polycondensation (Hildebrand, 2008; Sumper & Kröger, 2004).

## 2.2 Globular chaperones as biomineralization scaffolds

Cells respond to heat shock by increased expression of heat shock proteins (Hsps) (Lindquist & Craig, 1988), many act as molecular chaperones and prevent the unspecific aggregation of other proteins (Morimoto, 1994; Beissinger & Buchner, 1998). Among these are the small heat shock proteins (sHsps) which are ubiquitous in nature (Haslbeck *et al*, 1999). They share conserved domains with high sequence homology to  $\alpha$ -crystallin (de Jong *et al*, 1993) while the N-terminal part is divergent in sequence and length for different organisms (Haslbeck *et al*, 1999; Andre-Patrick Arrigo & Jacques Landry, 1994; Ehrnsperger *et al*, 1997). They form complexes in the range of 150-800 kDa with varying subunit stoichiometry (Haslbeck *et al*, 1999; de Jong *et al*, 1993). The interaction of non-native proteins with sHsps has been shown first for  $\alpha$ -crystallin and murine Hsp25 (Horwitz, 1992; Jakob *et al*, 1993).

The small heat shock protein Hsp26 was reported to non-covalently bind to substrates and build stable chaperone/substrate complexes in an ATP-independent way (Haslbeck *et al*, 1999; Haslbeck, 2002), (Jakob *et al*, 1993). Hsp26 was chosen for this study since it was reported to be a large 24-mer showing regular, spherical complexes with a diameter of 15-18 nm (Haslbeck *et al*, 1999; Ehrnsperger *et al*, 1999; Bentley *et al*, 1992).

The GroEL/ES system (Hsp60) is formed by the cylindrical GroEL and its co-chaperone GroES (Beissinger & Buchner, 1998; Hartl & Hayer-Hartl, 2002; Frydman, 2001). GroEL consists of 14 identical subunits that form two stacked rings. Each subunit is characterized by an equatorial ATP binding domain, a central hinge-like domain and an apical substrate binding domain, containing a number of highly conserved amino acids responsible for substrate binding as well as for interacting with the co-chaperone GroES (Braig *et al*, 1994).

### **2.3 Fibrillar proteins as chaperone substrates for the directed biomineralization**

The biomineralization of fibrils was interesting with regards to current bone mineralization research: it has been found that silica-collagen-composites represent a preliminary phase in bone development which has been conserved from the time when silica-collagen composites were necessary for the construction of the first metazoan skeletons (Bäuerlein *et al*, 2007). Relating to bone formation, it was recently reported that a chaperone from the Hsp70 family, GRP-78 shows calcium phosphate biomineralization activity and binds to type 1 collagen (Altmeyer *et al*, 1996; Ravindran *et al*, 2011). It was shown that collagen type I fibers (as well as tobacco mosaic virus) could be used as biomineralization-active scaffolds for the preparation of silica nano-tubes due to their cationic character at low pH and high pl (Pickett-Heaps, 1998; Blank & Sullivan, 1983; Schmid, 1980).

Furthermore, it was shown that the small heat shock chaperone Hsp26 interacts with actin (Haslbeck *et al*, 1999; Benndorf *et al*, 1994; Ehrnsperger *et al*, 1997). Possibly, chaperone-actin complexes could be interesting biomineralization templates.

### **2.4 Aim of the study**

A fundamental challenge for the directed biomineralization is the determination of useful template structures inducing biomineralization. Molecular chaperones are unique in their structural variability combined with their ability to non-covalently form stable complexes with a multitude of substrates (Haslbeck *et al*, 1999; Ehrnsperger *et al*, 1997; Haslbeck, 2002). This study investigates the application of a family of molecular chaperones, the small heat shock proteins (sHsps) that form large spherical particles, as scaffold proteins for the directed biomineralization and the influence of different organic polyamines and synthetic silaffin on chaperone/substrate templates and their biomineralization activity. The goal was to obtain biomimetic silica with the nano-structure of the protein template. Specific nano-structured morphologies based on globular or fibrillar protein scaffolds resulting in core-shell silica nano-spheres or silica nano-wires are of great interest for research on nano-materials.

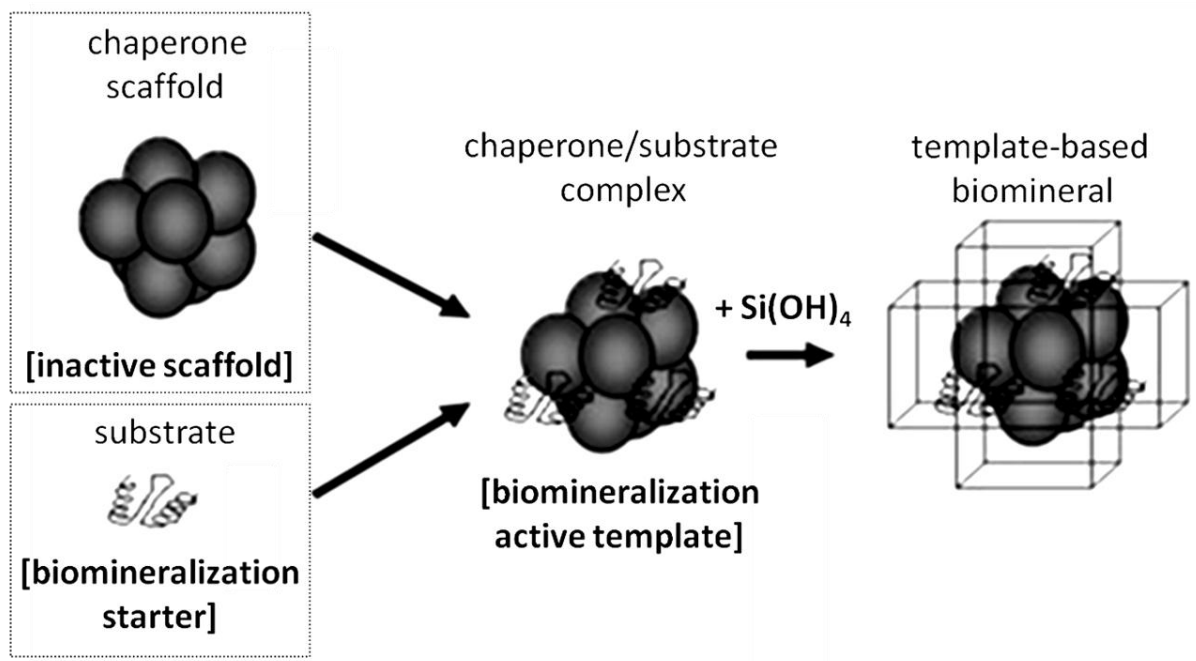


**Fig. 2: Scheme of scaffolding with sHsps bound to biomineralization active substrates leading to biomineralized structures with the nano-structure of the complex template.**

Oligomeric chaperones (e.g. Hsp26, GroEL/ES) would be of interest as structural scaffolds (without biomineralization activity) for the biomineralization of SiO<sub>2</sub> under mild conditions. Substrates with high biomineralization activity ("*strong starter*"), e.g. Silaffin and LCPAs or structurally similar organic molecules like PEI (Kröger & Poulsen, 2008), could provide biomineralization activity to the chaperone scaffold, if specific binding of the substrate (*starter*) to the chaperone (*scaffold*) leads to a stable chaperone/substrate complex with lower biomineralization activity ("*controlled starter/scaffold*" *template*). The biomineralization activity of the substrate must be controlled in order to obtain silica deposition thin enough for the biomineralized particle to retain the nano-structure of the template.

### 3 Results

#### 3.1 Biomineralization on globular protein templates

In order to retain the nano-structure of protein templates, biomineralized silica layers < 5 nm around the template were estimated to be required. In the case of Hsp26 as a scaffold, ideal biomineralized particles would be around 20 nm. To investigate multiple different biomineralization templates and conditions, light scattering measurements have been established (Fleckenstein, 2008) and commercially available Ludox silica particles (20 nm) (Stöber *et al*, 1968; Deželić *et al*, 1960) were used as a control sample to estimate differences in light scattering at different particle concentrations (Fig. 3A).

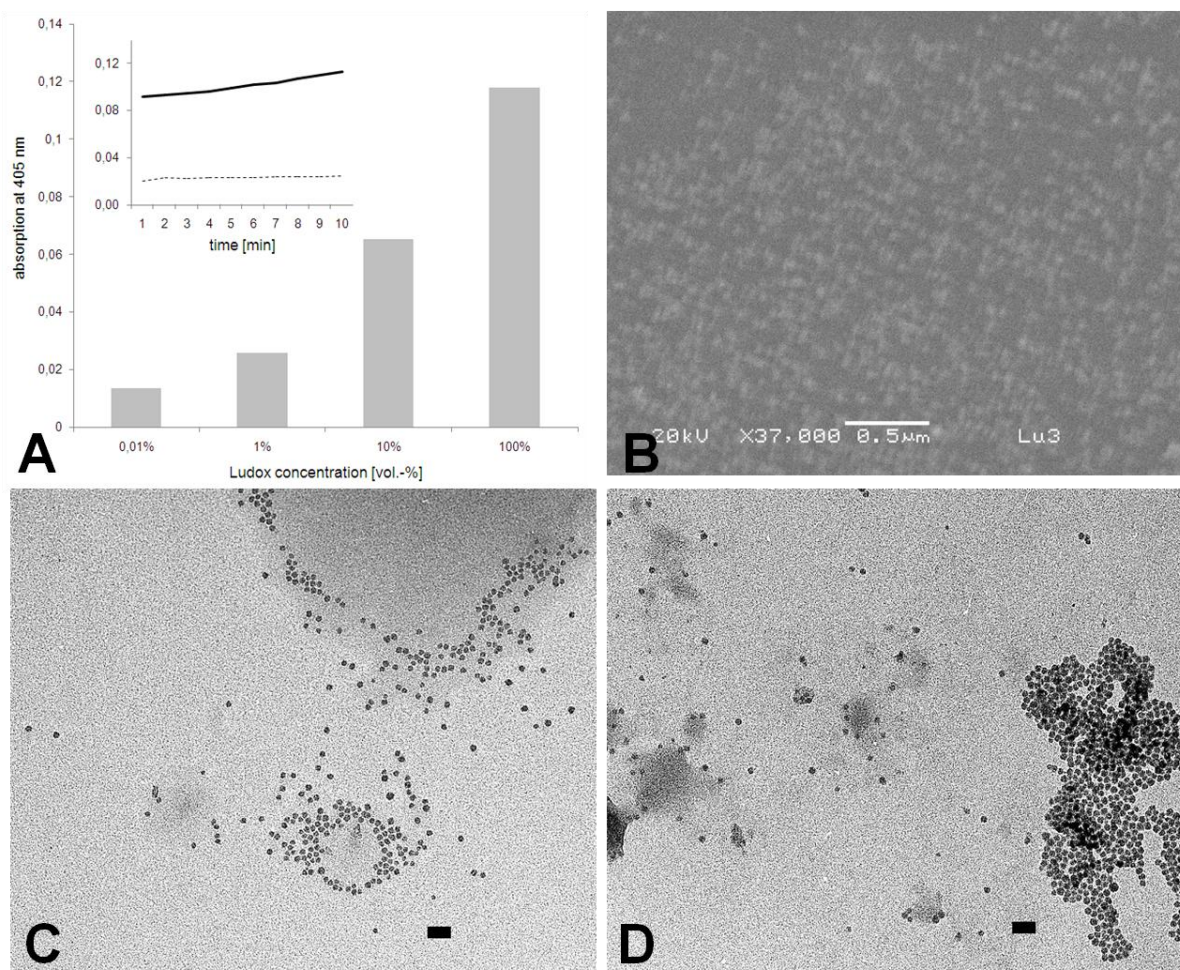


**Fig. 3:** A) Light scattering at 405 nm by different Ludox silica particle (20 nm) concentrations in 0.1 M potassium phosphate after 10 min incubation at r.t.. Inset: absorption measurement over time of 1 vol.-% (dashed line) and 10 vol.-% (solid line) Ludox. B) SEM micrograph of sputtered 0.1 vol.-% Ludox solution in H<sub>2</sub>O. Scale bar: 0.5  $\mu$ m. C-D) TEM micrographs of 0.01 vol.-% Ludox solutions in H<sub>2</sub>O observed on C) glow-discharge treated and D) untreated carbon-coated copper grids. Scale bar: 100 nm.

At high concentrations, Ludox caused an increase in absorption due to particles sedimenting while the absorption of diluted Ludox solutions was constant over time (Fig. 3A, inset). Different concentrations of silica particles in suspension led to detectable changes in

absorption (Fig. 3A). Thus, determination of the absorption at 405 nm allowed a qualitative assessment of particle formation by biomineralization.

Ludox particles were observed microscopically as a standard silica sample for comparison with biomineralized silica particles (Fig. 3B-D). Using conventional SEM measurements, 20 nm silica particles could not be clearly resolved (Fig. 3B), possibly due to sputter-coating of the sample with a ~2 nm layer of gold which was necessary for image acquisition. Therefore, samples that can be resolved with conventional SEM are bigger than the required particle size of ideal biomineralized nanoparticles (with silica layers < 5 nm around the template). For the investigation of biomineral morphologies, samples must therefore be analyzed by TEM.

The process of drying silica particles in aqueous suspension on microscopic grids can lead to changes in association of silica particles (Perry & Lu, 1992). Ludox associated locally on carbon-coated grids for TEM (Fig. 3C-D), especially for high particle concentrations. Highly diluted Ludox (0.01 vol.-%) silica particles did not stick together strongly when carbon-coated TEM grids were rendered hydrophilic (i.e., with a net negative charge with glow discharge in a reduced atmosphere of air (Fig. 3C) compared to untreated grids (Fig. 3D) (Dubochet *et al*, 1971; Aebi & Pollard, 1987).

The final goal was to establish biomineralization conditions leading to the controlled deposition of the thinnest silica layer possible around a stable substrate/chaperone-complex. The faster the kinetics, the more challenging the control of the biomineralization process was expected to be and the more unspecific silica particle formation independent of the template would be observed. Therefore, the biomineralization conditions needed to be optimized for slow, controllable template-specific silica deposition allowing the control of the silica layer thickness by removal of the particles from the reaction solution.

Light scattering due to silica particle formation was used to extensively investigate different additives, globular Hsp26 scaffolds and potential chaperone-substrate complexes under biomineralization conditions. In order to control silica deposition, the biomineralization conditions were optimized (Fleckenstein, 2008). (The screening procedure used is illustrated in Materials and Methods 8.2.1)

Silica deposition was observed to be slowest at pH 7 (Bauer *et al*, 2007; Pascal J. Lopez *et al*, 2005), which was applicable for chaperone-substrate binding. Substrates with low individual biomineralization activity (*weak starters*) resulting in cooperatively higher particle formation when bound by chaperone scaffolds were of primary interest. Additives that did not lead to any significant light scattering when added to silicic acid were assumed to be inactive in biomineralization. Controls were measured for the biomineralization of the chaperone

scaffold without starter. From all additives analyzed for controlled biomineralization activity and cooperative light scattering with chaperones, spermidine (Spd) yielded the most interesting results.

### 3.2 Chaperone scaffolds show biomineralization activity

The optimal potassium phosphate (PPB) concentration for controlled particle formation kinetics was investigated for combinations of Spd and Hsp26 (Fig. 4A-C). Silicic acid was obtained from TMOS hydrolysis in 1 mM HCl (Materials and Methods, 8.2.1). The prehydrolysis time  $t_{pre}$  is defined as the time TMOS was hydrolyzed to silicic acid in 1 mM HCl before adding it to the reaction solution (Hench & West, 1990; Iler, 1979; Patwardhan, 2002). Decreasing potassium phosphate molarities (0.5 to 0.01 M) caused decreasing silica particle formation both by the starters (Fig. 4A-C) and by silicic acid auto-condensation (Fig. 4D) (Potapov *et al*, 2007). Higher potassium phosphate concentration led to higher background auto-condensation of silicic acid (Fig. 4D); biomineralization with 0.5 M potassium phosphate was predicted to result in higher amounts of unspecific auto-condensated silica particles and seemed therefore less useful than 0.1 M potassium phosphate which was optimal for controlled but significant biomineralization activities (i.e. significantly higher than silicic acid auto-condensation) (Fig. 4B).

It has been reported before that silica formation activity is strongly dependent upon the presence of amines (Currie & Perry, 2007). Although amino-groups are present in all proteins, specific biomineralization activity was shown only for specific organic proteins like silaffins and LCPA (Kröger & Poulsen, 2008), PEI (Hildebrand, 2008; Sumper & Kröger, 2004; Kröger & Poulsen, 2008) or spermine (Belton *et al*, 2005). Surprisingly, the scaffold Hsp26 possessed significant biomineralization activity and was in fact even a stronger starter than Spd: 4.2  $\mu$ M Hsp26 (1 mg/ml) caused significant light scattering (Fig. 4A-C). In comparison, light scattering induced by 4.2  $\mu$ M up to 6.9 mM (1 mg/ml) Spd did not significantly increase. However, the combination of Hsp26 and Spd caused higher absorption than the sum of each component, as predicted for a Hsp26/Spd chaperone/substrate-complex.

A chaperone-complex with its substrate Spd in high excess (6.9 mM or 1 mg/ml Spd, corresponds to a 1640:1 ratio of Spd:Hsp26, in relation to Hsp26 monomers) or lower excess (10:1 Spd:Hsp26, data not shown) to Hsp26 (4.2  $\mu$ M) did not surpass light scattering caused by an equimolar Hsp26/Spd complex (4.2  $\mu$ M). This could possibly indicate that a potential Hsp26/Spd complex was already saturated and excess Spd activity was not observed due to the much higher biomineralization activity of the Hsp26/Spd complex.



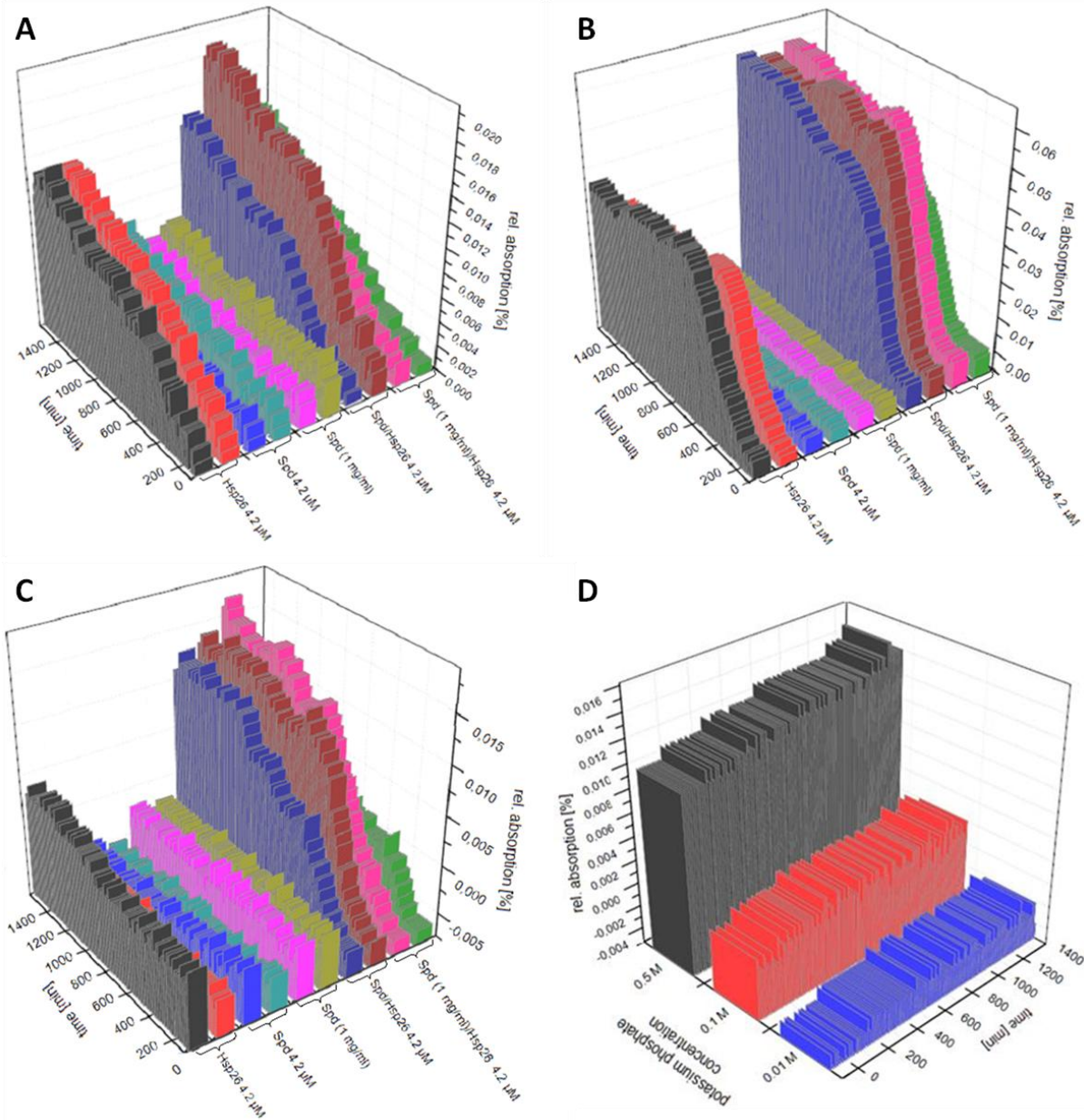


**Fig. 4:** Light scattering caused by particle formation by Spd, Hsp26 and Hsp26/Spd dependent on the potassium phosphate concentration (TMOS  $t_{pre}$ : 3 min): A) 0.5 M, B) 0.1 M, C) 0.01 M. D) Light scattering caused by particle formation by silicic acid auto-condensation in potassium phosphate buffer (PPB). Absolute light scattering values were corrected for the absorption caused by the control solutions without silicic acid.

The observation of biomineralization activity of the scaffold Hsp26 and complex formation with Spd was consistent and reproducible for 0.5 and 0.01 M potassium phosphate (Fig. 4A and C). Silica particles obtained from biomineralized Hsp26 scaffold in the absence of the starter Spd were observed by TEM (Fig. 5).

Bigger particle size was observed with 0.1 M potassium phosphate; however the contrast of the particles was higher than with 0.5 M potassium phosphate.



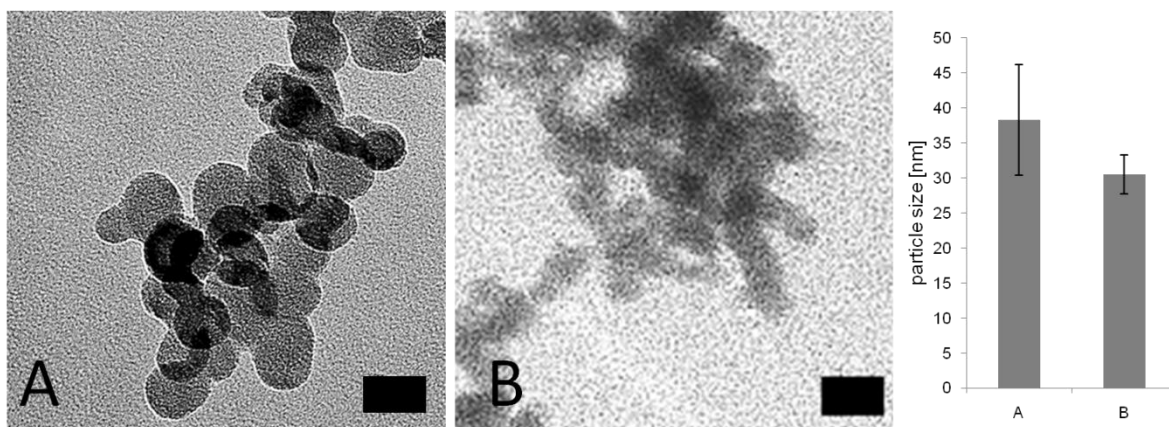


**Fig. 5: TEM micrographs of biom mineralized Hsp26 using A) 0.1 M, B) 0.5 M potassium phosphate buffer. Scale bar: 50 nm. Average particle sizes are shown in the diagram and were determined as described in Materials and Methods 8.6.3.3. Biom mineralization conditions: A) 0  $\mu$ M Spd, 0.1 M potassium phosphate, B) 0  $\mu$ M Spd, 0.5 M potassium phosphate. Other biom mineralization conditions are described in Materials and Methods 8.2.2.1.**

With 0.01 M potassium phosphate, the biom mineralization ability of Hsp26 decreased significantly (Fig. 4C). Due to the low background auto-condensation at 0.01 M potassium phosphate (Fig. 4D), the additional absorption for the Hsp26/Spd complex compared to that of Hsp26 was most visible at this potassium phosphate concentration.

### 3.2.1 Optimized biom mineralization conditions are determined by light scattering

Further screening controls with light scattering were carried out (data not shown) with varied reaction conditions and confirmed optimal biom mineralization conditions in potassium phosphate at neutral pH with significantly faster particle formation at slightly alkaline pH of 7.7 and irregular light scattering signals at a slightly acidic pH of 5.7 (data not shown).

Reaction conditions with harsh pH values and higher concentrations of silicic acid were eliminated to prevent protein denaturation and possibly loss of the chaperone function. Variation of the incubation time of the complex at r.t. as well as heat-shock activation of Hsp26 (Haslbeck *et al*, 1999; Haslbeck, 2002) did not influence the light scattering significantly (data not shown). Reaction kinetics were slowest for chaperone and/or substrate concentrations above 4.2  $\mu$ M in the screening assay. Hsp26/Spd-complexes were observed to have slower particle formation kinetics (data not shown).

Higher  $t_{pre}$  (up to 40 min) led to slower light scattering for screening kinetics with 0.5 M potassium phosphate (no difference was detected for 0.1 M potassium phosphate) and were reported to lead to decreased silica particle size in the literature (Patwardhan, 2002; Patwardhan & Clarkson, 2003).

However, the screening of the biom mineralization kinetics did not reveal any structural information of particle morphologies at the time points indicated. To determine the optimal reaction time sufficient for controlled biom mineralization, the exact particle size needed to be

continuously measured *in situ*, as opposed to intermittent measurement of the particle size after centrifugation and washing steps for different reaction times.

### 3.2.2 A controlled increase of particle size is observed during biomineralization

To determine if the hydrodynamic particle size (Berne & Pecora, 1976) of Hsp26 increased upon Spd binding Hsp26, Spd and an Hsp26/Spd complex were analyzed with DLS (Fig. 6A) (Chu, 1997; Hendrix & Leipertz, 1984; Berne & Pecora, 2000). The size determined for Hsp26 and the Hsp26/Spd complex was ~18 nm. This value corresponds well to the expected size for the oligomeric complex of Hsp26 (Haslbeck *et al*, 1999; Bentley *et al*, 1992) and the potential Hsp26/Spd substrate complex. Spd was not detected by DLS.

Knowing the hydrodynamic particle size of the scaffold, the reaction time could be investigated at which the silica layer was expected to be thinnest. The size of silica particles formed in the presence of the starter Spd, the scaffold Hsp26 and the Hsp26/Spd template was measured at optimized conditions (0.1 M TMOS,  $t_{pre}$ : 3 min, 0.5 M potassium phosphate, 4.2  $\mu$ M Spd, Hsp26 or Hsp26/Spd, described in Materials and Methods 8.2.2.3) (Fig. 6B).

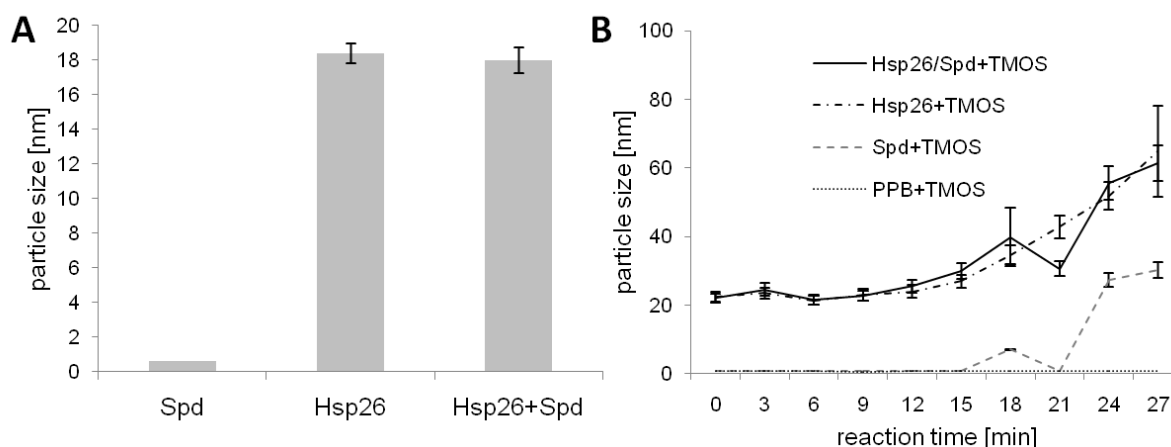


**Fig. 6:** A) DLS measurement of Hsp26, Spd and Hsp26/Spd solutions. Error bars were calculated from 3 DLS measurements. B) Particle sizes determined *in situ* by DLS over time during the biomineralization reaction with silicic acid: Hsp26 (solid line), Spd (dashed line), Hsp26/Spd complex (strong line) and a control (buffer with silicic acid, dotted line) are shown.

The weak starter Spd generated silica particles of detectable size after 15 min reaction time. These increased to particle sizes ~30 nm after 30 min. The DLS measurement showed that the scaffold Hsp26 indeed induced biomineralization of silica particles with hydrodynamic particle sizes of 24.5 nm after 3 min reaction time and ~60 nm after 30 min, confirming previous findings (Fig. 4A-C, Fig. 6) that Hsp26 scaffolds formed bigger silica particles than the starter Spd alone. The particle size detected for the Hsp26/Spd-complex used as a template did not differ significantly in DLS measurements.

Since no significantly bigger particle size was detected for the Hsp26/Spd-complex template compared to Hsp26 as a scaffold, although the light scattering was significantly higher for the

complex (Fig. 4A-C), the difference in light scattering might be due to the number of particles obtained. Significant changes in the hydrodynamic particle size of biomineralized Hsp26 scaffold or Hsp26/Spd template were detected only after 10 min.

In the biomineralization reaction with the Hsp26/Spd template, a reaction time of 10 min or less leads to biominerals containing the Hsp26 scaffold. Silica particles obtained at reaction times between 15-20 min or higher may contain biominerals generated from Spd alone. Therefore, isolating the silica particles after reaction times shorter than 10 min separated biomineralized silica particles generated from the Hsp26/Spd template from those generated from the starter Spd alone.

Anisotropy decay measurements are another powerful tool for analyzing the growth of silica particles with bound dyes *in situ* (Tleugabulova *et al*, 2004; Birch & Geddes, 2000). During Hsp26/Spd biomineralization (biomineralization conditions: 0.1 M TMOS,  $t_{pre}$ : 3 min, 0.5 M potassium phosphate, 1.05  $\mu$ M Hsp26/Spd, described in Materials and Methods 8.2.2.3), an anisotropy decay was expected to be observed due to the rotation of a fluorescent “dye”, i.e. the intrinsic fluorescence of Hsp26, bound to charged silica particles (Geddes *et al*, 2000). The anisotropy ( $r$ ) is a dimensionless quantity independent of the total fluorescence intensity and fluorophore concentration (Johnson, 2009). During the anisotropy measurement, Spd was added to Hsp26 in phosphate buffer at  $t$ : 0 s (Fig. 7).

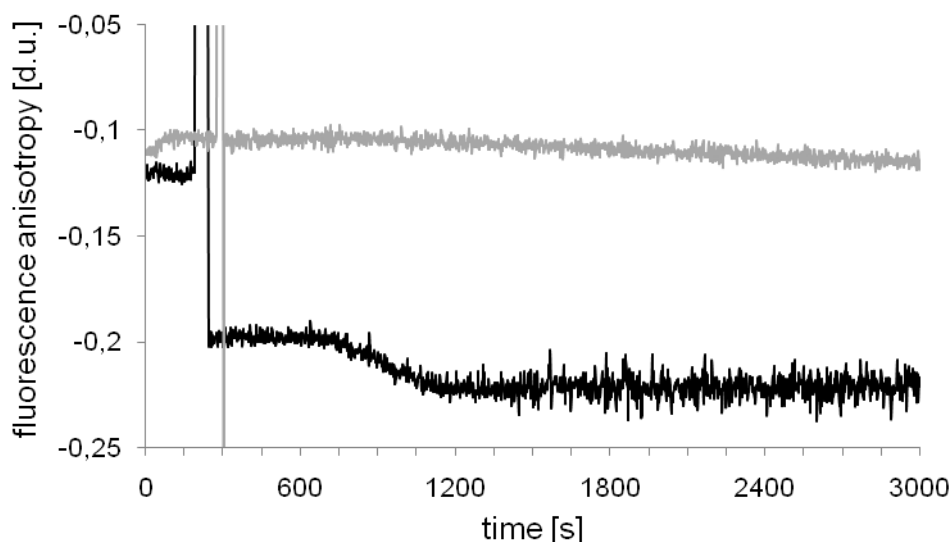


**Fig. 7:** Fluorescence anisotropy ( $r$ ) measurements of Hsp/Spd biomineralization at 20 °C. Spd was added to Hsp26 (Hsp26:Spd ratio 1:1) at  $t$ : 0 s and the biomineralization reaction was started by the addition of 0.5 M TMOS after 5 min.

Adding Spd to Hsp26 did not seem to lead to any significant change in fluorescence anisotropy ( $t$ : 0-300 s). After 5 min, TMOS was added and a sharp decrease of  $r$  was observed, followed by a lag phase of  $\sim$ 10 min and a slower additional decrease of  $r$ . After  $\sim$ 25 min, a residual anisotropy was observed with increasing noise of the signal. The kinetics

thus followed a decay expected for fluorophores intercalated in silica structures (Birch & Geddes, 2000). The anisotropy decay of a dye strongly bound to silica oligomers and nanoparticles can be fit to three components: a fast scale component associated with free dye, a slower rotational component of dye associated to primary silica particles and a residual non-decaying anisotropy component of dye bound to larger particles with slowed down rotation (Tleugabulova *et al*, 2004). Changes in the fluorescence anisotropy are explained by changes in the relative abundance of solvated fluorophore and encapsulated fluorophore, changes in silica particle size and sol micro-viscosity (Birch & Geddes, 2000). Negative fluorescence anisotropy values were caused by the automatic scaling of the spectrophotometer software (Geddes *et al*, 2000).

Fluorescence anisotropy kinetics with Hsp26 solution in the absence of Spd did not yield significantly different shapes (data not shown) and confirmed that Spd did not have a significant influence on biomineralization.

Fluorescence anisotropy experiments present promising alternatives to DLS and microscopic methods for its ability to follow silica particle formation *in situ* without the need for drying of the samples as is the case of SEM or TEM (Birch & Geddes, 2000; Lakowicz, 2006). Since DLS and fluorescence anisotropy measurements did not show significantly different particle formation kinetics for biomineralization of the Hsp26 scaffold and the Hsp26/Spd-template (Fig. 6), it remained to be determined whether the complex was not stable during biomineralization or whether the binding of the starter Spd did not increase the biomineralization activity observed for the scaffold Hsp26 significantly.

### 3.3 Hsp26 forms stable substrate complexes with spermidine

The complex formation between temperature-activated Hsp26 and a potential substrate (Spd) were analyzed using SEC-HPLC. The elution volume ( $V_e$ ) gives an estimate for the molecular mass of the species investigated. A shift to higher masses (lower  $V_e$ ) of Hsp26 was expected for a stable chaperone-substrate complex and one monomer of substrate was expected to bind to each Hsp26 dimer (Haslbeck *et al*, 1999). However, no shift in the  $V_e$  of Hsp26 was observed in comparison to Hsp26/Spd (data not shown). This may be due to the much lower MW of Spd in comparison to Hsp26.

Fluorescently labeled Spd would be expected to show a shift of the fluorescence signal upon binding to Hsp26. Aliphatic amines like Spd can be fluorescently labeled with NBD-Cl (Heberer *et al*, 1985; Ghosh & Whitehouse, 1968). The labeling procedure was adapted from the literature (Jachmann, 2001). The crude NBD-labeled Spd (NBD-Spd) was used directly in HPLC runs to test if complex formation could be observed. NBD-Spd could be detected at 475 nm. Prior to HPLC measurements, Hsp26 was temperature-activated at

43 °C for 5 min to stimulate substrate binding (Haslbeck *et al*, 1999; Haslbeck, 2002). With NBD-Spd, a complex between the chaperone and the organic starter could be observed (Fig. 8).

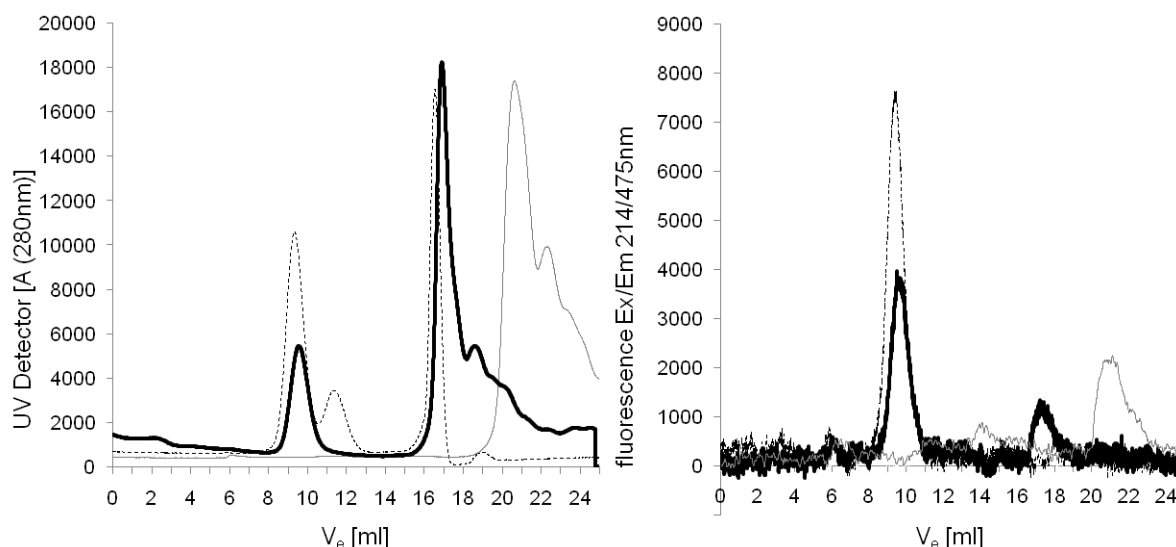


**Fig. 8:** HPLC analysis of Hsp26/NBD-Spd-complex formation. HPLC-detectors: UV-absorption at 280 nm (left) and fluorescence (Ex/Em 214/475 nm) (right). HPLC samples in this figure: Hsp26 solution (dashed line, 1 mg/ml), NBD-Spd solution (gray line, 1 mg/ml), Hsp26/NBD-Spd solution (strong solid line, 0.5 mg/ml). NBD-Spd:Hsp26 was 77:1

The  $V_e$  of NBD-Spd shifted considerably from ~22 ml to ~17 ml, which corresponds to Hsp26 dimers expected to form when submitting Hsp26 to heat shock [1]. This shift of NBD-Spd to higher mass was observed both for the fluorescence signal as well as for the absorption at 280 nm. Since no residual peak of NBD-Spd was observed in the complex, it was concluded that all NBD-Spd was bound to Hsp26. NBD-Spd was purified and used for biomineralization experiments, in order to prove the presence of NBD-Spd within the silica particles generated by the Hsp26/NBD-Spd complex.

### 3.4 Hsp26 and spermidine are localized within the biomineral

Although DLS measurements did not detect significant differences in the particle size of biomineralized Hsp26 and the Hsp26/Spd complex (Fig. 6), light scattering experiments clearly showed a higher signal for the complex (Fig. 4). Furthermore, the stability of an Hsp26/Spd complex has been proven with the HPLC measurements shown in Fig. 8.

Silica particles generated with the Hsp26/NBD-Spd complex (biomineralization conditions: 0.1 M TMOS,  $t_{pre}$ : 3 min, 0.5 M potassium phosphate, 4.2  $\mu$ M Spd, Hsp26 or Hsp26/Spd, described in Materials and Methods 8.2.2.3) showed specific fluorescence and no label-free silica particles were observed (Fig. 9A). Since all silica particles showed fluorescence and silica particles were induced by the biomineralization activity of the Hsp26 scaffold, this experiment indicated that NBD-Spd must be localized within the biomineral induced by the complex.

A major fluorescence loss by photo-bleaching was observed within  $\sim 1$  s (Fig. 9B). In comparison, the free NBD-Spd solution even higher fluorescence loss by photo-bleaching (not shown). It was shown that encapsulation of a fluorescent dye in a silica matrix suppressed the decay of the dye fluorescence with increasing local rigidity of the silica environment (Larson *et al*, 2008), which would explain the slightly decreased photo-bleaching of encapsulated NBD-Spd (expected to be bound to Hsp26) compared to NBD-Spd in solution.

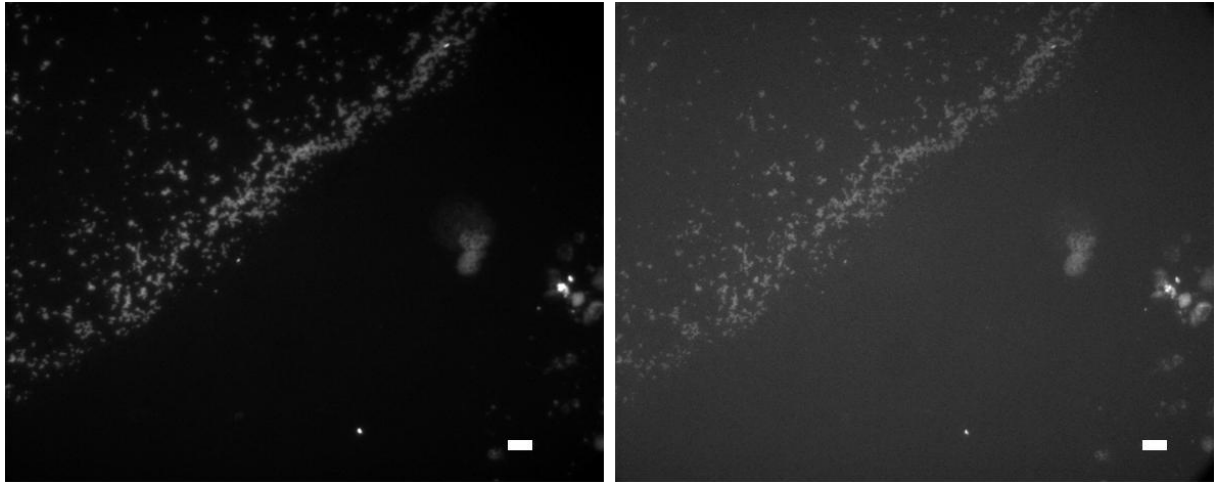


**Fig. 9: Visualization of silica particles generated with Hsp26/NBD-Spd via fluorescence (535 nm). Left: 0.1 s exposure, right: micrograph after 1 s exposure. Scale bar: 5  $\mu$ m.**

The silica particles formed in the presence of the scaffold Hsp26 and the Hsp26/Spd template (biomineralization conditions: 0.1 M TMOS,  $t_{\text{pre}}$ : 3 min, 0.5 M potassium phosphate, 4.2  $\mu$ M Spd, Hsp26 or Hsp26/Spd, described in Materials and Methods 8.2.2.3) were isolated after  $t_{\text{react}}$ : 3 min. The biomineralized Hsp26/Spd-complex used as a template resulted in silica particles small enough that after removal of the organic template by calcination, i.e. heating to 800  $^{\circ}$ C (Materials and Methods, 8.2.3), cavities within the silica particles were observed by TEM (Fig. 10).

Calcinated Hsp26/Spd complexes appeared as hollow particles with a size of  $\sim 48$  nm and with cavities of  $\sim 18.5$  nm. The size of the cavities correlated well with the size of Hsp26 oligomers in solution (Fig. 6A). Therefore, the calcination experiment indicated the localization of the Hsp26 scaffold within the biomineral.

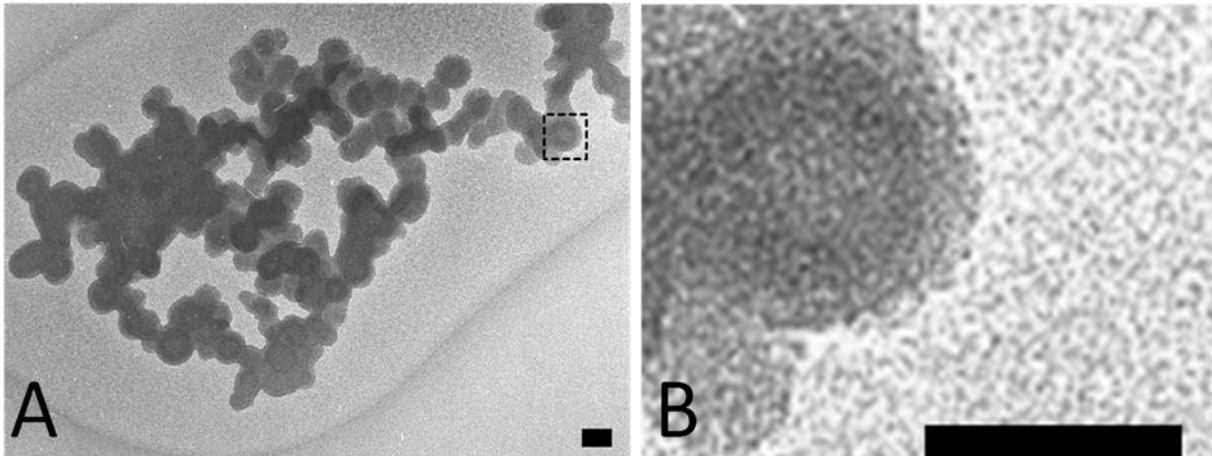


**Fig. 10:** TEM micrographs of biomaterialized Hsp26/Spd after calcination. Scale bar: 50 nm. A) hollow particle is highlighted by a square. B) Magnification of the highlighted hollow silica particle. Biomaterialization conditions: 4.2  $\mu$ M Hsp26, 4.2  $\mu$ M Spd, 0.5 M potassium phosphate, 0.1 M TMOS,  $t_{pre}$ : 3min,  $t_{react}$ : 3 min. Other biomaterialization conditions are described in 8.2.2.1.

The thickness of the silica layer was still far away from a minimal layer < 5 nm. Therefore, the biomaterialization conditions of Hsp26/Spd biomaterialization were modified in order to find the minimal particle size. To confirm the localization of the Hsp26 scaffold, all particles were calcinated (Fig. 11).

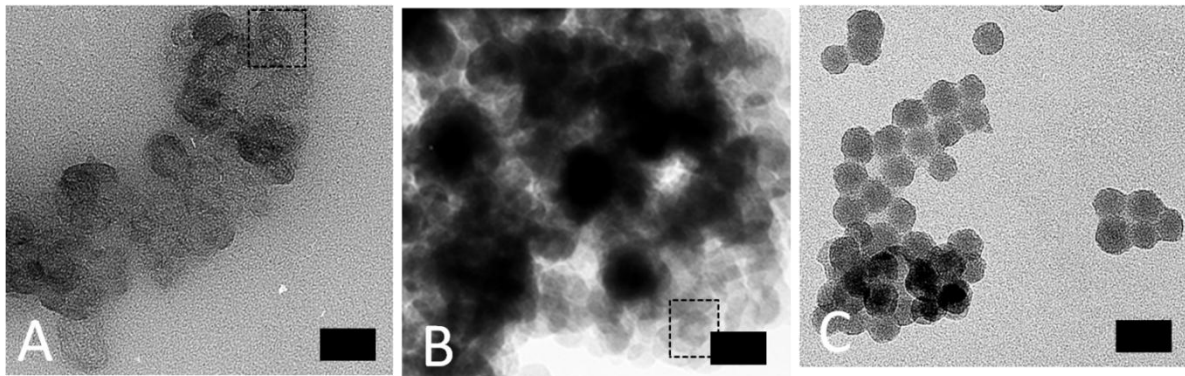


**Fig. 11:** TEM micrographs of biomaterialized and calcinated Hsp26/Spd. Scale bar: 50 nm. A-B): A hollow particle is highlighted by a square. A) pH 6.7,  $t_{pre}$ : 42 min; B) pH 7,  $t_{pre}$ : 42 min. C) 4 °C reaction temperature,  $t_{pre}$ : 42. Other biomaterialization conditions are described in 8.2.2.1.

Increasing the  $t_{pre}$  at 20 °C led to smaller particles at pH 7 and 6.7 (Fig. 11, average particle size A) ~33 nm, B) ~27 nm). However, after calcination a hollow cavity in silica particles generated at a higher  $t_{pre}$  was challenging to detect in most cases. Hollow cavities of ~16 nm could be observed which corresponded to the predicted size of Hsp26. The contrast of silica calcinated particle at lower particle size also decreased significantly.

Additionally reducing the reaction temperature to 4 °C caused unspecific silica particle formation (Fig. 11C), since after calcination no hollow cavity was found. Apparently, the chaperone/substrate-template did not associate to silica at low temperatures. Screening

further reaction conditions with the Hsp26/Spd-complex as template did not result in any morphologies with thinner silica deposition.

### **3.5 Scaffold induced biomineralization activity is too high for retention of nano-structure**

It is known that amines and polyamines have catalytic activity for silicic acid polymerization in water at neutral pH (Mizutani *et al*, 1998). The presence of amino-groups on the surface of oligomeric protein scaffold seemed to be sufficient for scaffold-induced silica deposition (Fig. 5).

Based on the biomineralization conditions that first allowed the formation of hollow silica particles (Fig. 10), reaction conditions were modified with only Hsp26 as a weakly silica-inducing scaffold in order to optimize silica deposition to minimal layer thickness. It was observed that no significant difference in particle size was detected for biomineralization at 0.5 M potassium phosphate for  $t_{\text{react}}$ : 3 min (Fig. 5B) or 1min. For biomineralization with 0.1 M potassium phosphate, a minimal  $t_{\text{react}}$ : 5 min was needed for defined structures to be observed. Increasing the concentration of the Hsp26 scaffold showed little influence.

It was necessary to test if the biomineralization activity of Hsp26 scaffolds was specific to Hsp26 or universal to all protein-based scaffolds. Since the silica layer thickness needed to be limited to < 5 nm and the protein scaffold showed biomineralization activity, then the use of a scaffold/starter template leading to an increase in silica layer thickness would not support the aim of the study. If reaction conditions can be found where scaffolds are inactive in biomineralization, then stronger starters are needed as chaperone substrates.

### **3.6 Hsp26 does not form complexes with Silaffin or PEI**

One aim of this study was to localize the biomineralization activity of a strong starter on a chaperone scaffold, possibly controlling silica particle formation. Since Hsp26 showed an unexpected scaffold biomineralization activity, it was of interest whether a stronger starter could be bound to Hsp26. If a set of biomineralization could be found where scaffold biomineralization was suppressed, e.g. at very low potassium phosphate concentrations (comparable to Fig. 4D) conditions, a substrate-specific biomineralization on an unreactive scaffold seemed possible.

Spd was a much weaker starter than e.g. PEI (MW: 1800, branched): PEI-induced silica particle formation causing a significant increase of turbidity clearly visible to the eye while Spd did not cause a visible turbidity change. A comparison of particle morphologies of biomineralized Spd and PEI is shown in SEM micrographs in Fig. 12.



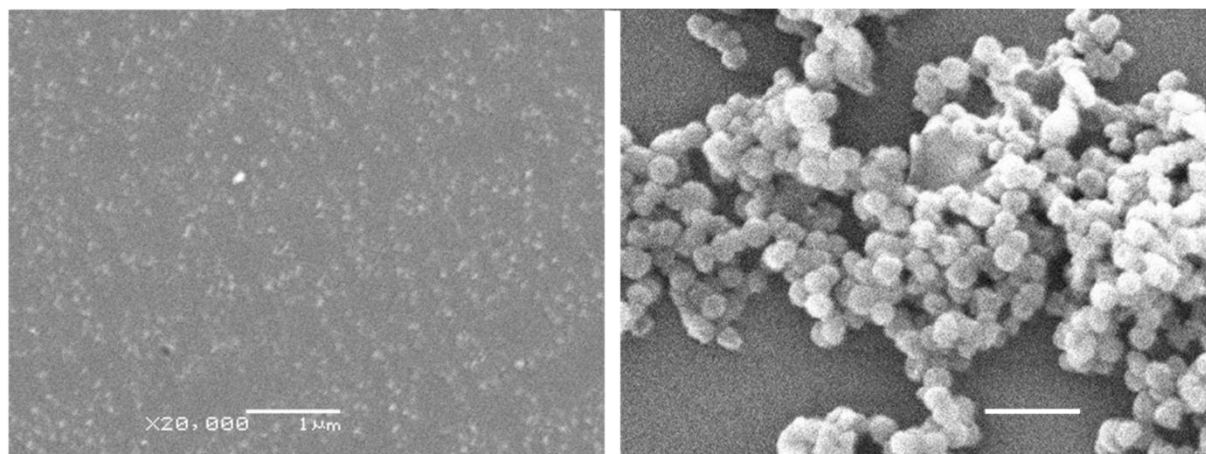


**Fig. 12: SEM micrographs of biomaterialized Spd (A) and PEI (B). Scale bar: 1  $\mu\text{m}$ . Biomaterialization conditions: 0  $\mu\text{M}$  Hsp26, 0.1 M potassium phosphate, TMOS  $t_{\text{pre}}$ : 3 min, 4.2  $\mu\text{M}$  A) Spd, B) 4.2  $\mu\text{M}$  PEI (no Spd),  $t_{\text{react}}$ : A) 30 min, B) 15 min. Other reaction conditions are described in Materials and Methods 8.2.2.1.**

However, testing PEI of different MW (1300-750 000 g/mol), no chaperone-substrate interaction could be detected (data not shown).

Silaffin was shown to be of crucial importance for silica biomaterialization in diatoms (Kröger & Poulsen, 2008). The C-terminally cys-modified R5 peptide cys-R5 (“Sil”; 1 mg/ml, sequence: sequence SSKKSGSYSG SKGSKRRILC) was used in the biomaterialization reaction instead of e.g. Spd and retained its biomaterialization activity under the conditions for the absorption measurement of the Hsp26/Spd complex (Fig. 4A). The SEM micrograph shows clear particle formation with a particle size of average 350 nm after  $t_{\text{react}}$ : 30 min (Fig. 13A).

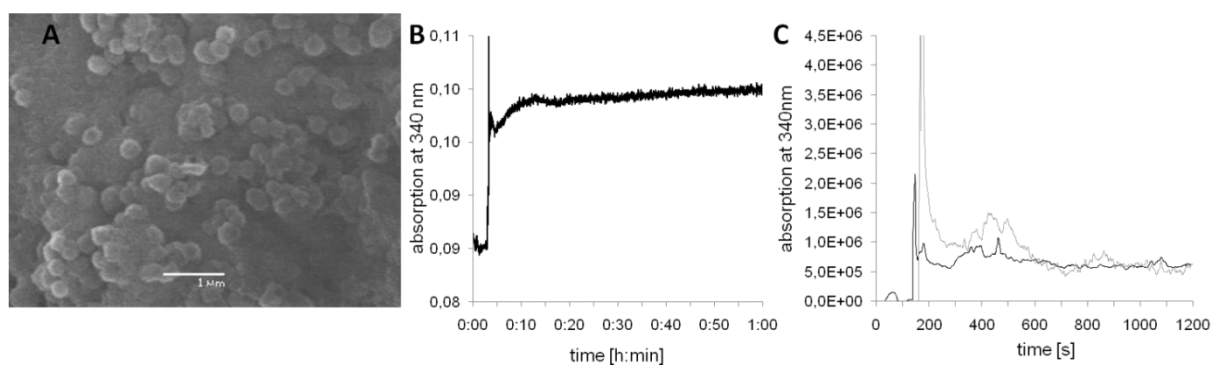


**Fig. 13: A) SEM micrograph of biomaterialized Sil. Biomaterialization conditions: 1 mg/ml Sil in 0.1 M potassium phosphate, 0.5 M potassium phosphate, TMOS  $t_{\text{pre}}$ : 3 min,  $t_{\text{react}}$ : 30 min. Other reaction conditions are described in Materials and Methods 8.2.2.1. Scale bar: 1  $\mu\text{m}$ . B) Absorption measured at 340 nm after dilution of Sil in 500 mM potassium phosphate, C) light scattering at 340 nm at 90° backscattering angle after dilution in 50 mM potassium phosphate (black line) or dilution in 500 mM potassium phosphate (gray line).**

Comparable to Spd, Sil (NBD-labeled and unlabeled) did not show any significant mass shift indicating a chaperone-substrate complex (data not shown). At physiological temperatures, the chaperone  $\alpha$ -crystallin has been shown to interact with the aggregation-prone B chains of insulin (Farahbakhsh *et al*, 1995; Haslbeck, 2002). To prove a stable chaperone-Sil-complex,

it was investigated if chaperones could prevent Sil aggregation. An increase in absorption was observed at 340 nm when Sil was diluted in 500 mM potassium phosphate, indicating a possible aggregation caused by the high buffer concentration (Fig. 13B) (Schrödel & de Marco, 2005; Nominé *et al*, 2001). The sudden increase in the baseline could have been caused by very rapid aggregation of Sil. However, a real Sil aggregation was not confirmed by light scattering measurements at 90 ° backscattering angle (Fig. 13C). Since Sil does not aggregate under the conditions investigated, an aggregation assay with chaperones could not be carried out.

### **3.7 Biom mineralization activity is observed for all protein scaffolds**

It was tested if protein scaffolds generally show biom mineralization activity. The slower particle formation with 0.1 M potassium phosphate was chosen as the best starting condition for testing biom mineralization with other scaffolds. An optimized set of generalized biom mineralization conditions for protein scaffolds based on the Hsp26 scaffold biom mineralization protocol is proposed in Materials and Methods 8.2.2.1.

#### **3.7.1 The chaperone GroEL/ES scaffold induces biom mineralization**

GroEL/ES possesses a central 45 Å cavity, which encloses the substrate proteins in a protected hydrophilic environment that allows them to fold in an ATP-dependent manner (Braig *et al*, 1994; Young *et al*, 2004; Fenton *et al*, 1994). GroEL is a cylindrical protein and depending on binding one or two units of GroES, bullet- or football-like structures were observed (Grallert *et al*, 2000). Non-spherical scaffolds present an opportunity for biom mineralized, non-spherical structures.

The GroEL/ES complex was prepared as described in the literature (Grallert *et al*, 2000). It was observed by TEM prior to the biom mineralization (Fig. 14C). The TEM micrograph clearly shows the bullet-like morphology of the GroEL/ES complex from different perspectives. The complex was observed to have a size of ~14-17 nm viewed from the side and ~ 9-11 nm viewed from the top.

Light scattering kinetics similar to previous experiments with Hsp26 (Fig. 4, Materials and Methods 8.2.2.1) were carried out with GroEL, GroES and the GroEL/ES chaperone complex which were used as a non-spherical scaffolds without any starter substrate. Biom mineralization was carried out in 0.1 M potassium phosphate (pH 7) and 0.5 M TMOS (Fig. 14A). Silica particles obtained after the kinetics with TMOS concentrations of 0.1 and 0.5 M were isolated and analyzed with DLS (Fig. 14B).

The light scattering signal showed a slightly higher signal for the GroEL/ES complex compared to GroEL. GroES alone did not show significant light scattering higher than the control with TMOS in the same buffer.

GroEL/ES was biomineralized based on the set of reaction conditions described in Materials and Methods 8.2.2.3. Morphologies of biomineralized GroEL/ES were observed by TEM for 0.1 and 0.5 M potassium phosphate (Fig. 14D-E). After GroEL/ES biomineralization with 0.5 M potassium phosphate, regular and spherical silica particles of ~32-40 nm were observed after  $t_{\text{react}}$ : 5 min (Fig. 14D); using 0.1 M potassium phosphate, more irregular and partially interconnected spherical silica particles of ~29-53 nm were observed after  $t_{\text{react}}$ : 10 min (Fig. 14E). DLS measurements confirmed smaller particle sizes with 0.1 M TMOS (Fig. 14B) and did not show significant differences in size for GroEL and GroEL/ES biomineralization (not shown). Despite the small particle size, the morphology in (Fig. 14E) was too inhomogeneous to confirm non-spherical morphologies. Calcination of both samples was carried out; however no clear cavities were observed (data not shown).

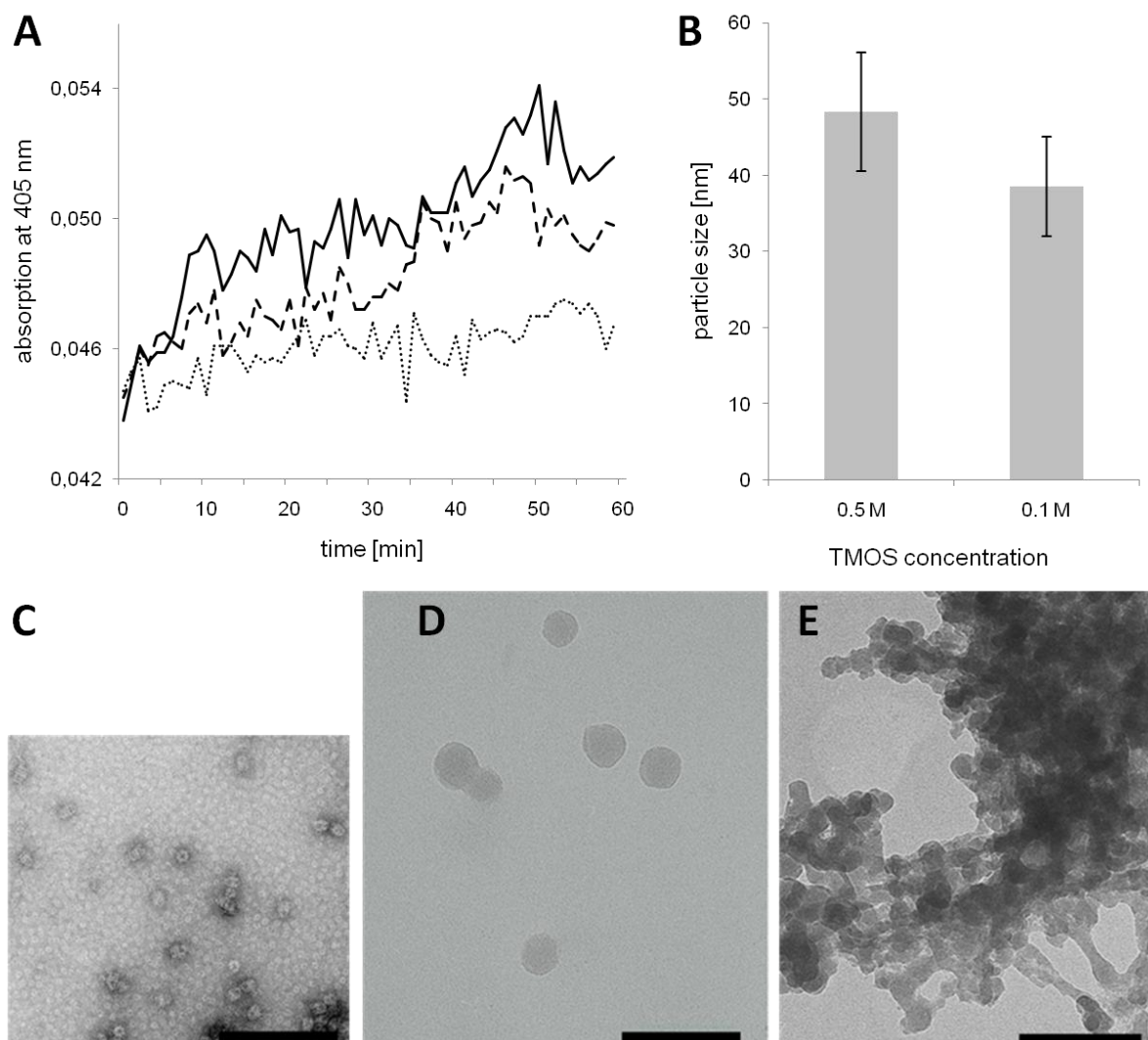


**Fig. 14:** GroEL/ES induced biomineralization. A) Light scattering caused by particle formation by GroEL, GroES and GroEL/ES solutions in 0.1 M potassium phosphate (pH 7) (0.1 M TMOS,  $t_{\text{pre}}$ : 6 min): 4.2  $\mu\text{M}$  GroEL (dashed line), 4.2  $\mu\text{M}$  GroES (dotted line), GroEL/ES (4.2  $\mu\text{M}$ ) complex (solid line). B) DLS measurement of biomineralized GroEL/ES after the light scattering kinetic ( $t_{\text{react}}$ : 60 min) using the intensity distribution (Materials and Methods 8.5.1.1). C) TEM micrograph of negative stained GroEL/ES complex, D-E) of biomineralized GroEL/ES. Biomineralization conditions: GroEL/ES (1 mg/ml in 0.1 M

potassium phosphate), 0.5 M TMOS, D)  $t_{\text{react}}$ : 5 min, E)  $t_{\text{react}}$ : 10 min. Other biomineralization conditions are described in Materials and Methods 8.2.2.3. Scale bar (C-D): 100 nm.

### 3.7.2 Different fibrillar scaffolds show biomineralization activity

The use of fibrillar scaffolds as 1D-templates for silica nano-wires presents promising applications in fields like micro-electronics, micro-fluidics and micro-electromechanical systems (Gazit, 2007). Actin filaments, that play a central role in the cytoskeleton (Mager & Ferreira, 1993), had been used as fibrillar scaffold (Fig. 15A-B).

Amyloid fibrils are naturally occurring fibrillar assemblies that are associated with human disorders (Scheibel, 2005; Hamada *et al*, 2004). They have been found to be useful templates for the formation of conductive metal wires (Scheibel, 2005). Different amyloid scaffolds could be formed by short peptide building blocks and may present novel approaches for biomineralized nano-wires with different structural and possibly functional properties (Reches *et al*, 2002; Tjernberg *et al*, 2002). In this study, actin fibers were biomineralized (Fig. 15C).

Negative stained fibrillar actin was analyzed by TEM (Fig. 15A). It showed an average fibril thickness of ~30 - 35 nm and a length of over 1  $\mu\text{m}$ . The most uniform fibrillar biominerals were observed with 0.1 M TMOS, as described in Materials and Methods 8.2.2.3, with a silica layer thickness of ~25 - 110 nm (Fig. 15B). Scaffold-directed biomineralization with 0.1 M TMOS also led to well-defined biomineralized amyloid fibrils with a thickness of ~15 - 25 nm. (Fig. 15C) Interestingly, lower TMOS concentrations did not lead to thinner silica nano-tubes, but ill-defined silica morphologies with heavily interconnected non-homogeneously coated fibrils (not shown). Lower reaction temperatures in combination with 0.1 M TMOS led also to ill-defined networks (data not shown).

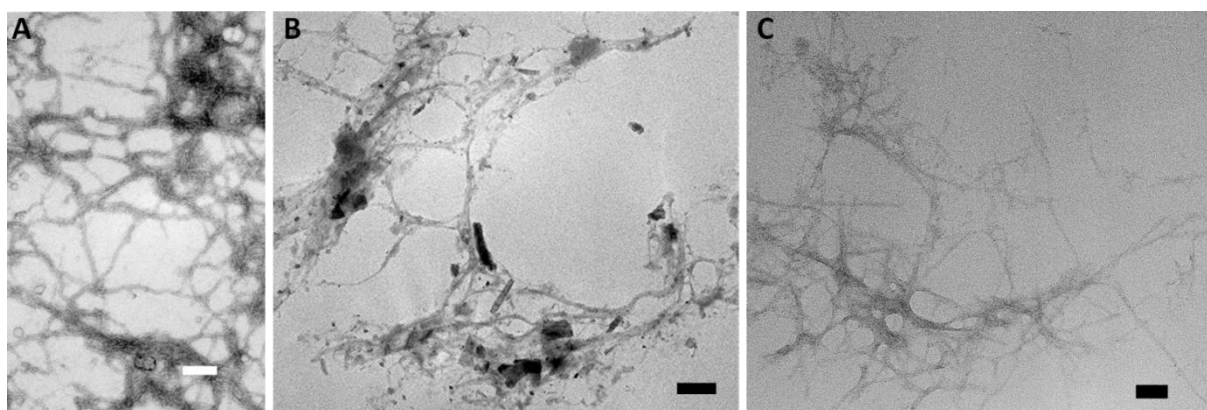


**Fig. 15:** TEM micrograph of A) negative stained fibrillar actin solution (refer to Materials and Methods 8.6.3.2). B) TEM micrographs of biomineralized actin fibrils. Biomineralization conditions: 0.4 mg/ml actin fibrils, 0.1 M TMOS,  $t_{\text{pre}}$ : 3min,  $t_{\text{react}}$ : 5 min. C) TEM micrographs of biomineralized amyloid fibrils. Biomineralization conditions: 0.1 M TMOS,  $t_{\text{pre}}$ : 3min,  $t_{\text{react}}$ : 10 min. (Amyloid concentration: refer to Materials and Methods 8.1.1.) Other biomineralization conditions for B) and C) are described in Materials and Methods 8.2.2.3. A-C) Scale bar: 400 nm.

Even if fibrils were very thin as in samples shown in Fig. 15A-B, calcination did not show any clearly visible hollow structures in the conventional TEM (data not shown), although the contrast of the samples seemed to decrease.

It seemed that at neutral pH, protein scaffolds showed biomineralization activity. The original aim of nano-structured scaffold-starter-templates with silica layers < 5 nm could not be achieved due to this effect. Changing the reaction conditions to suppress scaffold biomineralization activity in order to control the biomineralization activity by binding of a strong starter to the scaffold was not successful. The biomineralization activity of the chaperone scaffold in absence of any substrate was therefore used to investigate new microscopic silica hybrid structures.

### 3.7.3 Scaffolds from microorganisms show biomineralization activity

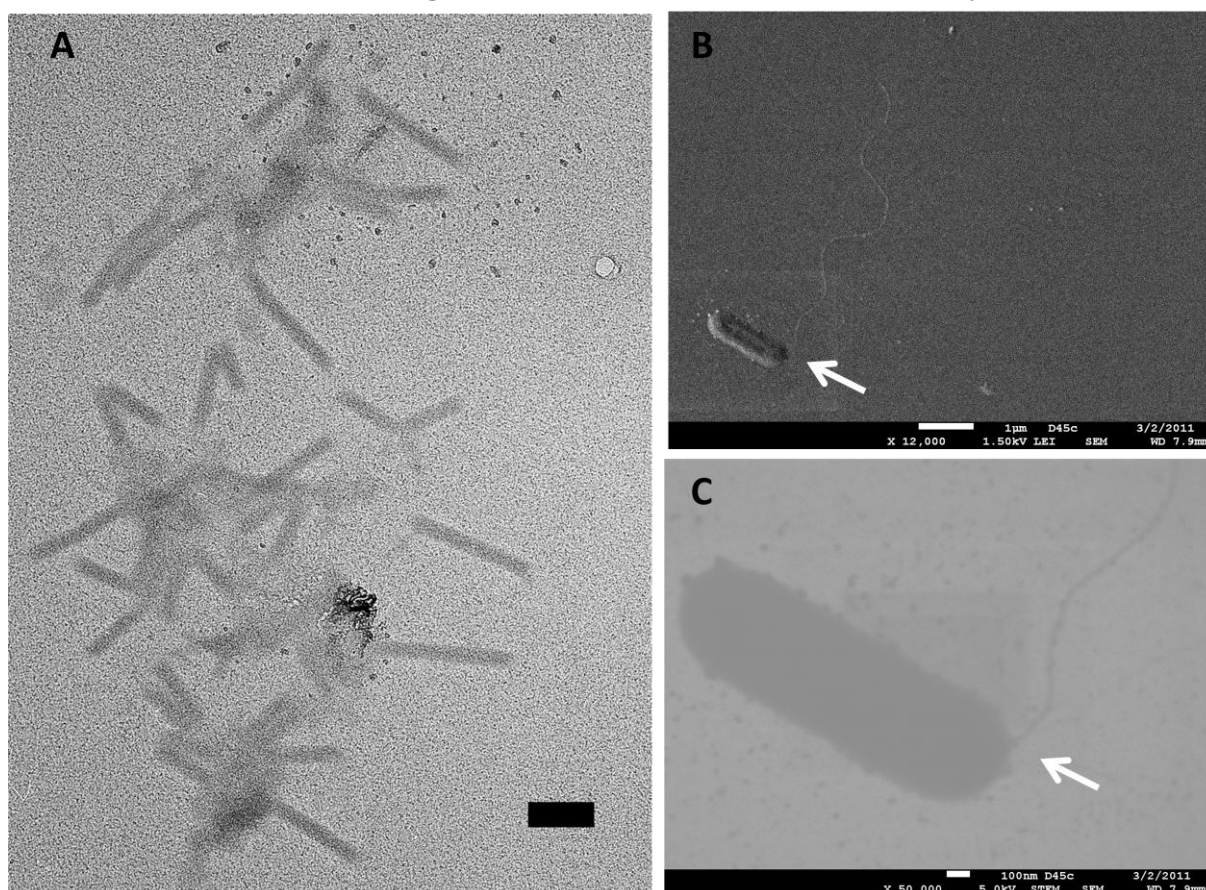


**Fig. 16:** TEM micrographs of biomineralized Baculovirus capsids after A)  $t_{\text{react}}$ : 5 min, B)  $t_{\text{react}}$ : 10 min. Scale bar: 200 nm. B) High resolution micrograph of unspattered biomineralized bacteria. SEM using the LEI detector at a working distance of 7.9 mm and 1.5 kV acceleration voltage; scale bar: 1  $\mu\text{m}$ . C) STEM at a working distance of 7.9 mm and 5 kV acceleration voltage; scale bar: 100 nm. Biomineralization conditions are described in Materials and Methods 8.2.2.3. The white arrows highlight the bacteria and flagellum.

The applicability of the encapsulation protocol to diverse scaffolds was tested with two different microorganisms. Viral structures are highly attractive organic templates (Gazit, 2007). The silification of tobacco mosaic virus particles has been one of the first studies in

---

bio-nanotechnology (Royston *et al*, 2006). Using the encapsulation process described in as described in Materials and Methods 8.2.2.3, it was tested whether Baculovirus capsids as scaffolds showed biomineralization activity. The resulting TEM micrograph of the silicified capsids is shown in Fig. 16A. The biomineralized capsids appeared as nano-rods in the TEM with a length of ~400 nm and a thickness of ~45 nm after 5 min (Fig. 16A) and ~40-60 nm after 10 min reaction time (data not shown). The sample was also analyzed after calcination, but other than decreased contrast resulting from the loss of the organic scaffold, no hollow cavity was observed (data not shown).

The encapsulation process was successful even with unconventional scaffolds such as living *E. coli* bacteria. Bacteria could be encapsulated within 5 min under mild conditions, retaining their original structure. The resulting silicified bacterium is shown in Fig. 16B-C. The silica-covered flagellum had a thickness of ~34 nm, comparable to biomineralized Hsp26 (e.g. Fig. 5A). The presence of the elements silicium and carbon was detected by EDX measurements in the SEM mode (data not shown) and the contrast observed in the STEM mode (Fig. 16C) confirmed the presence of silica. To further confirm the presence of carbon in the biomineralized structures, calcination was carried out. However, other than decreased contrast, no cavities were observed.

## 4 Discussion

Screening with different types of short amines like Spd can be carried out using light scattering and HPLC measurements and *in situ* DLS measurements as fast and reliable tools to determine possible biomineralization complexes. The localization of the scaffold was confirmed by calcination and that of the substrate by e.g. fluorescence microscopy. The presence of the organic scaffold in the silica structures could also be confirmed by elementary analysis with EDX spectroscopy with the JSM 7500 microscope (data not shown). The biomineralization activity from the scaffold and the starter was observed separately (Fig. 4).

The Hsp26/Spd complex improved the biomineralization activity of the Hsp26 scaffold which surprisingly showed significant biomineralization activity on its own (Fig. 4A-C). Since it has been discussed that a molecule's biomimetic silica formation activity is strongly dependent upon the presence of amines (Currie & Perry, 2007), Spd was a valuable starting point for the templating of chaperone/biomineralization starter complexes. Hsp26 which could be expressed in high amounts (as described in Materials and Methods 8.4.1) and fulfilled the need for high amounts of protein scaffolds for numerous experiments. In extensive TEM studies on Hsp26 which was available in large amounts, a set of biomineralization conditions could be pre-optimized (as described in Materials and Methods 8.2.2.3) for other, less readily available protein scaffolds.

It was expected that one Spd would bind to each Hsp26 dimer (Haslbeck *et al*, 1999). However, based on the results of from the SEC-HPLC measurements (Fig. 8), it was observed that a great excess of NBD-labeled Spd (77:1 relative to Hsp26 monomers) was able to completely bind to the chaperone. Future studies of the stability of this Hsp26/Spd complex with regards to the NBD-labeled Spd excess binding to the chaperone would be of interest.

Anisotropy measurements (Fig. 7) did not correlate well with TEM measurements. A significant change in the anisotropy was observed for higher  $t_{\text{react}}$ , while particle formation was observed after 1-5 min (Fig. 5, Fig. 6). The anisotropy measurements were possibly not precise enough to detect nano-spheres. However, they could be a great tool for investigating chaperones bound to fluorescent substrates during biomineralization.

Hollow silica particles below 100 nm have been reported before, e.g. using single  $\text{Fe}_3\text{O}_4$  nanocrystals as cores and cetyltrimethylammonium bromide as surfactant and organic template leading to mesopores in a sol-gel reaction (Kim *et al*, 2008). Removal of the  $\text{Fe}_3\text{O}_4$  core was carried out by heating the silica particles at reflux at pH 1.4. Other methods for hollow silica particle formation involved multiple steps, e.g. templating of condensed silica

particles on preformed spheres (Caruso *et al*, 1998) or condensed *in situ* onto polymer droplets stabilized by surfactants (Fowler *et al*, 2001), were cost-intensive, e.g. due to growth in supercritical CO<sub>2</sub> (Wang & Caruso, 2005). It has been reported that silicic acid polycondensation catalyzing amines formed hollow particles at neutral pH and mild temperatures in aqueous media (Belton *et al*, 2008). This amine droplet microemulsion approach led to bigger silica particles of 200-300 nm with a central void of 50-100 nm and mixture of solid and hollow particles were observed in all cases.

The biomineralization process has the advantage that it can be applied to different scaffolds with a multitude of protein morphologies and that it leads to hollow silica < 50 nm. Nano-scaled processing (< 50 nm) in silicification is referred to as micro-morphogenesis (Crawford *et al*, 2001). Except for the calcination step, the process occurs in one step and within a few minutes at mild temperatures and pH. The resulting hollow particles (Fig. 10) seem to present similar morphologies than those presented in the mentioned study on mesoporous silica shells (Kim *et al*, 2008). Mesoporous properties of biominerals need to be investigated, since they could present an opportunity for application as drug-delivery vehicles that would be small enough to circulate through blood vessels (Slowing *et al*, 2007; Drummond *et al*, 1999; Johnson *et al*, 2007).

It was of interest to further investigate if Hsp26 binds Sil, in case reaction conditions can be found where the chaperone scaffold was biomineralization-inactive and biomineralization would be induced by the substrate Sil only. However, Sil did not spontaneously aggregate (Fig. 13B-C) and a chaperone effect of Hsp26 suppressing aggregation could therefore not be tested. In another approach, NBD-labeling of Sil was also too unstable to determine complex formation using HPLC (data not shown). The organic starter PEI did also not form complexes with Hsp26 (data not shown).

Organic nano- and micro-structures generally showed biomineralization activity at neutral pH. Although this effect hindered the aim of nano-structured morphologies, this phenomenon could be used for application to diverse protein templates with a generalized approach without extensive optimization for each substrate.

Non-spherical chaperone scaffolds like GroEL/ES (with football/bullet morphologies) were of higher interest, since non-spherical silica particles are more challenging to synthesize than spherical particles. The biomineralization conditions have to be controlled to obtain thinner silica layers as observed in (Fig. 14D-E) to observe a hollow cavity from the GroEL/ES scaffold after calcination and to prevent a thick silica layer from delete all non-spherical structural information of the non-spherical scaffold.



Challenges with the preparation of biomineralized particles were the localization of silica particles with TEM. As opposed to silica particles obtained by silaffin or PEI catalysis, which can be easily investigated using SEM and DLS, biomineralized nanoparticles on scaffolds like Hsp26 were not visible to the eye. After calcination experiments, in some cases particles could not be measured due to loss during the sample preparation (e.g. particle adhesion to the quartz tubes). For practical purposes, carbon grids prepared without glow discharge led to local assemblies of particles that could be investigated. A useful method for the separation and investigation of small biominerals < 50 nm could be the flow field-flow fractionation, which, coupled with MALS leads to better results than e.g. DLS (Augsten *et al*, 2008).

Comparing actin and amyloid biomineralization (Fig. 15), it was observed that the nature of the fibrillar scaffold influenced the silica layer thickness slightly. This probably was due to different surface charges and/or amino groups of the different fibrillar scaffolds.

As shown in Fig. 16, the preparation of 3D hybrid micro/nano-silica architectures using living bacteria as scaffolds was possible using the one-step biomineralization protocol, resulting in structures which have previously been described as possible bioreactors (Wang & Mao, 2009).

It was also demonstrated that a biomimetically constructed extracellular nano-coat with a thickness of 100 nm can confer thermotolerance on living cells and that a uniform silica nano-shell suppresses water loss of coated cells (Wang *et al*, 2010; Baca *et al*, 2006). Since the biomineralization process was shown to work with bacteria without any further optimization, further studies with other living cells would be of interest. Coating different types of cells with silica could allow novel applications in cell engineering (Neethirajan *et al*, 2009). To investigate viability of cells after biomineralization, genetically encoded biosensors utilizing fluorescent proteins like GFP could be used to investigate biological activity (Wang *et al*, 2009).

It was shown that nanostructured silica diatom frustules could be converted into nanocrystalline silicon replicas using magnesiothermic reduction (at comparably low temperatures of 650 °C), leading to photoluminescent replicas that retained their microscale morphology (Bao *et al*, 2007). Other approaches like the gas/silica displacement technique displace silica with magnesia or titania while retaining the nanoscale structures (Sandhage *et al*, 2002). Using similar treatment on different morphologies upon biomineralization, this would open new opportunities in the fields of biosensors and catalytically active materials.

It was observed that the encapsulation process with one set of biomineralization conditions was slow and unspecific with regards to silica deposition on any protein scaffold. In order to reach nano-structured morphologies, the silica deposition must be controlled to be as

substrate-specific as possible. The opposite strategy leads to applications of generalized protein immobilization, which was applied for studying protein entrapment.

---

## Part 2: Entrapment of enzymes and antibodies in silica particles

### 5 Introduction

In the last decade a variety of different approaches of encapsulating biomolecules in silica particles have been investigated (Hanefeld *et al*, 2008; Shtelzer *et al*, 1992; Reetz *et al*, 1996). However, the methods utilized for immobilization of different enzymes vary substantially.

#### 5.1 Directed entrapment as a bioinspired immobilization technique

The *in vivo* process of silicic acid condensation in diatoms is profoundly influenced by biosilica-associated peptides (e.g. silaffins in diatoms (Kröger & Poulsen, 2008; Kröger *et al*, 2001; Sumper & Kröger, 2004), silicateins in marine sponges (Cha *et al*, 1999) and long-chain polyamines (LCPA) (Poulsen *et al*, 2003) that are capable of precipitating silica. Recently, an enzyme immobilization via silaffin-mediated entrapment was reported in this context (Marner *et al*, 2009). However, the synthesis of silaffin or silaffin-like peptides is cost intensive in comparison to classical sol-gel chemicals (Ramanathan *et al*, 2009). Amines and polyamines have catalytic activity for silicic acid polymerization in water at neutral pH (Mizutani *et al*, 1998). In general, these positively charged biomacromolecules interact with anionic silicates to form silica nanoparticles enhancing the process of sol-gel formation at mild conditions (Coradin & Livage, 2007).

Alternatively, for several enzymes, directed entrapment methods utilizing proteins covalently linked to silica-affine sequences (Johnson *et al*, 2007), magnetic nanoparticles (Chien & Lee, 2008) or silaffins (Luckarift *et al*, 2004; Marner *et al*, 2009) were described. After silification, the enzymes proved to be active and thermally stabilized (Marner *et al*, 2009). The drawback of these direct entrapment methods is the need for an additional covalent binding the target protein to the silaffin sequence (Nam *et al*, 2009).

#### 5.2 Immobilization of enzymes into mesoporous silica is highly protein-specific

Besides direct entrapment, the immobilization of enzymes into mesoporous particles has been investigated (Díaz & Balkus Jr, 1996; Lei *et al*, 2002; Han *et al*, 1999; Fan *et al*, 2003). Mesoporous silica are porous materials with extremely high surface areas and pore sizes in the range of 2-50 nm (Kresge *et al*, 1992). Their pore sizes are comparable to the diameter of enzymes, making them useful as supports for enzyme immobilization (Díaz & Balkus Jr, 1996; Lei *et al*, 2002). However, this method presents some disadvantages, like leaching of the proteins due to relatively weak physical adsorption between the enzyme and the siliceous surface (Wang & Caruso, 2005; Takahashi *et al*, 2000). To prevent these leaching effects,

further reaction steps such as crosslinking (Kim *et al*, 2005), specific variation of the pore size (Sierra & Guth, 1999; Wei *et al*, 2002) or coating of immobilized enzymes with nanoscale multilayer shells of mesoporous silica (Wang & Caruso, 2005) are necessary to stabilize protein binding.

In general, mesoporous silica immobilization of enzymes seems to be dependent on the size and isoelectronic point (pI) of the enzyme as well as of the size of the mesopores and pH of the solution (Lei *et al*, 2002; Díaz & Balkus Jr, 1996). Thus, mesoporous silica is rather ill-suited in terms of a robust, general entrapment strategy. Especially the control of the pore size of the particles is technically complicated and optimization is needed specifically for each protein to be entrapped. To cover a large number of target proteins, a more general strategy enabling the generation of particles in a wide range of pore sizes and more independent of the pI of the target protein is needed.

### **5.3 Sol-gel entrapment is a mild and versatile method for enzyme immobilization**

A widely used enzyme immobilization methodology utilizes silica sol-gel techniques (Pierre, 2004), where entrapping of an enzyme or whole cells is achieved randomly throughout the chemical formation of highly porous silica (Hanefeld *et al*, 2008; Avnir *et al*, 2005). "Sol-gel entrapment" has been employed to describe the immobilization of numerous enzymes (such as glucose oxidase, phosphatase, trypsin, aspartase, carbonic anhydrase, chinitase and monoamine oxidase) into amorphous silica (SiO<sub>2</sub>) derived majorly from the precursor tetra methyl ortho-silicate TMOS (Shtelzer *et al*, 1992). For the enzymes, this technical approach is rather mild since the sol-gel process can be carried out at physiological temperature and pH conditions (Hench & West, 1990), avoiding degradation during entrapment (Wright & Sommerdijk, 2001). Since the most important goal during the entrapment of enzymes is the retention of enzymatic activity, techniques which work at mild processing conditions are preferable.

In the sol-gel process, the reaction kinetics of the hydrolysis of the silica precursor and subsequent polycondensation of silicic acid as well as the resulting silica particle sizes and morphologies are influenced by the solvent in which the silica precursor was hydrolyzed, the type of silicon alkoxide, reaction temperatures, reaction media and additives (Hench & West, 1990). Only operating below the crystallization temperature of the silicium oxide, allows the generation of amorphous silica (Wright & Sommerdijk, 2001). Although standard sol-gels are relatively brittle (Hanefeld *et al*, 2008), they can be mechanically strengthened by including porous glass beads or silica glass fibers during the sol-gel synthesis (Orçaire *et al*, 2006; Reetz *et al*, 2003).

Since the enzyme is incorporated in the silica sol-gel passively during the chemical gel-forming reaction, different enzymes may have significant influence on the silica gelation process itself (Pierre, 2004). Protein backbones can act as templates for silica networks (Dunn *et al*, 1998; Zusman *et al*, 1992; Perry & Keeling-Tucker, 2000), and possible influences of enzymes on silica gelation have been discussed (Pierre, 2004). E.g. for lipase, an interaction between the enzyme and the silica network, which is based only on a biopolymer-templating effect, was discussed (El Rassy *et al*, 2004).

#### **5.4 Immobilized enzymes present numerous advantages and applications**

Silica encapsulated enzymes show a number of advantages in comparison to the respective free enzymes. Upon immobilization, enzymes are often stabilized, and thus less sensitive toward environmental conditions (Hanefeld *et al*, 2008). Additionally, the solid support might allow multiple or repetitive use of a single batch of enzymes (Jaeger & Reetz, 1998; Jaeger *et al*, 1999; Gómez *et al*, 2006) and to stop the enzymatic reaction rapidly by removing the enzyme-containing silica particles from the catalysis reaction (Gómez *et al*, 2006; Ricca *et al*, 2010). Thus, the product of the catalyzed reaction is usually not contaminated with the silica incorporated enzyme, which is highly important in the context of applications in production of food and pharmaceuticals (Gómez *et al*, 2006). Besides such applications in industrial catalysis, the enzyme-loaded silica particles gained increasing interest from a biomedical point of view as biodegradable materials (Finnie *et al*, 2008) and diagnostic biosensing or screening devices (Podbielska & Ulatowska-Jarza, 2005; Lebert *et al*, 2008).

#### **5.5 Aim of the study**

Protein/silica interactions are a key point for the control of silica polymerization (Coradin *et al*, 2003). The aim of the second part of this PhD study was to establish a generalized support-free sol-gel entrapment protocol for different enzymes using a silica formation starter which would suppress protein-specific effects. Efficiently immobilized, fully functional enzymes and antibodies are of interest in the context of biosensors and biocatalysts.

## 6 Results

### 6.1 PEI-induced silica particle formation is controlled by the reaction conditions

The polymer PEI is a positively charged polyelectrolyte (pK 9.7) and is characterized by the general formula  $(-\text{CH}_2-\text{NH}-\text{CH}_2-)_n$  (Lukovkin *et al*, 1973). Polyelectrolytes are charged polymers that interact with oppositely charged proteins (Chen *et al*, 1999; Nath, 1995). As a polycationic molecule PEI catalyzes silica polymerization in the presence of phosphate anions that facilitate self-association of the positively charged molecules (Hildebrand, 2008; Sumper & Kröger, 2004). Both linear polyamines (Brunner *et al*, 2004; Yuan & Jin, 2005) and dendritic polyamines (Knecht *et al*, 2005) have been documented to form biogenic silica.

As a simple, commercial and robust polyamine starter, polyethyleneimine (PEI), a branched cationic polymer (MW: 1800 g/mol) with high positive charge density was chosen. Unless stated otherwise, PEI will refer to the polymer with MW: 1800 g/mol. It was shown to have the ability to form silica sol-gels from monosilicic acid *in vitro* (Patwardhan, 2002; Bauer *et al*, 2007; Demadis & Stathoulopoulou, 2006). PEI is also environmentally friendly and has found several uses in biomedical applications proving its compatibility with biological systems (Mavredaki *et al*, 2007). In a comparative approach, it was studied how variations in the reaction conditions influenced the resulting morphologies of the sol-gel in terms of particle size and surface area.

#### 6.1.1 Light scattering is used to determine silica particle formation kinetics

Previous studies showed that at basic pH, silica particle formation with PEI was fastest and led to higher particle sizes with increasing pH. At pH 7-8 slow deposition of an amorphous silica matrix has been observed and no precipitation at acidic pH (Bauer *et al*, 2007). For controlled silica deposition, the pH value of all buffer solutions used for entrapment reactions was set to 7.

The process of particle formation was first analyzed in the absence of target protein. 0.1 M potassium phosphate (pH 7) and PEI as starter of the reaction were mixed and the reaction was initiated by the addition of freshly prepared silicic acid. The reaction was incubated at temperatures between 20 °C and 25 °C for 1 hour. Biomineralization was recorded by following the changes in turbidity of the reaction at 405 nm (Fig. 17A). This experiment aimed to determine the optimal PEI concentration for particle formation.

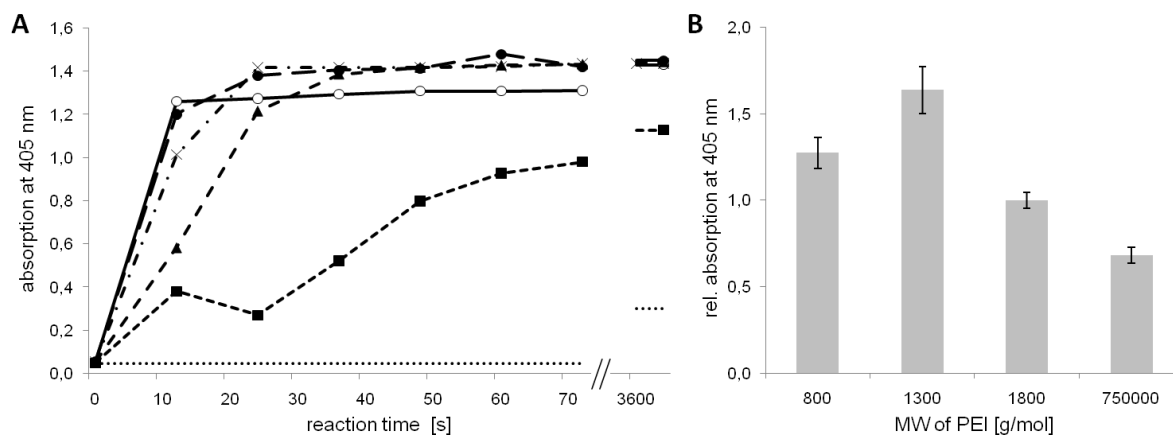


**Fig. 17: Kinetics of PEI-induced formation of silica particles in solution. A) Dependence on PEI concentration: —○— 333 ng/ml, —●— 267 ng/ml, —×— 200 ng/ml, —▲— 133 ng/ml, —■— 67 ng/ml, ⋯ 0 ng/ml. B) Dependence on the MW of PEI. Light scattering was measured after 60 min reaction time at 20 °C. PEI concentration was 133 ng/ml.**

Immediately after addition of silicic acid in the presence of PEI, the turbidity of the reaction increased rapidly and reached maximum values after 1 min. Analyzing the dependence of the reaction on the PEI concentration, it was observed that PEI influenced the kinetics of biomineralization as well as the end values of turbidity. This indicates that higher concentrations of PEI lead to the faster formation of more and/or larger silica particles. The highest increase in turbidity was observed for PEI concentrations above 133 ng/ml. A further increase in PEI concentration did not yield higher turbidity during the course of the experiment.

Interestingly, a slight increase in turbidity was also observed in the absence of PEI after ~10 min, reaching an absorption signal of 0.26 after one hour. The observed absorption signal in the absence of PEI (⋯ 0 ng/ml in Fig. 17) after one hour (3600 s in Fig. 17A) is due to the light scattering of particles formed by auto-condensation of silicic acid, present at concentrations of 200 mmol/L, which is two orders of magnitude above the predicted solubility (2 mmol/L) of silicic acid in pure water at 25 °C (Potapov *et al*, 2007; William, 1980).

### 6.1.2 Dependence of PEI MW on particle formation

PEI (MW: 1800 g/mol) was compared to PEI of other chain lengths (MW: 800, 1300 and 750 000 g/mol) and the turbidity was measured over time (Fig. 17B). For all PEI starter templates, the light scattering signals increased significantly within the first seconds of the measurement, comparable to Fig. 17A. Final light scattering intensities after an hour reaction time qualitatively showed that all PEI templates led to silica particle formation. PEI with the highest MW (750 000 g/mol) showed the smallest absorption signal. This was associated to fewer polymer chains available for self association needed for particle formation compared to PEI with significantly lower MWs (Hildebrand, 2008; Sumper & Kröger, 2004). Since

branched PEI (1800 g/mol) was widely described in the literature (Patwardhan, 2002; Bauer *et al*, 2007; Demadis & Stathouloupoulou, 2006), it was used for all the following experiments.

### 6.1.2.1 Light scattering correlates with the silica particle size

Depending on the PEI concentration, different morphologies were observed (Fig. 18A). While gel-like partially interconnected silica particles under 100 nm were observed in the absence of PEI, much larger, distinct, isolated and spherical beads with a diameter of ~200 nm were observed at concentrations of 67 ng/ml PEI.

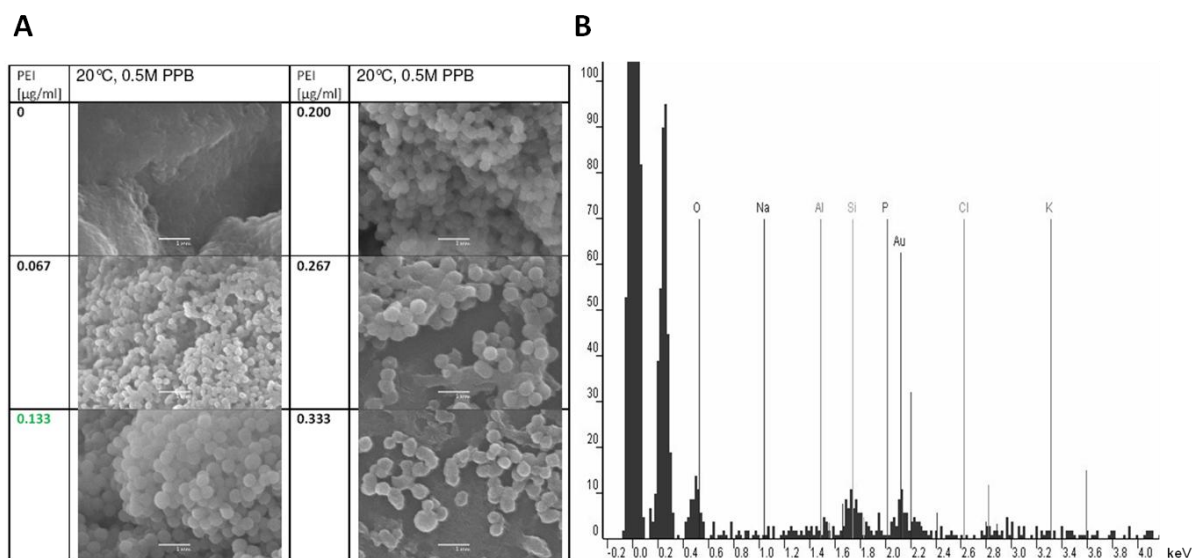


**Fig. 18: A) SEM morphologies of silica particles obtained for different concentrations of PEI. Scale bar: 1 µm. B) Characteristic EDX spectrum of PEI-induced silica particles. Elements expected in the sample are highlighted in the spectrum.**

The elemental compositions silica particles was analyzed by energy-dispersive X-ray spectrometry (EDX) using the built-in EDX detector system of the SEM (Fig. 18B). The signals of the elements Si and O by far exceeded those of C and N which would be expected from PEI and were too small to detect within the noise. Signals from Al were detected from the sample holder and from Au due to the sputtering. After washing the silica particles with water, signals from the elements K and P were mostly removed. In some cases, small amounts of P were detected within the silica particles, due to incorporation of phosphate ions needed for particle formation (Hildebrand, 2008; Sumper & Kröger, 2004). Interestingly, the particle size, as determined with SEM, increased with the PEI concentration in an almost linear way (Fig. 19).



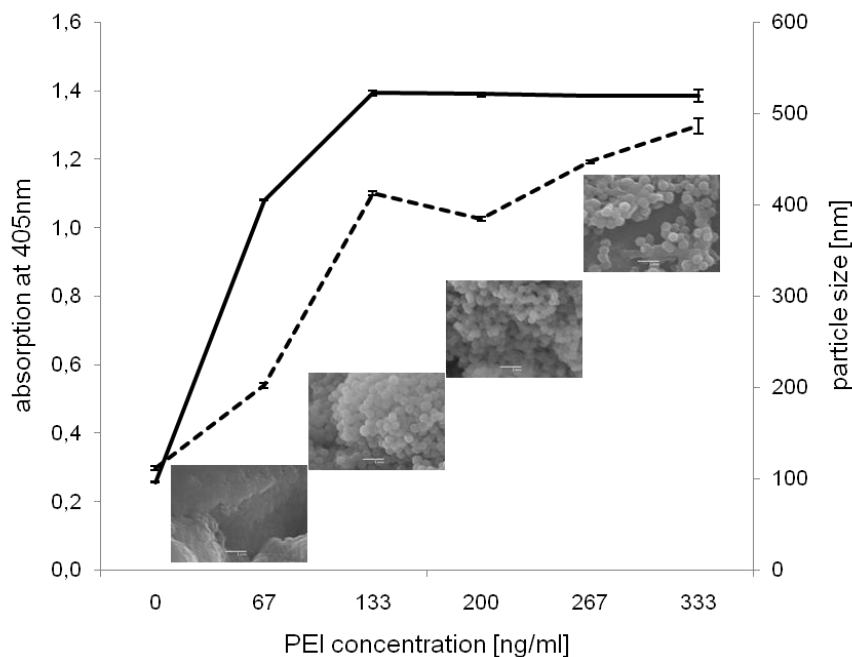


**Fig. 19:** The kinetic of the formation and particle growth of PEI-induced silica particle was followed by monitoring the final absorbance (straight line) at 405 nm and particle size (dotted line) after one hour. Insets of SEM images show the morphology of the particles at the respective data point (PEI concentrations of 67, 133, 200 and 333 ng/ml). Particle size was determined by analysis of SEM micrographs. Scale bar: 1  $\mu\text{m}$ .

As observed in Fig. 17, the final absorbance is saturated above 133 ng/ml PEI concentration. The particle size of the bigger silica particles increases with the PEI concentration nevertheless. The consequence of this observation would be the dependence of the absorbance of the suspension from the small, gel-like particles and not from the bigger, clearly distinguishable silica particles.

The silica beads of several hundred nm were assumed to be filled with silica. However, in some samples of silica particles created with PEI at high concentrations (1.3  $\mu\text{g/ml}$ ), hole-like morphologies were observed in the SEM (Fig. 20).

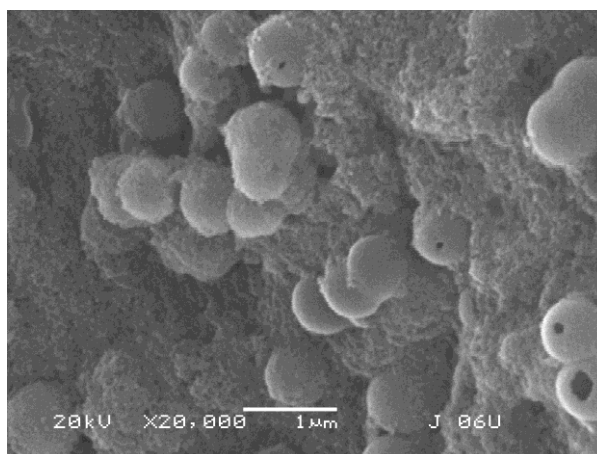


**Fig. 20:** SEM micrograph of silica particles generated at 20 °C, 0.5 M potassium phosphate with PEI (1.33  $\mu\text{g/ml}$ ).

The samples were prepared similarly for the different PEI concentrations and no specific mechanical stress was applied to them. These singular observations encouraged further analysis of this specific morphology. Since the observation of seemingly hollow beads was rare when conventional SEM was used, and only occurred in samples at high PEI concentrations, it was necessary to investigate if bigger silica particles generally possessed hollow morphologies with alternative methods.

### **6.1.3 The silica particle morphology is controlled by the entrapment conditions**

The morphologies of the silica pellets formed in presence of the 133 ng/ml PEI were investigated with SEM and DLS (Fig. 21) for different reaction conditions after lyophilization. Distinct, isolated, spherical beads with a diameter of ~370 nm were observed at low reaction temperatures (15 °C) with 0.1 M potassium phosphate. Much larger, gel-like agglomerates of biomineral seemingly formed from very small (below 100 nm) and partially interconnected silica particles were observed at reaction temperatures above 20 °C. The number of spherical beads (~200 -300 nm in diameter) decreased at 20 and 30 °C, respectively. Similarly, when 0.5 M potassium phosphate was used at 15 °C, the particle size increased (~500 nm) compared to 0.1 M potassium phosphate, respectively. At higher reaction temperatures, the effect of the potassium phosphate concentration on the particle size was not as significant.

Drying the samples and placing them near a surface, as was necessary for SEM measurements, can cause changes in the system that may not accurately reflect the nature of the sample in liquid suspension (Pecora, 2000). Samples were analyzed using DLS after the same treatment than for SEM preparation (Fig. 21). Using dried or lyophilized silica particles resuspended in water, only aggregates of silica particles could be detected with DLS. Due to the high influence of the aggregates on the light scattering signal, the size of single silica particles could not be determined correctly. However, the size of the aggregates follows roughly the same trend as the particle size determined by SEM. The size of the aggregates increased with reaction temperature and potassium phosphate concentration.

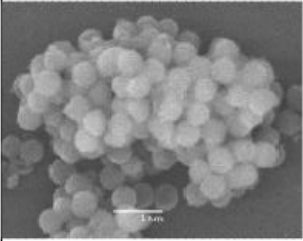
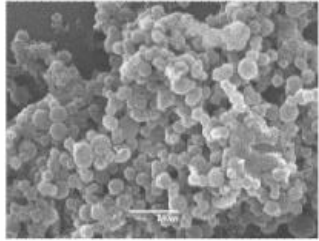
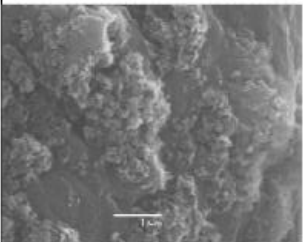
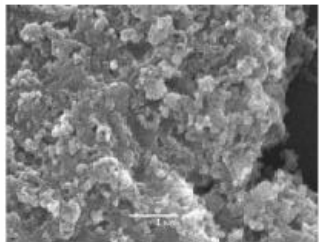
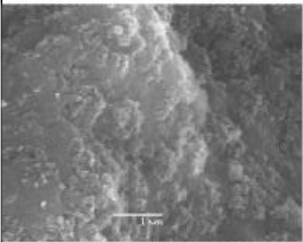
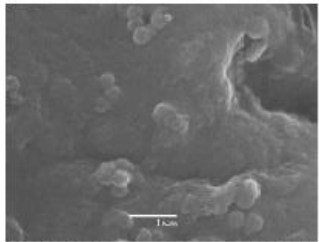
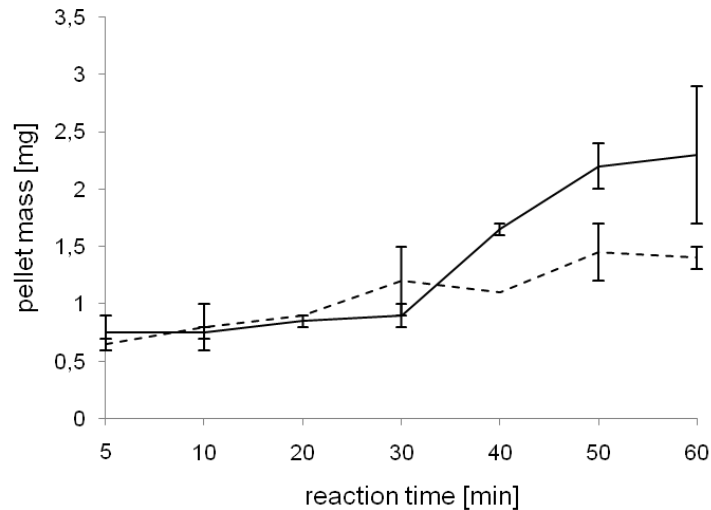
	0.5 M PPB	0.1 M PPB
15 °C	 SEM: 515 +/- 30 nm DLS: 2250 +/- 460 nm	 SEM: 370 +/- 60 nm DLS: 1775 +/- 455 nm
20 °C	 SEM: 230 +/- 25 nm DLS: 3080 +/- 830 nm	 SEM: 200 +/- 20 nm DLS: 1780 +/- 240 nm
30 °C	 SEM: 255 +/- 15 nm DLS: 2870 +/- 540 nm	 SEM: 270 +/- 15 nm DLS: 1880 +/- 555 nm

Fig. 21: Variations in morphologies of PEI-induced silica particles for different temperatures and potassium phosphate molarities after a reaction time of one hour with a PEI concentration of 133 ng/ml. Particle size detected by DLS and SEM after washing and lyophilization of the silica particles.

#### 6.1.3.1 Higher reaction temperatures yield more silica particles

To determine silica particle yields, the particles were sedimented by centrifugation and the mass of the lyophilized pellets was weighted analyzed for different reaction time points (Fig. 22).



**Fig. 22:** Mass of the pellet obtained from the silica particle formation over time. Reaction conditions: 30 °C, 0.1 M potassium phosphate (solid line) and 20 °C, 0.5 M potassium phosphate (dashed line).

Higher masses of pellets were obtained for the reactions performed at 30 °C, 0.1 M potassium phosphate compared to 20 °C, 0.5 M potassium phosphate. After one hour, no significant additional increase in the mass of the pellets was observed for both reaction conditions. Based on this data, the standard reaction time for particle formation was fixed to one hour, unless stated otherwise.

### 6.1.3.2 Particle growth is observed only at the beginning of the reaction

The kinetics of the silica particle size was investigated by SEM measurements over time (Fig. 23).

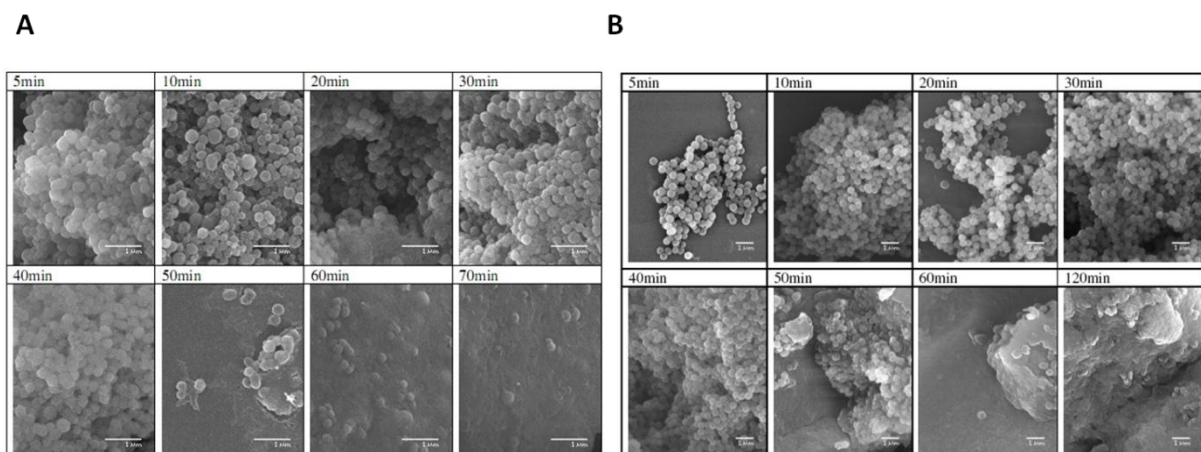


**Fig. 23:** Particle growth analyzed by SEM for the entrapment conditions A) 30 °C, 0.1 M potassium phosphate; B) 20 °C, 0.5 M potassium phosphate. Scale bar: 1  $\mu$ m.

Within 5 min, distinct particles were formed which seem to assemble to gel-like silica further on. This was observed for both entrapment conditions (Fig. 23A and B). The particle size of the bigger particles appears to be constant over time. While after 60 min mainly gel-like

material was observed, distinct particles resembling the ones after 5 min reaction time were still present in the samples.

### 6.1.3.3 Initial particle growth is confirmed by *in situ* DLS measurements

Since DLS is a versatile measuring technique for analyzing the particle size distribution *in situ* (Brown, 1993; Chu, 1997; Hendrix & Leipertz, 1984; Berne & Pecora, 2000), silica particles were investigated during the particle formation reaction. DLS measurements were performed *in situ* over one hour in a cuvette containing the reaction solution (Fig. 24). DLS measurements performed at the end of the reaction with washed and lyophilized and therefore associated silica particles (Fig. 21) detected only aggregates, not single particles.

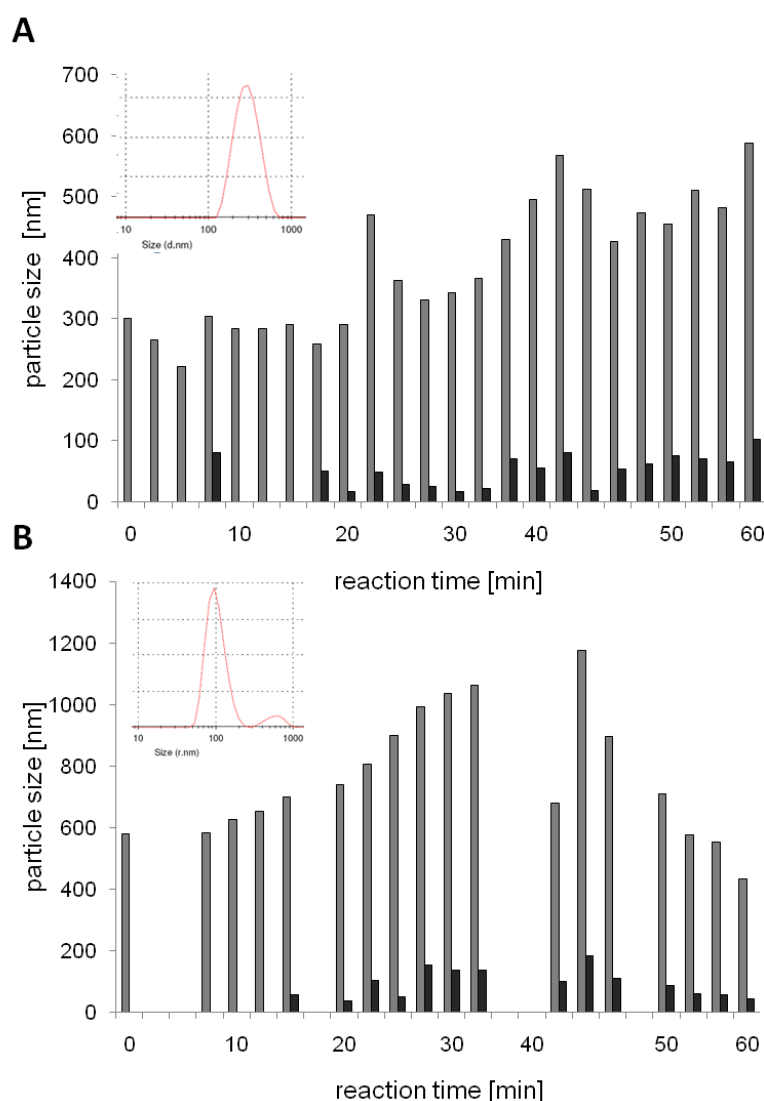


**Fig. 24: Particle size determined *in situ* by DLS over time for A) 30 °C, 0.1 M potassium phosphate, B) 20 °C, 0.5 M potassium phosphate. Inset: typical DLS measurement.**

Within the time frame of the first DLS size detection (2 min), the apparent particle size reached 300/600 nm (entrapment at 30 °C, 0.1 M and 20 °C, 0.5 M potassium phosphate respectively), confirming the fast formation of particles as observed in Fig. 17.

Over one hour, the particle size seemed to increase, reaching 500/650 nm. A possible explanation for this observation could be aggregation of big and small particles together (indeed observed in Fig. 28). Interestingly, after 10 to 15 min, DLS signals for particles smaller than 100 nm appeared, comparable to particle formation by auto-condensation of silicic acid as observed by SEM (Fig. 18). In the case of the entrapment at 20 °C, 0.5 M potassium phosphate, the apparent particle size reached values higher than 1  $\mu\text{m}$  due to aggregation (Fig. 24B). Sedimentation of these aggregates over the course of the measurement led to the observed apparent maximum particle size.

#### 6.1.3.4 PEI is depleted at the end of the reaction

It was observed that particle formation occurred after reaction times as short as 5 min (Fig. 23 and Fig. 24). To investigate the effect of the concentration of PEI shortly after addition of silicic acid, its concentration was determined using the Bradford assay. To determine PEI concentration with the Bradford assay, calibration curves of different PEI concentrations needed to be measured, since both 0.5 M potassium phosphate and PEI interfered strongly with the assay (Gupta *et al*, 2000) (refer to Materials and Methods 8.4.5.1).

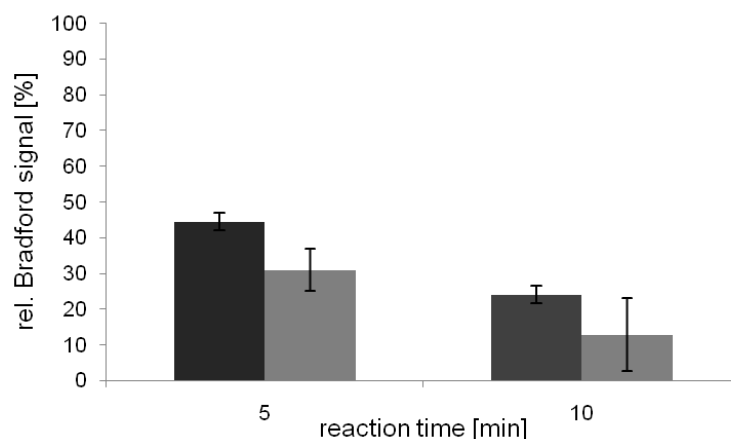


**Fig. 25: PEI concentration determined by the Bradford assay. Reaction conditions: light column: 30 °C, 0.1 M potassium phosphate; dark column: 20 °C, 0.5 M potassium phosphate.**

As shown in Fig. 25, PEI was depleted by 65 % (resp. 70 %) for reaction conditions of 20°C, 0.1 M potassium phosphate (resp. 30 °C, 0.1 M potassium phosphate) within 5 min reaction time. At high PEI concentrations, formation of bigger silica particles as observed in Fig. 23 was favored. With higher reaction times, PEI was depleted further. For reaction conditions of 30 °C, 0.1 M potassium phosphate, PEI was depleted faster than for reaction conditions of 20°C, 0.1 M potassium phosphate. Comparing these observations with Fig. 24, detection of smaller particles in the DLS seemed to be consistent with 85 % depletion of PEI for reaction conditions of 30 °C, 0.1 M potassium phosphate.

### 6.1.3.5 Depletion of PEI at the end of the reaction is confirmed by DLS

To investigate the concentration of PEI at the end of the silica particle formation reaction, fresh silicic acid was added to the reaction solutions after a reaction time of one hour at both entrapment conditions (Fig. 26).

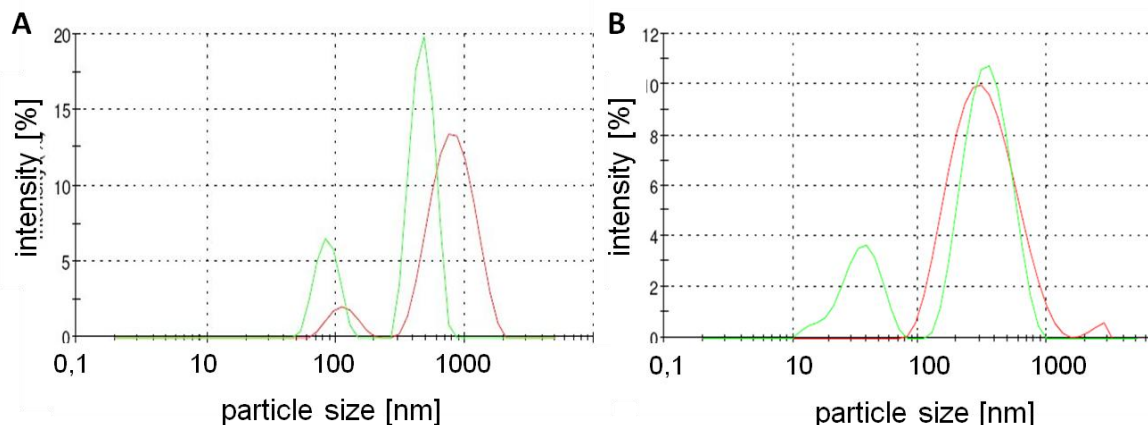


**Fig. 26: DLS measurement of silica particles *in situ* after one hour reaction time (red line). Subsequently, TMOS was added again to the existing suspension and the silica particles were measured again after another hour with DLS (green line). Entrapment conditions at 30 °C, 0.1 M (A) and 20 °C, 0.5 M (B).**

The particle size distribution after one hour reaction time was observed *in situ* by DLS (Fig. 26A-B, red line). At entrapment conditions of 30 °C, 0.1 M (Fig. 26A), the particle sizes detected were 750 and 120 nm. At entrapment conditions of 20 °C, 0.5 M (Fig. 26B), the particle size was detected to be a very broad distribution with a mean value of 300 nm.

Fresh silicic acid was added to the suspension in order to confirm if further particle growth takes place after an additional hour (Fig. 26A and B, green line). The observed particle sizes (500 and 85 nm for entrapment conditions of 30 °C, 0.1 M; 360 and 40 nm for entrapment conditions of 20 °C, 0.5 M) did not increase significantly. Although no substantial additional particle growth was observed, the peak intensity for gel-like particles (85 nm for entrapment conditions of 30 °C, 0.1 M; and 40 nm for entrapment conditions of 20 °C, 0.5 M) increased noticeably.

Taken together, these observations confirmed that PEI was mostly depleted after 60 min reaction time and that further addition of silicic acid only leads to the formation of additional small, gel-like particles caused by PEI at low concentrations.

### 6.1.3.6 Silicic acid is depleted by PEI-induced particle formation at the end of the reaction

The concentration of silicic acid after the particle formation was unknown. Therefore, another control experiment was carried out to check if substantial amounts of silicic acid were present after one hour of particle formation. At this time point (at 20 °C, 0.5 M potassium phosphate), fresh PEI was added and the particle size distribution measured *in situ* with DLS (Fig. 27).

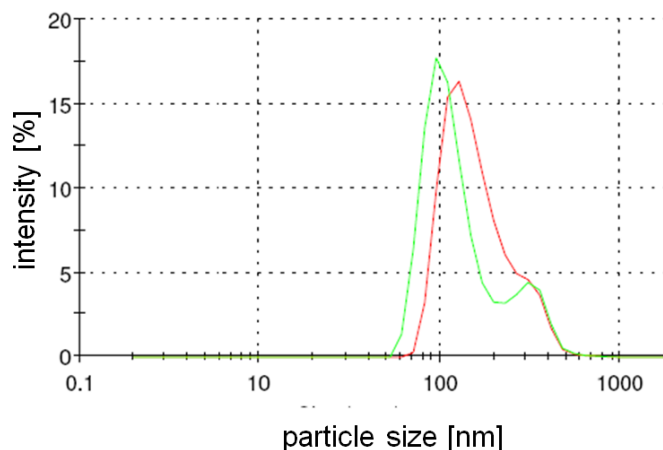


**Fig. 27:** DLS measurement of silica particles *in situ* after one hour reaction time (red line). Subsequently, PEI was added again to the suspension and the silica particles were measured after 15 min with DLS (green line). Entrapment conditions are 20 °C, 0.5 M potassium phosphate.

After addition of PEI to the reaction solution, the particle size observed by DLS did not increase, it even seemed to decrease. The overall shift to lower particle sizes was due to increased formation of smaller silica particles at around 100 nm (Fig. 27, green line). This control experiment was only carried out for entrapment conditions at 20 °C, 0.5 M potassium phosphate, since it was assumed that these conditions most likely still contained substantial amounts of silicic acid, as the mass of the silica pellets was lower after one hour reaction time (Fig. 22).

Results are shown for 15 min after addition of further PEI, since PEI-induced higher-sized particle formation within 5 min (Fig. 23B). Also, 30 min after addition of additional PEI, the DLS signal showed only small, gel-like particles of varying particle size distributions, all below 100 nm, possibly due to the sedimentation of bigger particles (as observed in Fig. 24B) and the higher statistical relevance of the small gel-like particles (data not shown).

The absolute results of DLS measurements varied significantly between single experiments and broad particle size distributions were determined. Nevertheless, the observation of the qualitative effect of the formation of small, gel-like particles below 100 nm at high reaction times (Fig. 24) and after reaction with additional TMOS (Fig. 26) was reproducible.

#### **6.1.3.7 Silica beads are formed by local association of primary particles**

It was of interest if bigger silica particles were hollow as it seemed in some experiments (Fig. 20). Furthermore, more precise methods were needed to characterize the gel-like particles. Therefore the silica particles needed to be mechanically degraded first. This was attempted with two simple approaches: First, silica suspensions were flash-frozen in liquid nitrogen and the solidified sample grinded between polished aluminium sample holders used for SEM. In the second approach, glass beads used for cell disruption (~0.2 mm) were added to the silica suspension. Bead-beating of the sample was done by vortexing the samples in



closed reaction tubes up to 5 min. However, both approaches did not degrade the silica particles significantly.

The gel-like silica particles that were observed to increase with reaction time (Fig. 23) represented the bulk of the sample and structural insight into the ill-defined gel was of interest to understand enzyme entrapment. It was important to know if the formation of silica particle beads influenced the overall morphologies and if they were massive or hollow silica spheres. The gel-like particles below 100 nm could not be clearly distinguished using the JSM 5900 SEM (e.g. Fig. 21). In order to find out if their morphology is influenced by the reaction conditions, a method capable of higher resolution was necessary. At magnifications of 30 000x and above, the JEOL JSM 7500 SEM was able to resolve the morphology and particle size of the small, gel-like particles below 100 nm at low acceleration voltages (Fig. 28A).

For both entrapment conditions (30 °C, 0.1 M and 20 °C, 0.1 M potassium phosphate), smaller particles of average 15 nm were observed at the surface of the bigger particles and interconnecting them (Fig. 28B and C). Interestingly, it seemed that the particle size of the small, gel-like silica particles was independent of the reaction temperature and phosphate buffer molarity in the investigated samples. In the literature, small silica particles of average 10 nm are referred to as primary silica nanoparticles (Matsoukas & Gulari, 1988; Harris *et al*, 1990).

The observation of smaller particles at the surface of bigger silica beads was in agreement with the hypothesis deduced from DLS measurements in Fig. 24. Similar to Fig. 23, the relative amount of gel-like particles seemed to be significantly higher compared to the silica beads for entrapment conditions of 30 °C, 0.1 M phosphate buffer. This confirmed the observations of increased gel-like structures at higher reaction time and temperature as observed in Fig. 21.

Conventional methods did not allow the investigation of the interior of the silica beads of both massive and apparently broken spheres as those observed in Fig. 20. Therefore, samples of silica particles generated at entrapment conditions of 20 °C, 0.5 M were cleaved with a scalpel in the cryo-transfer system of the JEOL JSM 7500 SEM before the measurement (Fig. 29).

As highlighted in Fig. 29A, the cleaved particles showed gel-like morphology in their interior. The silica beads sized several hundred nm seem to be formed from assembled gel-like silica particles of average 15 nm size, which are more clearly visible in Fig. 29B. At pH 7, gelation by aggregation of silica particles in concentrated silica suspensions was expected (Iler, 1979; Heath & Tadros, 1983).

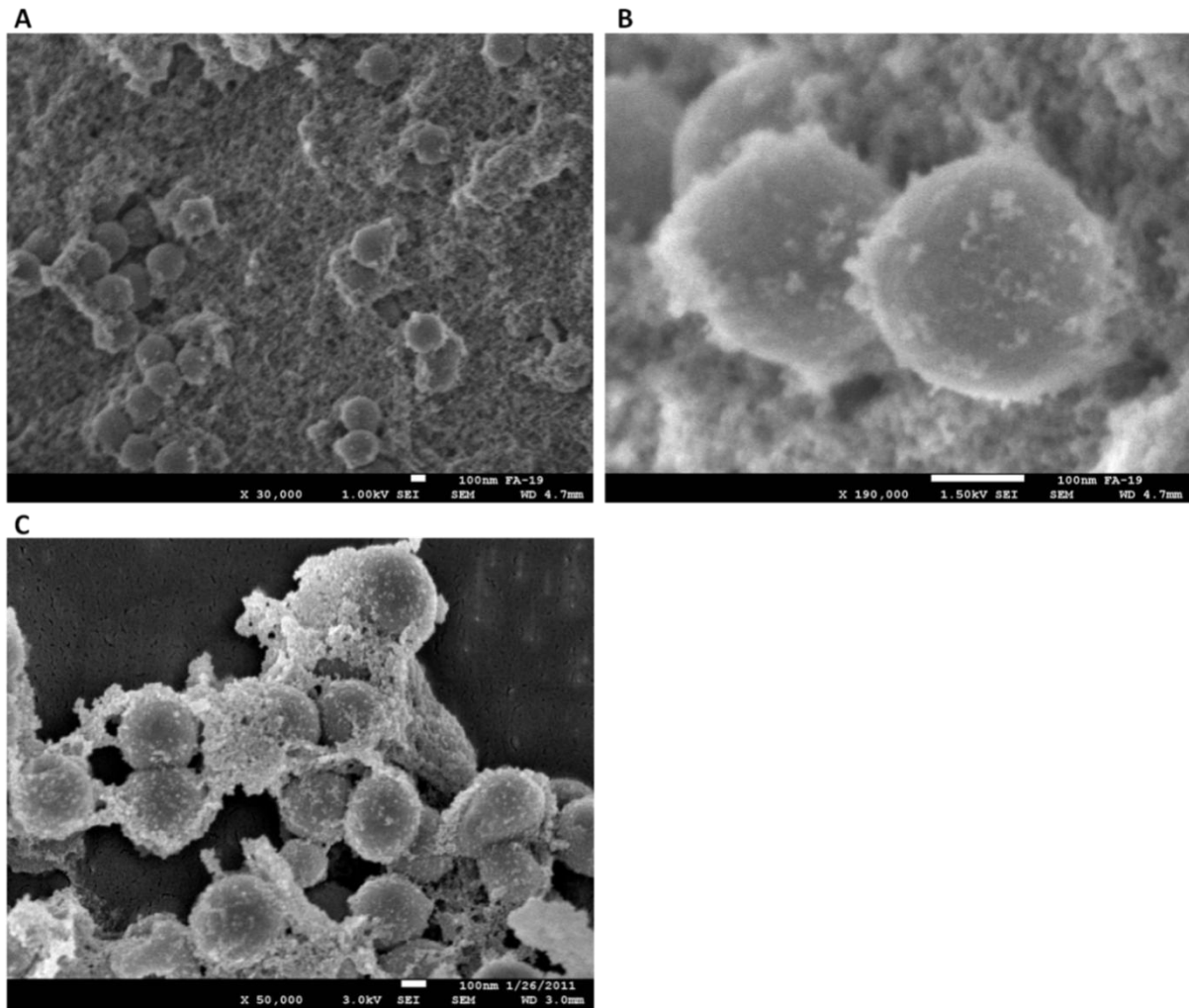


Fig. 28: High resolution SEM micrograph of unspattered, lyophilized silica particles obtained at entrapment conditions of A-B) 30 °C, 0.1 M potassium phosphate, C) 20 °C, 0.5 M. Scale bar: 100 nm. Micrographs have been recorded with the SEI detector at A) 1 kV, B) 1.5 kV and C) 3 kV acceleration voltage. Working distances were A) and B) 4.7 mm, C) 3 mm.

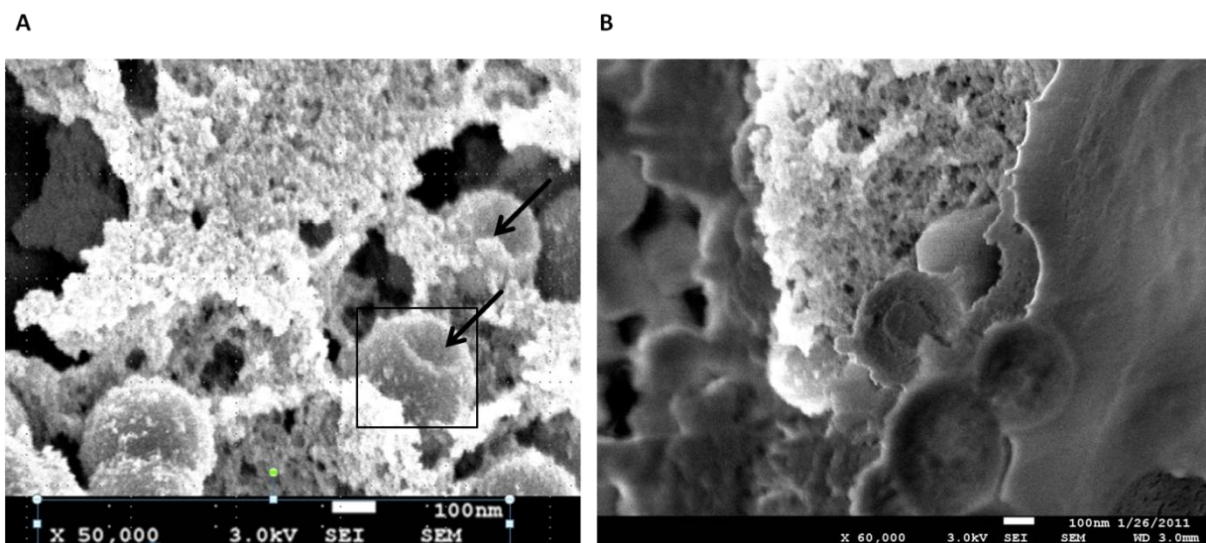
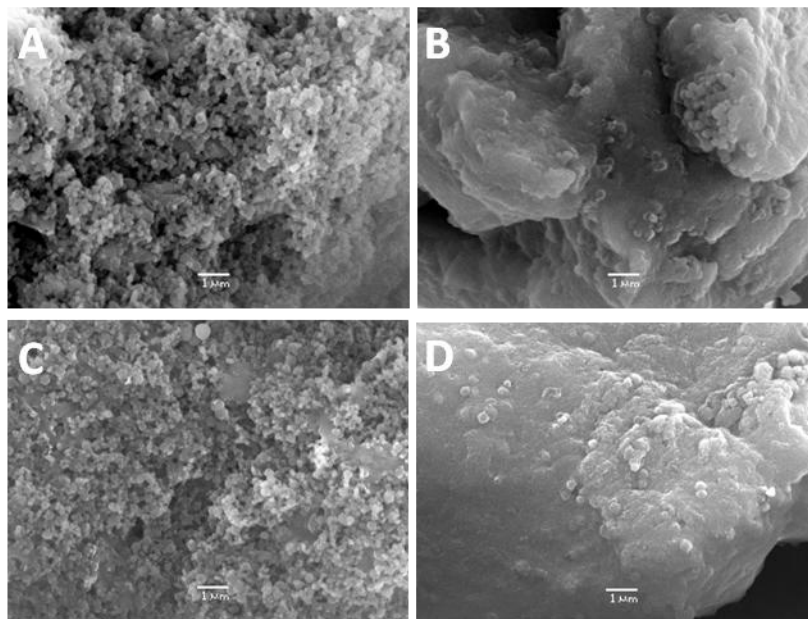


Fig. 29: A) and B) High resolution SEM micrograph of unspattered, lyophilized silica particles obtained at entrapment conditions of 20 °C, 0.5 M. Arrows in A) indicate particles cleaved by a scalpel in the cryo-

transfer system. Scale bar: 100 nm. Micrographs have been recorded with the SEI detector at 3 kV acceleration voltage. Working distances were 3 mm.

#### 6.1.4 The porosimetric properties are optimized for protein entrapment

To investigate the porosity of the biosilica obtained at different reaction conditions, the process was up-scaled in order to obtain enough particles to perform Hg-porosimetry and BET surface area measurement (Brunauer *et al*, 1938). SEM micrographs of silica particles obtained from the entrapment protocol and for the up-scaled protocol showed no significant differences in morphologies (Fig. 30).



**Fig. 30: SEM morphologies of silica particles after entrapment at 20 °C, 0.5 M potassium phosphate (A, C) and 30 °C, 0.1 M potassium phosphate (B, D) for the normal entrapment protocol (A, B: scale down) and the up-scaled process (C, D: scale up). Scale bar: 1 μm.**

For the determination of the surface area of the silica particles, the first measurements were carried out with Hg-porosimetry (Fig. 31; measurements were carried out at WACKER as described in Materials and Methods 8.3.2.1). The technique is based on the principle of the intrusion of a non-wetting liquid such as mercury into porous material at high pressure (Abell *et al*, 1999).

The difference in the specific surface area of the silica particles was significantly dependent on the reaction temperature and phosphate concentration. The surface area increased with the reaction temperature. For temperatures of 15 and 20 °C, higher surface areas were observed with 0.5 M potassium phosphate. At 30 °C, the phosphate concentration did not seem to greatly influence the surface area of the silica particles.

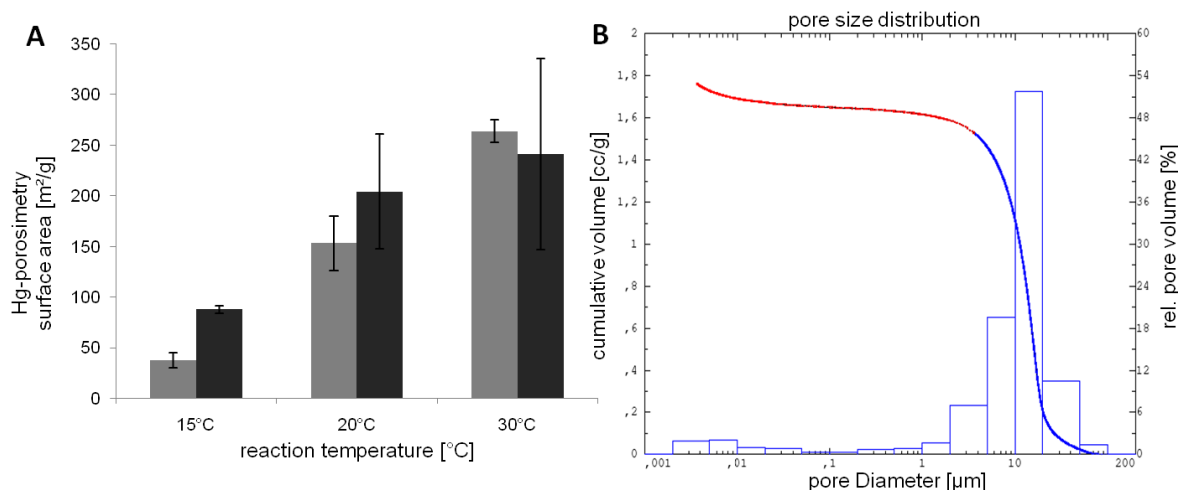


**Fig. 31: A) Porosity determined by Hg-porosimetry of silica particles obtained from two entrapment conditions (light: 0.1 M potassium phosphate; dark: 0.5 M potassium phosphate). B) Characteristic Hg-porosimetry measurement showing similar pore size distribution for both entrapment conditions. Red: high pressure area, blue: low pressure area. The histogram shows the relative pore volume and the line diagram the cumulative Hg volume.**

To determine the pore volume of silica particles generated at different entrapment conditions, Hg-porosimetry measurements were carried out (results are summarized in Fig. 31A). The appearance a single Hg-porosimetry measurement gave insights into the broad pore size distribution. The data summarized in Fig. 31A was interpreted from repeat Hg-porosimetry measurements, each of which qualitatively resembled the graph shown in Fig. 31B. The pore sizes and calculated porosimetric data differed for each measurement, but the appearance of the curve progression looked similar for different samples.

The Hg-porosimetry measurement indicated an apparent mean pore size of ~10 µm (Fig. 31B). The pore size distribution was very broad with pore sizes between 1 and 100 µm. The Hg volume used in the measurement is an indicator for the pore size. However, the cumulative Hg volume increased significantly only in the area of lower pressure (Fig. 31B, shown in blue) therefore only filling pores from 1-100 µm size. The smallest pores sized measured were between 10 and 400 nm and were only detected at higher pressure of Hg (Fig. 31B, shown in red).

Porous materials are classified according to the size of pores: material with pores less than 2 nm are called micropores, materials with pores between 2 and 50 nm are called mesopores, and material with pores greater than 50 nm are macropores (Sing *et al*, 1985). The micropores of the samples cannot be accessed by Hg-porosimetry and needed to be determined with a separate pore size determination.

#### 6.1.4.1 Micro- and mesopores are shown by BET N<sub>2</sub>-adsorption measurements

To determine if micropores were present in our samples, they needed to be accessed by BET nitrogen gas adsorption/desorption measurements (Fig. 32; measurements were carried

out at WACKER as described in Materials and Methods 8.3.2.1), which are based on the measurement of physically adsorbed gas molecules on a solid surface in order to determine the specific surface area of a material.

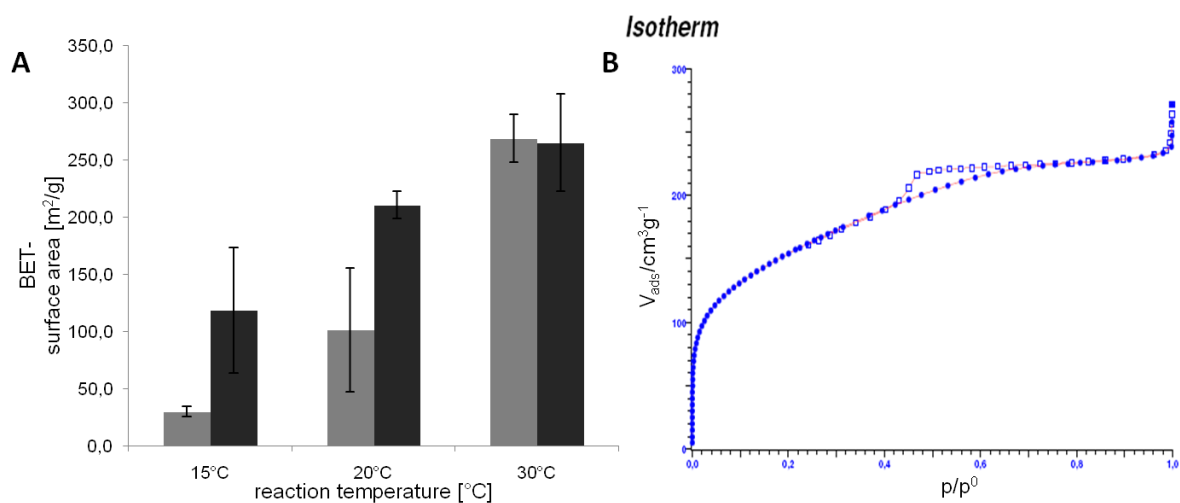


**Fig. 32: A) Porosity determined by BET nitrogen adsorption of silica particles obtained from two entrapment conditions (light: 0.1 M potassium phosphate; dark: 0.5 M potassium phosphate). B) Characteristic BET gas adsorption measurement. The lower curve is the adsorption and the top curve the desorption process. (For the entrapment conditions 20 °C, 0.5 M potassium phosphate and 30 °C, 0.1 M potassium phosphate, the measurements looked highly similar).**

The dependence of the specific surface area on the reaction temperature and phosphate concentration (Fig. 32A) was comparable to the surface area determined by Hg-porosimetry (Fig. 31) and confirmed the Hg-porosimetry results qualitatively with an independent method. The surface area also was confirmed to be very similar for entrapment conditions at 30 °C independent of the potassium phosphate concentration.

However, at 20 °C and 0.5 M potassium phosphate, the specific surface area was significantly higher in the BET measurements compared to the Hg-porosimetry results (Fig. 31). It seemed that with increasing reaction temperature, the potassium phosphate dependence of the surface area decreases. The values of the surface areas determined by nitrogen sorption for all samples were characteristic for mesoporous silica (Djojoputro *et al*, 2006).

Adsorption of low partial-pressure  $\text{N}_2$  gas is assumed to be caused by microporosity. The exact pore dimensions cannot be determined by this method (Belton *et al*, 2008; Groen, 2003). A characteristic BET measurement (Fig. 32B) showed both microporous and mesoporous behavior for the observed samples. At high partial pressure, a plateau was observed, which is needed for reliable calculation of the pore size. The steep increase of the signal at lower partial pressure (partial pressure between 0 and 0.04) is a clear indicator for micropores (Brunauer *et al*, 1938). The signal does not show a plateau right after the steep ascent (partial pressure between 0.04 and 0.4), once more indicating the presence of

mesopores. From this, it can be concluded that the silica particles in the measured samples show a broad distribution of micro- and mesopores with a mean pore size smaller than 10 nm (Fig. 31). A more exact interpretation of the porosimetry data based on a specific microporous or mesoporous model is not possible due to the extremely broad distribution of pore sizes.

Taken together, the observed broad pore size distribution of mesopores (10 and 400 nm) and macropores is estimated to be of importance for the formation of a robust and generalized support able to entrap protein substrates of different sizes. The highest surface areas were detected for the reaction at 30 °C in 0.1 M potassium phosphate and at 20 °C in 0.5 M potassium phosphate (Fig. 31 and Fig. 32). These conditions were expected to have the highest potential for the entrapment of proteins.

### 6.1.5 Morphologies with highest surface area also show the highest fluidity in suspension

Silica particles were obtained as suspensions in aqueous medium. In order to investigate the fluidity of the silica particle suspensions, their viscosity in water was measured at 25 °C (where the viscosity of water is 1.002 mPa\*s) (Fig. 33).

Sedimentation of the silica particles occurred within minutes after mixing, i.e. the suspension was not stable over a long period of time. However, viscosity measurements could be performed in several seconds with each of the different samples. The viscosity of the suspensions increased with decreasing temperature and increasing potassium phosphate concentrations. The measurements showed that particle suspensions of biosilica prepared at 30 °C, 0.1 M potassium phosphate were more fluid than biosilica prepared at 20 °C, 0.5 M potassium phosphate.

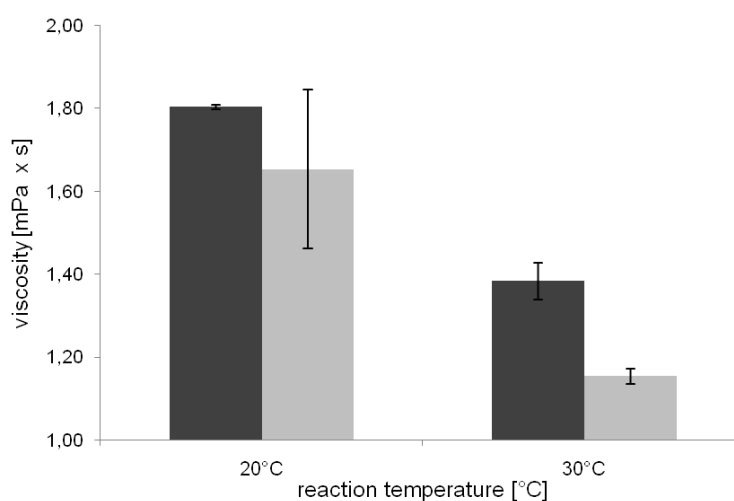


**Fig. 33: Viscosity of suspensions of silica particles obtained from different entrapment conditions (Materials and Methods 8.3.2.3). The investigated potassium phosphate molarities were 0.1 M (dark column) and 0.5 M (light column).**

### 6.1.5.1 The robust entrapment conditions tolerate the presence of a swelling agent

It was tested if the entrapment conditions were influenced by the presence of a swelling agent, to assess if the silica particle properties were inert against exterior interaction. Previous studies showed that mesitylene produces microemulsions in its mixture with aqueous solutions, essentially acting as a swelling agent leading to siliceous mesostructured cellular foams (Kang & Rhee, 2005; Schmidt-Winkel *et al*, 1998, 2000).

Silica particles were prepared using the reaction conditions of 30 °C, 0.1 M potassium phosphate that yielded high specific surface areas (Fig. 31, Fig. 32) in the presence or absence of 1.5 vol.-% mesitylene or 1.5 vol.-% mesitylene and 10 vol.-% ethanol. They were investigated with Hg-porosimetry regarding their specific surface area (Fig. 34A) and with SEM regarding their morphologies (Fig. 34B). Mesitylene was poorly miscible in the aqueous solution and at 1.5 vol.-% partially phase-separated within seconds from the aqueous solution but it was soluble in ethanol. Adding 10 vol.-% ethanol, the non-miscible fraction of mesitylene formed a stable emulsion in the reaction solution.

It was expected that the surface area of silica particles generated with mesitylene would increase, however, a slight decrease was measured (Fig. 34A). Additional ethanol suppressed this loss of specific surface area. SEM measurements showed similar morphologies (Fig. 34B), which indicated that the particle morphologies were not influenced significantly by the presence of a swelling agent.

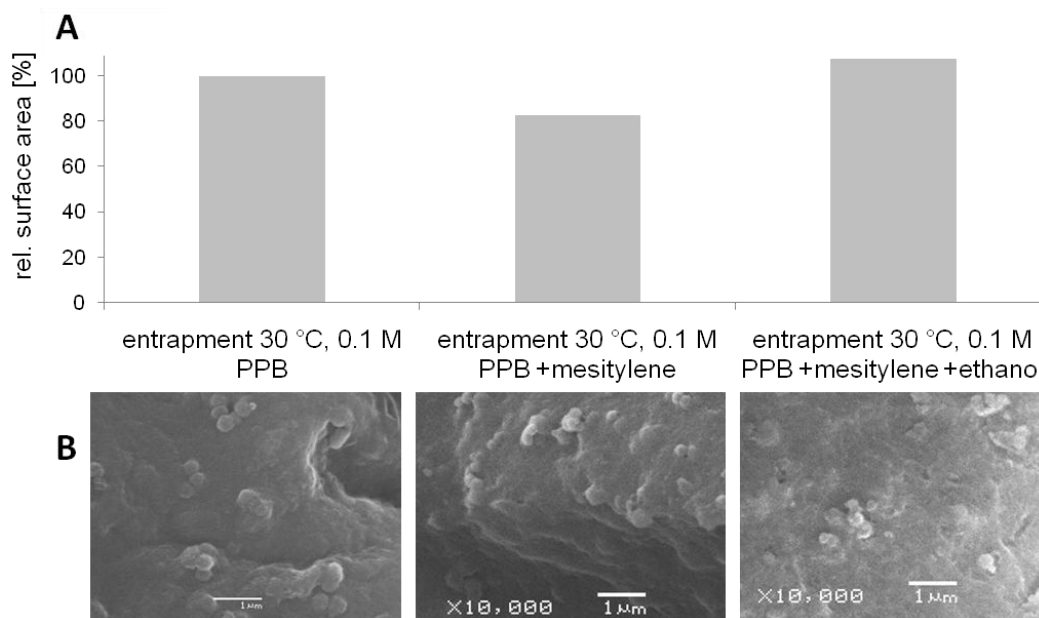


**Fig. 34: Porosity and morphology of silica particles at entrapment conditions of 30 °C, 0.1 M potassium phosphate in the presence of additional mesitylene and ethanol during the entrapment reaction. A) Relative specific surface area determined with Hg-porosimetry (surface area of silica particles generated without mesitylene or ethanol was set to 100%). B) SEM morphologies of the silica particles. Scale bar: 1 μm.**

### 6.1.6 Conclusions and outlook

The results of PEI-induced silica particle formation are illustrated in Fig. 35.

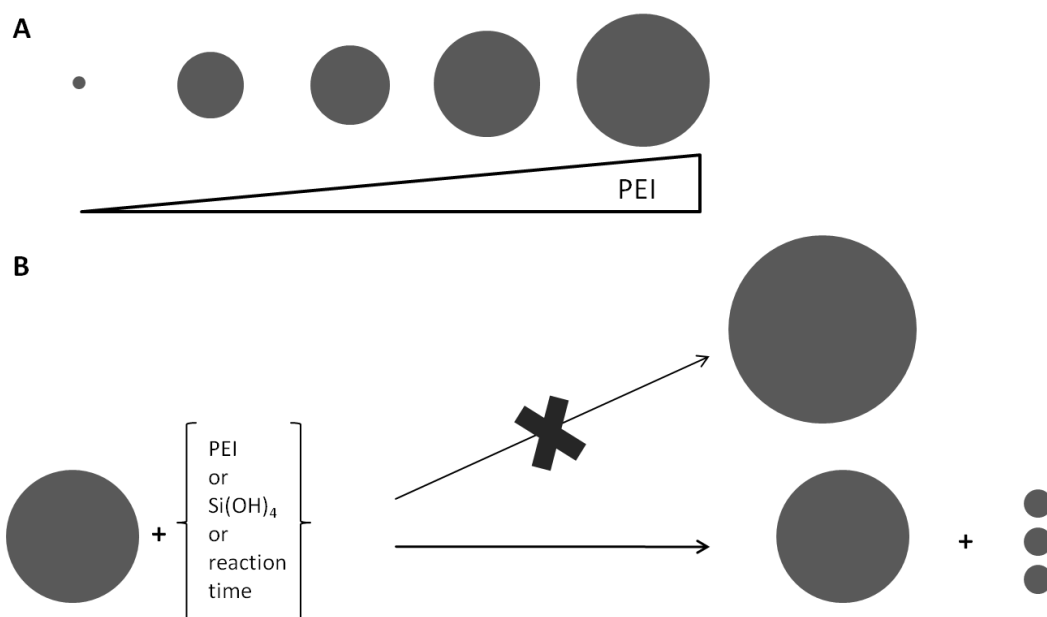


**Fig. 35: Schematic illustration of PEI-induced silica particle formation. A) Particle size dependence on the PEI concentration. B) Summarized results from the particle size determination experiments.**

The results showed that PEI-induced fast formation of silica particles within minutes (Fig. 17, Fig. 23, Fig. 24) (Bauer *et al*, 2007) with particle size control by the PEI concentration (Fig. 18, Fig. 19, schematic illustration in Fig. 35A). The particle size did not increase significantly with higher reaction time (Fig. 23), or upon addition of additional PEI (Fig. 26) or TMOS (Fig. 27) after the bigger, bead-like particles have already been formed (schematic illustration in Fig. 35B). The combination of those last two results suggests that high PEI and silicic acid concentrations are needed for the initial formation of bead-like particles (Fig. 25).

It has been shown previously that polycationic PEI catalyzes silica polymerization in the presence of phosphate anions that facilitate self-association of the positively charged PEI (Hildebrand, 2008). Prior to the addition of silicic acid, the polymerization determinant PEI self-associates to the lowest free energy form (Hildebrand, 2008; Brunner *et al*, 2004). At high PEI concentrations, the resulting silica structures are the lowest free energy form of interconnected spheres which can vary in size depending on polyamine chain length and the phosphate concentration (as seen in Fig. 21) (Hildebrand, 2008).

The morphologies observed with high resolution SEM, which showed clearly that the silica beads (of 300  $\mu\text{m}$  or more) are formed from gel-like silica particles of  $\sim 15$  nm at the surface of the beads (Fig. 28) as well as inside them (Fig. 31), further support this model. Therefore, lower PEI concentration leads to less silica beads formed by locally concentrated PEI and



further decrease in relative number with the reaction time, since PEI is depleted over time. Instead, gel-like particles not associated into beads were increasingly observed (Fig. 23).

The reaction speed increased with the reaction temperature (observed by earlier appearance of gel-like particles in Fig. 24A), which led to higher masses of silica particles precipitated by PEI from silicic acid (Fig. 22). More gel-like particles led to higher porosity (Fig. 31, Fig. 32) and also higher fluidity of the silica particle suspensions (Fig. 33). The PEI-catalyzed silica particle growth mechanism of flocculation and intimate connection of nanospheres is reminiscent of the hypothesized dynamic formation of the siliceous diatom shells (Sumper *et al*, 2003).

## 6.2 The model protein eGFP is stably entrapped in silica particles

Next, it was investigated how the characteristics of silica particle formation affected the entrapment efficiencies, activities and leaching characteristics of different proteins. EGFP was investigated first as a model protein for co-entrapment during the silica particle formation catalyzed by PEI as the fluorescence of eGFP made it easy to follow its incorporation process.

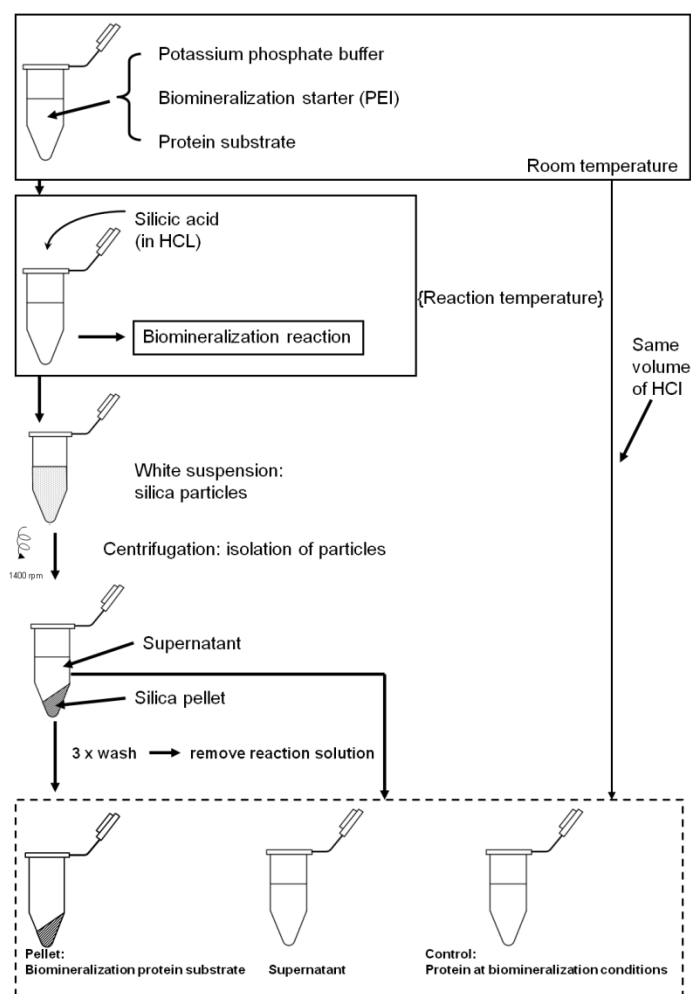
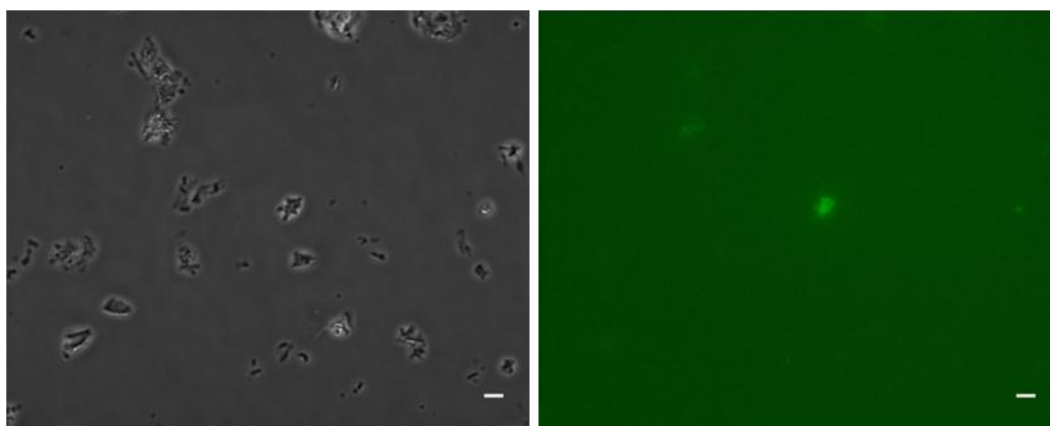


Fig. 36: Schematic protocol for protein entrapment.

If not indicated otherwise, all proteins were entrapped following the generalized protocol illustrated in Fig. 36.

### 6.2.1 EGFP shows specific fluorescence in silica particles

The localization of the entrapped eGFP was investigated by fluorescence microscopy. As a control, silica particles without eGFP (generated at the entrapment conditions of 30 °C, 0.1 M potassium phosphate) were analyzed (Fig. 37). Single silica particles could not be visualized due to the relatively low resolution of the fluorescence microscope (Axiovert 200), even if it was used with the oil immersion technique. Bigger aggregates of silica particles however were clearly visible in the bright field and no significant intrinsic fluorescence of the silica particles was observed.



**Fig. 37: Protein-free silica particles (entrapment condition: 30 °C, 0.1 M potassium phosphate) in the fluorescence microscope. Left: bright field; right: fluorescence filter (535 nm). Scale bar: 5  $\mu$ m.**

Entrapped eGFP (using the entrapment conditions of 30 °C, 0.1 M potassium phosphate) showed specific fluorescence clearly localized in the particle agglomerates (Fig. 38A), indicating that eGFP was entrapped in functionally active form.

Since no significant fluorescence was observed in the background and between silica particles, entrapping eGFP after incubation in 0.1 M potassium phosphate for up to a week, it was concluded that no significant leaching into the surrounding buffer medium occurred. Similar observations were made with samples of freshly prepared entrapped eGFP as well as with samples incubated at r.t. in 0.1 M potassium phosphate buffer for a week (data not shown).

Bigger aggregates of entrapped eGFP showed more intensive fluorescence since more eGFP was entrapped functionally (Fig. 38B). This indicates that bigger aggregates of silica particles do not necessarily deactivate the entrapped eGFP.

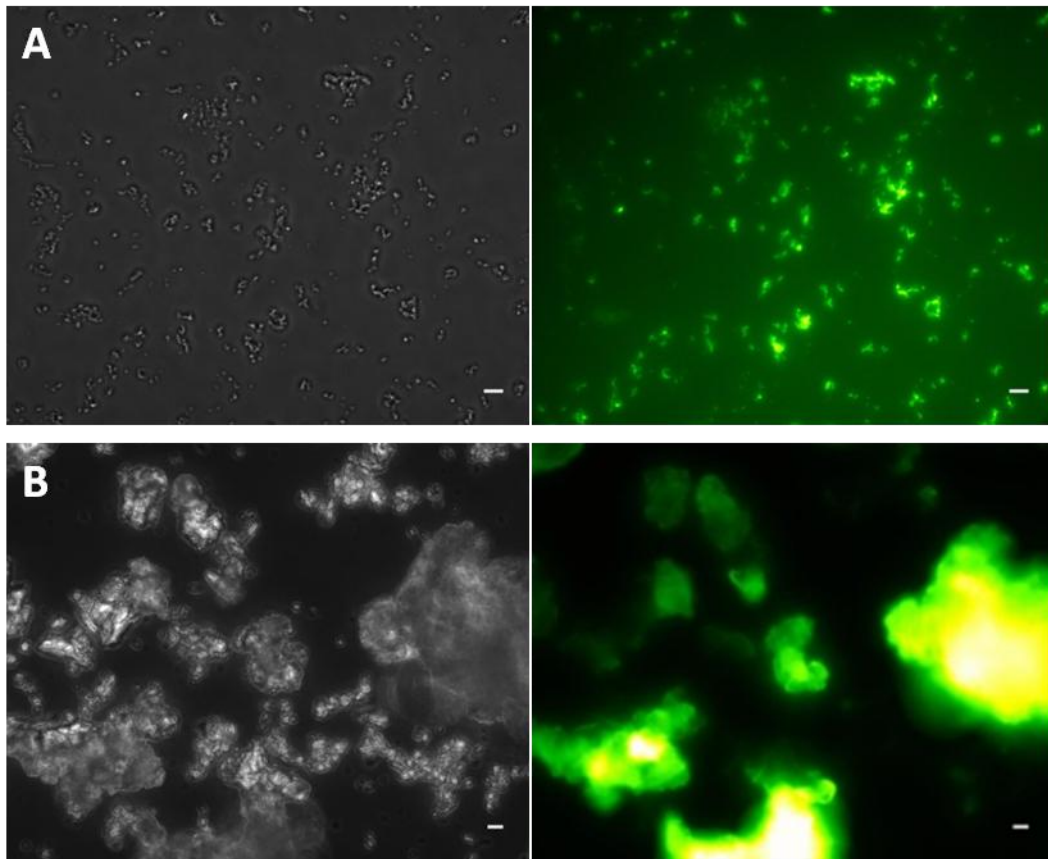


**Fig. 38:** Visualization of entrapped eGFP in silica particles (entrapment condition: 30 °C, 0.1 M potassium phosphate) by fluorescence microscopy. Left: bright field; right: fluorescence filter (535 nm). A) Scale bar: 5  $\mu\text{m}$ . B) Aggregates of the same entrapped eGFP in silica particles. Scale bar: 10  $\mu\text{m}$ .

### 6.2.2 The model protein eGFP is used for the optimization of the entrapment conditions

In order to determine the best entrapment conditions in terms of functional protein amounts in the silica pellet for the model protein eGFP, a screening for the best combination of reaction temperature and buffer molarity was performed (Fig. 39).

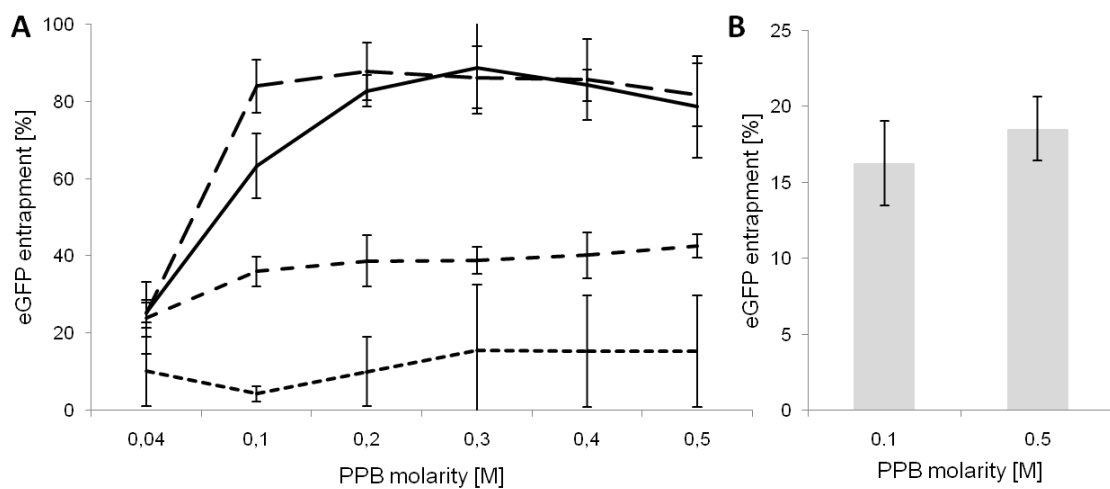


**Fig. 39:** A) Dependence of the entrapment efficiency of eGFP on phosphate concentration and reaction temperature (---- 15 °C, --- 20 °C, — 30 °C, -·- 40 °C) after a reaction time of 60 min. B) eGFP

---

**fluorescence in the silica pellet after entrapment at higher temperatures (50 °C) for 0.1 and 0.5 M potassium phosphate.**

The dependence of the entrapment efficiency on the reaction at different molarities (0.04 to 0.5 M) of potassium phosphate and varying reaction temperatures (15-40 °C) were analyzed in this screening. The activity of the supernatant (not shown in Fig. 39A) corresponded to the difference of the pellet to a control sample. Therefore, no eGFP activity was lost during entrapment.

The lowest phosphate concentration of 0.04 M results from using dist. water instead of the potassium phosphate component, as eGFP and PEI are dissolved in 0.1 M potassium phosphate. At this minimal potassium phosphate concentration, entrapment was low (under 30 % for reaction temperatures above 20 °C). The concentration of potassium phosphate influenced the entrapment efficiencies significantly only in the range between 0.1 and 0.2 M (leading to an increase in entrapment by 20 % at 30 °C). Above this critical potassium concentration the reaction temperature seemed to be limiting. Higher reaction temperatures (30 or 40 °C) combined with potassium phosphate concentrations above 0.2 M led to the highest entrapment ratios (up to 80 %). However, reaction temperatures of 50 °C and higher, resulted in a dramatic drop of the entrapment efficiencies irrespective of the phosphate concentration used (Fig. 39B) (15-20 % entrapment).

Interestingly, as indicated in Fig. 21, the resulting particle morphology and porosity is different for particles at saturated entrapment efficiency (30°C; 0.1 M potassium phosphate) and half maximum saturation, the conditions with highest entrapment at lower concentration (20 °C, 0.5 M of potassium phosphate). At 20 °C, 0.5 M potassium phosphate yielded silica particles with higher specific surface area than 0.1 M potassium phosphate (Fig. 32). Those two rather mild conditions were used for all investigated proteins, since they should have low denaturation potential for most target proteins.

It was expected that polyamines of different length influence particle formation significantly (Mizutani *et al*, 1998). To exclude any negative influence of PEI MW on the entrapment efficiency, a screen with those conditions was carried out for PEI of different MW (Fig. 40). The results in Fig. 40 confirmed that using PEI (MW: 1800 g/mol) led to the highest amounts of protein entrapment.

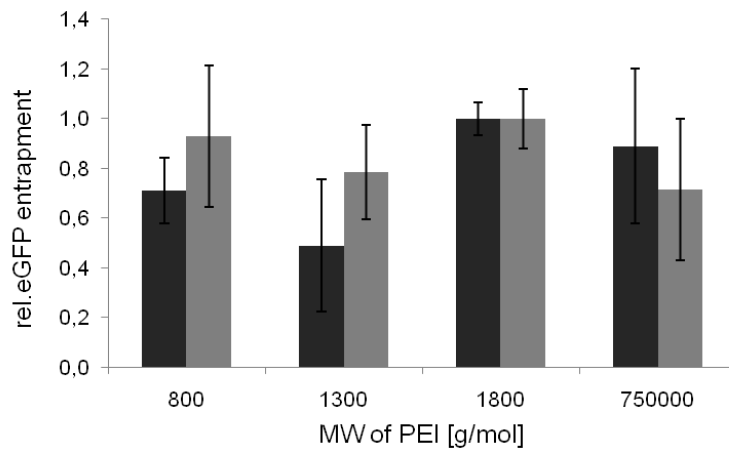


**Fig. 40: Relative eGFP entrapment with PEI of different MW at different entrapment conditions (30 °C, 0.1 M potassium phosphate: gray columns; 20 °C, 0.5 M potassium phosphate: dark columns). Entrapment with PEI (MW: 1800 g/mol) was set to 1.**

Since entrapment of eGFP with PEI was optimized with regard to the entrapment conditions, it was of interest if higher entrapment ratios can be obtained using an alternative agent able to induce silica particles. Previous studies have reported that the cationic surfactant cetyltrimethylammonium chloride (CTMA-Cl) forms mesoporous silica particles through acidic surfactant templating and condensation of silicic acid (Sokolov *et al*, 2007). Entrapment with CTMA-Cl was tested under similar entrapment conditions as investigated in Fig. 39, the entrapment ratios with CTMA-Cl did however not exceed those obtained with PEI (MW: 1800 g/mol) (data not shown).

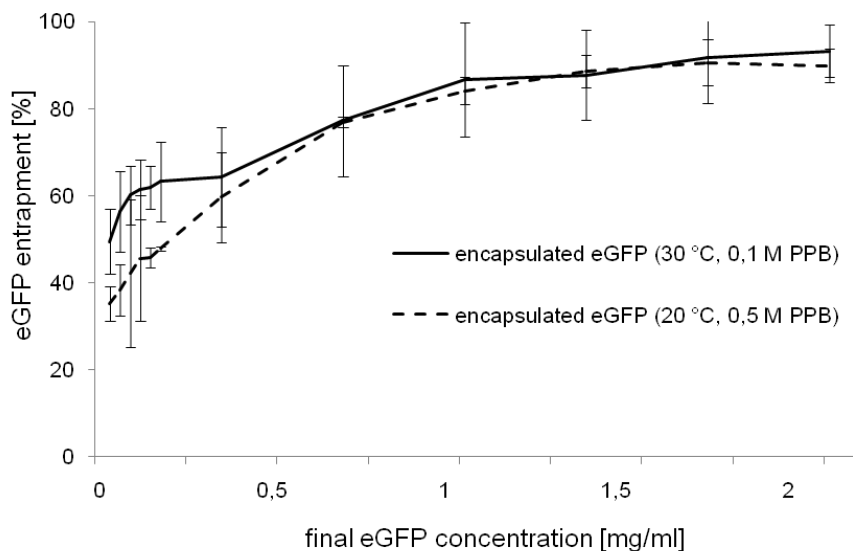


**Fig. 41: Influence of the concentration of eGFP on the total yield of entrapment.**

Therefore, all further entrapment studies were carried out with the optimal starter PEI. Using the PEI concentration yielding the highest entrapment efficiencies (133 ng/ml PEI 1800 g/mol), it was investigated to which degree the protein concentration further influences the entrapment (Fig. 41).

The entrapment efficiencies increased with rising concentration of eGFP, reaching saturation at 90% entrapment efficiency at concentrations above 1 mg/ml of eGFP for both conditions. Correlating protein concentration with the weight of the silica pellets, the maximum loading of the silica particles corresponds to a molecular ration of Protein : SiO<sub>2</sub> = 1 : 2. Interestingly, the morphology of the silica particles was not influenced significantly by different concentrations of eGFP (Fig. 42; in absence of protein substrate: Fig. 21).

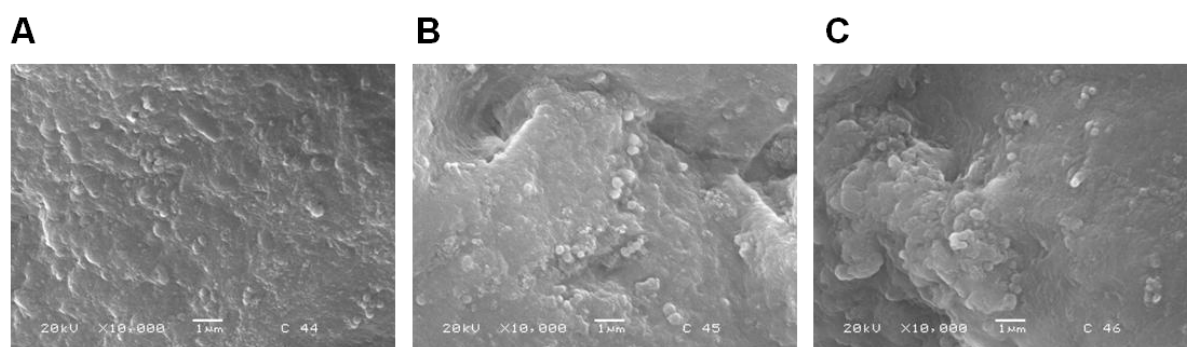


**Fig. 42: SEM morphologies of eGFP entrapped in silica. (Loading concentrations: A) 0.03 mg/ml, B) 0.12 mg/ml, C) 0.18 mg/ml. Entrapment conditions: 30 °C, 0.1 M potassium phosphate.)**

### 6.2.3 EGFP entrapment kinetics are time-linear

To follow the kinetics of protein entrapment, the relative fluorescence of the supernatant and the pellet of entrapped protein were measured over time (Fig. 43).

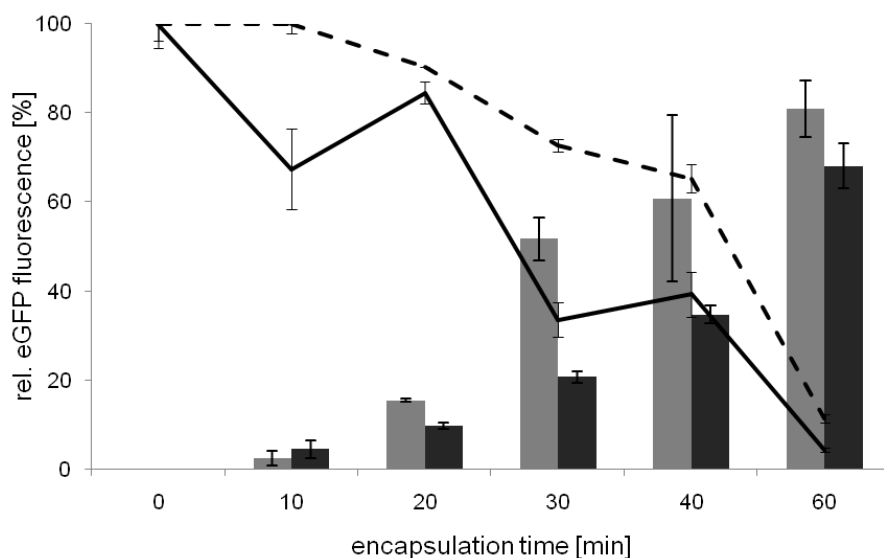


**Fig. 43: Kinetic analysis of the distribution of eGFP during the entrapment reaction (eGFP fraction in the silica pellet (bar plot) or in the supernatant (line plot)) at different entrapment conditions (30 °C, 0.1 M potassium phosphate: straight line/ gray columns; 20 °C, 0.5 M potassium phosphate: dashed line/dark columns).**

While the supernatant is depleted from eGFP over time, eGFP is subsequently entrapped into the pellet following nearly linear entrapment kinetics (refer to the histograms in Fig. 43). It is interesting to notice that after 10 min, the amount of entrapped eGFP was negligible.

This correlates with the formation of bigger silica particles at the beginning of the entrapment reaction (Fig. 23). Taking both sets of data together, it is clear that the majority of the protein entrapment takes place during the formation of the smaller, gel-like silica particles.

#### 6.2.4 Entrapped eGFP is stabilized against heat stress

eGFP is highly stable even at elevated temperatures (Bokman & Ward, 1981; Verkhusha *et al*, 2003; de Lencastre Novaes *et al*, 2011). Entrapped eGFP and a control of eGFP in solution were incubated at temperatures above their unfolding temperature at 80 °C and their fluorescence measured over time (Fig. 44).

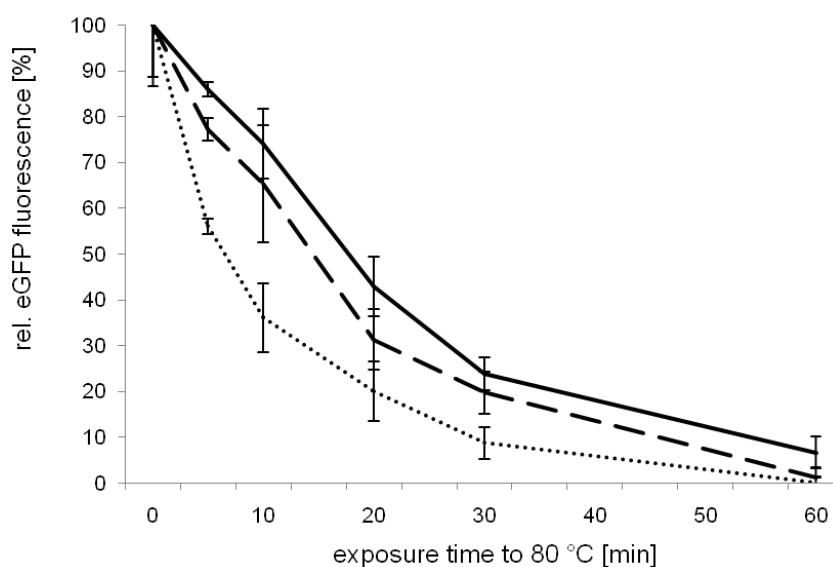


**Fig. 44:** Resistance of entrapped eGFP against denaturation by incubation at 80 °C. Dotted lines correspond to eGFP in solution, dashed lines to proteins entrapped at 20 °C, 0.5 M potassium phosphate and solid lines at 30 °C, 0.1 M potassium phosphate.

As shown in Fig. 44, after 1 h at 80 °C, eGFP in solution was completely denatured. Entrapped eGFP denatured slower, and the effect of stabilization by entrapment can be compared to the stabilization effect which is typical for chaperones (Haslbeck, 2002). A higher stabilization effect was observed for entrapment conditions at 30 °C, 0.1 M potassium phosphate compared to the entrapment conditions at 20 °C, 0.5 M potassium phosphate. Interestingly, the entrapment conditions with higher thermal stabilization properties were also more efficient for entrapment as shown in Fig. 39.

At higher temperatures, it could be possible that the morphology of the silica particles may have changed. To exclude that the harsh temperature treatment influences the particle morphology, SEM analysis of the samples incubated up to 1h at 80 °C was performed. The silica particles were measured prior and after heating up to 80 °C (Fig. 45). No alterations of the silica particles were observed, indicating that once formed, the silica matrix is structurally stable and the loss of activity is due to the denaturation of the protein.

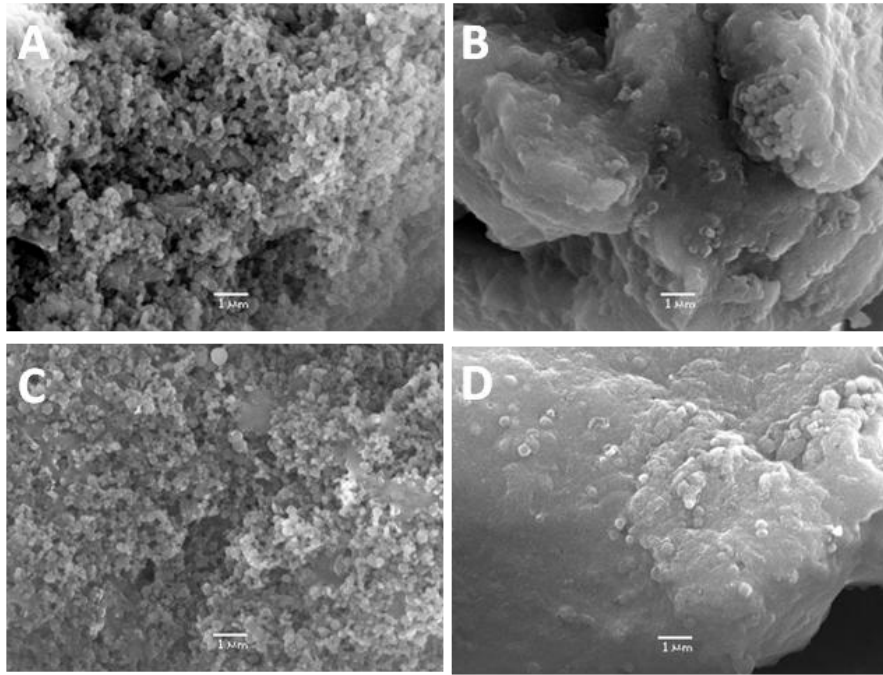


**Fig. 45:** SEM morphologies of eGFP entrapped in silica. Entrapment conditions: A, C) 20 °C, 0.5 M potassium phosphate, B), D) 30 °C, 0.1 M potassium phosphate. Samples were analyzed A), B) without heat treatment and C), D) after heat treatment at 80 °C for 1 hour.

### 6.2.5 Entrapped eGFP is stabilized against proteolytic digest

Next, it was tested if the entrapped eGFP was stabilized against treatment with proteases by incubating the immobilized and native eGFP with proteinase K, respectively. The fluorescence of native and entrapped eGFP was measured over 4 hours at 20 °C (Fig. 46).

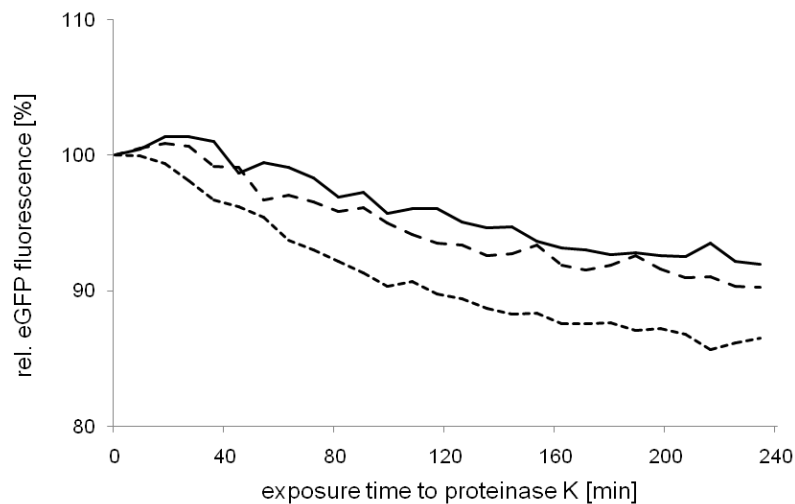


**Fig. 46:** Resistance of entrapped eGFP against denaturation by proteinase K. Dotted lines correspond to eGFP in solution, dashed lines to proteins entrapped at 20 °C, 0.5 M potassium phosphate and solid lines at 30 °C, 0.1 M potassium phosphate.

EGFP showed little loss of fluorescence in solution despite the high concentration of proteinase K. Still, the effect of stabilization by entrapment could be observed. The



stabilization potential corresponded qualitatively to the results of the thermal denaturation experiment (Fig. 44).

### 6.2.6 Entrapped eGFP is stabilized against denaturation by chaotropes

Since the eGFP solution showed high stability in the presence of proteinase K, the stabilization by entrapment against other chaotropic agents was investigated.

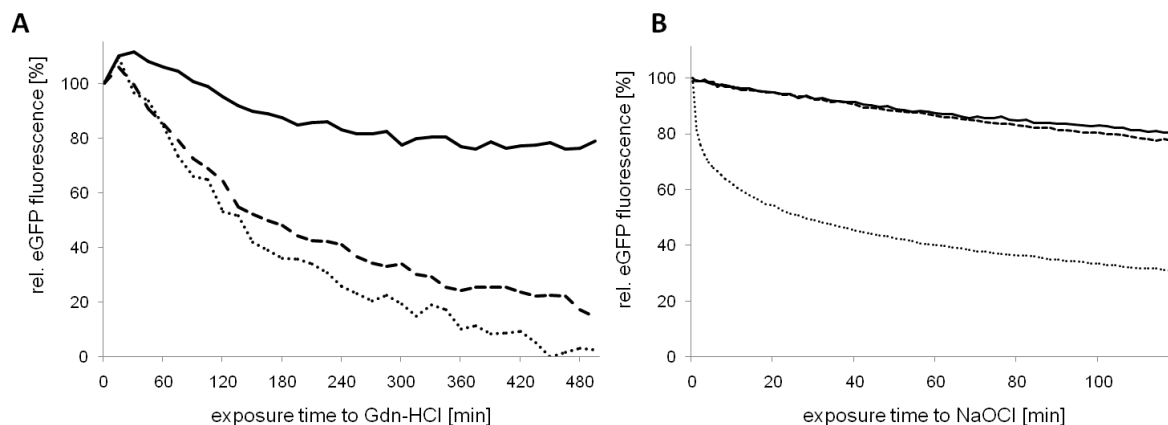


**Fig. 47:** A) eGFP fluorescence in the presence of Gdn-HCl. Dotted lines correspond to eGFP in solution, dashed lines to entrapped proteins (reaction conditions 20 °C, 0.5 M potassium phosphate) and solid lines to entrapped proteins (reaction conditions 30 °C, 0.1 M potassium phosphate). B) eGFP fluorescence in the presence of NaOCl. Dotted lines correspond to eGFP in solution, dashed lines to proteins entrapped at 20 °C, 0.5 M potassium phosphate and solid lines at 30 °C, 0.1 M potassium phosphate.

In a first experiment, Gdn-HCl was added to the eGFP solution to a final concentration of 3 M in the absence of proteinase K (Toca-Herrera *et al*, 2006). The fluorescence of eGFP was monitored over time at 16 °C (Fig. 47A). After 8 hours, the eGFP solution was completely denatured. Entrapped eGFP again showed slower denaturation, with significant stabilization effects of the entrapment conditions of 30 °C, 0.1 M potassium phosphate.

In a second experiment (Fig. 47B), NaOCl at a final concentration of 3 mM active chlorine was used as denaturing agent (Mazzola *et al*, 2006). After 30 min, the eGFP solution was denatured to 50 %. Entrapped eGFP showed again slower denaturation. The entrapment conditions differ only slightly in their protective effect. For chaotropic agents (Fig. 47A-B), the same pattern of protection efficiency as for the protection against heat (Fig. 44) and proteinase K (Fig. 46) was observed, qualitatively.

### 6.2.7 Entrapped eGFP is stabilized against dehydration stress

Entrapped proteins have a potential application for protein storage in a water-free state. To investigate if proteins are stabilized against drying and retain higher activity upon resuspension in buffer, the native or entrapped (entrapment conditions: 20 °C, 0.5 M potassium phosphate and 30 °C, 0.1 M potassium phosphate) model protein eGFP was dried at r.t. over night until no further weight loss was measured and the remainder was

resuspended in 0.1 M potassium phosphate. The eGFP fluorescence was monitored over repeated drying and resuspension steps (Fig. 48).

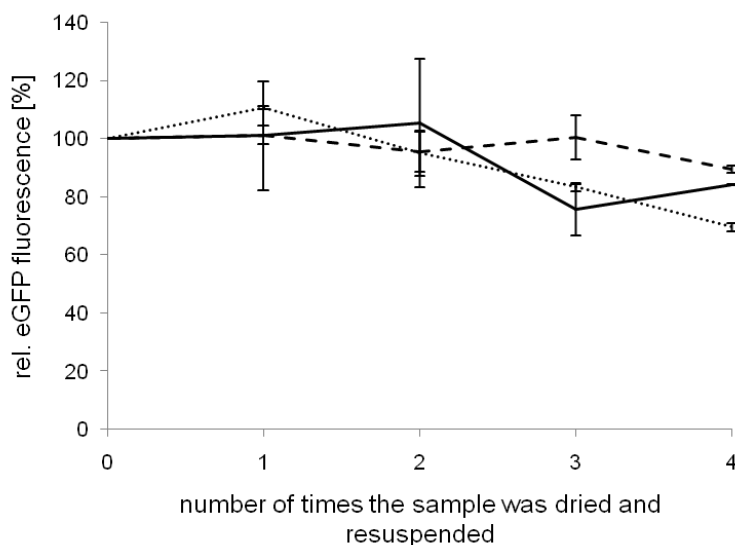


**Fig. 48:** Fluorescence of eGFP in solution and after entrapment after repeated drying and resuspension at r.t.. Dotted lines correspond to eGFP in solution, dashed lines to proteins entrapped at 20 °C, 0.5 M potassium phosphate and solid lines at 30 °C, 0.1 M potassium phosphate.

The highly stable eGFP in solution showed only little loss in fluorescence (20 %) after 4 cycles of drying and rehydration. Nevertheless, entrapped eGFP showed less deactivation over four drying cycles. Taking into account the error bars, a clear difference in protection efficiency against dehydration stress could not be noted between both entrapment conditions.

### 6.2.8 Entrapped eGFP can be recovered from the silica particles by leaching

The silica particles entrapping the proteins show differences in fluidity in suspension depending on their reaction conditions (Fig. 33). To investigate if the entrapped eGFP is able to diffuse into the surrounding solution, leaching experiments were performed.

#### 6.2.8.1 Adsorbed eGFP is weakly immobilized compared to entrapped eGFP

To compare the stability of the protein immobilization techniques, eGFP was immobilized in two ways: entrapment and physical adsorption by centrifugating an eGFP solution with preformed protein-free silica particles generated at 20 °C, 0.5 M potassium phosphate. Immobilized eGFP was incubated or stirred in 0.1 M potassium phosphate (pH 7) or Tris buffer (pH 9) and leaching was measured (Fig. 49).

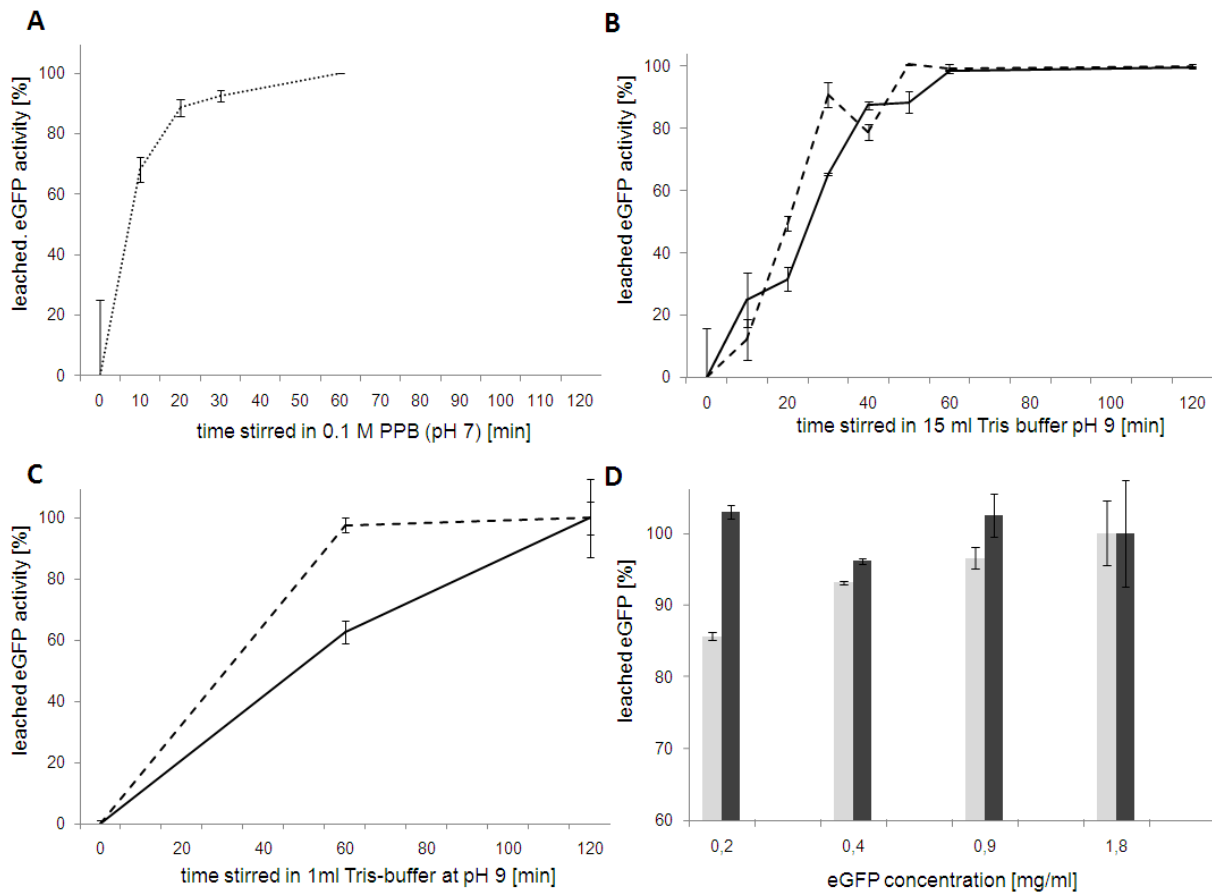


**Fig. 49:** A) Leaching of adsorbed eGFP at neutral pH. Leaching conditions: stirring at 500 rpm in 0.1 M potassium phosphate, pH 7. B) Leaching of entrapped eGFP. Leaching conditions: stirring at 500 rpm in 15 ml 0.1 M Tris buffer, pH 9 (C) 1 ml 0.1 M Tris buffer, pH 9). Dashed lines correspond to proteins entrapped at 20 °C, 0.5 M potassium phosphate and solid lines at 30 °C, 0.1 M potassium phosphate. D) Total eGFP leaching for different eGFP concentrations used in the entrapment step under leaching conditions (stirring at 500 rpm with 0.1 M Tris buffer, pH 9) after one hour. Entrapment conditions: 30 °C, 0.1 M potassium phosphate (light column), 20 °C, 0.5 M potassium phosphate (dark column)

Incubating or gently shaking a suspension of physically adsorbed eGFP at 20 °C at 200 rpm over night did not lead to loss of fluorescence when 0.1 M potassium phosphate (pH 7) was used. However, physically adsorbed eGFP leached into the solution when stirred in 0.1 M potassium (pH 7) at 500 rpm in under an hour (Fig. 49A). Leakage of adsorbed proteins into solutions is a commonly known property of the adsorption-immobilization technique (Zaborsky, 1972). For leaching induced by stirring at neutral pH, adsorption on preformed silica particles was sufficient. Buffers of higher pH were shown to increase leakage for immobilized papain from MCM-41 (Díaz & Balkus Jr, 1996). With adsorbed eGFP, stirring in 0.1 M Tris buffer (pH 9) caused complete leaching of eGFP in less than 10 min (data not shown).

Entrapped eGFP showed no loss of fluorescence when incubated or stirred at 500 rpm in 0.1 M potassium phosphate (pH 7) (data not shown). Entrapment therefore is the more stable immobilization technique, where no leaching was observed at pH 7. Leaching at buffer conditions mimicking blood was tested with 1x PBS, but entrapped eGFP did not show any

leaching for this condition, either. Next, entrapped eGFP was stirred at 500 rpm in 0.1 M Tris buffer (pH 9) and leaching was measured over time (Fig. 49B). Entrapped eGFP stirred in 0.1 M Tris buffer (pH 9) showed leaching depending on the entrapment conditions. Leaching was completed faster for the entrapment conditions 20 °C, 0.5 M potassium phosphate, which previously also showed lower surface area (Fig. 31, Fig. 32), higher viscosity (Fig. 33), lower protection against different types of stress (Fig. 44, Fig. 46, Fig. 47) and a higher relative amount of bead-like particles (smaller mass of silica pellet in Fig. 22 with late appearance of gel-like particles in Fig. 24B). A higher volume 0.1 M Tris buffer (pH 9) (15 ml in Fig. 49B) accelerated leaching esp. for entrapment conditions of 30 °C, 0.1 M potassium phosphate compared to lower volumes of leaching buffer (1 ml in Fig. 49C).

Finally, leaching for different ratios of entrapped eGFP was investigated (Fig. 49D). With increasing protein load of the silica pellet, the difference in leaching between both entrapment conditions diminishes. At eGFP concentrations of 1.8 mg/ml in the entrapment step, the amount of protein leached from the silica particles is so high that the relatively small difference in leaching observed with 0.2 mg/ml eGFP in the entrapment step was not observed comparing the two entrapment protocols.

### 6.2.9 Conclusions

For the model protein eGFP, the entrapment strategy yielded functionally immobilized proteins in silica particles (Fig. 38). The optimal entrapment conditions were determined (Fig. 39). Depending on the entrapment conditions, significant protection of the model protein against heat stress (Fig. 44), digestion by proteinase K (Fig. 46), denaturation by chaotropes (Fig. 47) and dehydration stress (Fig. 48) was observed. Finally, the model protein eGFP could be recovered by leaching under specific conditions, while the immobilization was stable at neutral pH (Fig. 49).

## 6.3 Enzymes are functionally entrapped in silica particles

Having analyzed the entrapment of eGFP in detail, the same entrapment protocol was applied to a series of enzymes, in order to investigate its adaptability to entrap functional proteins of different sizes and reactivity. Proteins from different organisms with molecular masses varying from 20 kDa (DHFR) to 464 kDa (tetrameric  $\beta$ -galactosidase), varying activities and different thermal and chemical stabilities were entrapped. Besides classical enzymes like lipase or luciferase, which were previously entrapped in silica (Reetz *et al*, 1996; Roth *et al*, 2004), other rather unstable enzymes like  $\beta$ -galactosidase and DHFR were analyzed as well (Edwards *et al*, 1990; Uedaira *et al*, 1990). An overview of the entrapment efficiencies of the investigated enzymes is shown in Fig. 50, compared with the results from eGFP.

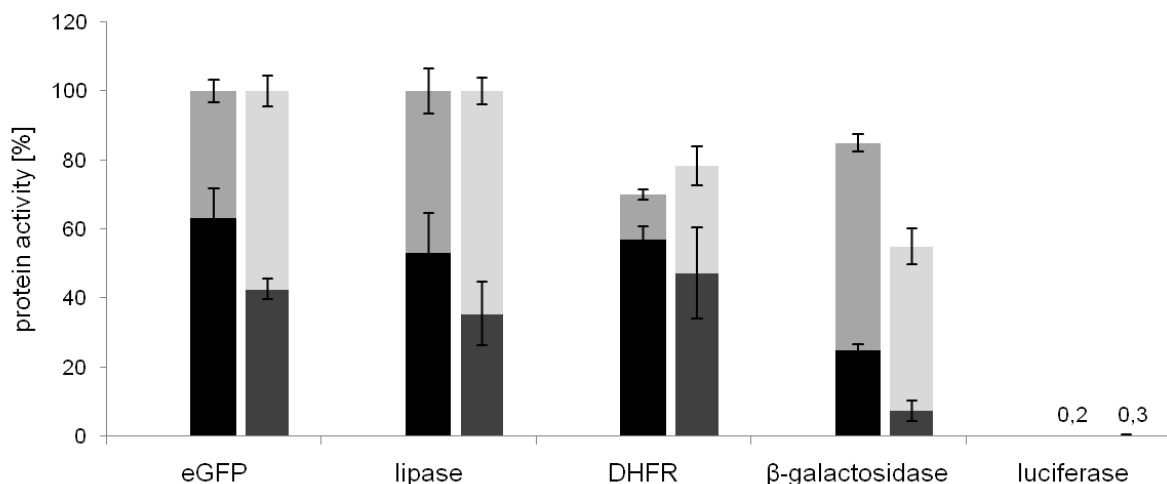


**Fig. 50: Protein activity after entrapment in silica particles.** For each of the different enzymes, one stacked column represents the sum of the activity of the pellet (bottom; entrapment conditions: left (30 °C, 0.1 M potassium phosphate); right (20 °C, 0.5 M potassium phosphate)) and the supernatant (top).

All proteins except luciferase were successfully sol-gel entrapped. The entrapment efficiencies varied for the different proteins: eGFP (42 and 63 %), lipase (from 35 and 53 %), DHFR (from 47 and 57 %) and β-galactosidase (from 7 and 25 %) for entrapment conditions of 20 °C, 0.5 M and 30 °C, 0.1 M potassium phosphate, respectively.

Interestingly, for all successful entrapment reactions, the levels of entrapment qualitatively corresponded to the results of the optimization of the eGFP entrapment (Fig. 39): in all cases, entrapment at 30 °C, 0.1 M potassium phosphate led to higher entrapment efficiencies.

Nevertheless, the absolute numbers for the entrapment efficiency were dependent on the entrapped protein. Entrapped DHFR showed activity comparable to eGFP and lipase, although a significant loss of DHFR activity of the supernatant was noticed. Especially the labile proteins β-galactosidase and luciferase showed significantly lower entrapment efficiencies. Luciferase displayed extremely little activity (0.2-0.3 % of the initial enzyme solution) after entrapment (with the supernatant showing little to no activity). The enzyme β-galactosidase showed significantly lower entrapment than other enzymes, while the supernatant was not deactivated compared to luciferase. It was investigated if the entrapment conditions yielding the highest entrapment efficiency for eGFP (Fig. 39) were also favorable for entrapment of β-galactosidase. A screening of the potassium phosphate molarities at 30 °C showed qualitatively similar results (Fig. 51).

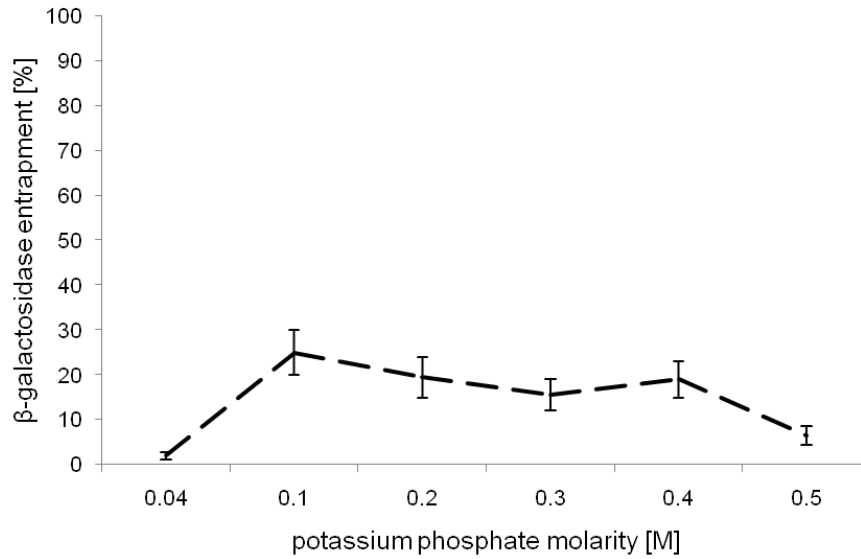


**Fig. 51: Dependence of the entrapment efficiency of  $\beta$ -galactosidase on phosphate concentration at 30 °C and a reaction time of 60 min.**

Entrapment efficiencies for  $\beta$ -galactosidase were also highest for 0.1 M potassium phosphate at 30 °C reaction temperature, indicating that the entrapment efficiencies for  $\beta$ -galactosidase were generally lower than for other enzymes. To exclude effects of the different proteins on the morphology of the silica particles, they were all investigated after entrapment by SEM (Fig. 52).

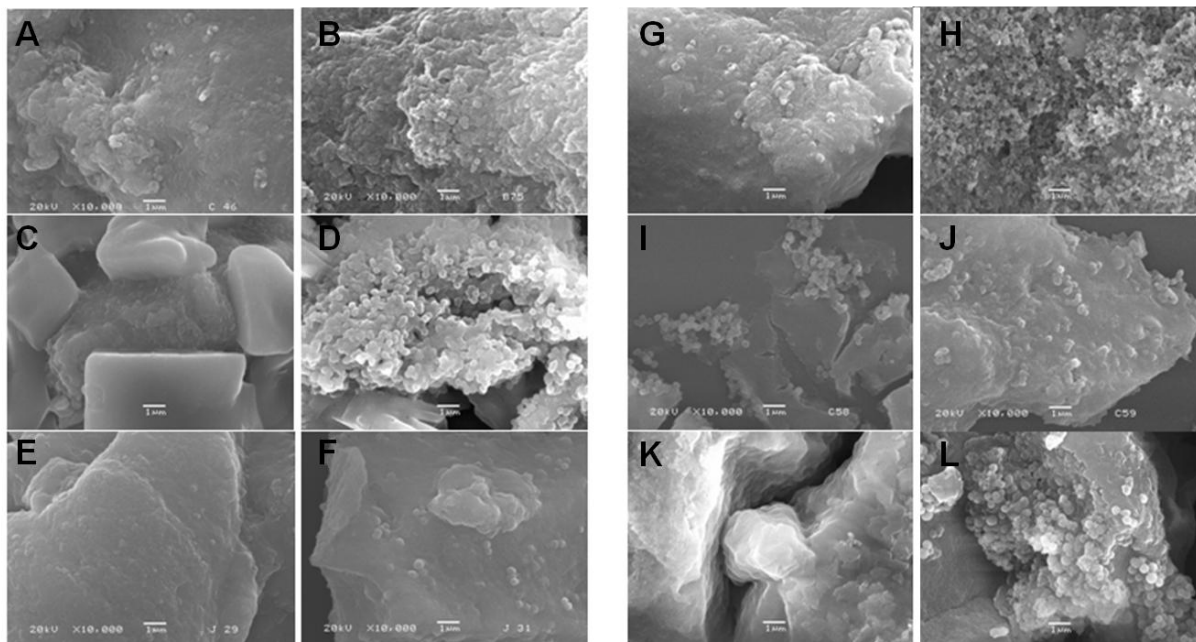


**Fig. 52: SEM overview of entrapped proteins in silica particles generated by two different entrapment protocols. Entrapment conditions: 30 °C, 0.1 M potassium phosphate for A, C, E, G, I, K and 20 °C, 0.5 M for B, D, F, H, J, L. Entrapment protocol was carried out with A, B) eGFP; C, D) DHFR; E, F) lipase; G, H)  $\beta$ -galactosidase; I, J) luciferase and K, L) without protein.**

The robust nature of the PEI-driven biomineralization reaction led to comparable morphologies independent of the nature of the entrapped protein for both investigated entrapment conditions. Significant changes in particle size or morphologies were not detected, independent of which protein (or none) was present.

### 6.3.1 The entrapment efficiency is increased by recycling the supernatant

Especially in cases where the entrapment efficiency was rather low, it is highly interesting if the enzyme containing supernatants of the reaction can be re-used in further reactions.  $\beta$ -galactosidase, which showed lower entrapment efficiency, remained active in the supernatant and could be re-used in two subsequent entrapment reactions (Fig. 53).

The second entrapment reaction was carried out with the supernatant of the first reaction, adding fresh starter (PEI) and silicic acid. An additional activity of 15 % (Fig. 53A) and 7% (Fig. 53B) to the pellet fraction was achieved, depending on the reaction conditions.

Combining three entrapment reactions the total activity found in the pellet fraction was increased from 30 to 55% for entrapment at 30 °C, 0.1 M potassium phosphate and from 10 to 27% at 20 °C, 0.5 M potassium phosphate. The total sum of activities in the supernatant and pellet of the entrapment reactions showed only little losses in enzyme activity.

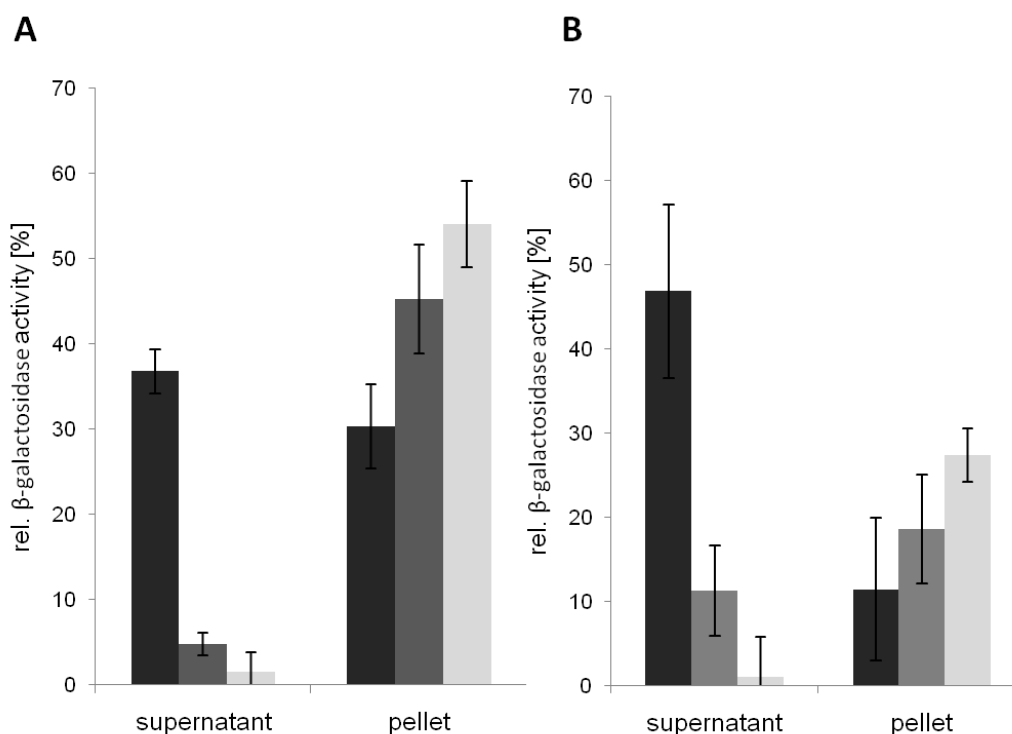


**Fig. 53: Activity of entrapped  $\beta$ -galactosidase for subsequent entrapment steps (dark: first, grey: second and white: third entrapment reaction step) by subsequently re-using the supernatant. Entrapment conditions A) 30 °C, 0.1 M potassium phosphate; B) 20 °C, 0.5 M potassium phosphate.**

### 6.3.2 Protein concentration and activity are equivalent in the case of entrapped lipase

The activity of the enzymes in the silica particles is not necessarily correlating with the protein concentration in the pellet. For eGFP, this could easily be monitored by its fluorescence, which was not impaired by the silica particles (Fig. 39). To prove the correlation of protein activity with protein content, both were determined for the enzyme lipase (Fig. 54).

Lipase concentration was determined via Bradford assay in the supernatant and the protein content in the pellet was calculated (Fig. 54A). Lipase activity could be measured in the silica particles as well as in the supernatant (Fig. 54B). The protein content and activity in the pellet correlated well, considering the error bars of the activity of the lipase pellet.

Having established a fast and easy method for entrapment of proteins in silica particles with high entrapment efficiency, the stabilization against heat stress of entrapped enzymes was investigated.

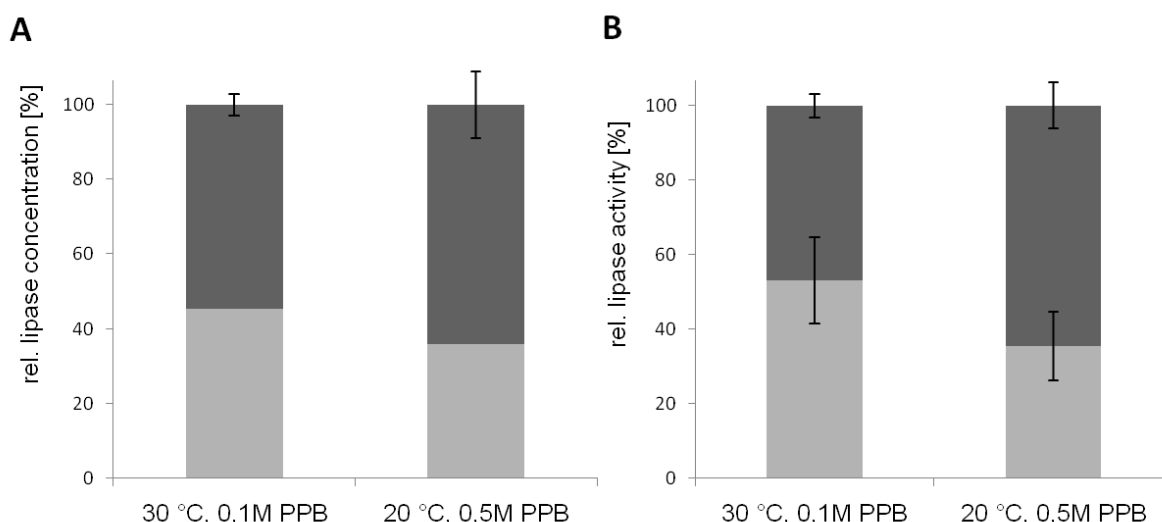


**Fig. 54: Comparison of protein activity and concentration after entrapment in the case of lipase. A) Lipase concentration measured with the Bradford assay in the supernatant (dark column, top) and calculated for the pellet (light column, bottom) after entrapment. B) Lipase activity measured in the supernatant (dark column, top) and pellet after entrapment (light column, bottom).**

#### 6.3.2.1 Entrapped enzymes are stabilized against heat stress

Stabilization against heat stress was investigated by incubating the immobilized and native proteins at temperatures above their unfolding temperature (80 °C for lipase, 60 °C for  $\beta$ -galactosidase and DHFR and 40 °C for Luciferase) (Fig. 55) (Edwards *et al*, 1990; Uedaira *et al*, 1990; Frank, 1989; Zhu *et al*, 2001; Ionescu *et al*, 2000; Schröder *et al*, 1993).



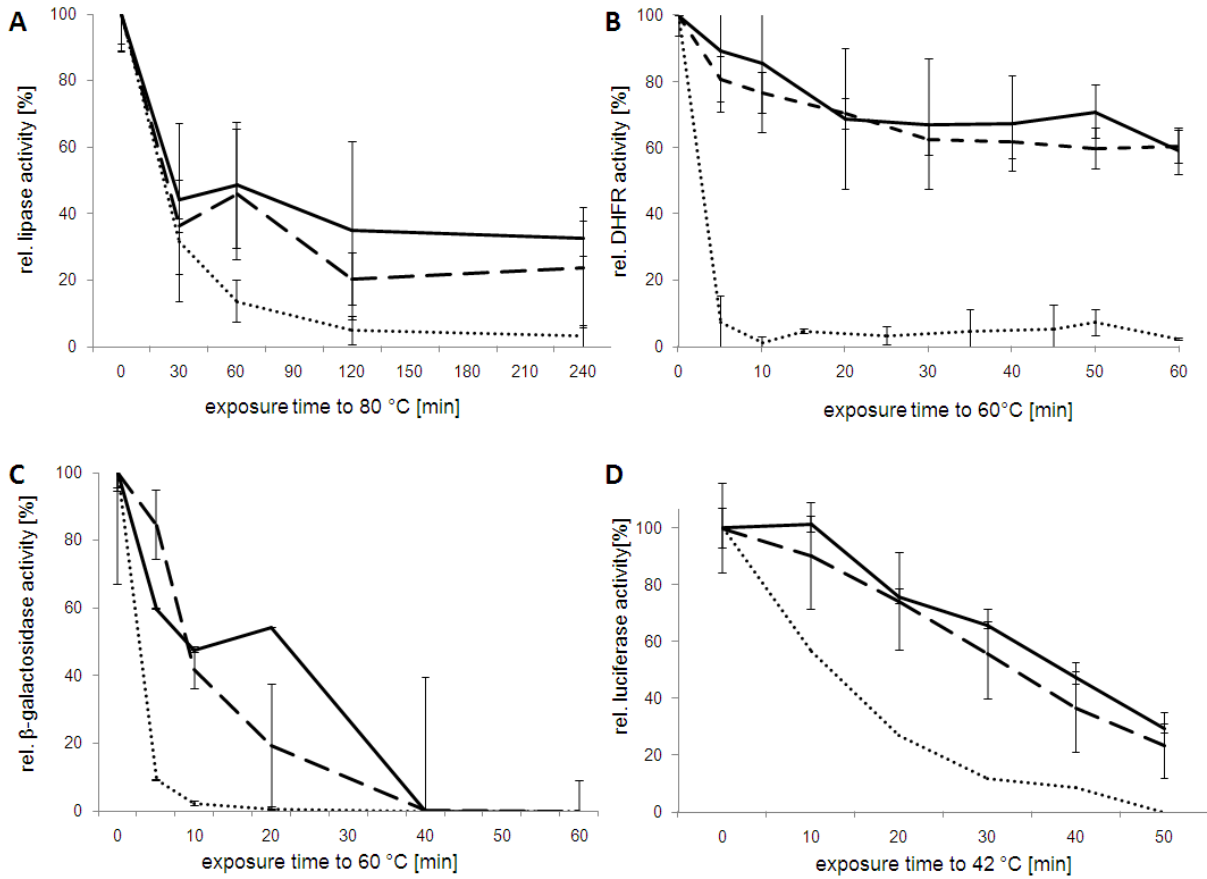


**Fig. 55: Resistance of entrapped proteins against heat stress. Activities of A) lipase, B) DHFR, C)  $\beta$ -galactosidase and D) Luciferase in solution and after entrapment. Dotted lines correspond to the protein in solution, dashed lines to proteins entrapped at 20 °C, 0.5 M potassium phosphate and solid lines at 30 °C, 0.1 M potassium phosphate.**

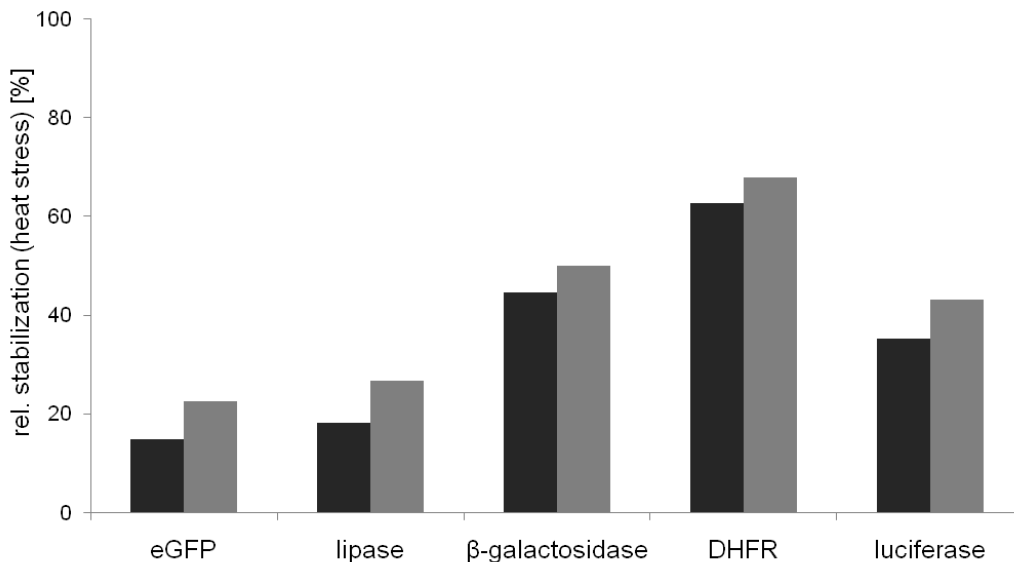


**Fig. 56: Relative stabilization by entrapment of eGFP and enzymes against thermal denaturation (0% corresponds to denaturation as in solution, 100% corresponds to the native activity, refer to Materials and Methods 8.4.8.4). Entrapment conditions: light column: 30 °C, 0.1 M potassium phosphate; dark column: 20 °C, 0.5 M potassium phosphate.**

As expected from the results for eGFP (Fig. 44), all entrapped enzymes were less affected by heat stress compared to the enzyme solution. Interestingly, in the amorphous gel-like particles (formed at 30°C in 0.1 M potassium phosphate) all entrapped enzyme were stabilized more efficiently than in isolated, bead-like particles (formed at 20°C and 0.5 M potassium phosphate), confirming the observations made with entrapped eGFP. As a control, the activity of the native protein was monitored in the same solution, i.e. in the presence of PEI without TMOS, but no stabilization could be observed. A summary of the thermal stabilization for all proteins investigated so far, including eGFP, is shown in Fig. 56. It clearly shows the protection against the denaturation process by thermal stress between 15-70%. DHFR and  $\beta$ -galactosidase were most strongly stabilized by the entrapment. The entrapment at 30 °C, 0.1 M potassium phosphate yielded 5-9% higher stabilization than the entrapment at 20 °C, 0.5 M potassium phosphate.

For the thermally labile enzyme  $\beta$ -galactosidase, it was of interest, if simple adsorption to silica particles would lead to significant stabilization as well. Therefore, a comparison between the thermal stabilization by entrapment or adsorption was carried out (Fig. 57).

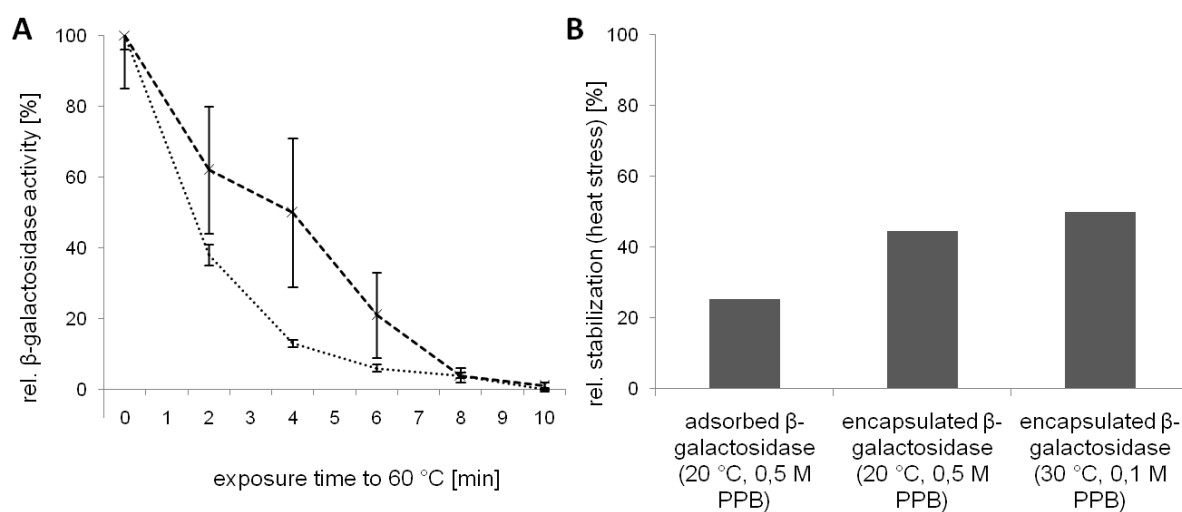


**Fig. 57: Resistance of adsorbed  $\beta$ -galactosidase against heat stress. A) Activities of  $\beta$ -galactosidase in solution and after adsorption to protein-free silica particles created at 20 °C, 0.5 M. Dotted lines correspond to the protein in solution, dashed lines with cross marks to adsorbed protein. B) Comparison of relative stabilization by adsorption or entrapment of  $\beta$ -galactosidase by different entrapment conditions (0% corresponds to denaturation as in solution, 100% corresponds to the native activity, refer to Materials and Methods 8.4.8.4).**

Adsorption of  $\beta$ -galactosidase did stabilize the enzyme against heat stress (Fig. 57A). However, the stabilization was less than half as effective as determined for the stabilization by entrapment (Fig. 57B).

Further studies of the stabilization of enzymes by protein adsorption, e.g. for lipase, were not carried out, since lipase immobilization has been widely investigated in the literature (Reetz *et al*, 1996).

### 6.3.2.2 Entrapped $\beta$ -galactosidase show increased long-time stability

Since entrapped proteins proved to be protected against heat stress (Fig. 55), it was presumed that protein entrapment leads to higher long time stability at r.t. To investigate long time stability, all entrapped proteins were stored at r.t. in 0.1 M potassium phosphate. The activity of the thermolabile enzyme  $\beta$ -galactosidase was measured before and after storage at r.t. for 16 days with or without entrapment at 30 °C, 0.1 M potassium phosphate (Fig. 58):

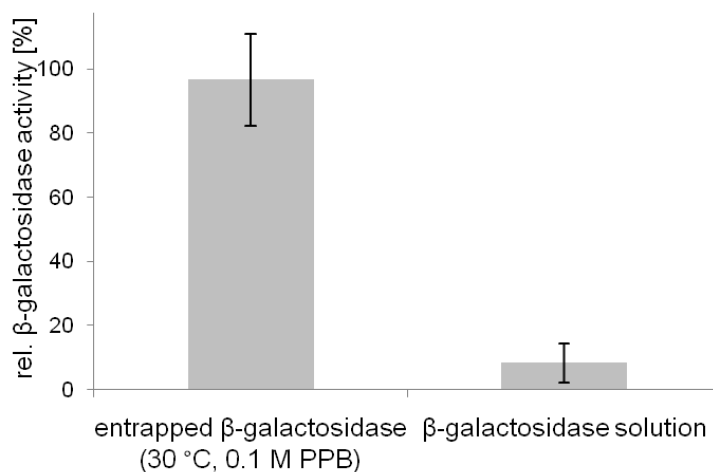


**Fig. 58: Relative activity of  $\beta$ -galactosidase (in solution or entrapped at 30 °C, 0.1 M potassium phosphate) after incubation at r.t. for 16 days. The activity of native  $\beta$ -galactosidase was set to 100 %.**

No significant loss of activity was observed for entrapped  $\beta$ -galactosidase stored for 16 days at r.t. In comparison, free  $\beta$ -galactosidase solution retained only < 10 % of its activity under these conditions. Similarly, all enzymes other showed higher tolerance to storage at r.t. after entrapment. Especially the very robust proteins eGFP and lipase could be stored at r.t. over several months without activity loss for both entrapment conditions, while the proteins in solution lost significant activity (> 50 %) after several days at r.t. (data not shown).

### 6.3.2.3 Entrapped proteins are incorporated more deeply into silica particles compared to physical adsorption

Adsorption and entrapment were compared regarding their ability to deeply embed proteins in silica particles. Lipase was used as a model enzyme for the comparative study of adsorbed and entrapped enzyme using thermo-gravimetric analysis (TGA) (Groshens & Hollins, 2009). TGA is a method that measures changes in weight as a function of the temperature. Its basic instrumental requirements are a precision balance and a furnace that is programmed for a linear rise of temperature over time (Coats & Redfern, 1963). The silica particle formation process was up-scaled, i.e. multiple amounts of all components of the entrapment protocol were used, in order to obtain entrapped and adsorbed lipase in sufficient quantities for TGA measurements (refer to Materials and Methods 8.3.2.2).

Oxidation at temperatures over 300 °C during TGA measurements causes burning-off of the organic compounds due to pyrolysis and desorption of organic products, while weight loss observed at lower temperatures than 300 °C is caused by desorption of physically bonded water and the Hoffman degradation (Kusak, 2005). In order to only observe weight loss caused by oxidation of organic matter, the weight loss of silica samples was investigated between 300 and 800 °C. To compare adsorbed lipase and entrapped lipase with regards to how stable the protein was incorporated into the silica matrix, the mass loss of immobilized lipase was measured with TGA (Fig. 59):

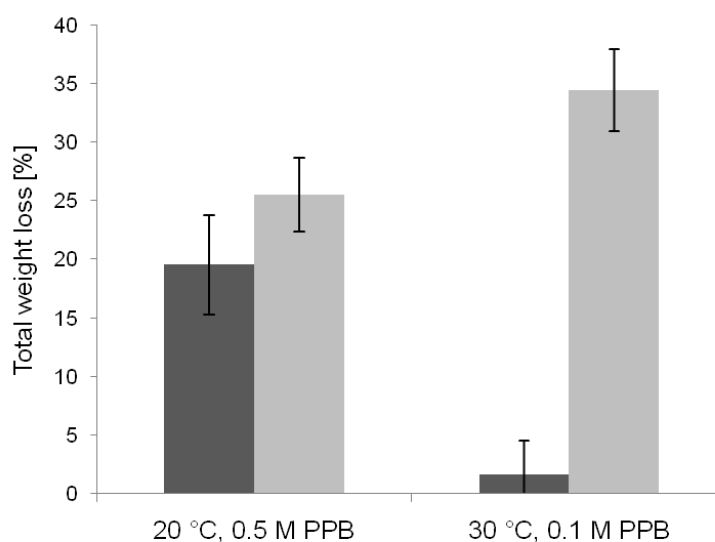


**Fig. 59: TGA measurements with entrapped (dark column) or physically adsorbed (light column) lipase on silica particles generated at the stated entrapment conditions. The relative weight loss after calcination at 800 °C is plotted (refer to Materials and Methods 8.3.2.2).**

Entrapped proteins are expected to be randomly immobilized throughout the silica structures. At 800 °C, entrapped lipase samples were calcinated, with a mass loss of 2% and 20% for entrapment at 30 °C, 0.1 M potassium phosphate and 20 °C, 0.5 M potassium phosphate, respectively. In comparison, physically adsorbed lipase showed higher loss of its relative protein mass (34% and 25% for entrapment at 30 °C, 0.1 M potassium phosphate and 20 °C, 0.5 M potassium phosphate, respectively), indicating that most of the adsorbed protein was attached superficially to the silica particles.

Higher mass loss for lipase adsorbed to silica particles generated at 30 °C, 0.1 M potassium phosphate than to those generated at 20 °C, 0.5 M potassium phosphate fits the higher specific surface of the former particles (Fig. 31, Fig. 32). Since pyrolyzed organic compounds desorbed less from the entrapped than from adsorbed samples during calcination, as seen from the lower weight loss of entrapped proteins, it was concluded that that entrapped protein was embedded more deeply into the biomineral than adsorbed protein.

### 6.3.3 Entrapped enzymes are stabilized against proteolytic digest

Next, it was tested if the entrapped enzymes were stabilized against treatment with proteases by incubating the immobilized and native proteins, respectively, with proteinase K (Fig. 60).

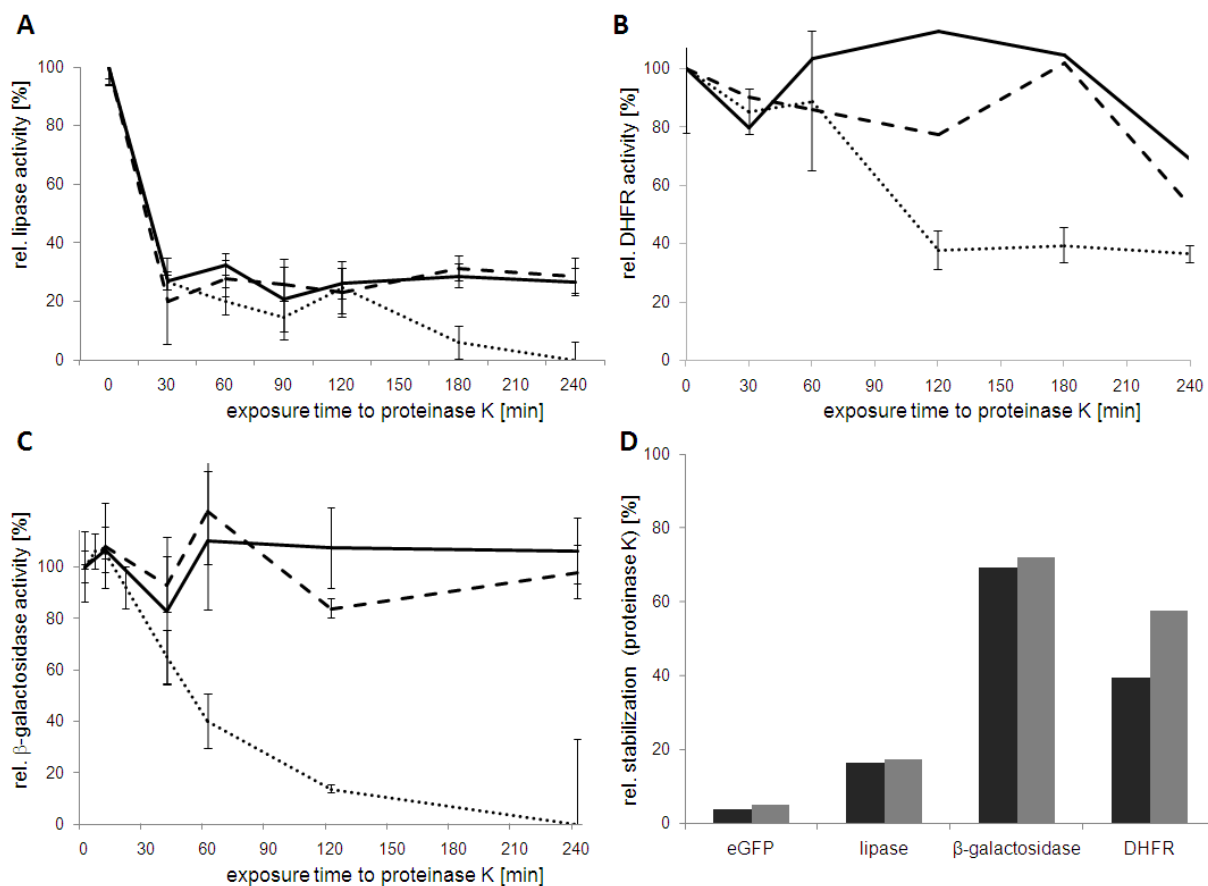


**Fig. 60: Resistance of entrapped proteins against proteinase K.** Activities of A) lipase, B) DHFR and C)  $\beta$ -galactosidase in solution and after entrapment. Dotted lines correspond to the protein in solution, dashed lines to proteins entrapped at 20 °C, 0.5 M potassium phosphate and solid lines at 30 °C, 0.1 M potassium phosphate. D) Relative stabilization by entrapment of eGFP and enzymes against proteinase K (0% corresponds to denaturation as in solution, 100% corresponds to the native activity, refer to Materials and Methods 8.4.8.4). Entrapment conditions: light column: 30 °C, 0.1 M potassium phosphate; dark column: 20 °C, 0.5 M potassium phosphate.

In accordance with previous results with eGFP (Fig. 46), all investigated enzymes (lipase, DHFR,  $\beta$ -galactosidase) were less affected by the proteolytic digest compared to the enzyme in solution. The representation in Fig. 60D is calculated from the proteinase K data of Fig. 60A-C and clearly shows protection against proteolytic digest between 3-70 %. DHFR and  $\beta$ -galactosidase were most strongly stabilized by entrapment, similar to the results for heat stress (Fig. 56). Entrapment at 30 °C, 0.1 M potassium phosphate yielded 1-18 % higher stabilization than entrapment at 20 °C, 0.5 M potassium phosphate.

### 6.3.4 Entrapped enzymes are stabilized against denaturation by chaotropes

Stabilization of entrapped luciferase against proteinase K could not be shown due to the challenging entrapment efficiency for this enzyme. Nevertheless, luciferase activity was

monitored against Gdn-HCl to a final concentration of 6 M in solution and for both entrapment methods, (Fig. 61).

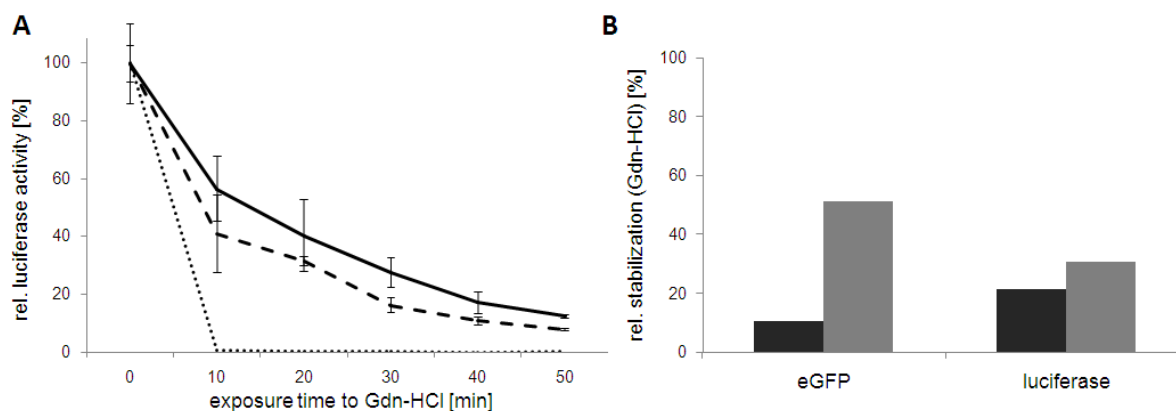


**Fig. 61:** A) Luciferase activity in the presence of Gdn-HCl. Dotted lines correspond to eGFP in solution, dashed lines to proteins entrapped at 20 °C, 0.5 M potassium phosphate and solid lines at 30 °C, 0.1 M potassium phosphate. B) Relative stabilization by entrapment of luciferase against Gdn-HCl (0% corresponds to denaturation as in solution, 100% corresponds to the native activity, refer to Materials and Methods 8.4.8.4). Entrapment conditions: light column: 30 °C, 0.1 M potassium phosphate; dark column: 20 °C, 0.5 M potassium phosphate.

Comparable to eGFP (Fig. 47), Luciferase was less denaturated by Gdn-HCl after entrapment (Fig. 61A). The representation in Fig. 61B is calculated from the Gdn-HCl data for eGFP and luciferase (Fig. 47, Fig. 61A). This comparison in Fig. 61B clearly shows protection for eGFP against Gdn-HCl between 10-50 %. Interestingly, luciferase exhibited nearly no differences in stabilization for both entrapment conditions (9 % in contrast to 40 % difference for eGFP).

### 6.3.5 Entrapped enzymes are stabilized against dehydration stress

Comparable to the results observed with eGFP (Fig. 48), it was measured how far enzymes can be protected against dehydration stress. Lipase, DHFR and  $\beta$ -galactosidase were entrapped at 20 °C, 0.5 M potassium phosphate and 30 °C, 0.1 M potassium phosphate, the buffer was removed by drying at r.t. over night until no further weight loss was measured and the dried silica particles were resuspended in 0.1 M potassium phosphate. The enzymatic activity was measured for repeated drying and resuspension steps of the entrapped enzymes (Fig. 62A-C).

Comparable to eGFP, entrapment of enzymes demonstrated a protective effect against denaturation induced by dehydration stress, with the entrapment conditions of 30 °C, 0.1 M potassium phosphate being superior in their ability to protect protein activity to those of 20 °C, 0.5 M potassium phosphate. In contrast to eGFP, the enzymes lipase, DHFR and  $\beta$ -galactosidase showed higher activity loss caused by repeated drying and resuspension. After four drying cycles, native eGFP lost only ~30 % activity and entrapped eGFP (both

entrapment conditions) only ~10-15 % activity (Fig. 48). In comparison, native lipase, DHFR and  $\beta$ -galactosidase were completely denatured and entrapped enzymes lost more than 60 % activity after four drying cycles.

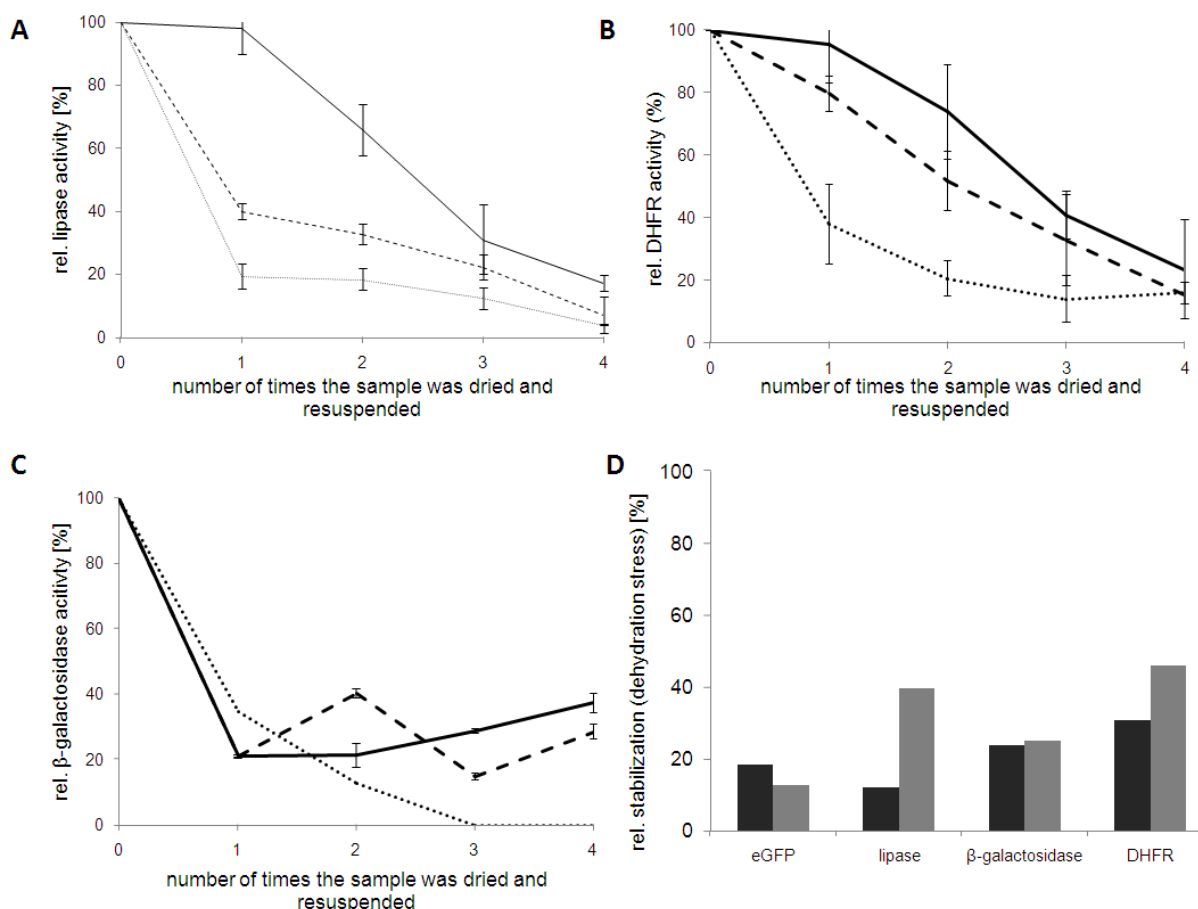


**Fig. 62: Activities of native and entrapped enzymes after repeated drying and resuspension at r.t.: A) lipase, B) DHFR, C)  $\beta$ -galactosidase. Dotted lines correspond to the protein in solution, dashed lines and solid lines to proteins entrapped at 20 °C, 0.5 M potassium phosphate and 30 °C, 0.1 M potassium phosphate, respectively. D) Relative stabilization by entrapment of eGFP and enzymes against dehydration stress (0% corresponds to denaturation as in solution, 100% corresponds to the native activity, refer to Materials and Methods 8.4.8.4). Entrapment conditions: light column: 30 °C, 0.1 M potassium phosphate; dark column: 20 °C, 0.5 M potassium phosphate.**

A comparison of the relative stabilization against dehydration stress for all proteins investigated so far including eGFP is shown in Fig. 62D. The overview in Fig. 62D shows protection against dehydration stress between 12-45 %. DHFR and  $\beta$ -galactosidase were most strongly stabilized by entrapment, just as they were against heat stress (Fig. 56) and proteolytic digest (Fig. 60).

### 6.3.6 Entrapped enzymes can be used repeatedly

All entrapped enzymes could be removed from their substrates by simple centrifugation and washing with 0.1 M phosphate buffer. In order to determine if an entrapped enzyme can be re-used after isolating and washing the silica pellet repeatedly, lipase was entrapped as a

model enzyme at 20 °C, 0.5 M potassium phosphate and 30 °C, 0.1 M potassium phosphate and measured in repetitive assays (Fig. 63).

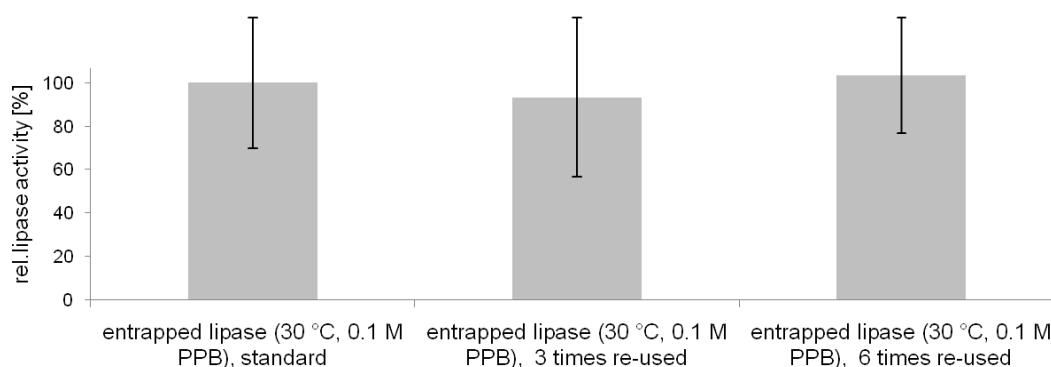


**Fig. 63: Relative activity of entrapped lipase (30 °C, 0.1 M) after repetitive enzymatic assay and subsequent washing of the entrapped lipase pellet with 0.1 M potassium phosphate.**

After 6 times of repetitive use of the immobilized enzyme followed by washing of the pellet between each lipase activity assay, no significant activity of the entrapped lipase was lost (Fig. 63).

### 6.3.7 Entrapped enzymes can be recovered from the silica particles by leaching

The leaching conditions established with eGFP (Fig. 49) were used in order to determine whether other proteins can similarly be recovered from entrapment. Entrapped enzymes (lipase, DHFR and  $\beta$ -galactosidase) were stirred at 500 rpm in 0.1 M Tris buffer (pH 9) and the enzyme activity in solution was measured over time (Fig. 64).

In all cases, leaching was completed faster for the entrapment conditions 20 °C, 0.5 M potassium phosphate (Fig. 49, Fig. 64), which previously also showed lower surface area (Fig. 31, Fig. 32), higher viscosity (Fig. 33), lower protection against different types of stress (Fig. 44, Fig. 46, Fig. 47) and a higher relative amount of bead-like particles (smaller mass of silica pellet in Fig. 22 with late appearance of gel-like particles in Fig. 24B).

The total leached activity of lipase and DHFR correlated with the sum of the activities of the pellet and the supernatant shown in Fig. 50. However, in the case of  $\beta$ -galactosidase, the activity in the pellet after entrapment and the leached activity from the pellet differed (Fig. 65).



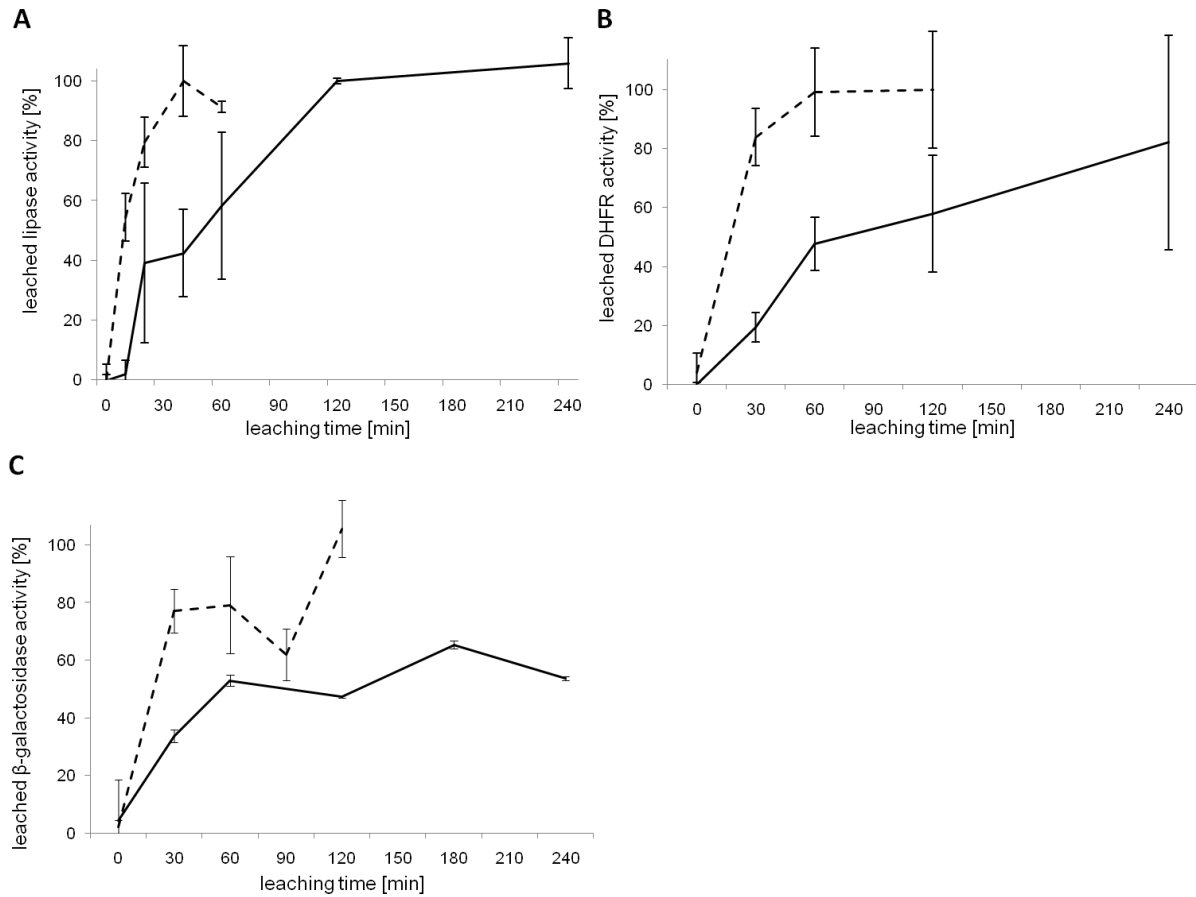


**Fig. 64:** Leaching of entrapped enzymes for different entrapment conditions under leaching conditions (pH 9 Tris buffer, stirring at 500 rpm) over time. A) lipase activity, B) DHFR activity and C)  $\beta$ -galactosidase activity. Dashed lines and solid lines correspond to the activity leached from proteins entrapped at 20 °C, 0.5 M potassium phosphate and 30 °C, 0.1 M potassium phosphate, respectively.

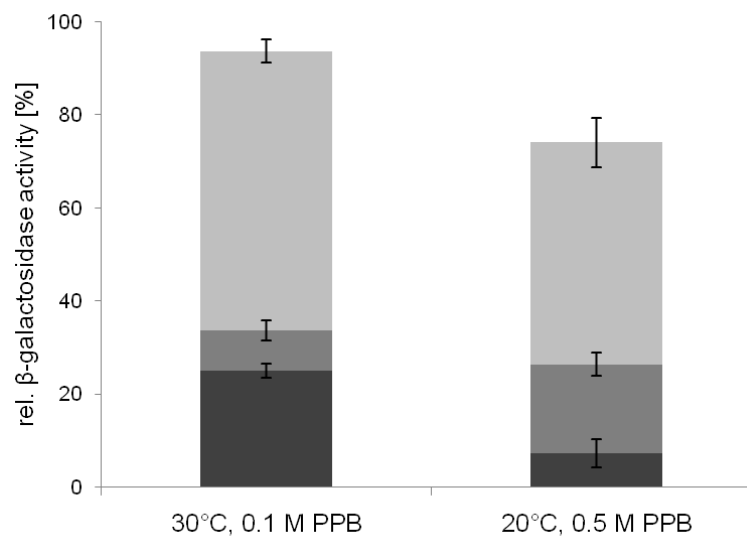


**Fig. 65:** Comparison of  $\beta$ -galactosidase activities after the entrapment with the total leached  $\beta$ -galactosidase after 240 min leaching time. Light gray: supernatant, dark gray: activity in the pellet. The gray fraction corresponds to the  $\beta$ -galactosidase activity measured in addition to that of the pellet after leaching.

Interestingly, the total  $\beta$ -galactosidase activity leached from the pellet was higher than the activity measured in the pellet before leaching. For entrapment conditions of 30 °C, 0.1 M potassium phosphate an additional 9 % activity was detected after leaching. For entrapment conditions of 20 °C, 0.5 M potassium phosphate, an additional 19 % activity was detected after leaching. This observation led to the conclusion that a fraction of the enzyme was entrapped in a non-active state, i.e. was not accessible for the substrate when bound in the silica pellet.

### 6.3.7.1 *The DnaJ/DnaK/GrpE chaperone system protects luciferase during entrapment and leaching*

As an exception from the investigated enzymes in this study, luciferase proved to deactivate readily under entrapment conditions (Fig. 50). The luciferase activity in the pellet and supernatant after the entrapment reaction is shown in Fig. 66A.

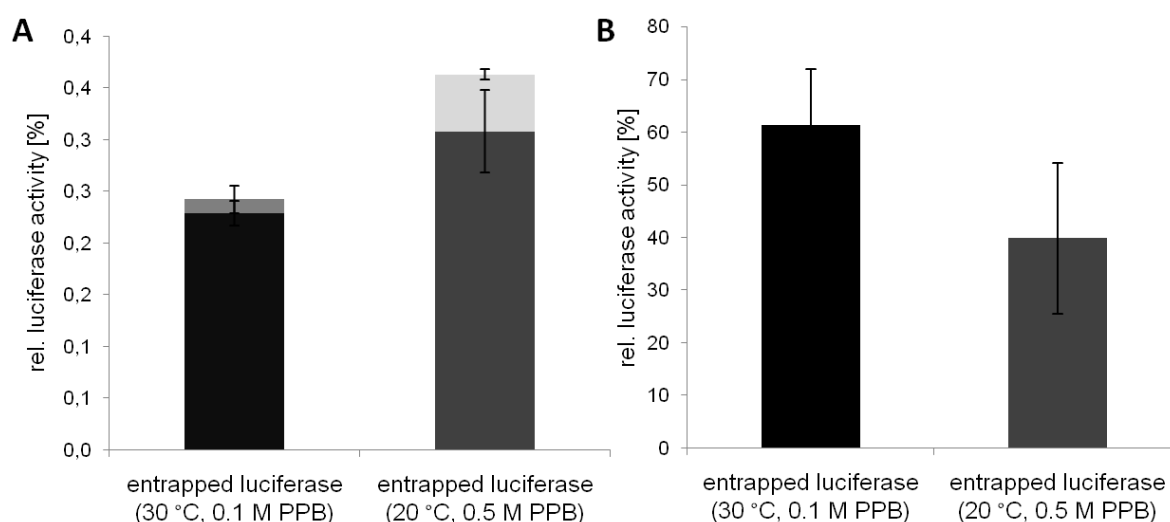


**Fig. 66: A) Entrapment of luciferase.** Each stacked column represents the sum of the activity of the pellet (bottom; entrapment conditions: left (30 °C, 0.1 M potassium phosphate); right (20 °C, 0.5 M potassium phosphate)) and the supernatant (top). **B) Relative activity of the entrapped luciferase in the pellet for both entrapment conditions for the second measurement after washing the silica particles.**

Although the entrapment ratio was minimal for both entrapment conditions (below 0.5 %), a complete deactivation of the supernatant was observed. To prove that the luciferase activity in the silica pellet was reproducible, the entrapped luciferase was washed and reused in a second enzymatic reaction (Fig. 66B, comparable to experiments with re-used entrapped lipase shown in Fig. 63). For the entrapment conditions of 30 °C, 0.1 M potassium phosphate, a higher activity could be recovered in the re-used pellet (Fig. 66B).

It was investigated which reaction condition caused luciferase deactivation in the supernatant. Since in the standard entrapment protocol TMOS is added to the protein solution in presence of PEI (Fig. 36), a control reaction was carried out where luciferase was

only added at different time points after starting the particle formation reaction with PEI and TMOS (Fig. 67).

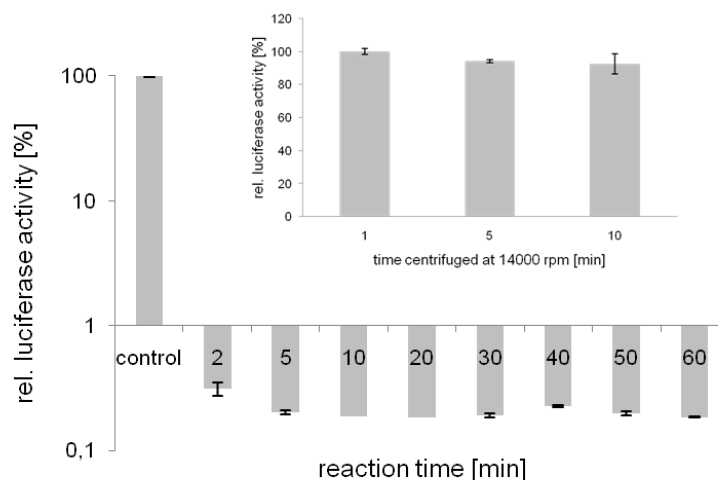


**Fig. 67:** Luciferase activity in the supernatant over the time of the entrapment at 30 °C, 0.1 M potassium phosphate (control: luciferase under the same entrapment conditions over an hour without TMOS). Inset: activity of luciferase in the absence of TMOS and in the presence of PEI and protein-free silica particles (obtained at 30 °C, 0.1 M potassium phosphate, washed to remove free silicic acid) for different centrifugation times.

Independent from the reaction time luciferase was added, its activity in the supernatant was still deactivated. Further experiments were carried out to test if methanol formed from TMOS hydrolysis influenced luciferase activity. Entrapment was carried out at 30 °C, 0.1 M potassium phosphate using methanol-free silicic acid obtained from degassed TMOS solution in 1 mM HCl, however luciferase was equally deactivated from degassed silicic acid alone (data not shown). In order to investigate if the centrifugation step needed for the isolation of entrapped proteins deactivated luciferase, native luciferase solution in the presence of PEI was incubated in 0.1 M potassium phosphate at 30 °C for an hour, and luciferase activity was measured after centrifugation in the presence of protein-free silica particles generated at 30 °C, 0.1 M potassium phosphate (Fig. 67, inset). No significant deactivation was observed from the reaction temperature, PEI or the centrifugation steps. These control experiments indicated that luciferase was denatured by silicic acid, since all other reaction conditions in the entrapment reaction did not cause significant luciferase deactivation. Therefore, a strategy was needed to temporarily protect luciferase against silicic acid during the entrapment reaction.

DnaK, in cooperation with its co-chaperones DnaJ and GrpE, forms a chaperone machinery that refolds substrate proteins in an ATP-dependent manner (Zylicz & Wawrzynow, 2001; Haslbeck, 2002). It was shown previously that luciferase can be activated by the chaperones DnaJ/DnaK/GrpE from the *E. coli* Hsp70 system (Veinger *et al*, 1998).

It was investigated whether the DnaJ/DnaK/GrpE system activated luciferase in the reaction solution containing PEI used for entrapment (30 °C, 0.1 M potassium phosphate) in the absence of TMOS. The activity of luciferase, luciferase in the presence of DnaJ/DnaK/GrpE and ATP, only DnaJ/DnaK/GrpE or only ATP was measured (Fig. 68, refer to Materials and Methods 8.3.1.1).

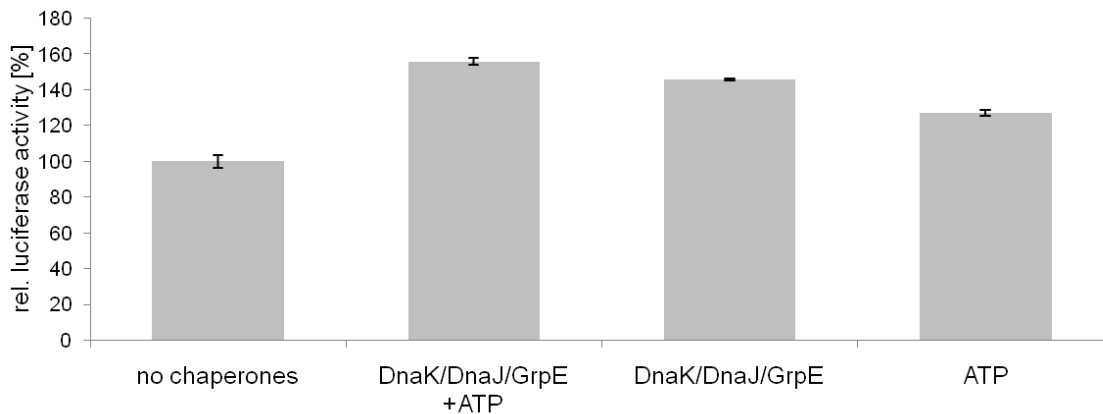


**Fig. 68:** Luciferase activity in the reaction solution containing PEI (at 30 °C, 0.1 M potassium phosphate, pH 7) in the absence or presence of the chaperones DnaJ/DnaK/GrpE and ATP. Luciferase activity was measured in absence of silicic acid.

At 30 °C and in the presence of PEI needed for the entrapment reaction, DnaJ/DnaK/GrpE increased luciferase activity, more so if ATP was present. The control reaction measured with luciferase and ATP alone showed an increase in luciferase activity which was lower than that observed for DnaJ/DnaK/GrpE alone. However, the chaperone system DnaJ/DnaK/GrpE+ATP did not improve the entrapment ratio nor retain luciferase activity in the supernatant for luciferase at 30 °C, 0.1 M potassium phosphate when the same TMOS concentration as for the previously investigated enzymes was used (data not shown).

Prior to the entrapment reaction, TMOS quantitatively reacted to silicic acid after prehydrolysis (Hench & West, 1990; Iler, 1979; Patwardhan, 2002). It was investigated which minimal concentration of silicic acid would be able to denature luciferase. The supernatant of the luciferase entrapment solution with DnaJ/DnaK/GrpE+ATP or without chaperones was analyzed for different TMOS (resp. silicic acid) concentrations (Fig. 69A).

TMOS at the concentration used to entrap the previously discussed enzymes (0.09 M) denatured luciferase in the supernatant (Fig. 67). Below 0.014 M TMOS, the supernatant showed significant activity (80 % in the absence of DnaJ/DnaK/GrpE+ATP). Interestingly, at 0.018 M TMOS (which is 20% of the TMOS concentration used for the other enzymes) the supernatant was completely deactivated in the absence of DnaJ/DnaK/GrpE+ATP, while a similar activity as in Fig. 68 was retained with DnaJ/DnaK/GrpE+ATP. The presence of ATP was necessary for stabilization of luciferase in the presence of 0.018 M TMOS (Fig. 69B).

Therefore, the DnaK/DnaJ/GrpE+ATP system stabilized luciferase against low concentrations of silicic acid. Above 0.018 M TMOS, luciferase was deactivated in all experiments even in the presence of DnaJ/DnaK/GrpE+ATP (data not shown). Entrapment with 0.018 M TMOS and DnaJ/DnaK/GrpE+ATP still led to a small luciferase activity after entrapment (Fig. 69C). Although 80 % luciferase activity was observed in the supernatant, less than 1 % activity was detected in the pellet.

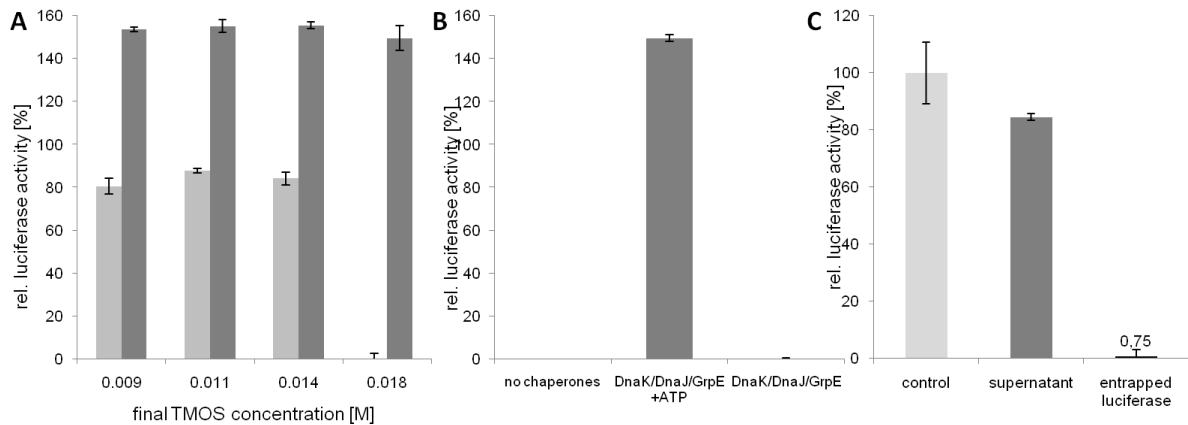


**Fig. 69:** A) Luciferase activity of the supernatant after the entrapment reaction in the presence or absence of the chaperones DnaJ/DnaK/GrpE+ATP at 30 °C, 0.1 M with different TMOS concentrations. Gray column: without the chaperones DnaJ/DnaK/GrpE+ATP, dark column: with DnaJ/DnaK/GrpE+ATP. B) Luciferase activity of the supernatant after the entrapment reaction at 30 °C, 0.1 M for the TMOS concentration: 0.018 M. Activities are shown in the presence or absence of DnaJ/DnaK/GrpE (with or without ATP). The activity of native luciferase in the absence of TMOS and chaperones was set to 100 %. C) Luciferase entrapment with 0.018 M TMOS and DnaJ/DnaK/GrpE+ATP at entrapment conditions of 30 °C, 0.1 M potassium phosphate. The control with DnaJ/DnaK/GrpE+ATP was set to 100 %.

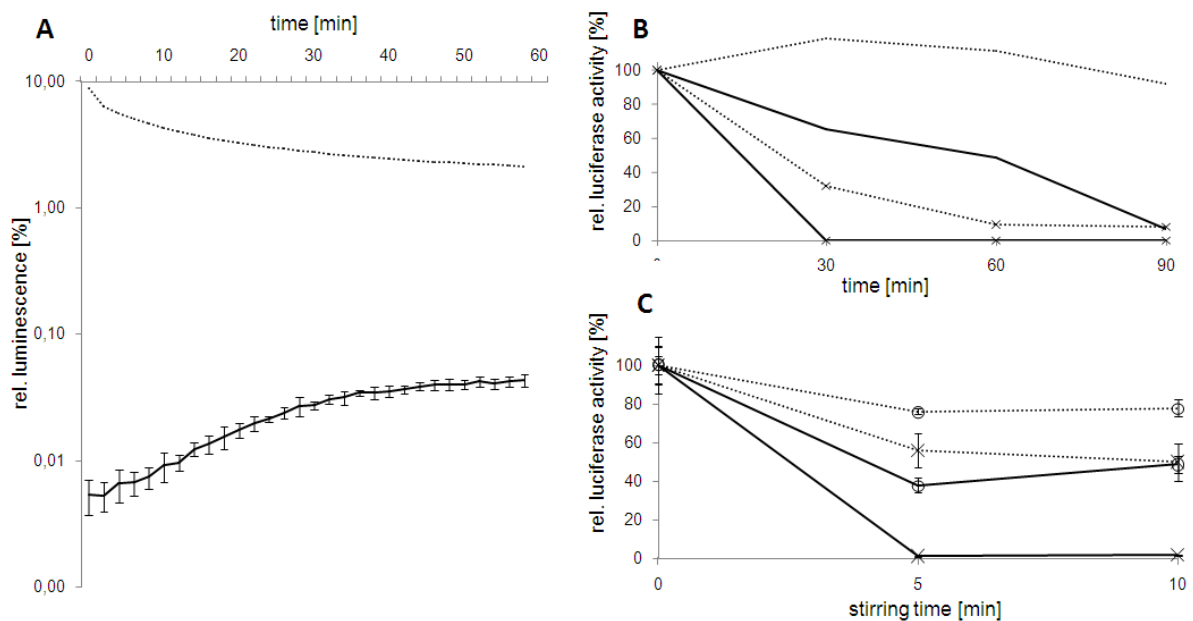


**Fig. 70:** A) Luminescence measurement of luciferase solution (dotted line: control; solid line: entrapped luciferase at 30 °C, 0.1 M potassium phosphate). A logarithmic scale was used and native luciferase luminescence measured at the start of the assay was set to 100 %. B) Luciferase activity over time while stirring at 500 rpm (lines marked with a cross) or incubating (no marking). C) Luciferase activity over time

---

while stirring at 500 rpm with DTT (lines marked with a cross) or with DTT and DnaK/DnaJ/GrpE+ATP (lines marked with circle). For B) and C) dotted line: pH 7, solid line: pH 9.

The influence of entrapment on the luciferase luminescence assay was investigated. The luminescence measurements of native luciferase and entrapped luciferase were compared over time (Fig. 70A).

Clearly different luminescence kinetics were observed for native and entrapped luciferase. It was hypothesized that the observed luciferase activity in the pellet may be limited by the surrounding silica particles. The slight increase of the entrapped luciferase activity may have caused by leaching of luciferase out of the silica pellet or permeation of the substrates into the silica pellet.

Since luciferase activity could not be determined correctly in the pellet, it was investigated whether luciferase could be leached from entrapment while preserving its activity, in order to indirectly quantify the entrapment ratio. To optimize the leaching conditions for the highly labile luciferase, the effect of stirring and pH value on the luciferase activity was investigated (Fig. 70B-C). Incubating a luciferase solution at r.t. for 90 minutes did not impair its activity at pH 7 but led to almost linear deactivation at pH 9 (Fig. 70B). Compared to incubation without stirring, the luciferase solution was deactivated even faster, especially at pH 9. Stirring at 500 rpm, comparable to the leaching conditions for the previously investigated enzymes (Fig. 64), led to fast inactivation of the luciferase. Adding DTT as a reducing agent to the leaching conditions slowed down the deactivation of luciferase while stirring (Fig. 70C). Combining DTT in the leaching buffer with DnaK/DnaK/GrpE+ATP further stabilized the luciferase solution against denaturation during stirring. Stirring luciferase at pH 9 led to deactivation after 60 min independent of the presence of DTT and DnaK/DnaK/GrpE+ATP (data not shown).

The ability of the chaperone system DnaK/DnaK/GrpE+ATP to recover luciferase activity after stirring or incubating was investigated dependent on neutral or alkaline pH values. Luciferase was diluted into 0.1 M potassium phosphate (pH 6.5) at r.t. and the luciferase activity monitored after 60 min (Fig. 71A, refer to Materials and Methods 8.3.3). As a control reaction, deactivated luciferase was incubated in absence of the chaperone system under the same conditions.

Luciferase activity could only be partially recovered after 60 min under leaching conditions (at pH 9 with stirring) after incubation at neutral pH for an hour in the presence of the chaperone system. It was nearly completely recovered from deactivation by incubating at pH 9 without stirring with or without the chaperone system. Irreversible deactivation under stirring

conditions was presumably caused by oxidation due to air being mixed into the protein solution.

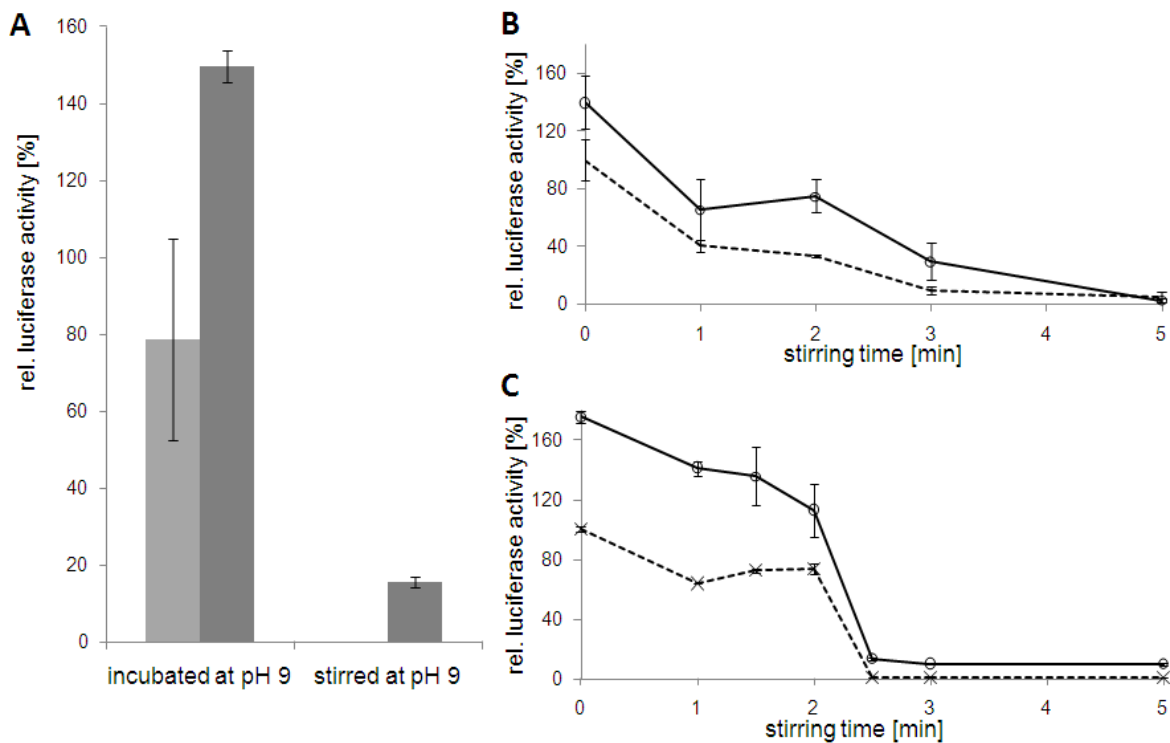


**Fig. 71:** A) Luciferase activity after refolding at neutral pH for 60 min after deactivation by incubation and stirring in pH 9 Tris buffer in the presence of DTT for 60 min. Light column: without chaperones, dark column, DnaK/DnaK/GrpE+ATP. B) and C) Luciferase activity over time while stirring at pH 9 in the presence of DnaK/DnaJ/GrpE+ATP (lines marked with circle) or without chaperones (B) dashed line, C) dashed line with cross marks). Luciferase activity was measured B) without DTT and C) with DTT. Native luciferase activity was set to 100 % for A)-C).

It was further investigated how long luciferase could be exposed to leaching conditions before it deactivated irreversibly and to which extent DnaJ/K/GrpE+ATP slowed down denaturation in the absence (Fig. 71B) and presence (Fig. 71C) of additional DTT, which should prevent oxidation presumed before. The chaperones stabilized luciferase against denaturation by stirring under leaching conditions (Fig. 71B). Further stabilization was observed with chaperones and DTT (Fig. 71C), confirming that stirring the luciferase caused oxidation.

Since most of the luciferase activity was lost after 2 min under leaching conditions (Fig. 71B-C), leaching experiments with entrapped luciferase were carried out with leaching times shorter than 2 min. To completely remove entrapped luciferase by leaching, it was therefore investigated whether luciferase activity could be preserved by leaching stepwise in the presence of fresh DnaJ/K/GrpE+ATP under non-denaturing conditions. Entrapped luciferase (30 °C, 0.1 M potassium phosphate) was submitted to leaching conditions with DTT and DnaK/DnaJ/GrpE+ATP for short time increments of 1 and 2 min and then luciferase activity was measured immediately (Fig. 72).

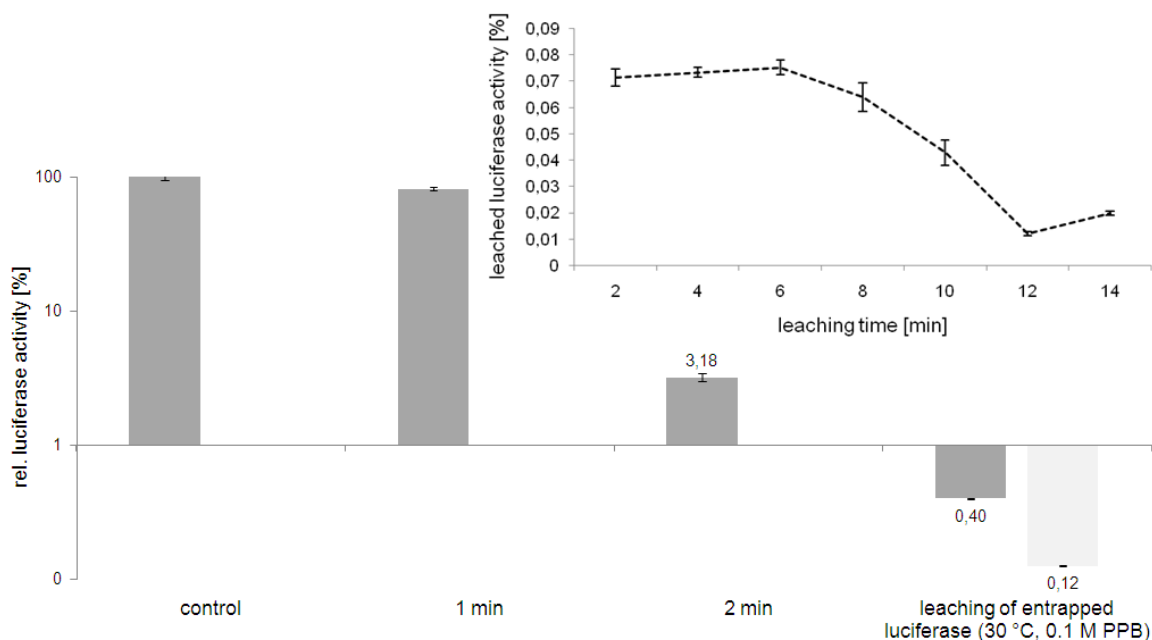


**Fig. 72: Leached luciferase activity after entrapment at 30 °C, 0.1 M potassium phosphate. Time points refer to luciferase in the entrapment solution under leaching conditions (with DnaK/DnaK/GrpE+ATP and DTT). Dark column: 2 min stepwise leaching; light column: 1 min stepwise leaching. Inset: leaching activities observed from entrapped luciferase for leaching reaction steps repeated stepwise every 2 min.**

Compared to the screening of the stirring time in the presence of chaperones (Fig. 71B), luciferase was strongly deactivated under leaching conditions after 2 min. Leaching of luciferase could be measured stepwise from the pellet (Fig. 72, inset) until the pellet was depleted. The total activity of leached luciferase was very low compared to the control (0.40 %). However, compared to the activity of luciferase under leaching conditions after 2 min, this represented 12 % of the activity. This activity would be compatible with the observation made in Fig. 69C, where the entrapment supernatant showed 80 % of the activity.

Nevertheless, the deactivation after 2 min under leaching conditions observed in this experiment made it necessary to further screen the luciferase leaching in smaller time increments. For 1 min leaching conditions, the activity was retained as expected. The summarized activity of leached luciferase was higher for leaching steps of 2 min (0.40 % compared to 0.12%), although no deactivation was observed for 1 min leaching conditions.

### 6.3.8 Conclusions

Comparable to the model protein eGFP, all investigated enzymes except luciferase were functionally entrapped in silica particles (Fig. 50, Fig. 66). The robust, PEI-driven particle formation (Fig. 23) yielded particle morphologies independent of the entrapped protein (Fig. 52). In the case of entrapped enzymes of higher MW (luciferase 62 kDa,  $\beta$ -galactosidase 464 kDa), a lower absolute entrapment ratio was observed (Fig. 50). Generally, the entrapment conditions (30 °C, 0.1 M potassium phosphate) leading to



particles with higher surface area (Fig. 31, Fig. 32) resulted in relatively higher entrapment ratios (Fig. 50). The protein activity was shown to be consistent with the protein content for the model enzyme lipase (Fig. 54).

Luciferase proved to be easily denaturated by the silicic acid concentration used in the entrapment protocol for all other proteins (Fig. 66A). Using lower concentrations of silicic acid as well as the chaperone system DnaK/DnaJ/GrpE, adapted entrapment conditions could be established where luciferase was protected against silicic acid at concentrations lower than 20 % of the general entrapment protocol (Fig. 69A). For silicic acid concentrations of exactly 20 % of the previously used entrapment protocol, ATP was crucial for the protection of luciferase by the chaperone system (Fig. 69B).

Depending on the entrapment conditions, significant protection of all enzymes was observed for heat stress (Fig. 55), proteolytic digest (Fig. 60), and dehydration stress (Fig. 62). Entrapment was significantly more efficient than physical adsorption for protection against heat stress (Fig. 57, Fig. 59) and entrapped enzymes could be recovered using the previously established leaching protocol (Fig. 64, Fig. 72). Entrapped protein seemed to be embedded more deeply into the biomineral than adsorbed protein, especially for entrapment conditions of 30 °C, 0.1 M potassium phosphate due to the higher specific surface. These results correlated well with the observation of slower leaching for entrapped proteins at 30 °C, 0.1 M potassium phosphate (Fig. 64).

For luciferase and  $\beta$ -galactosidase, part of the entrapped protein activity was inactivated (Fig. 73), but could be recovered by leaching the enzyme out of the silica particles (Fig. 65, Fig. 72). For the highly labile enzyme luciferase, the leaching conditions were optimized using DTT (Fig. 71B) as a reducing agent to compensate denaturation induced by oxidation (Fig. 70B) as well as by DnaK/DnaJ/GrpE and ATP (Fig. 71C) and refolding in neutral pH (Fig. 71), in order to stabilize luciferase in the leaching conditions for up to 2 minutes (Fig. 72B). Using entrapped luciferase however, stepwise leaching must be further optimized. Only this highly labile enzyme proved to be challenging for the entrapment process.

#### **6.4 Antibodies retain their specific activity after entrapment in silica particles**

In previous studies, an antibody targeting prostate specific antigen was conjugated to the outer surface of silica nanocomposites (Piao *et al*, 2008). The use of mesoporous silica nanoparticles for biomedical applications and drug delivery was also reported before (Slowing *et al*, 2007). Biodegradability is a key parameter for the acceptance of new drug delivery systems by regulatory authorities and the biodegradability of porous sol–gel silica in physiological buffers has been proven before (Finnie *et al*, 2008). Furthermore, silica is

“generally recognized as safe” by the US Food and Drug Administration (FDA) (Piao *et al*, 2008). Establishing a protocol for entrapping antibodies with potential clinical applications using the entrapment approach of this PhD study was therefore of highest interest.

#### 6.4.1 A fluorescent labeled antibody shows specific fluorescence in silica particles

FITC labeled Anti-mouse IgG (whole molecule) was investigated as a model antibody for co-entrapment during the silica particle formation. The localization of the entrapped FITC-IgG was investigated by fluorescence microscopy (Fig. 74).

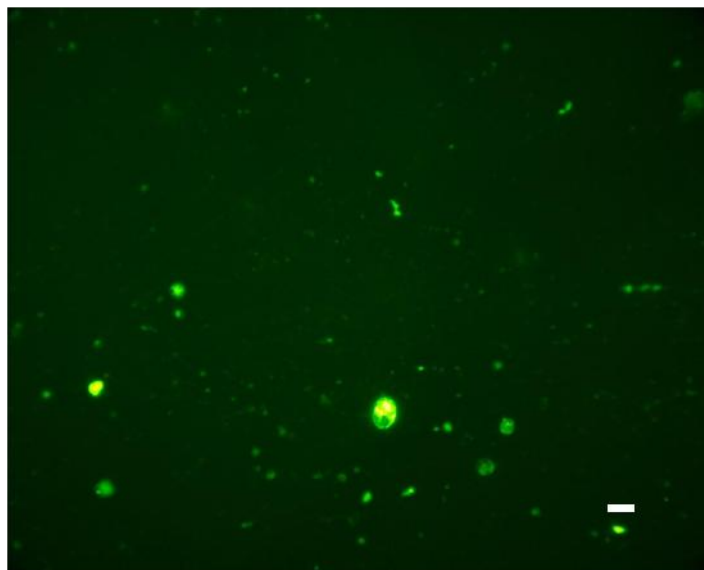


Fig. 74: Visualization of entrapped FITC-labelled IgG (entrapment conditions: 30 °C, 0.1 M potassium phosphate) in silica particles by fluorescence microscopy using the fluorescence filter (535 nm). Scale bar: 5 µm.

Entrapped FITC-IgG showed specific fluorescence clearly localized in the particles, and no significant fluorescence was observed outside the silica particles. The fluorescent FITC label allowed quantification of IgG in the silica particles after the entrapment reaction (Fig. 75A):

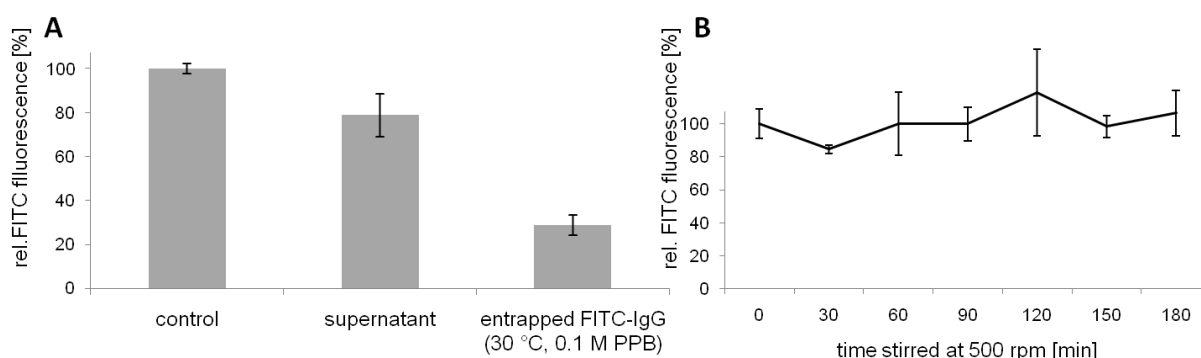


Fig. 75: A) Entrapment ratio of FITC-labeled IgG (entrapment conditions: 30 °C, 0.1 M potassium phosphate). B) Fluorescence of entrapped FITC-IgG (30 °C, 0.1 M potassium phosphate) when stirred over time in 0.1 M potassium phosphate buffer, pH 7.

With the entrapment conditions optimized for the enzymes previously discussed, 29 % of the fluorescence of FITC-IgG was found in the pellet after entrapment. Since the sum of the fluorescence found in the supernatant and pellet correlated sufficiently well with the control, it can be concluded that no loss of fluorescence occurred during entrapment. Furthermore, FITC-IgG was stably entrapped in the silica particles and no loss of fluorescence was observed when stirring the pellet at pH 7 (Fig. 75B).

However, fluorescence is not necessarily an indication of the actual antibody activity after entrapment. Therefore, it was determined if antibody activity was retained after immobilization.

#### 6.4.2 Entrapped MAK33 is active in the ELISA

To investigate the activity of a potentially clinically interesting antibody, the monoclonal MAK33 from mouse was investigated as a model substrate (Buchner *et al*, 1991; Lilie *et al*, 1995a, 1995b). This antibody is directed against muscle type creatin-kinase and its activity was measured as described in 8.4.7.1 (Fig. 76).

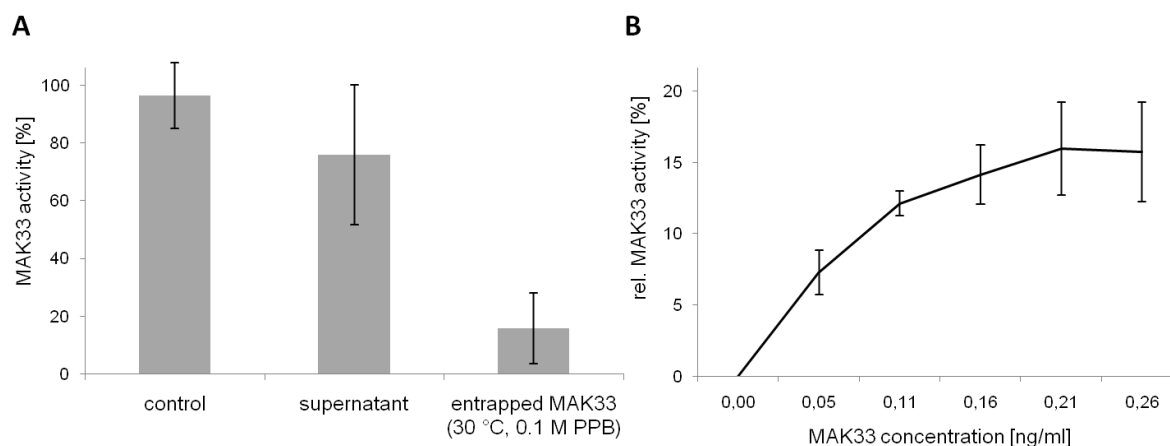


**Fig. 76:** A) MAK33 activities determined by ELISA before and after entrapment at 30 °C, 0.1 M potassium phosphate. Control: MAK solution under entrapment conditions in absence of TMOS. B) Activity of entrapped MAK33 (30 °C, 0.1 M potassium phosphate) for different MAK33 concentrations in the entrapment reaction.

To determine the activities of MAK 33 after entrapment, a calibration measurement of different MAK33 concentrations in solution was carried out with native MAK33 solution (set to 100 % activity), MAK33 under entrapment conditions (at 30 °C, 0.1 M potassium phosphate) in the absence of TMOS (control) and of the supernatant after the entrapment reaction. The activity of entrapped MAK33 was determined with an adapted ELISA (Buchner *et al*, 1991; Mayer *et al*, 2000). Due to physical adsorption of the secondary antibody to the silica particles, the background activity was checked. To eliminate this signal, protein-free silica particles without MAK33 were measured by ELISA in each experiment. The background activity was calculated as the difference of the activity detected from entrapped MAK33 and

protein-free silica particles, and set to 0 %. The final entrapment ratio of MAK33 was determined to be ~16 % (Fig. 76).

Interestingly, the activities of the supernatant were consistent with those of experiments with FITC-IgG (Fig. 75A). The activity of entrapped MAK33 was 13 % lower than expected from the fluorescence measurements of FITC-IgG. Therefore, it was assumed that part of the protein was inactivated while entrapment, as observed for  $\beta$ -galactosidase (Fig. 50) and luciferase (Fig. 69). When concentrations higher than 0.21 mg/ml were used for MAK33 entrapment, the entrapment ratio did not increase further (Fig. 76B). Comparable to previously discussed experiments with eGFP (Fig. 41), a saturation of MAK33 activity in the silica pellet was reached.

#### 6.4.3 MAK33 is stabilized against heat stress and proteolytic digest

In order to investigate if MAK33 is stabilized against heat stress (Bjerner *et al*, 2002) and proteolytic digest as was shown for different enzymes, it was entrapped at 30 °C, 0.1 M potassium phosphate and another sample of MAK33 was adsorbed MAK33 to protein-free silica particles generated at 30 °C, 0.1 M potassium phosphate.

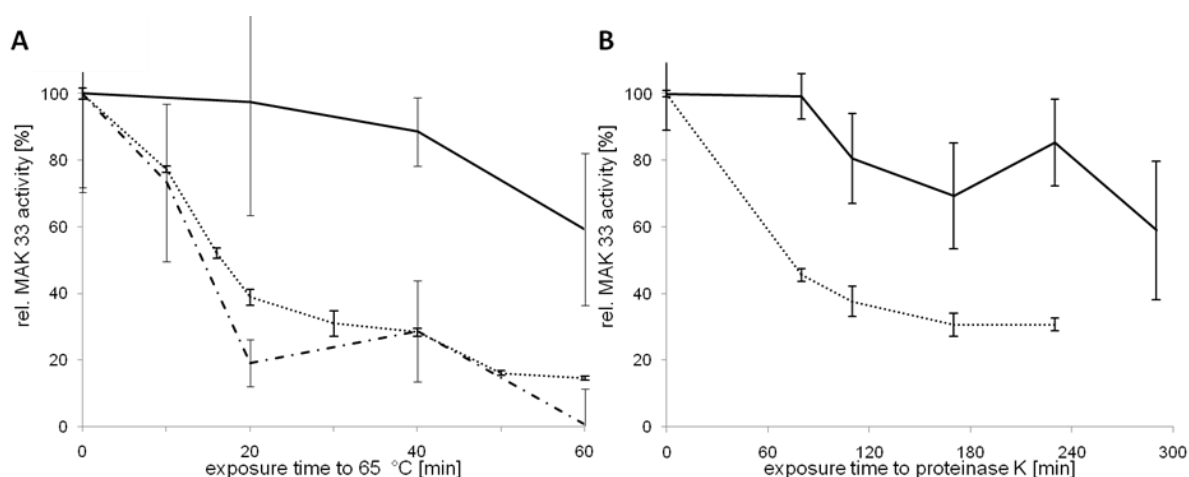


**Fig. 77:** A) Resistance of MAK33 against denaturation by heat stress at 65 °C. B) Resistance of MAK33 against denaturation by proteinase K. Dotted lines correspond to MAK33 in solution, dashed lines to adsorbed MAK33 at the reaction conditions 30 °C, 0.1 M potassium phosphate and solid lines to entrapped MAK 33 at 30 °C, 0.1 M potassium phosphate.

Adsorbed or entrapped MAK33 were exposed to heat stress (65 °C) and the MAK33 activity was monitored at different time points (Fig. 77A). In another set of experiments, similarly entrapped MAK33 was exposed to proteolytic digest by proteinase K and the activity was measured (Fig. 77B).

A relative stabilization of 100% corresponds to a total protection against stress, whereas a stabilization of 0% was set to correspond to the activity of the protein solution under stress conditions (refer to Materials and Methods 8.4.8.4). MAK protection was calculated to 54 %

against the denaturation by heat stress (Fig. 77A) and 45 % protection against proteolytic digest (Fig. 77B). In comparison, adsorption to silica particles generated at 30 °C, 0.1 M potassium phosphate did not lead to significant stabilization against heat stress (Fig. 77A).

#### 6.4.4 Entrapped antibodies can be recovered from the silica particles under leaching conditions

For possible applications, it was of interest if antibodies can be recovered from silica particles. To test this, entrapped MAK33 was extracted from the silica particles with the standard leaching experiments (Fig. 78).

As expected, increased activity was observed when using 0.1 M potassium phosphate (pH 7) for leaching. With 0.1 M Tris-buffer (pH 9), MAK33 was recovered from the pellet within two hours (Fig. 78). Interestingly, the total leached activity (27 %) exceeded the activity of MAK33 determined in the pellet (16 %). The sum of the activity in the supernatant and the activity after leaching from the pellet was consistent with the activity of the control.

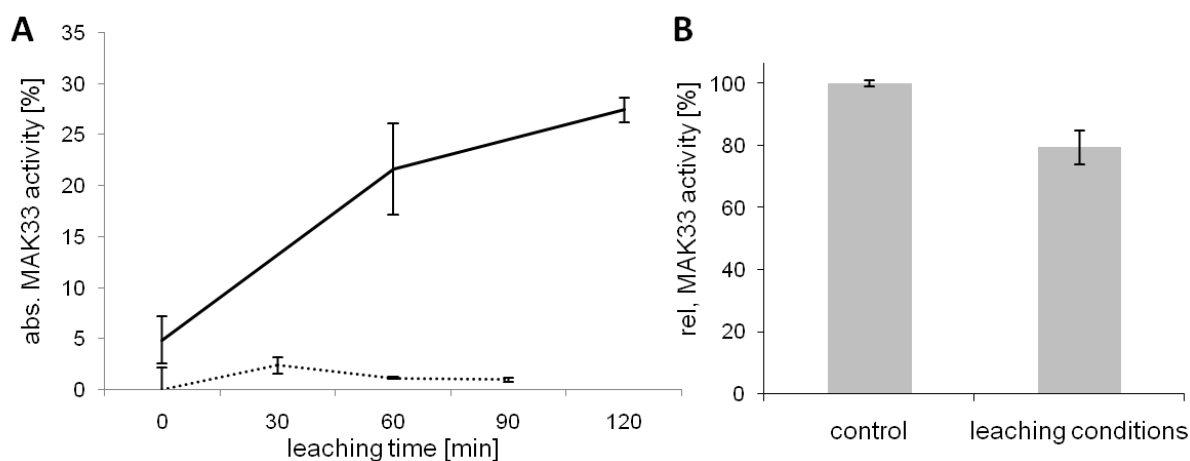


**Fig. 78:** A) Leaching of entrapped MAK33 (entrapment conditions: 30 °C, 0.1 M potassium phosphate). Leaching conditions: solid line: Tris buffer pH 9; dotted line: potassium phosphate buffer, pH 7. B) Activity of MAK33 solution before and after leaching conditions at pH 9 for 120 min.

#### 6.4.5 Conclusions and outlook

The antibodies MAK33 and FITC-IgG were functionally entrapped in silica particles (Fig. 75A, Fig. 76A). The antibody activity was consistent with the antibody concentration as shown by fluorescence measurements and ELISA. Consistent with entrapped enzymes of higher MW (luciferase,  $\beta$ -galactosidase), MAK33 (150 kDa for the completely assembled heterotetrameric antibody (Simmons *et al*, 2002)) showed a low entrapment ratio. After one entrapment step, although ~10 % MAK33 activity was lost, ~75 % activity could be detected in the supernatant (Fig. 76A). Therefore, this supernatant could be re-used in subsequent entrapment steps with fresh PEI, similar to the experiments shown for  $\beta$ -galactosidase (Fig. 53), or it can be stored away for later use (data not shown). The multiple use of free

---

protein remaining in the supernatant increases the entrapment efficiency, as long as the target protein is stable under entrapment conditions.

MAK33 was stabilized against heat (Fig. 77A) and proteolytic digest (Fig. 77B) after entrapment. Physically adsorbing MAK33 to silica particles proved to be inefficient to stabilize against high temperatures (Fig. 77A).

Comparable to the partially deactivated enzymatic activity of luciferase and  $\beta$ -galactosidase, part of activity of entrapped MAK33 was deactivated or inaccessible but could be recovered by leaching (Fig. 78). This simple and mild approach to immobilize antibodies in a reservoir might be promising for future biomedical applications (Podbielska & Ulatowska-Jarza, 2005).

## 7 Discussion

The methodology presented here utilizes the silica sol-gel technique (Pierre, 2004), where entrapment of an enzyme is achieved randomly during the chemical formation of highly porous silica under physiological temperature and pH conditions (Hench & West, 1990; Hanefeld *et al*, 2008; Avnir *et al*, 2005). In the first step a tetra-alkoxysilane (TMOS) is hydrolyzed via acid catalysis (Shtelzer *et al*, 1992). Hydrolysis is followed by condensation (catalyzed by PEI or CTMA-Cl) and the sol, a mixture of partially hydrolysed and partially condensed monomers, is formed. It further condensates until a gel like state, the sol-gel, is reached (Hanefeld *et al*, 2008). In general, mesoporous silica immobilization of enzymes seems to be dependent on the size and pI of the enzyme as well as of the size on the mesopores and the pH of the solution (Díaz & Balkus Jr, 1996; Lei *et al*, 2002). Thus, mesoporous silica with specific pore size is rather ill-suited in terms of a robust, general entrapment strategy. Especially the control of the pore size of the silica particles is technically complicated and optimization is needed specifically for each protein to be entrapped.

### 7.1 Entrapment is independent of the pI of the immobilized protein

For a wider range of proteins with lower pI than investigated in previous studies (Lei *et al*, 2002), mild entrapment conditions seemed to be advantageous. To cover a wide range of hosted proteins, a broader approach yielding a wide range of pore sizes and which is compatible with different pIs of proteins was established with the entrapment protocol presented here. As an alternative sol-gel catalyst to PEI, CTMA-Cl showed competitive entrapment efficiencies for eGFP, which were improved further by the use of mesitylene as a swelling agent. However, the CTMA-Cl/mesitylene system was not useful for labile proteins like  $\beta$ -galactosidase.

Electrostatic forces have been used to entrap proteins in mesoporous silica because silica has a pI of around 3 (Díaz & Balkus Jr, 1996; Lei *et al*, 2002; Yiu *et al*, 2001; Kisler *et al*, 2001). Directly entrapping negatively charged proteins (pI < 7) was reported to prove challenging, due to their repulsion of the negatively charged silica nanoparticles (He *et al*, 2007). Previous research solved that limitation by reverse-microemulsion of His-tagged eGFP anchored to the silica shell (Cao *et al*, 2010). Entrapment with the protocol presented here circumvents the limitation of protein-silica interaction in a single-step approach.

Entrapment for MAK33 worked better than for luciferase, despite that both proteins having similar pI values. Therefore, entrapment with PEI-driven particle formation proved to be largely independent of the pI of the entrapped protein. Interestingly, the morphologies were also largely independent of the nature of the entrapped protein (Fig. 52).

## 7.2 Increasing protein size decreases entrapment efficiency

Larger enzymes are expected to lead to lower entrapment efficiency, as observed for  $\beta$ -galactosidase (tetrameric, 464 kDa) in Fig. 50, luciferase (62 kDa) in Fig. 69C and MAK33 (tetrameric, 150 kDa) in Fig. 76, while larger pore sizes (Fig. 31 and Fig. 32) lead to higher amounts of immobilized enzymes (observed at entrapment conditions of 30 °C, 0.1 M potassium phosphate in Fig. 50) (Wang & Caruso, 2005).

The size of the silica matrix has to correlate with the size of the enzyme in order to stabilize it (Vamvakaki & Chaniotakis, 2007). It was shown that  $\beta$ -galactosidase cannot completely fit within the central cavity of GroEL (Ayling & Baneyx, 1996) that possesses approximately 35-40 Å in diameter (Chen *et al*, 1994). Sol-gel entrapment however, due to the broad distribution of pore sizes between 1 and 100  $\mu$ m (Fig. 31, Fig. 32), allowed the entrapment of proteins with different MW and oligomeric states.

Although there was no clear dependence between oligomeric state and entrapment efficiency, proteins with higher MW consistently showed lower entrapment efficiency. This challenge of low entrapment efficiency could be overcome by re-using the free protein in the supernatant (Fig. 53). Since  $\beta$ -galactosidase is a relatively labile protein, this approach seems therefore promising for other sensitive, expensive and potentially clinically relevant protein substrates.

## 7.3 Luciferase is destabilized by high silicic acid concentrations during entrapment

Luciferase entrapment was challenging due to its denaturation in the presence of silicic acid (Fig. 66A). In this case, the approach needed to be adapted with sufficiently diluted silicic acid solutions in the entrapment protocol (Fig. 69A). For further enhancement of protein stability, the chaperones DnaK/DnaJ/GrpE in the presence of ATP could be used to protect luciferase in the entrapment protocol (Fig. 69B). Future research might focus on establishing alternative entrapment protocols using more biocompatible silicic acid precursors like THEOS (Shchipunov, 2003, 2008).

## 7.4 Electrostatic interactions between silica particles and proteins cause stable protein entrapment

It was of interest if protein-silica interactions were influenced the PEI-driven protein immobilization. At several pH units away from the pI of the enzyme, electrostatics provide a driving force for enzyme immobilization (Wang & Caruso, 2005).

Entrapment was carried out at neutral pH for controlled particle formation kinetics and entrapment kinetics (Fig. 43) (Bauer *et al*, 2007). It was observed that fast initial particle formation (Fig. 23, Fig. 24) did not necessarily lead to high entrapment efficiency (Fig. 43,



after 10 min reaction time). When the pI of the enzyme is close to the pH of the reaction solution (pH 7), the factors driving protein immobilization are difficult to discern and must be attributed to a number of simultaneous interactions (e.g., electrostatics, hydrogen bonding, and van der Waals forces) (Wang & Caruso, 2005). The bioinspired approach avoids extreme pH conditions needed for syntheses of the classical mesoporous silica MCM-41 but detrimental for entrapment of pH-sensitive proteins (Kresge *et al*, 1992; Sayari & Hamoudi, 2001).

It had been shown for the enzyme lysozyme that the environment within the silica pore as well as its internal dynamics is similar to that in aqueous solution, although the entrapped protein showed slower global motion but retained its internal angularly restricted segmental rotation (Pastor *et al*, 2007). Since the pores between the silica particles generated by sol-gel are filled with water, sol-gels are also referred to as aquagel (Hanefeld *et al*, 2008).

Similarly, superoxide dismutase-peroxidase preserved its enzymatic activity after sol-gel encapsulation (Pastor *et al*, 2004). A strong electrostatic interaction is established between the protein molecule and the negatively charged sol-gel walls, which is ultimately responsible for the total arrest of the overall rotation of the protein, but without significant effect upon its segmental rotational relaxation (Pastor *et al*, 2007). Apparently, the segmental movement of the entrapped enzyme is sufficient for substrate turnover, since high levels of protein activity were retained after entrapment (Fig. 50).

The interaction of the entrapped protein with the surrounding silica particles and the decreased global motion of the protein after entrapment were consequently responsible for the decreased denaturation upon thermal stress (Fig. 56) (Pastor *et al*, 2007). Denaturation by proteolytic digest (Fig. 60) is slowed down due to sterical confinement of the enzyme in the silica matrix. Since the proteins proved to retain their activity in the silica pores, the main limiting factor for activity measurements of entrapped protein is their accessibility. Entrapment conditions leading to higher porosity (Fig. 31 and Fig. 32) resulted in higher fluidity (lower viscosity) of silica particle suspensions in water (Fig. 33), which explained the higher entrapment ratios. Although the entrapped proteins were suspended in aqueous solution, in some cases the protein-substrate interaction was partially or completely shielded by the aquagel: for  $\beta$ -galactosidase (Fig. 65) and MAK33 (Fig. 78), a fraction of the protein was entrapped in a non-active state which could only be recovered by leaching; in the case of luciferase (Fig. 72), almost all activity was suppressed in the sol-gel (Fig. 69C).

These observations were confirmed for MAK33 by fluorescence measurements of entrapped FITC-IgG in the silica particles (Fig. 75A). Interestingly, the activity of entrapped MAK33, which required interaction with secondary antibodies in the ELISA, was higher than that of

luciferase, for which three components (luciferase, luciferin and ATP) needed to interact. Since MAK33 was detected using ELISA after entrapment, and the antibody-antigen construct is bigger than luciferase, it can be excluded that luciferase was deactivated due to its size being bigger than e.g. lipase. It therefore seemed that the luminescence assay to quantify luciferase in the silica pellet was impaired kinetically, since the time needed for three components of the luciferase assay to interact in the aquagel was significantly higher than in solution. This led to the observation of an extremely low but rising luminescence signal in the pellet as opposed to a high and decreasing luminescence signal in solution (Fig. 70). It seemed that luciferase either was unstable or the multi-component luminescent assay was deactivated in the presence of silicic acid.

### **7.5 Leaching of entrapped proteins is influenced by the entrapment conditions**

Adsorption of proteins to silica particles resulted in weak protein-silica interactions, causing leaching at pH 7 (Zaborsky, 1972). Entrapped protein could only be recovered by leaching at pH 9 but showed no leaching at neutral pH (Fig. 49). Even stronger protein-silica interactions are observed for silaffins embedded in the biosilica of diatom cell walls: they could only be characterized by extraction from the silica structures of diatoms using aqueous ammonium fluoride solution (Kröger *et al*, 2002).

For all entrapped proteins, morphologies generated at 20 °C, 0.1 M potassium phosphate led to faster leaching (Fig. 64, Fig. 78). At these reaction conditions, more bead-like silica particles were observed (Fig. 79) which favor leaching effects (Vamvakaki & Chaniotakis, 2007), lead to lower fluidity (Fig. 33) and specific surface area (Fig. 31 and Fig. 32). The lower specific surface area results in less interaction opportunities of the entrapped protein with the surrounding silica particles. Highest leaching is therefore predicted for entrapment conditions at low temperature and high phosphate concentration (Fig. 21), the latter having been shown to increase the particle size of biosilica (Gröger *et al*, 2007).

Additionally, increase protein size decreased the leaching speed of the entrapped protein slightly. For the tetrameric proteins  $\beta$ -galactosidase (120 min, Fig. 64) and MAK33 (120 min, Fig. 78), leaching was completed slower than for the smaller proteins eGFP, lipase and DHFR (60 min, Fig. 64) for the entrapment condition at 20 °C, 0.1 M potassium phosphate. Higher buffer volumes (Fig. 49B-C) or higher protein concentration in the silica pellet (Fig. 49D) also increased leaching speed.

Luciferase leaching (Fig. 72) was challenging due to its high instability at high pH values under leaching conditions (Fig. 71A). The chaperone system DnaK/DnaJ/GrpE+ATP

improved the activity after leaching conditions (Fig. 71B-C); however, activity losses were significant and further stabilization experiments with chaperones need to be carried out.

In previous research, spray drying for the encapsulation of glucose oxidase and the growth factor TGF- $\beta$ 1 in dried silica xerogel microparticles, or sol-gel layers for immobilization of glucose oxidase allowed first applications for controlled release of entrapped protein from the silica matrix, or stable biosensors (Wei *et al*, 2002; Quintanar-Guerrero *et al*, 2009). The entrapment protocol established here allows immobilization of proteins in a much simpler manner, specifically allowing leaching by simple stirring at pH 9, with the leaching speed tunable by the reaction conditions (Fig. 21). The disadvantage of the leaching conditions was a refolding step at neutral pH necessary for pH labile proteins, which might fail for proteins which are irreversibly denatured by the leaching conditions.

## **7.6 Entrapped proteins are highly interesting for medical applications and as biocatalysts**

Entrapped proteins in gel-like morphologies might be highly interesting for applications of pharmaceuticals since they are usually biodegradable under physiological conditions, highly inert and not inflammatory (Drummond *et al*, 1999), (Finnie *et al*, 2008). No loss of protein activity was observed *in vitro* in the studies presented here, since silica particles were stored in small buffer volumina without any flow-through of fresh buffer. The silica particle size can be tailored to the application by adjusting the reaction conditions.

For industrial applications of entrapped enzymes, systems are required that are not only stable and active, but are low in cost and can undergo repeated re-use (Hanefeld *et al*, 2008). The proposed one-step entrapment protocol fulfilled these requirements for a range of proteins: PEI, TMOS and potassium phosphate are extremely low-cost chemicals, technical equipment and temperatures needed for entrapment are minimal and the process can be up-scaled (Fig. 30). Furthermore, protein which was not entrapped could be re-used in repeated entrapment steps to enhance entrapment efficiency (Fig. 53). The resulting entrapped proteins showed many advantages over free enzymes in terms of higher thermal and chemical stability reported in the literature (Hanefeld *et al*, 2008) with more expensive and less universal approaches which often needed several steps: re-usability (Fig. 63, Fig. 66B), stopping the enzymatic reaction by removing the immobilized enzymes from the reaction solution and storage in dried form (Fig. 48, Fig. 62) (Gómez *et al*, 2006; Ricca *et al*, 2010) or in suspension at r.t. over weeks (Fig. 58). The initially lower activity of the entrapped proteins compared to protein solution was compensated by significant stabilization against heat stress (Fig. 56) or proteolytic digest (Fig. 60).

## 8 Materials and Methods

### 8.1 Materials

#### 8.1.1 Proteins and chemicals

Several proteins and materials were kindly provided for this study:

EGFP, DHFR	Dr. Tetyana Dashivets
Firefly luciferase and $\beta$ -galactosidase	Dr. Andreas Schmid
Ludox solution	Dr. Markus Gretz (Technische Universität München, Department Bauchemie, Prof. Dr. Plank)
Purified Sil (Sil-R5-Cys (Naik <i>et al</i> , 2004), sequence SSKKSGSYSG SKGSKRRILC) and NBD-Sil	Carolin Lechner (Technische Universität München, Department Proteinchemie, Prof. Dr. Becker)
GroEL and GroES	Anja Osterauer
Quartz tubes for calcination of biomineralized samples	Sebastian Bähr (Technische Universität München, Department Fluorchemie, Prof. Dr. Fässler)
Amyloid fibrils produced under acidic conditions at 37 °C from a 50 $\mu$ M protein concentration were a pool derived from different variants of an antibody light chain variable domain ( $V_L$ ) dialysed to 0.1 M potassium phosphate (pH 7) before use	Cardine N. Nokwe
Baculovirus capsids obtained from Sf9 cells ( <i>Spodoptera frugiperda</i> )	Edgar Boczek
DnaJ, DnaK, GrpE, pQE60 plasmid and samples of <i>Thalassiosira pseudonana</i> diatoms	Dr. Martin Haslbeck

Other proteins and chemicals were purchased:

ABTS-substrate buffer	Roche Diagnostics GmbH (Penzberg, Germany)
ABTS-tablets	Roche Diagnostics GmbH (Penzberg, Germany)
Amicon membrane filter units	Sigma, Aldrich (Saint Louis, Missouri, USA)

---

Anti-mouse-IgG-POD-conjugate	Roche Diagnostics GmbH (Penzberg, Germany)
Biotinylated creatin kinase	Roche Diagnostics GmbH (Penzberg, Germany)
Blocking reagent for ELISA	Roche Diagnostics GmbH (Penzberg, Germany)
Coomassie Protein Assay Reagent	Pierce (Rockford, USA)
FITC Conjugated Goat Anti-Rabbit IgG	Sigma, Aldrich (Saint Louis, Missouri, USA)
Gel filtration molecular weight markers (29 000-660 000 Da)	Sigma, Aldrich (Saint Louis, Missouri, USA)
LiChrosolv MS-H <sub>2</sub> O	Merck KGaA (Darmstadt, Germany)
Lipase ( <i>Thermomyces Lanuginosus</i> )	Sigma, Aldrich (Saint Louis, Missouri, USA)
MAK33	Roche Diagnostics GmbH (Penzberg, Germany)
PEI (MW 800; 1300; 1800; 750 000 g/mol; all branched)	Sigma, Aldrich (Saint Louis, Missouri, USA)
pNPP	Sigma, Aldrich (Saint Louis, Missouri, USA)
Prefomed Actin filaments (rabbit skeletal muscle)	Cytoskeleton inc., (Denver, CO, USA)
Streptavidin covered 96-well plates	Roche Diagnostics GmbH (Penzberg, Germany)
TMOS (>99%)	Sigma, Aldrich (Saint Louis, Missouri, USA)

All other chemicals were obtained from VWR (Darmstadt, Germany). All solutions were prepared using double dist. water and all buffers were sterilized by filtration through 0.2 µm filter units.

### 8.1.2 Technical Equipment

Analytical balance KERN ABT 220-5DM	Kern & Sohn GmbH (Balingen, Germany)
Analytical balance KERN PLS S10-3	Kern & Sohn GmbH (Balingen, Germany)
BET porosimeter Sorptomatic 1990	Porotec GmbH (Hofheim/Taunus, Germany)
Centrifuge 5418	Eppendorf (Hamburg, Germany)
Centrifuge Rotina 420R	Hettich (Tuttlingen, Germany)
DLS LB-550 with built-in viscometer	Horiba Instruments Inc (USA)

---

Hg-porosimeter PASCAL 140 and 440	Porotec GmbH (Hofheim/Taunus, Germany)
L3/11/P330 muffle furnace	Nabertherm GmbH (Lilienthal, Germany)
Magnet stirrer MR Hei-Standard	Heidoph Instruments (Schwabach, Germany)
Plate reader Genios	TECAN Group Ltd. (Männedorf, Switzerland)
Plate reader Sunrise	TECAN GmbH (Grödig, Austria)
Spectrofluorometer FluoroMax-3	Horiba Ltd. (Kyoto, Japan)
Spectrofluorometer FP-6500	Jasco (Umstadt, Germany)
Spectrophotometer Ultrospec 2100	GE Healthcare (Munich, Germany)
Speed Vac Sc110 lyophilizer	Savant Instruments Inc. (Holbrook, USA)
Temperature sensor EKT Hei-Con	Heidoph Instruments (Schwabach, Germany)
TGA Q5000 analyzer	TA Instruments (New Castle, USA)
ThermoMixer MKR 23	HLC (Frankfurt, Germany)
Ultrasonic bath	Bandelin Sonorex (Berlin, Germany)
Vacuum chamber	Heraeus GmbH (Hanau a. Main, Germany)
Vortex Mixer	Heidolph Instruments (Schwabach, Germany)
Zetasizer Nano-ZS	Malvern Instruments Ltd. (Worcestershire, UK)

### 8.1.3 HPLC system

FP-1520 Intelligent Fluorescence Detector	JASCO inc. (Tokyo, Japan)
LC-NetII/ADC Chromatography Interface	JASCO inc. (Tokyo, Japan)
LG-980-O2S Ternary Gradient Unit	JASCO inc. (Tokyo, Japan)
PU-1580 Intelligent HPLC Pump	JASCO inc. (Tokyo, Japan)
Superdex 200 HR 10/30 column	GE Healthcare (Princeton, NJ, USA)
UV-1575 Intelligent UV/VIS Detector	JASCO inc. (Tokyo, Japan)

### 8.1.4 Microscopes

Fluorescence microscope Axiovert 200	Carl Zeiss AG (Leipzig, Germany)
--------------------------------------	----------------------------------

---

SEM JSM 5900 LV	JEOL GmbH (Eching, Germany)
EDX detection system	Röntec GmbH (Berlin, Germany)
Plastic coverslips	Thermanox (Rochester, NY, USA)
SEM aluminium tape	PLANO GmbH (Wetzlar, Germany)
Sputter coater SCD 005	Bal-Tec AG (Balzers, Liechtenstein)
SEM JSM 7500F	JEOL
Cryo transfer system Alto 2500	Gatan, inc.
EDX detector system X-Max	Oxford Instruments (Oxfordshire, UK)
TEM JEM 100CX	JEOL
Carbon-coated 3 mm copper grids	PLANO (Wetzlar, Germany)
<b>8.1.5 Software</b>	
Adobe programs	Adobe Systems Incorporated
Borwin software	JASCO inc. (Tokyo, Japan)
FWAP-6512/6612 Fluorescence Polarization measurement program	Jasco (Umstadt, Germany)
MacBiophotonics Image J [195]	MacBiophotonics ( <a href="http://macbiophotonics.ca/">http://macbiophotonics.ca/</a> )
Microsoft Office 2007	Microsoft (Redmond, USA)
Origin®	OriginLab Corporation (Northampton, USA)
ProtParam Tool	Expasy ( <a href="http://expasy.org/">http://expasy.org/</a> )
Thermal Advantage Universal Analysis	TA Instruments (New Castle, DE, USA)
Zetasizer software (6.20)	Malvern Instruments Ltd. (Worcestershire, UK)
Zotero reference manager	Zotero ( <a href="http://zotero.org/">http://zotero.org/</a> )

## 8.2 Biomineralization

### 8.2.1 Detection of biomineralization by light scattering

The presence of silica particles in solution was observed qualitatively by light scattering measurements at 405 nm and 20 °C (Fleckenstein, 2008). This fast method was used for screening of multiple biomineralization conditions, substrates and chaperones in a 96-well plate reader (refer to Results, Fig. 4).

10  $\mu$ l additive (e.g. Spd, concentration 0.53-4.2  $\mu$ M) and/or 10  $\mu$ l Hsp26 (0.53-4.2  $\mu$ M) dissolved in 0.5 M potassium phosphate (pH 7) were diluted to a final volume of 110  $\mu$ l with potassium phosphate (pH 7) at the designed concentration (0.01-0.5 M). Unless stated otherwise chaperones and substrates were incubated for 10 min at r.t. and no heat shock activation was used (Haslbeck *et al*, 1999; Haslbeck, 2002). 110  $\mu$ l potassium phosphate (pH 7) at the designed concentration were used as a control for light scattering caused by silicic acid auto-condensation.

Biomineralization was started by addition of silicic acid obtained from TMOS hydrolysis: to each sample, 10  $\mu$ l TMOS in 1 mM HCl (unless stated otherwise, TMOS concentration was 0.5 M and  $t_{pre}$  was 3 min) was added and absorption was measured immediately after shaking the wells for 5 s at 400 rpm. The prehydrolysis time  $t_{pre}$  is defined as the time TMOS was hydrolyzed in 1 mM HCl before adding it to the reaction solution (Hench & West, 1990; Iler, 1979; Patwardhan, 2002). As a control for the absorption of the samples, 10  $\mu$ l 1 mM HCl was used instead of the TMOS solution. The absorption of the control samples without TMOS was subtracted from the absorption of the samples containing TMOS to determine absolute absorption values.

### 8.2.2 Biomineralization samples

#### 8.2.2.1 Reaction conditions for EM and DLS samples

For particle analysis of biomineralized templates via EM or DLS, reaction conditions based on the light scattering screening (8.2.1) were used with a higher total sample volume: 50  $\mu$ l Spd (4.2  $\mu$ M) and/or 50  $\mu$ l Hsp26 (4.2  $\mu$ M) were dissolved in 0.5 M potassium phosphate (pH 7) and diluted to a final volume of 550  $\mu$ l with 0.1 M potassium phosphate (pH 7).

#### 8.2.2.2 Biomineralization induction and reaction work-up

The biomineralization reaction was started by addition of silicic acid obtained from TMOS hydrolysis: 50  $\mu$ l 0.1 M TMOS in 1 mM HCl ( $t_{pre}$ : 3 min) was added to the protein solution. After  $t_{react}$ : 3 min at 20 °C, the biomineralization reaction was stopped by diluting 100  $\mu$ l of the reaction solution into 1 ml MS-H<sub>2</sub>O at 0 °C and immediate centrifugation for 3 min at 14 000 rpm followed by washing with 1 ml MS-H<sub>2</sub>O and centrifugation for two more times.



The washed silica particles were resuspended with 50  $\mu\text{l}$  MS-H<sub>2</sub>O and prepared for TEM or SEM measurement.

### **8.2.2.3 Biom mineralization conditions of non-spherical protein scaffolds**

As a generalized scaffold biom mineralization protocol used e.g. for fibrillar scaffolds, the following set of reaction conditions was used: 50  $\mu\text{l}$  protein solution (4.2-16.8  $\mu\text{M}$ ) were dissolved in 0.1 M potassium phosphate (pH 7) and diluted to a final volume of 550  $\mu\text{l}$  with 0.1 M potassium phosphate (pH 7). Other reaction conditions:  $t_{\text{react}}$ : 5 min, 50  $\mu\text{l}$  0.1 M TMOS in 1 mM HCl ( $t_{\text{pre}}$ : 3 min) and a reaction temperature of 20 °C. Reaction conditions not described were carried out as detailed in 8.2.2.2.

### **8.2.3 Calcination of biom mineralized Hsp 26, GroEL/ES and fibrillar proteins**

Protein templates were removed from the biom mineral by calcination. Calcination of biom mineralized samples in quartz tubes was carried out by Sebastian Bähr (Technische Universität München, AG Fluorchemie, Prof. Dr. Fässler) in a L3/11/P330 muffle furnace at 800 °C for 4-8 h with a heating rate of 10 °C/min. Calcinated samples were retrieved from the quartz tubes by adding 0.5 ml MS-H<sub>2</sub>O, gently shaking for 3 min, removing the suspension from the quartz tubes and centrifugation for 5 min at 14 000 rpm.

## **8.3 Protein entrapment methods**

### **8.3.1 Entrapment protocol**

If not indicated otherwise, all proteins were entrapped following a generalized protocol (Fig. 36) and measured at least in triplicates.

360  $\mu\text{l}$  of (0.5 or 0.1 M) potassium phosphate (pH 7), 80  $\mu\text{l}$  PEI (1 mg/ml in potassium phosphate, pH 7, 0.1 M) and 120  $\mu\text{l}$  protein solution in potassium phosphate, pH 7, 0.1 M were incubated at a reaction temperature (20 or 30 °C) for 10 min. The final concentrations of the proteins were: 176 ng/ml for eGFP, lipase and luciferase, 26.5 ng/ml for DHFR and 1.2 ng/ml for  $\beta$ -galactosidase. Antibodies were prepared with final concentrations of 1.76 ng/ml for FITC-IgG and 0.26 ng/ml for MAK33. For correction, an identical volume of pure potassium phosphate, pH 7, 0.1 M or 0.5 M, was used as blank.

Freshly prepared silicic acid was obtained from the precursor TMOS in 1mM HCl according to the literature to a final concentration of 0.5 M TMOS in 1 mM HCl (Kröger *et al*, 1999), incubated at r.t. for 7 min for prehydrolysis and 120  $\mu\text{l}$  of this silicic acid solution was added to the reaction solution. The sample was vortexed for 10 s in order to mix the silicic acid with the reaction solution and incubated at the reaction temperature for 1 h. Samples were centrifuged for 5 min at 14 000 rpm and pellets were washed three times with H<sub>2</sub>O to remove free silicic acid and PEI. Washed pellets were resuspended in 400  $\mu\text{l}$  potassium phosphate,

pH 7, 0.1 M. When not specified otherwise, all experiments with 0.1 M potassium phosphate were performed at 30 °C and all experiments with 0.5 M potassium phosphate at 20 °C.

The theoretical pI values of the proteins investigated here were determined using the ProtParam tool (Gasteiger *et al*, 2005): eGFP 5.67, lipase 5.36, DHFR 6.09,  $\beta$ -galactosidase 5.2, luciferase 7.08 and MAK33 6.4-7.6 (Hamilton *et al*, 1987).

### **8.3.1.1 Entrapment protocol for luciferase with chaperones**

For entrapment of luciferase in the presence of chaperones, different entrapment conditions were used. Luciferase was used in the entrapment protocol with 8.82 ng/ml final concentration. For luciferase entrapment with DnaK/DnaJ/GrpE, the final concentrations used for the chaperones DnaK/DnaJ/GrpE were: DnaK: 46.4  $\mu$ M, DnaJ: 104.6  $\mu$ M, GrpE: 98.6  $\mu$ M. ATP was added to a final concentration of 5 mM where indicated.

### **8.3.1.2 Preparation of physically adsorbed proteins**

The efficiency of protein immobilization by entrapment was compared with the immobilization by adsorption of a protein solution on protein-free silica particles. Adsorbed enzyme samples were prepared by adding the enzyme solution to enzyme-free silica particles generated by a similar protocol. The suspension was centrifuged for 5 min at 14 000 rpm and pellets were washed three times with H<sub>2</sub>O to remove free enzyme solution. Washed pellets of adsorbed enzymes were resuspended in 400  $\mu$ l potassium phosphate, pH 7, 0.1 M.

### **8.3.1.3 Determination of the entrapment ratio**

After the biomineralization reaction, the supernatant obtained from the first centrifugation and the washed pellets were each added to their enzymatic activity assay. The resulting activities were compared to a standard solution of the biomineralization assay with the same protein concentration. For the standard solution, TMOS-free 1 mM HCl solution was used instead of the silicic acid solution. The activity of the pellet relative to the standard solution was defined as the entrapment efficiency. The relative enzymatic activities were calculated by setting the activities of the free enzymes in the same dilution to 100%. Blanks, biomineralized or in solution, without enzyme were monitored and set to 0% activity.

## **8.3.2 Characterization of silica particles from entrapment experiments**

### **8.3.2.1 Specific surface area measurements**

BET N<sub>2</sub> adsorption and Hg-porosimetry measurements were performed at the Wacker Chemie AG Consortium für electrochemische Industrie by Martina Ruhland, using lyophilized powder of enzyme free silica particles generated at different entrapment conditions (15-30 °C and 0.1-0.5 M potassium phosphate). For each measurement, 1-2 g sample was required. In order to obtain sufficient amounts of silica particles, the entrapment protocol was up-scaled

up to 400 times. Particle formation was carried out in a 500 ml glass flask under mild stirring (75 rpm) and using a water bath for temperature control.

### **8.3.2.2 Thermal analysis**

For one TGA measurement, 5 mg lyophilized silica particles were measured in a standard platinum crucible with a heating rate of 10 °C/min up to 800 °C in air. Measurements were carried out in a TGA Q5000 analyzer and analysis of the data was analyzed using the software TA Universal Analysis at the WACKER Chair of Macromolecular Chemistry and Institute of Silicon Chemistry (Technische Universität München, Prof. Dr. Rieger). Lipase was entrapped (at 30 °C, 0.1 M potassium phosphate and at 20 °C, 0.5 M potassium phosphate) or adsorbed by centrifugation to protein-free silica particles (obtained at 30 °C, 0.1 M potassium phosphate and at 20 °C, 0.5 M potassium phosphate). In order to obtain sufficient amounts of silica particles, the lipase entrapment or adsorption protocol was up-scaled up to 400 times. Particle formation was carried out in a 500 ml glass flask under mild stirring (75 rpm) and using a water bath for temperature control.

The amount of organic material entrapped or adsorbed was determined by calculating the weight loss caused by oxidation at temperatures from 300-800 °C. As a control, samples of protein-free silica were measured with TGA.

### **8.3.2.3 Fluidity measurements**

Rotational viscometer operates on the principle of measuring the rate of rotation of a solid shape in a viscous medium upon application of a known force required to rotate the solid shape at a definite angular velocity (Viswanath, 2007). Measurements of the fluidity of silica suspensions were carried out on the built-in viscometer of the Dynamic Light Scattering Particle size analyzer LB-550 at the Department Bauchemie, Prof. Dr. Plank. Fluidity of enzyme free silica particles in suspension was measured using 20 ml aqueous suspension of silica particles obtained at entrapment conditions as described, lyophilized and suspended in dist. water with ~0.25 mg/ml silica particle content for all samples.

### **8.3.3 Leaching of entrapped proteins**

Generally, leaching experiments were performed using entrapped protein with 20 µl 0.1 M potassium phosphate (pH 7) and 980 µl 0.1 M Tris buffer (pH 9). Stirring of the suspension was done at r.t. at 500 rpm. In the case of eGFP, 15 ml 0.1 M Tris buffer (pH 9) was used for leaching experiments. Control experiments at leaching conditions were carried out with 20 µl protein solution containing protein corresponding to 100 % entrapment ratio, i.e. protein solution had the same activity as the control solution. After the leaching experiment, the protein solution was diluted with the same volume of 0.1 M potassium phosphate (pH 6.5) and incubated at r.t. for 60 min.

### **8.3.3.1 Luciferase leaching with DnaK/DnaJ/GrpE**

The chaperones DnaK/DnaJ/GrpE, dissolved in 0.1 M potassium phosphate (pH 7), were added to luciferase solution or entrapped luciferase at 20 °C, where indicated, to final concentrations of DnaK: 46.4 µM, DnaJ: 104.6 µM, GrpE: 98.6 µM. ATP was added to a final concentration of 5 mM where indicated. For luciferase leaching, DTT was added to the 0.1 M Tris buffer (pH 9) to a final concentration of 0.5 mM where indicated.

## **8.4 Protein chemistry methods**

### **8.4.1 Purification of Hsp26**

Expression and purification of Hsp26 was carried out in collaboration with Thomas Kriehuber (purification data not shown). Hsp26 was expressed from a pQE60 plasmid in the *E. coli* strain HB101 with 1 mM IPTG at 37 °C over night. Purification of Hsp26 was carried out as described previously (Haslbeck *et al*, 2004). Purified Hsp26 was dialyzed into 0.1 M potassium phosphate (pH 7) and concentrated with a membrane filter system to a final concentration of 9.36 mg/ml in order to minimize buffer influences when dilutions into other buffer systems were carried out.

### **8.4.2 GroEL/ES complex formation**

The GroEL/ES complex was formed as described elsewhere (Grallert *et al*, 2000). GroEL and GroES were diluted into a 50 mM Tris buffer, pH 8 with 25 µl GroEL (110 µM), 25 µl GroES (254 µM), 2 µl MgCl<sub>2</sub> (50 mg/ml) and 2 µl 0.5 M potassium phosphate (pH 7) where incubated at 43 °C under mild stirring (200 rpm) for 90 min. The temperature was increased to 45 °C, 1 µl 0.1 M ADP was added and the solution was incubated at 45 °C for 5 min. The complex was stored on ice and used within 12 h. For negative staining, the GroEL and the GroEL/ES complex were diluted to 0.1 mg/ml in 5 mM HEPES with 5 mM NaCl (pH 7).

### **8.4.3 NBD-labeling of Spd and PEI (MW 1800)**

2.5 mmol NBD-Cl (Babià *et al*, 2001; Schramm *et al*, 1993) were dissolved in 1 ml acetonitrile in a closed 15 glass flask at r.t. The glass flask was covered by tin foil in order to block out light and 0.25 mmol pure Spd resp. PEI (MW 1800) was added under stirring (500 rpm). The rapid formation of a dark precipitate was observed. The reaction solution was stirred for 2 h at r.t and 200 rpm and the precipitate was isolated by filtration, washed 2 ml acetonitrile and dried in a desiccator. 0.9 mg NBD-Spd (orange solid) and 2.2 mg NBD-PEI (brown viscous oil) crude product were obtained and 1 mg/ml solutions were prepared in 0.5 M potassium phosphate by dissolving the crude product after 10 min sonication. Further purification of NBD-Spd by RP-HPLC and ESI-MS analysis was carried out by Carolin Lechner (Technische Universität München, Department Proteinchemie, Prof. Dr. Becker).

#### 8.4.4 Size Exclusion HPLC

Gel filtration chromatography (Size Exclusion HPLC) separates analytes solved in aqueous solution by their molecular weight while preserving the biological activity of the proteins (Skoog, 1985; Paul-Dauphin *et al*, 2007). A standard HPLC calibration set of molecular weight marker proteins (MW: 29 kDa (Carbonic Anhydrase, Bovine Erythrocytes), 66 kDa (Albumin, Bovine Serum), 150 kDa (Alcohol Dehydrogenase, Yeast), 200 kDa ( $\beta$ -Amylase, Sweet Potato), 443 kDa (Apo ferritin, Horse Spleen), 669 kDa (Thyroglobulin, Bovine)) was used to be able to estimate the MW of an analyte based on its  $V_e$ . Hsp26 was incubated for 5 min at 43 °C up to 1 h prior to the HPLC measurement.

HPLC measurements were carried out with a Superdex 200 HR 10/30 gel filtration column (column volume: 23 ml). For each HPLC run, 20  $\mu$ l sample were measured. The elution buffer was 0.1 M potassium phosphate buffer, adjusted to a pH of 7 and the flow-rate was set to 0.5 ml/min.

#### 8.4.5 Protein determination via Bradford assay

Protein concentration determination according to Bradford is based on binding of a chromophore to proteins, causing a shift of the absorption maximum of the chromophore from 465 nm to 595 nm (Bradford, 1976).

50  $\mu$ l solution was added to 1 ml Bradford chromophore solution and the absorption at 595 was measured after 2 min incubation at r.t. in a photometer.

PEI interferes strongly with all standard methods to determine protein concentration (Gupta *et al*, 2000). Due to interference of 0.5 M potassium phosphate and PEI with the Bradford assay, a calibration curve with BSA could not be used to determine protein concentration. Specific calibration curves were measured dependent on which component needed to be determined. Volumes of 50  $\mu$ l sample were used in order to dilute the concentration of below the interference level (Zhao *et al*, 1990; Dissing & Mattiasson, 1996).

##### 8.4.5.1 Determination of PEI concentration

For both entrapment conditions, separate calibration curves were measured for protein-free solutions with defined amounts of PEI in absence of silicic acid. To determine PEI content after addition of silicic acid, the reaction solution was measured with the Bradford assay at specific reaction times and the absorption values compared with the calibration curve. 100 % Bradford signal was set for the PEI concentration of the entrapment conditions and the Bradford signal in absence of PEI from the calibration measurements was set to 0 %.

#### **8.4.5.2 Determination of lipase concentration**

To eliminate the interference of PEI with the signal measured from lipase with the Bradford assay, calibration curves for both entrapment conditions were measured with the supernatant of lipase-free entrapment solutions after 60 min reaction time. Calibration curves were measured with freshly prepared and filtrated enzyme-free entrapment supernatant to which known amounts of lipase were added. Lipase concentration in the supernatant of the lipase entrapment reaction was measured using Bradford assay and the signal compared to the calibration curve. 100 % Bradford signal was set for the lipase concentration of the entrapment conditions and the Bradford signal in absence of lipase from the calibration measurements was set to 0 %.

#### **8.4.6 Protein activity assays**

##### **8.4.6.1 eGFP**

All activities of proteins were determined at least in triplicate. The activity of eGFP (variant F64L and S65T) was determined according to the fluorescence emission of the folded and oxidized protein (Topell *et al*, 1999). Fluorescence was analyzed with an excitation filter at 405 nm and an emission filter at 535 nm. The signal intensities were compared with the intensity of equally treated native eGFP. The light absorption of the silicified eGFP did not influence its fluorescence intensity.

##### **8.4.6.2 DHFR**

The activity of DHFR was assayed spectrophotometrically using the decrease in absorbance at 340 nm that occurs when NADPH and DHF are converted to NADP and THF (Hillcoat *et al*, 1967). The assay buffer contained 50 mM Tris/HCl buffer, pH 7.5, 10 mM  $\beta$ -mercaptoethanol (Lebrun *et al*, 1990), to which DHF and NADPH were added to final concentrations of 80  $\mu$ M and 120  $\mu$ M, respectively. To 1ml of this solution, 50 $\mu$ l DHFR solution or the biomineralized DHFR pellet was added to start the reaction.

##### **8.4.6.3 $\beta$ -galactosidase**

The hydrolytic activity of  $\beta$ -galactosidase on ONPG was determined in aqueous medium according to literature (Zhang & Bremer, 1995; Miller, 1977). 50 $\mu$ l  $\beta$ -galactosidase solution (resp. 1/12 of the biomineralized lipase pellet, resuspended in 100  $\mu$ l 0.1 M potassium phosphate (pH 7)) and 200  $\mu$ l Z buffer (Miller, 1977) were added to 50  $\mu$ l ONPG (0.8 mg/ml, dissolved in 0.1 M potassium phosphate, pH 7). The absorbance was monitored over 15 min at 405 nm.

##### **8.4.6.4 Lipase**

The hydrolytic activity of lipase (from *Thermomyces lanuginosus*) on emulsified pNPP was determined in aqueous medium according to literature (Kordel *et al*, 1991). 100 $\mu$ l lipase

solution (resp. 10 % of the biomineralized lipase pellet, resuspended in 100  $\mu$ l 0.1 M potassium phosphate (pH 7)) was added to 13.5  $\mu$ l of a 16.5 mM solution of pNPP in 2-propanol and the absorbance was monitored over 15 min at 405 nm.

#### **8.4.6.5 Luciferase**

Luciferase catalyzes the oxidation of luciferin to oxyluciferin in the presence of oxygen, which leads to the emission of light (Branchini *et al*, 2005; Marques & Esteves da Silva, 2009). The assay buffer (modified from (Groemping *et al*, 2001)) contained 20 mM Hepes/NaOH (pH 7,5), 50 mM KCl, 6 mM MgCl<sub>2</sub>, 300  $\mu$ M Coenzyme A, 2 mM DTE, 0.05 mg/ml BSA, 2 mM ATP, 0.1 M luciferin. 100 $\mu$ l 0.1 M potassium phosphate (pH 7) and 50  $\mu$ l luciferase solution (resp. 1/12 of the biomineralized luciferase pellet) were added to 50  $\mu$ l assay buffer and the resulting luminescence was measured immediately over an hour at 30 °C with a gain of 85.

#### **8.4.7 Antibody activity assays**

The fluorophore FITC had excitation/emission maxima at 494/518 nm, therefore the fluorescence of the FITC labeled IgG could be monitored using a set of filters at 485/535 nm. Fluorescence of FITC-IgG was analyzed with an excitation filter at 485 nm and an emission filter at 535 nm.

##### **8.4.7.1 ELISA**

The activity of MAK33 in solution and after entrapment was measured with ELISA (Buchner *et al*, 1991). An antigen, creatin-kinase, is bound over biotin to a streptavidin-covered 96-well plate. The antibody, which is to be detected, MAK33, binds to its specific antigen, anti-mouse-IgG-pOD-conjugate. After addition of ABTS, the chromogene substrate of the peroxidase (POD), a colorimetric reaction occurs. ABTS is cleaved homolytically into two stable cation radicals, which can be observed as a green color. The intensity of the color, detected in a photospectrometer at 405 nm, correlates to the amount of active antibody.

##### **8.4.7.2 ELISA in solution and after entrapment**

MAK33 (calibration), MAK33 under entrapment conditions (using the 1mM HCl instead of TMOS), MAK33 in the biomineralization supernatant or entrapped MAK33 were measured with the ELISA. The concentrations of entrapped MAK33 were 10-fold compared to the calibration in solution. MAK33 at these concentrations resulted in measurements outside of the linear range for the calibration curve; therefore the activity for the calibration at such high concentrations was linearly extrapolated. At the concentrations of the calibration (i.e. 0-0.026 ng/ml total MAK33 concentration in the control at entrapment conditions), too little activity in the silica pellet was detected due to high background signal from protein-free silica particles.

Washing steps for entrapped MAK33 and protein-free silica particles were done as described in the entrapment protocol. After washing the silica particles, they were resuspended with 100 µl 2 mM EDTA in 1x PBS. PBS was prepared using standard procedures. For 1 L 10x PBS: 1.15 M NaCl, 160 mM Na<sub>2</sub>HPO<sub>4</sub>, 40 mM KH<sub>2</sub>PO<sub>4</sub>; pH of PBS buffer solution was adjusted to 7.4 with HCl. 1x PBS was prepared by diluting 10x PBS 1:10 with water. Washing in the streptavidin-covered 96-well plate was carried out by adding and removing 100 µl dist. water three times.

#### **8.4.7.3 ELISA reagents**

All reagents for ELISA were sterile filtrated and stored at 4 °C for no longer than a week.

Reagent 1: 1.35 g Blocking reagent for ELISA and a bottle Creatin-Kinase were dissolved in 50 ml dist. water.

Reagent 2: 100 µl anti-mouse-IgG-POD-conjugate and 0.5 g blocking Reagent for ELISA were dissolved in 50 ml POD-conjugate buffer (50 mM NaCl, 0,5 mM EDTA, 0.1 % Tween-20, 1 % blocking reagent).

Reagent 3: 0.835 ABTS-substrate buffer and 1 ABTS tablet were dissolved in 50 ml dist. water.

First, 100 µl MAK33 solution was added to the streptavidin-covered 96-well plate. 100 µl washed and resuspended protein-free silica particles or entrapped MAK33 were placed in reaction containers. 100 µl Reagent 1 was added to 100 µl sample (MAK33 solution in a streptavidin-covered 96-well plate or entrapped MAK33 suspension in a reaction container) and the resulting solution or suspension shaken at 200 rpm at 20 °C for 45 min. The solution was removed by washing three times. 100 µl Reagent 2 was added and the resulting solution or suspension shaken at 200 rpm at 20 °C for 45 min. The solution was removed by washing three times. After adding 100 µl Reagent 3, the colorimetric reaction was monitored in a plate reader at 405 nm over 45 min.

### **8.4.8 Determination of protein stabilization**

#### **8.4.8.1 Measurement of protein activity under heat stress**

Samples were heated up as described and after different time points, and then cooled down to 20 °C and their activity was measured.

#### **8.4.8.2 Measurement of protein activity under proteolytic digest**

50 µl proteinase K solution was added to the proteins for different amounts of time and the activity of the samples was measured. Proteinase K dilution in 0.1 M potassium phosphate



was for MAK33 1:400, DHFR 1:100, lipase and  $\beta$ -galactosidase 1:50 and for eGFP, 25  $\mu$ l undiluted proteinase K was used.

#### **8.4.8.3 Measurement of protein activity with repeated drying cycles**

Proteins (eGFP, Lipase, DHFR,  $\beta$ -galactosidase) in solution and after entrapment were dried at r.t. overnight in a vacuum chamber at r.t. and 80 Torr or lower. They were resuspended in 400  $\mu$ l 0.1 M potassium buffer and incubated for an hour at 20 °C before measurement of their activity. These drying and resuspension steps were repeated up to four times. Standards which were not dried were measured at each step.

#### **8.4.8.4 Comparing stability measurements**

The stabilities of proteins in solution and after entrapment (that were measured as described in 8.4.8.1 - 8.4.8.3) were compared by evaluating the surface area below the curve of the native protein stability measurements and setting it to 100%. The surface area below the curve of the entrapped protein stability measurements was compared to that of the native protein to determine the relative protection.

## **8.5 Spectroscopic methods**

### **8.5.1 Dynamic Light Scattering**

DLS (Brown, 1993; Chu, 1997; Hendrix & Leipertz, 1984; Berne & Pecora, 2000), also known as PCS (Photon Correlation Spectroscopy), measures Brownian motion and relates this to the size of the particles (Berne & Pecora, 1976). An important feature of Brownian motion is that small particles move quickly in suspension and large particles move more slowly. Particles illuminated by a light source such as a laser scatter the light in all directions. Moving particles cause the intensity of scattered light to fluctuate. The DLS system detects the rate of the intensity fluctuation of scattered light and uses this to calculate the particle size.

#### **8.5.1.1 Particle size distribution methods**

The particle size distribution generated by DLS is an intensity distribution that can be converted mathematically to a volume distribution and a number distribution (Bohren & Huffman, 1998). A signal generated by the number distribution for a theoretical suspension containing two equal populations of different particle sizes ( $d$ ) results in two peaks at a ratio 1:1. Bigger particles have significantly higher volume (the volume of a sphere is proportional to  $d^3$ ) and cause higher light scattering than smaller particles. This results in a theoretical ratio of 1:1000 for the volume distribution. An intensity distribution results in a theoretical ratio of 1:10<sup>6</sup> (due to Rayleigh's approximation, the intensity of scattering is proportional to  $d^6$ ).

In the presence of silica particles > 100 nm in suspension, as it was the case for all samples from the protein entrapment experiments (refer to pages 32f.), small particles < 100 nm could only be determined with the number distribution. Samples containing only silica particles < 100 nm, as it was the case for biomineralization experiments (refer to pages 7f.), were measured using the intensity distribution, unless stated otherwise.

#### **8.5.1.2 DLS measurement parameters**

DLS measurements were carried out with a Zetasizer Nano-ZS at a light scattering angle of 173 °, also known as backscatter detection. The backscatter detection, where the incident light beam does not have to travel through the entire sample, reduces multiple scattering and allows the analysis of higher particle concentrations. Such highly turbid samples were typical for entrapment experiments.

*In situ* particle size measurements were carried out with the reaction conditions described for the biomineralization conditions or the entrapment protocol, respectively. Data were interpreted using an RI value of 1.544 as a standard value for the material and water as internal parameter for the dispersant. The Zetasizer software calculated an estimation of the polydispersity of the samples. A polydispersity index (PDI) below 0.1 corresponds to a monodisperse sample. PDI values > 1 designate highly polydisperse samples. PDI values for the silica particle suspensions studied strongly varied between 0.2 and 1.

#### **8.5.1.3 Biomineralization kinetics**

For DLS measurements, the reaction conditions were used as described in 8.2.2.1 and biomineralization was induced as described in 8.2.2.2. The particle size was analyzed with DLS at 20 °C over time unless stated otherwise.

#### **8.5.1.4 Particle growth experiments with DLS**

To test for PEI after the entrapment reaction, 120 µl freshly prepared silicic acid solution with the same concentration as in the entrapment protocol was added after 60 min reaction time and the particle size was investigated with DLS measurements with a Zetasizer Nano-ZS over time.

To test for remaining silicic acid after the entrapment reaction, 80 µl PEI (1 mg/ml in 0.1 M potassium phosphate, pH 7) was added after 60 min reaction time and the particle size was investigated with DLS measurements over time.

### **8.5.2 Aggregation measurements**

Potential protein aggregates in solution can be detected by their light scattering 340 nm and above (Nominé *et al*, 2001; Schrödel & de Marco, 2005). 184.4 µl 0.5 or 0.05 M potassium phosphate was incubated at 20 °C, 15.6 µl 200 µM Sil (Sil-R5-Cys (Naik *et al*, 2004) in

0.05 M potassium phosphate) were added and absorption at 340 was measured with an Ultrospec spectrophotometer over time at 20 °C.

Protein aggregation can be detected by light scattering at 90 ° backscattering angle more accurately (Schmidt, 2010). 184.4 µl 0.5 or 0.05 M potassium phosphate was incubated at 20 °C, 15.6 µl 200 µM Sil (in 0.05 M potassium phosphate) were added and light scattering at 340 nm at 90 ° backscattering angle was measured with a FluoroMax-3 spectrofluorometer over time at 20 °C.

### 8.5.3 Fluorescence anisotropy

Fluorescence anisotropy analyzes the growth of silica particles with bound dyes *in situ* (Tleugabulova *et al*, 2004; Birch & Geddes, 2000). A fluorophore immobilized in a gel does not depolarize fluorescence, therefore particle size studies can be carried out after the sol-to-gel transition time (Lakowicz, 2006). As described in the theory and application of fluorescence depolarization (Eftink, 2006; Szabo, 1984), from polarized fluorescence decay curves (F) that are orthogonal to vertically polarized excitation (P), the anisotropy function (r) can be calculated (Lakowicz, 2006). For intrinsic fluorescent Hsp26 bound to rotating silica particles the decay of the fluorescence anisotropy (r) describes depolarization of the fluorescence due to Brownian rotation (Geddes *et al*, 2000), assuming that energy transfer between different molecules can be neglected (Minutolo *et al*, 2010).

Fluorescence anisotropy measurements were carried out with a spectrofluorometer FP-6500 with an excitation wavelength of 290 nm (band width: 5 nm) and an emission wavelength of 330 nm (band width: 10 nm), a response time of 0.05 s and 2 s data pitch. Measurements of 1.5 ml 0.5 M potassium phosphate and 1.5 ml Hsp26 (1.05 µM) were carried out to determine the G-factor (0.93) (Lakowicz, 2006). The anisotropy of 1.5 ml Hsp26 (1.05 µM) in 0.5 M potassium phosphate was measured and 375 µl Spd (4.2 µM) in 0.5 M potassium phosphate was added on-line following the fluorescence anisotropy until values were constant. Subsequently, 150 µl 0.1 M TMOS ( $t_{pre}$ : 8 min) was added. A solution of 1 mM HCl in place of TMOS was measured as a control solution.

## 8.6 Microscopic methods

### 8.6.1 Fluorescence microscopy

Fluorescence microscopy uses a light source of short excitation wavelength, leading to the emission of light with lower energy by fluorescent samples (Bradbury & Evennett, 1996; Murphy, 2001). When the reflected light and background fluorescence is filtered the targeted parts of a given sample can be imaged (Bradbury & Evennett, 1996).

All samples were washed three times with dist. water to avoid potassium phosphate crystal formation obstructing the microscopic analysis. 10  $\mu\text{l}$  silica particles dispersed in dist. water were placed onto a 75 by 25 mm glass slide and the droplet covered by a 20 x 20 mm glass cover slip. Fluorescence microscopy was performed either in bright field mode or using an Endow GFP bandpass emission filter for the detection of specific fluorescence (Endow, 1999).

### **8.6.2 Electron microscopy: SEM**

Scanning Electron Microscopy (SEM) images a sample by scanning it with an electron beam that produces secondary electrons containing structural information from the atoms of the sample. Part of the secondary electrons are collected and translated as a series of picture elements (pixels) on a monitor, each pixel corresponding to a point where the electron beam on the specimen generated secondary electrons. The three-dimensional appearance of SEM images is due to different contrast of various structural features of the sample (Bozzola & Russell, 1999).

#### **8.6.2.1 Sample preparation for SEM**

High acceleration voltages result in lower contrast, greater electron beam penetration and enhanced secondary yield from all parts of the topography. Higher atomic numbered elements yield more secondary and backscattered electrons and appear brighter in the SEM, therefore gold sputtering leads to increased contrast. Since the angle with which the electron beam enters the specimen surface affects the yield of secondary electrons (Bozzola & Russell, 1999), samples were sputtered at a 45 and 90 ° angle to further increase the contrast.

Sample preparation was carried out as described before (Spector *et al*, 1998). All samples were washed three times with dist. water to avoid potassium phosphate crystal formation obstructing the microscopic analysis. 50  $\mu\text{l}$  silica particles dispersed in dist. water were placed onto the surface of an aluminium sample stage and dried at r.t. The silica suspension was dried at r.t. on a 13 mm plastic coverslip, this slide placed on a double-sided sticky carbon tape and then mounted on an aluminium sample stage holder with aluminium tape connecting the stage holder and the sample. Each sample was sputter-coated with a thin layer of gold (thickness approximately 2 nm). SEM was performed with the JSM 5900 LV (Technische Universität München, Electron Microscopy, Prof. Dr. Weinkauff) at a constant acceleration voltage of 20 kV. Micrographs were obtained with a spot size of 20 nm and working distance of 15 mm at magnifications up to 60 000 x. EDX measurements were performed with the built-in EDX detector of the JSM 5900 LV with measuring times of up to 120 s.

### **8.6.3 Electron microscopy: TEM**

In Transmission Electron Microscopy (TEM) (Bozzola & Russell, 1999; Goodhew *et al*, 2001), a beam of electrons passes through ultra thin specimens and a micrograph showing the two-dimensional projection of the sample is obtained from the interactions of the transmitted electrons (Fultz, 2008). Typically operated in the bright field imaging mode, the contrast is formed directly by occlusion and absorption of electrons in the sample, leading to dark regions for samples with high thickness or atomic number (Fultz, 2008). Therefore, samples containing silica were observed by TEM without prior staining while protein samples needed staining in order to be imaged with TEM (Bozzola & Russell, 1999).

TEM was performed with the JEM 100CX (Technische Universität München, Electron Microscopy, Prof. Dr. Weinkauff) at a constant acceleration voltage of 100 kV.

#### **8.6.3.1 Preparation of silica samples**

Samples containing silica were washed three times with MS-H<sub>2</sub>O and prepared for TEM measurements by placing a 300-mesh carbon-coated 3 mm copper grid on a droplet (10 µl) of sample placed on a piece of parafilm for 30 min, followed by removal of any liquid on the grid by draining with filter paper and drying at r.t. The thickness of the carbon film was between 10-15 nm.

#### **8.6.3.2 Negative staining of protein samples**

Glow-discharged carbon grids were briefly washed with water. 10 µl protein solution (0.05 mg/ml) were applied onto carbon grid for 1 min and excess liquid was blotted off. 5 µl uranyl acetate (1.5 % wt/vol) were immediately placed on the grid for 30 s and excess liquid was blotted off. Grids were air dried at r.t. and measured within 1 h with TEM.

#### **8.6.3.3 Particle size analysis**

The average particle size of biomineralized samples was determined from TEM micrographs with the ImageJ program. Due to the relatively small amount of particles obtained in some experiments, an average particle size of a sample was determined from the data of 10 or more measured particles.

### **8.6.4 Electron microscopy: High resolution SEM and STEM**

Cold cathode analytical field emission SEM, which combines SEM, TEM and STEM in one instrument, allows higher resolution at lower kV than conventional SEM. Low voltage increases image contrast and reduced the need to stain samples (Nebesárová & Vancová, 2007; Drummy *et al*, 2004). Non-sputtered samples show further increased contrast due to charge accumulation (Bozzola & Russell, 1999). In the scanning transmission electron microscopy (STEM) mode, electrons pass through the specimen. However, a focused electron beam is scanned over the sample (Goodhew *et al*, 2001).

---

Lyophilized samples were measured without sputtering as described for SEM (8.6.2.1). STEM samples were prepared as described for TEM (8.6.3.1). High resolution SEM and STEM was performed by Katia Rodewald (Technische Universität München, WACKER-Department für Makromolekulare Chemie, Prof. Dr. Rieger) with a cold field emission source JEOL JSM 7500F at 1-3 kV acceleration voltage.

---

## 9 Abbreviations

ABTS, 2,2'-azino-bis(3-ethylbenzothiazoline-6-sulphonic acid)

ADP, adenosine 5'-diphosphate

ATP, adenosine 5'-triphosphate

BET, Brunauer, Emmett, Teller

BSA, bovine serum albumin

CTMA-Cl, cetyltrimethylammonium chloride

d.u., dimensionless units

Da, Dalton

Da, kDa, Dalton, kilo Dalton

DHF, dihydrofolic acid

DHFR, dihydrofolate reductase

dist., distilled

DLS, dynamic light scattering

DNA, deoxyribonucleic acid

DTE, dithioerythritol

DTT, 1,4-dithiothreitol

E. coli, Escherichia coli

e.g., "exempli gratia", for example

EDTA, ethylenediaminetetraacetic acid

EDX, energy-dispersive X-ray

eGFP, enhanced green fluorescent protein

ELISA, enzyme linked immunosorbent assay

EM, electron microscopy

ESI, electrospray ionization

Ex/Em, excitation/emission wavelength

FITC, fluorescein isothiocyanate

Gua-HCl, guanidinium hydrochloride

---

h, hour(s)

HCl, hydrochloric acid

HEPES, [4-(2-Hydroxyethyl)-piperazino]-ethanesulfonic acid

His-tag, hexa histidine-tag

HPLC, high-performance liquid chromatography

HRP, horseradish peroxidase

Hsp, heat shock protein

i.e., "id est", that is

IgG, immunoglobulin G

IPTG, isopropyl- $\beta$ -D-thio-galactoside

kDa, kilo Dalton

kV, kilo volt

LCPA, long-chain polyamine(s)

LEI, lower secondary electron image

M, mM,  $\mu$ M, molar, millimolar, micromolar

MAK 33, mouse specific IgG, directed against muscle-specific human creatine kinase

MALS, multiangle light scattering

MCM, Mobil Composition of Matter (mesoporous amorphous silica)

mesitylene, 1,3,5-trimethylbenzene

min, minute(s)

MS, mass spectroscopy

MS-H<sub>2</sub>O, water for mass spectrometry (LiChrosolv grade)

MW, molecular weight

NADP, nicotinamide adenine dinucleotide phosphate

NADPH,  $\beta$ -nicotinamide adenine dinucleotide phosphate, reduced form

NaOCl, sodium hypochlorite

NaOH, sodium hydroxide

NBD-Cl, 4-chloro-7-nitro-2,1,3-benzoxadiazole or NBD-chloride

ONPG, ortho-nitrophenyl- $\beta$ -galactoside



---

PAGE, polyacrylamide gel electrophoresis

PBS, phosphate buffered saline

PCS, photon correlation spectroscopy

PDI, polydispersity index

PEI, polyethyleneimine (unless stated otherwise, PEI refers to MW: 1800 g/mol)

pI, isoelectric point

pNPP, p-nitrophenyl palmitate

POD, peroxidase

PPB, potassium phosphate buffer

R5 peptide, polypeptide derived from the silaffin protein of *Cylindrotheca fusiformis*

r.t., room temperature

RI, refractive index

RP-HPLC, reversed-phase high-performance liquid chromatography

rpm, rotations per minute

SDS, sodium dodecyl sulfate

SEI, secondary electron imaging

SEM, scanning electron microscopy

sHsp, small heat shock protein

Sil, Sil-R5-Cys, cys-modified R5 peptide

Spd, N-(3-aminopropyl)tetramethylenediamine or spermidine

STEM, scanning transmission electron microscopy

TEM, transmission electron microscopy

TEOS, tetraethyl orthosilicate

TGA, thermo-gravimetric analysis

THEOS, tetrakis(2-hydroxyethyl) orthosilicate

THF, tetra-hydrofolate

TMOS, tetramethyl orthosilicate

$t_{\text{pre}}$ , prehydrolysis time, time that TMOS was hydrolyzed in 1 mM HCl before the reaction start

$t_{\text{react}}$ , reaction time

Tris, tris(hydroxymethyl)aminomethane

UV/VIS, ultraviolet/visible

$V_e$ , elution volume

$V_L$ , variable light chain

vol.-%, volume percent

wt/vol, weight by volume concentration

YAG, Yttrium Aluminium Garnet activated by  $Ce^{3+}$

## 10 Literature

- Abell AB, Willis KL & Lange DA (1999) Mercury Intrusion Porosimetry and Image Analysis of Cement-Based Materials. *Journal of Colloid and Interface Science* **211**: 39-44
- Aebi & Pollard TD (1987) A glow discharge unit to render electron microscope grids and other surfaces hydrophilic. *Journal of Electron Microscopy Technique* **7**: 29-33
- Altmeyer, Maki RG, Feldweg AM, Heike M, Protopopov VP, Masur SK & Srivastava PK (1996) Tumor-specific cell surface expression of the-KDEL containing, endoplasmic reticular heat shock protein gp96. *International Journal of Cancer* **69**: 340-349
- Andre-Patrick Arrigo & Jacques Landry (1994) Expression and Function of the Low-molecular-weight Heat Shock Proteins. *The Biology of Heat Shock Proteins and Molecular Chaperones* **26**: 335-373
- Augsten C, Kiselev MA, Gehrke R, Hause G & Mäder K (2008) A detailed analysis of biodegradable nanospheres by different techniques--a combined approach to detect particle sizes and size distributions. *Journal of Pharmaceutical and Biomedical Analysis* **47**: 95-102
- Avnir D, Coradin T, Lev O & Livage J (2005) Recent bio-applications of sol-gel materials. *Journal of Materials Chemistry* **16**: 1013-1030
- Ayling A & Baneyx F (1996) Influence of the GroE molecular chaperone machine on the in vitro refolding of Escherichia coli beta-galactosidase. *Protein Science* **5**: 478-487
- Babià T, Ledesma MD, Saffrich R, Kok JW, Dotti CG & Egea G (2001) Endocytosis of NBD-sphingolipids in neurons: exclusion from degradative compartments and transport to the Golgi complex. *Traffic* **2**: 395-405
- Baca HK, Ashley C, Carnes E, Lopez D, Flemming J, Dunphy D, Singh S, Chen Z, Liu N, Fan H, López GP, Brozik SM, Werner-Washburne M & Brinker CJ (2006) Cell-Directed Assembly of Lipid-Silica Nanostructures Providing Extended Cell Viability. *Science* **313**: 337 -341
- Bao Z, Weatherspoon MR, Shian S, Cai Y, Graham PD, Allan SM, Ahmad G, Dickerson MB, Church BC, Kang Z, Abernathy III HW, Summers CJ, Liu M & Sandhage KH (2007) Chemical reduction of three-dimensional silica micro-assemblies into microporous silicon replicas. *Nature* **446**: 172-175
- Bauer CA, Robinson DB & Simmons BA (2007) Silica Particle Formation in Confined Environments via Bioinspired Polyamine Catalysis at Near-Neutral pH. *Small* **3**: 58-62
- Beissinger M & Buchner J (1998) How chaperones fold proteins. *Biological Chemistry* **379**: 245-259
- Belton DJ, Patwardhan SV & Perry CC (2005) Spermine, spermidine and their analogues generate tailored silicas. *Journal of Materials Chemistry* **15**: 4629-4638
- Belton DJ, Patwardhan SV, Annenkov VV, Danilovtseva EN & Perry CC (2008) From biosilicification to tailored materials: optimizing hydrophobic domains and resistance to protonation of polyamines. *Proceedings of the National Academy of Sciences* **105**: 5963-5968

- Benndorf R, Hayess K, Ryazantsev S, Wieske M, Behlke J & Lutsch G (1994) Phosphorylation and supramolecular organization of murine small heat shock protein HSP25 abolish its actin polymerization-inhibiting activity. *Journal of Biological Chemistry* **269**: 20780-20784
- Bentley NJ, Fitch IT & Tuite MF (1992) The small heat-shock protein Hsp26 of *Saccharomyces cerevisiae* assembles into a high molecular weight aggregate. *Yeast* **8**: 95-106
- Berne BJ & Pecora R (1976) Dynamic light scattering: With applications to chemistry, biology and physics Wiley, New York
- Berne BJ & Pecora R (2000) Dynamic light scattering: with applications to chemistry, biology, and physics New York: Wiley
- Birch DJS & Geddes CD (2000) Fluorescence metrology of silica sol-gels - The effect of D2O and inorganic salts. *Journal of Chemical Sciences* **112**: 311-322
- Bjerner J, Nustad K, Norum LF, Olsen KH & Bormer OP (2002) Immunometric assay interference: incidence and prevention. *Clinical Chemistry* **48**: 613
- Blank GS & Sullivan CW (1983) Diatom Mineralization of Silicic Acid. VII. Influence of Microtubule Drugs on Symmetry and Pattern Formation in Valves of *Navicula Saprophila* During Morphogenesis. *Journal of Phycology* **19**: 294-301
- Bohren CF & Huffman DR (1998) Absorption and Scattering of Light by Small Particles New York; Chichester: John Wiley & Sons
- Bokman SH & Ward WW (1981) Renaturation of *Aequorea* green-fluorescent protein. *Biochemical and Biophysical Research Communications* **101**: 1372-1380
- Bozzola JJ & Russell LD (1999) Electron microscopy: principles and techniques for biologists Sudbury, Massachusetts: Jones & Bartlett Learning
- Bradbury S & Evennett P (1996) Contrast techniques in light microscopy Oxford: Bios Scientific Publishers
- Bradford MM (1976) A rapid and sensitive method for the quantitation of microgram quantities of protein utilizing the principle of protein-dye binding. *Analytical Biochemistry* **72**: 248-254
- Braig K, Otwinowski Z, Hegde R, Boisvert DC, Joachimiak A, Horwich AL & Sigler PB (1994) The crystal structure of the bacterial chaperonin GroEL at 2.8 Å. *Nature* **371**: 578-586
- Branchini BR, Southworth TL, Murtiashaw MH, Wilkinson SR, Khattak NF, Rosenberg JC & Zimmer M (2005) Mutagenesis evidence that the partial reactions of firefly bioluminescence are catalyzed by different conformations of the luciferase C-terminal domain. *Biochemistry* **44**: 1385-1393
- Brott LL, Naik RR, Pikas DJ, Kirkpatrick SM, Tomlin DW, Whitlock PW, Clarson SJ & Stone MO (2001) Ultrafast holographic nanopatterning of biocatalytically formed silica. *Nature* **413**: 291-293
- Brown W (1993) Dynamic light scattering: the method and some applications Oxford: Clarendon Press

- Brunauer S, Emmett PH & Teller E (1938) Adsorption of Gases in Multimolecular Layers. *Journal of the American Chemical Society* **60**: 309-319
- Brunner E, Lutz K & Sumper M (2004) Biomimetic synthesis of silica nanospheres depends on the aggregation and phase separation of polyamines in aqueous solution. *Physical Chemistry Chemical Physics* **6**: 854-857
- Buchner J, Renner M, Lilie H, Hinz HJ, Jaenicke R, Kiefhabel T & Rudolph R (1991) Alternatively folded states of an immunoglobulin. *Biochemistry* **30**: 6922-6929
- Bäuerlein E, Behrens P & Epple M (2007) Handbook of Biomineralization: Biological aspects and structure formation Berlin: Wiley-VCH
- Cao A, Ye Z, Cai Z, Dong E, Yang X, Liu G, Deng X, Wang Y, Yang S, Wang H, Wu M & Liu Y (2010) A Facile Method To Encapsulate Proteins in Silica Nanoparticles: Encapsulated Green Fluorescent Protein as a Robust Fluorescence Probe. *Angewandte Chemie International Edition* **49**: 3022-3025
- Caruso F, Caruso RA & Möhwald H (1998) Nanoengineering of Inorganic and Hybrid Hollow Spheres by Colloidal Templating. *Science* **282**: 1111 -1114
- Cha JN, Shimizu K, Zhou Y, Christiansen SC, Chmelka BF, Stucky GD & Morse DE (1999) Silicatein filaments and subunits from a marine sponge direct the polymerization of silica and silicones in vitro. *Proceedings of the National Academy of Sciences* **96**: 361-365
- Chen LA, Carbonell RG & Serad GA (1999) Recovery of proteins and other biological compounds using fibrous materials: II. Flocculation by polyelectrolyte addition. *Journal of Chemical Technology and Biotechnology* **74**: 740-750
- Chen S, Roseman AM, Hunter AS, Wood SP, Burston SG, Ranson NA, Clarke AR & Saibil HR (1994) Location of a folding protein and shape changes in GroEL-GroES complexes imaged by cryo-electron microscopy. *Nature* **371**: 261-264
- Chien L-J & Lee C-K (2008) Biosilicification of dual-fusion enzyme immobilized on magnetic nanoparticle. *Biotechnology and Bioengineering* **100**: 223-230
- Chu B (1997) Laser light scattering of polymer solutions. *Applied Optics* **36**: 7650-7656
- Coats AW & Redfern JP (1963) Thermogravimetric analysis. A review. *The Analyst* **88**: 906
- Coradin T & Livage J (2007) Aqueous Silicates in Biological Sol–Gel Applications: New Perspectives for Old Precursors. *Accounts of Chemical Research* **40**: 819-826
- Coradin T, Coupé A & Livage J (2003) Interactions of bovine serum albumin and lysozyme with sodium silicate solutions. *Colloids and Surfaces B: Biointerfaces* **29**: 189-196
- Crawford SA, Higgins MJ, Mulvaney P & Wetherbee R (2001) Nanostructure of the Diatom Frustule as Revealed by Atomic Force and Scanning Electron Microscopy. *Journal of Phycology* **37**: 543-554
- Crookes-Goodson WJ, Slocik JM & Naik RR (2008) Bio-directed synthesis and assembly of nanomaterials. *Chemical Society Reviews* **37**: 2403-2412
- Currie HA & Perry CC (2007) Silica in plants: biological, biochemical and chemical studies. *Annals of Botany* **100**: 1383-1389

- Demadis KD & Stathouloupoulou A (2006) Solubility Enhancement of Silicate with Polyamine/Polyammonium Cationic Macromolecules: Relevance to Silica-Laden Process Waters. *Industrial & Engineering Chemistry Research* **45**: 4436-4440
- Deželić G, Wrischer M, Devidé Z & Kratochvíl J (1960) Electron microscopy of Ludox colloidal silica. *Colloid & Polymer Science* **171**: 42-45
- Dissing U & Mattiasson B (1996) Polyelectrolyte complexes as vehicles for affinity precipitation of proteins. *Journal of Biotechnology* **52**: 1-10
- Djojoputro, Zhou XF, Qiao SZ, Wang LZ, Yu CZ & Lu GQ (2006) Periodic mesoporous organosilica hollow spheres with tunable wall thickness. *Journal of the American Chemical Society* **128**: 6320-6321
- Drummond DC, Meyer O, Hong K, Kirpotin DB & Papahadjopoulos D (1999) Optimizing liposomes for delivery of chemotherapeutic agents to solid tumors. *Pharmacological Reviews* **51**: 691-743
- Drummy LF, Yang J & Martin DC (2004) Low-voltage electron microscopy of polymer and organic molecular thin films. *Ultramicroscopy* **99**: 247-256
- Dubochet J, Ducommun M, Zollinger M & Kellenberger E (1971) A new preparation method for dark-field electron microscopy of biomacromolecules. *Journal of Ultrastructure Research* **35**: 147-167
- Dunn B, Miller J, Dave B, Valentine J & Zink J (1998) Strategies for encapsulating biomolecules in sol-gel matrices<sup>1</sup>. *Acta Materialia* **46**: 737-741
- Díaz JF & Balkus Jr KJ (1996) Enzyme immobilization in MCM-41 molecular sieve. *Journal of Molecular Catalysis B: Enzymatic* **2**: 115-126
- Edwards RA, Jacobson AL & Huber RE (1990) Thermal denaturation of  $\beta$ -galactosidase and of two site specific mutants. *Biochemistry* **29**: 11001-11008
- Eftink MR (2006) Fluorescence Techniques for Studying Protein Structure. In *Methods of Biochemical Analysis*, Suelter CH (ed) pp 127-205. Hoboken, NJ, USA: John Wiley & Sons, Inc.
- Ehrnsperger M, Gräber S, Gaestel M & Buchner J (1997) Binding of non-native protein to Hsp25 during heat shock creates a reservoir of folding intermediates for reactivation. *The EMBO Journal* **16**: 221-229
- Ehrnsperger M, Lilie H, Gaestel M & Buchner J (1999) The dynamics of Hsp25 quaternary structure. Structure and function of different oligomeric species. *The Journal of Biological Chemistry* **274**: 14867-14874
- El Rassy H, Maury S, Buisson P & Pierre AC (2004) Hydrophobic silica aerogel-lipase biocatalysts: Possible interactions between the enzyme and the gel. *Journal of Non-Crystalline Solids* **350**: 23-30
- Endow SA (1999) GFP fusions to a microtubule motor protein to visualize meiotic and mitotic spindle dynamics in *Drosophila*. *Methods in Cell Biology* **58**: 153-163
- Fan J, Yu C, Gao F, Lei J, Tian B, Wang L, Luo Q, Tu B, Zhou W & Zhao D (2003) Cubic Mesoporous Silica with Large Controllable Entrance Sizes and Advanced Adsorption Properties. *Angewandte Chemie* **115**: 3254-3258

- Farahbakhsh ZT, Huang QL, Ding LL, Altenbach C, Steinhoff HJ, Horwitz J & Hubbell WL (1995) Interaction of alpha-crystallin with spin-labeled peptides. *Biochemistry* **34**: 509-516
- Fenton WA, Kashi Y, Furtak K & Norwich AL (1994) Residues in chaperonin GroEL required for polypeptide binding and release. *Nature* **371**: 614-619
- Field CB, Behrenfeld MJ, Randerson JT & Falkowski P (1998) Primary Production of the Biosphere: Integrating Terrestrial and Oceanic Components. *Science* **281**: 237 -240
- Finnie KS, Waller DJ, Perret FL, Krause-Heuer AM, Lin HQ, Hanna JV & Barbé CJ (2008) Biodegradability of sol-gel silica microparticles for drug delivery. *Journal of Sol-Gel Science and Technology* **49**: 12-18
- Fleckenstein T (2008) Biomineralisation an globulären Protein-Multimeren Lehrstuhl für Biotechnologie, Institut für organische Chemie und Biochemie Technische Universität München.
- Fowler CE, Khushalani D & Mann S (2001) Facile synthesis of hollow silica microspheres. *Journal of Materials Chemistry* **11**: 1968-1971
- Frank T (1989) Stabilization of lipase from *Thermomyces lanuginosus* with p-chloromercuribenzoic acid. *Journal of Fermentation and Bioengineering* **68**: 141-143
- Frydman J (2001) Folding of newly translated proteins in vivo: the role of molecular chaperones. *Annual Review of Biochemistry* **70**: 603-647
- Fultz B (2008) Transmission electron microscopy and diffractometry of materials New York: Springer
- Gasteiger E, Hoogland C, Gattiker A, Duvaud S, Wilkins MR, Appel RD & Bairoch A (2005) Protein Identification and Analysis Tools on the ExPASy Server. In *The Proteomics Protocols Handbook*, Walker JM (ed) pp 571-607. Totowa, NJ: Humana Press
- Gazit E (2007) Use of biomolecular templates for the fabrication of metal nanowires. *The FEBS Journal* **274**: 317-322
- Geddes CD, Apperson K & Birch DJS (2000) New fluorescent quinolinium dyes — applications in nanometre particle sizing. *Dyes and Pigments* **44**: 69-74
- Ghosh PB & Whitehouse MW (1968) 7-chloro-4-nitrobenzo-2-oxa-1,3-diazole: a new fluorogenic reagent for amino acids and other amines. *Biochemical Journal*: 155-156
- Goodhew PJ, Humphreys FJ & Beanland R (2001) Electron microscopy and analysis New York: Taylor & Francis
- Grallert H, Rutkat K & Buchner J (2000) Limits of Protein Folding Inside GroE Complexes. *Journal of Biological Chemistry* **275**: 20424 -20430
- Groemping Y, Klostermeier D, Herrmann C, Veit T, Seidel R & Reinstein J (2001) Regulation of ATPase and chaperone cycle of DnaK from *Thermus thermophilus* by the nucleotide exchange factor GrpE. *Journal of Molecular Biology* **305**: 1173-1183
- Groen (2003) Pore size determination in modified micro- and mesoporous materials. Pitfalls and limitations in gas adsorption data analysis. *Microporous and Mesoporous Materials* **60**: 1-17

- Groshens TJ & Hollins RA (2009) New chemical hydrogen storage materials exploiting the self-sustaining thermal decomposition of guanidinium borohydride. *Chemical Communications*: 3089-3091
- Gröger C, Lutz K & Brunner E (2007) Biomolecular Self-assembly and its Relevance in Silica Biomineralization. *Cell Biochemistry and Biophysics* **50**: 23-39
- Gupta V, Nath S & Chand S (2000) Estimation of proteins in the presence of polyethylenimine. *Biotechnology Letters* **22**: 927–929
- Gómez L, Ramírez HL, Neira-Carrillo A & Villalonga R (2006) Polyelectrolyte complex formation mediated immobilization of chitosan-invertase neoglycoconjugate on pectin-coated chitin. *Bioprocess and Biosystems Engineering* **28**: 387-395
- Hamada D, Yanagihara I & Tsumoto K (2004) Engineering amyloidogenicity towards the development of nanofibrillar materials. *Trends in Biotechnology* **22**: 93-97
- Hamilton RG, Roebber M, Reimer CB & Rodkey LS (1987) Isoelectric focusing-affinity immunoblot analysis of mouse monoclonal antibodies to the four human IgG subclasses. *Electrophoresis* **8**: 127-134
- Han Y-J, Stucky GD & Butler A (1999) Mesoporous Silicate Sequestration and Release of Proteins. *Journal of the American Chemical Society* **121**: 9897-9898
- Hanefeld U, Gardossi L & Magner E (2008) Understanding enzyme immobilisation. *Chemical Society Reviews* **38**: 453-468
- Harris MT, Brunson RR & Byers CH (1990) The base-catalyzed hydrolysis and condensation reactions of dilute and concentrated TEOS solutions. *Journal of Non-Crystalline Solids* **121**: 397-403
- Hartl FU & Hayer-Hartl M (2002) Molecular Chaperones in the Cytosol: from Nascent Chain to Folded Protein. *Science* **295**: 1852 -1858
- Haslbeck M (2002) sHsps and their role in the chaperone network. *Cellular and Molecular Life Sciences* **59**: 1649-1657
- Haslbeck M, Ignatiou A, Saibil H, Helmich S, Frenzl E, Stromer T & Buchner J (2004) A domain in the N-terminal part of Hsp26 is essential for chaperone function and oligomerization. *Journal of Molecular Biology* **343**: 445-455
- Haslbeck M, Walke S, Stromer T, Ehrnsperger M, White HE, Chen S, Saibil HR & Buchner J (1999) Hsp26: a temperature-regulated chaperone. *The EMBO Journal* **18**: 6744-6751
- He X, Chen J, Wang K, Qin D & Tan W (2007) Preparation of luminescent Cy5 doped core-shell SFNPs and its application as a near-infrared fluorescent marker. *Talanta* **72**: 1519-1526
- Heath D & Tadros T. (1983) Influence of pH, electrolyte, and poly(vinyl alcohol) addition on the rheological characteristics of aqueous dispersions of sodium montmorillonite. *Journal of Colloid and Interface Science* **93**: 307-319
- Heberer H, Kersting H & Matschiner H (1985) Derivatisierung von Aminen mit 4-substituierten 7-Nitrobenz-2,1,3-oxadiazolen. *Journal für Praktische Chemie* **327**: 487-504



- Hench LL & West JK (1990) The sol-gel process. *Chemical Reviews* **90**: 33-72
- Hendrix M & Leipertz A (1984) Photonenkorrelationsspektroskopie. *Physik in unserer Zeit* **15**: 68-75
- Heuer AH, Fink DJ, Laraia VJ, Arias JL, Calvert PD, Kendall K, Messing GL, Blackwell J, Rieke PC & Thompson DH (1992) Innovative materials processing strategies: a biomimetic approach. *Science* **255**: 1098-1105
- Hildebrand M (2008) Diatoms, biomineralization processes, and genomics. *Chemical Reviews* **108**: 4855-4874
- Hillcoat BL, Nixon PF & Blakley RL (1967) Effect of substrate decomposition on the spectrophotometric assay of dihydrofolate reductase. *Analytical Biochemistry* **21**: 178-189
- Horwitz J (1992) Alpha-crystallin can function as a molecular chaperone. *Proceedings of the National Academy of Sciences* **89**: 10449-10453
- Iler R (1979) The chemistry of silica: solubility, polymerization, colloid and surface properties and biochemistry New York: Wiley
- Ionescu RM, Smith VF, O'Neill JC Jr & Matthews CR (2000) Multistate equilibrium unfolding of Escherichia coli dihydrofolate reductase: thermodynamic and spectroscopic description of the native, intermediate, and unfolded ensembles. *Biochemistry* **39**: 9540-9550
- Jachmann N (2001) Flüssigchromatographische Bestimmung aliphatischer und aromatischer Amine mit 4-Chloro-7-nitrobenzo-2-oxa-1,3-diazol.
- Jaeger KE & Reetz MT (1998) Microbial lipases form versatile tools for biotechnology. *Trends in Biotechnology* **16**: 396-403
- Jaeger KE, Dijkstra BW & Reetz MT (1999) Bacterial biocatalysts: molecular biology, three-dimensional structures, and biotechnological applications of lipases. *Annual Review of Microbiology* **53**: 315-351
- Jakob U, Gaestel M, Engel K & Buchner J (1993) Small heat shock proteins are molecular chaperones. *The Journal of Biological Chemistry* **268**: 1517-1520
- Johnson AK, Zawadzka AM, Deobald LA, Crawford RL & Paszczyński AJ (2007) Novel method for immobilization of enzymes to magnetic nanoparticles. *Journal of Nanoparticle Research* **10**: 1009-1025
- Johnson M (2009) Biothermodynamics: Part B Boston Massachusetts: Academic Press
- de Jong WW, Leunissen JA & Voorter CE (1993) Evolution of the alpha-crystallin/small heat-shock protein family. *Molecular Biology and Evolution* **10**: 103-126
- Kang K-K & Rhee H-K (2005) Synthesis and characterization of novel mesoporous silica with large wormhole-like pores: Use of TBOS as silicon source. *Microporous and Mesoporous Materials* **84**: 34-40
- Kim DJ, Lee K, Lee TG, Shon HK, Kim W, Paik H & Choi IS (2005) Biomimetic Micropatterning of Silica by Surface-Initiated Polymerization and Microcontact Printing. *Small* **1**: 992-996

- Kim J, Kim HS, Lee N, Kim T, Kim H, Yu T, Song IC, Moon WK & Hyeon T (2008) Multifunctional uniform nanoparticles composed of a magnetite nanocrystal core and a mesoporous silica shell for magnetic resonance and fluorescence imaging and for drug delivery. *Angewandte Chemie (International Ed. in English)* **47**: 8438-8441
- Kisler JM, Dähler A, Stevens GW & O'Connor AJ (2001) Separation of biological molecules using mesoporous molecular sieves. *Microporous and Mesoporous Materials* **44-45**: 769-774
- Knecht MR, Sewell SL & Wright DW (2005) Size Control of Dendrimer-Templated Silica. *Langmuir* **21**: 2058-2061
- Kordel M, Hofmann B, Schomburg D & Schmid RD (1991) Extracellular lipase of *Pseudomonas* sp. strain ATCC 21808: purification, characterization, crystallization, and preliminary X-ray diffraction data. *Journal of Bacteriology* **173**: 4836 -4841
- Kresge CT, Leonowicz ME, Roth WJ, Vartuli JC & Beck JS (1992) Ordered mesoporous molecular sieves synthesized by a liquid-crystal template mechanism. *Nature* **359**: 710-712
- Kröger N & Poulsen N (2008) Diatoms-from cell wall biogenesis to nanotechnology. *Annual review of genetics* **42**: 83-107
- Kröger N, Deutzmann R & Sumper M (1999) Polycationic Peptides from Diatom Biosilica That Direct Silica Nanosphere Formation. *Science* **286**: 1129 -1132
- Kröger N, Deutzmann R & Sumper M (2001) Silica-precipitating Peptides from Diatoms. *Journal of Biological Chemistry* **276**: 26066 -26070
- Kröger N, Lorenz S, Brunner E & Sumper M (2002) Self-Assembly of Highly Phosphorylated Silaffins and Their Function in Biosilica Morphogenesis. *Science* **298**: 584 -586
- Kusak R (2005) Template transformations in preparation of MCM-41 silica. *Journal of Thermal Analysis and Calorimetry* **79**: 555-560
- Lakowicz J (2006) Principles of Fluorescence Spectroscopy 3rd ed. New York: Springer
- Larson DR, Ow H, Vishwasrao HD, Heikal AA, Wiesner U & Webb WW (2008) Silica Nanoparticle Architecture Determines Radiative Properties of Encapsulated Fluorophores. *Chemistry of Materials* **20**: 2677-2684
- Lebert JM, Forsberg EM & Brennan JD (2008) Solid-phase assays for small molecule screening using sol-gel entrapped proteins. *Biochemistry and Cell Biology* **86**: 100-110
- Lebrun E, Tu YX, van Rapenbusch R, Banijamali AR & Foye WO (1990) Inhibition of bovine dihydrofolate reductase and enhancement of methotrexate sensitivity by N4-(2-acetoxyethoxymethyl)-2-acetylpyridine thiosemicarbazone. *Biochimica Et Biophysica Acta* **1034**: 81-85
- Lei C, Shin Y, Liu J & Ackerman EJ (2002) Entrapping Enzyme in a Functionalized Nanoporous Support. *Journal of the American Chemical Society* **124**: 11242-11243
- de Lencastre Novaes LC, Mazzola PG, Pessoa Jr. A & Penna TCV (2011) Citrate and phosphate influence on green fluorescent protein thermal stability. *Biotechnology Progress* **27**: 269-272

- Lilie H, Rudolph R & Buchner J (1995a) Association of antibody chains at different stages of folding: prolyl isomerization occurs after formation of quaternary structure. *Journal of Molecular Biology* **248**: 190-201
- Lilie, Jaenicke R & Buchner J (1995b) Characterization of a quaternary-structured folding intermediate of an antibody Fab-fragment. *Protein Science* **4**: 917-924
- Lindquist S & Craig EA (1988) The heat-shock proteins. *Annual Review of Genetics* **22**: 631-677
- Lowenstam HA & Weiner S (1989) On biomineralization Oxford, UK: Oxford University Press
- Luckarift HR, Spain JC, Naik RR & Stone MO (2004) Enzyme immobilization in a biomimetic silica support. *Nature Biotechnology* **22**: 211-213
- Lukovkin GM, Pshezhetsky VS & Murtazaeva GA (1973) NMR <sup>13</sup>C study of the structure of polyethyleneimine. *European Polymer Journal* **9**: 559-565
- Mager WH & Ferreira PM (1993) Stress response of yeast. *Biochemical Journal* **290**: 1-13
- Mann S (1993) Molecular tectonics in biomineralization and biomimetic materials chemistry. *Nature* **365**: 499-505
- Mann S & Ozin GA (1996) Synthesis of inorganic materials with complex form. *Nature* **382**: 313-318
- Marner WD 2nd, Shaikh AS, Muller SJ & Keasling JD (2009) Enzyme immobilization via silaffin-mediated autoencapsulation in a biosilica support. *Biotechnology Progress* **25**: 417-423
- Marques SM & Esteves da Silva JCG (2009) Firefly bioluminescence: a mechanistic approach of luciferase catalyzed reactions. *IUBMB Life* **61**: 6-17
- Matsoukas T & Gulari E (1988) Dynamics of growth of silica particles from ammonia-catalyzed hydrolysis of tetra-ethyl-orthosilicate. *Journal of colloid and interface science* **124**: 252-261
- Mavredaki E, Stathoulopoulou A, Neofotistou E & Demadis KD (2007) Environmentally benign chemical additives in the treatment and chemical cleaning of process water systems: Implications for green chemical technology. *Desalination* **210**: 257-265
- Mayer M, Kies U, Kammermeier R & Buchner J (2000) BiP and PDI cooperate in the oxidative folding of antibodies in vitro. *The Journal of Biological Chemistry* **275**: 29421-29425
- Mazzola PG, Ishii M, Chau E, Cholewa O & Penna TCV (2006) Stability of green fluorescent protein (GFP) in chlorine solutions of varying pH. *Biotechnology Progress* **22**: 1702-1707
- Miller J (1977) Experiments in molecular genetics 3rd ed. Cold Spring Harbor: Cold Spring Harbor Laboratory
- Minutolo P, Ossler F, De Lisio C, Bruno A & D'Anna A (2010) Time Resolved Fluorescence Anisotropy measurements of nanoparticle sizes in a diffusion flame. In *International Conference on "Processes and Technologies for a Sustainable Energy"* pp 1-6. Ischia, Napoli, Italy

- Mizutani T, Nagase H, Fujiwara N & Ogoshi H (1998) Silicic Acid Polymerization Catalyzed by Amines and Polyamines. *Bulletin of the Chemical Society of Japan* **71**: 2017-2022
- Morimoto R (1994) The Biology of heat shock proteins and molecular chaperones Plainview New York: Cold Spring Harbor Laboratory Press
- Murphy D (2001) Fundamentals of light microscopy and electronic imaging New York: Wiley-Liss
- Naik RR, Tomczak MM, Luckarift HR, Spain JC & Stone MO (2004) Entrapment of enzymes and nanoparticles using biomimetically synthesized silica. *Chemical Communications*: 1684-1685
- Nam DH, Won K, Kim YH & Sang BI (2009) A novel route for immobilization of proteins to silica particles incorporating silaffin domains. *Biotechnology Progress* **25**: 1643-1649
- Nath S (1995) Complexation behavior of proteins with polyelectrolytes and random acrylic polyampholytes using turbidimetric titration. *Journal of Chemical Technology and Biotechnology* **62**: 295-300
- Nebesárová J & Vancová M (2007) How to Observe Small Biological Objects in Low Voltage Electron Microscope. *Microscopy and Microanalysis* **13**: 248-249
- Neethirajan S, Gordon R & Wang L (2009) Potential of silica bodies (phytoliths) for nanotechnology. *Trends in Biotechnology* **27**: 461-467
- Nominé Y, Ristriani T, Laurent C, Lefèvre J-F, Weiss É & Travé G (2001) A strategy for optimizing the monodispersity of fusion proteins: application to purification of recombinant HPV E6 oncoprotein. *Protein Engineering* **14**: 297 -305
- Orçaire O, Buisson P & Pierre AC (2006) Application of silica aerogel encapsulated lipases in the synthesis of biodiesel by transesterification reactions. *Journal of Molecular Catalysis B: Enzymatic* **42**: 106–113
- Pascal J. Lopez, Clementine Gautier, Jacques Livage & Thibaud Coradin (2005) Mimicking Biogenic Silica Nanostructures Formation. *Current Nanoscience* **1**: 73-83
- Pastor I, Esquembre R, Micol V, Mallavia R & Mateo CR (2004) A ready-to-use fluorimetric biosensor for superoxide radical using superoxide dismutase and peroxidase immobilized in sol-gel glasses. *Analytical Biochemistry* **334**: 335-343
- Pastor I, Ferrer ML, Lillo MP, Gómez J & Mateo CR (2007) Structure and Dynamics of Lysozyme Encapsulated in a Silica Sol–Gel Matrix. *Journal of Physical Chemistry B* **111**: 11603-11610
- Patwardhan SV (2002) Synthesis of silica nano and micrometer size structures at neutral pH and under ambient conditions.
- Patwardhan SV & Clarkson SJ (2003) Silicification and biosilicification: Part 5. An investigation of the silica structures formed at weakly acidic pH and neutral pH as facilitated by cationically charged macromolecules. *Materials Science and Engineering: C* **23**: 495-499
- Paul-Dauphin S, Karaca F, Morgan TJ, Millan-Agorio M, Herod AA & Kandiyoti R (2007) Probing Size Exclusion Mechanisms of Complex Hydrocarbon Mixtures: The Effect of Altering Eluent Compositions. *Energy Fuels* **21**: 3484-3489

- Pecora R (2000) Dynamic light scattering measurement of nanometer particles in liquids. *Journal of Nanoparticle Research* **2**: 123–131
- Perry CC & Keeling-Tucker T (2000) Biosilicification: the role of the organic matrix in structure control. *Journal of Biological Inorganic Chemistry* **5**: 537-550
- Perry CC & Lu Y (1992) Preparation of silicas from silicon complexes: role of cellulose in polymerisation and aggregation control. *Journal of the Chemical Society* **88**: 2915-2921
- Piao Y, Burns A, Kim J, Wiesner U & Hyeon T (2008) Designed Fabrication of Silica-Based Nanostructured Particle Systems for Nanomedicine Applications. *Advanced Functional Materials* **18**: 3745-3758
- Pickett-Heaps J, Schmid A-MM & Edgar LA (1990) The Cell Biology of Diatom Valve Formation. *Progress in Phycological Research* **7**: 1-168
- Pickett-Heaps JD (1998) Cell Division and Morphogenesis of the Centric Diatom *Chaetoceros Decipiens* (bacillariophyceae) I. Living Cells. *Journal of Phycology* **34**: 989-994
- Pierre AC (2004) The sol-gel encapsulation of enzymes. *Biocatalysis and Biotransformation* **22**: 145-170
- Podbielska H & Ulatowska-Jarza A (2005) Sol-gel technology for biomedical engineering. *Technical Sciences* **53**: 261-271
- Potapov VV, Serdan AA, Kashpura VN, Gorbach VA, Tyurina NA & Zubakha SV (2007) Polycondensation of orthosilicic acid in hydrothermal solutions at different temperatures, pH values, and ionic strengths. *Glass Physics and Chemistry* **33**: 44-49
- Poulsen N, Sumper M & Kröger N (2003) Biosilica formation in diatoms: Characterization of native silaffin-2 and its role in silica morphogenesis. *Proceedings of the National Academy of Sciences* **100**: 12075 -12080
- Quintanar-Guerrero D, Ganem-Quintanar A, Nava-Arzaluz MG & Piñón-Segundo E (2009) Silica xerogels as pharmaceutical drug carriers. *Expert Opinion on Drug Delivery* **6**: 485-498
- Ramanathan M, Luckariff HR, Sarsenova A, Wild JR, Ramanculov EK, Olsen EV & Simonian AL (2009) Lysozyme-mediated formation of protein–silica nano-composites for biosensing applications. *Colloids and Surfaces B: Biointerfaces* **73**: 58-64
- Ravindran S, Gao Q, Ramachandran A, Blond S, Predescu SA & George A (2011) Stress chaperone GRP-78 functions in mineralized matrix formation. *The Journal of Biological Chemistry* **286**: 8729-8739
- Reches M, Porat Y & Gazit E (2002) Amyloid fibril formation by pentapeptide and tetrapeptide fragments of human calcitonin. *The Journal of Biological Chemistry* **277**: 35475-35480
- Reetz MT, Tielmann P, Wiesenhöfer W, Könen W & Zonta A (2003) Second Generation Sol-Gel Encapsulated Lipases: Robust Heterogeneous Biocatalysts. *Advanced Synthesis & Catalysis* **345**: 717-728
- Reetz MT, Zonta A & Simpelkamp J (1996) Efficient immobilization of lipases by entrapment

- in hydrophobic sol-gel materials. *Biotechnology and Bioengineering* **49**: 527-534
- Ricca E, Calabrò V, Curcio S, Basso A, Gardossi L & Iorio G (2010) Fructose Production by Inulinase Covalently Immobilized on Sepabeads in Batch and Fluidized Bed Bioreactor. *International Journal of Molecular Sciences* **11**: 1180-1189
- Roth KM, Zhou Y, Yang W & Morse DE (2004) Bifunctional Small Molecules Are Biomimetic Catalysts for Silica Synthesis at Neutral pH. *Journal of the American Chemical Society* **127**: 325-330
- Round FE, Crawford RM & Mann DG (1990) *Diatoms: Biology and Morphology of the Genera* New York: Cambridge University Press
- Royston E, Lee S-Y, Culver JN & Harris MT (2006) Characterization of silica-coated tobacco mosaic virus. *Journal of Colloid and Interface Science* **298**: 706-712
- Sandhage KH, Dickerson MB, Huseman PM, Caranna MA, Clifton JD, Bull TA, Heibel TJ, Overton WR & Schoenwaelder ME. (2002) Novel, Bioclastic Route to Self-Assembled, 3D, Chemically Tailored Meso/Nanostructures: Shape-Preserving Reactive Conversion of Biosilica (Diatom) Microshells. *Advanced Materials* **14**: 429-433
- Sayari A & Hamoudi S (2001) Periodic Mesoporous Silica-Based Organic-Inorganic Nanocomposite Materials. *Chemistry of Materials* **13**: 3151-3168
- Scheibel T (2005) Protein fibers as performance proteins: new technologies and applications. *Current Opinion in Biotechnology* **16**: 427-433
- Schmid (1980) Valve morphogenesis in diatoms: A pattern related filamentous system in pennates and the effect of APM, colchicine and osmotic pressure. *Nova Hedwigia* **33**: 811-847
- Schmidt R (2010) Dynamic Light Scattering for Protein Characterization. In *Encyclopedia of Analytical Chemistry*, Meyers RA (ed) Chichester, UK: John Wiley & Sons, Ltd
- Schmidt-Winkel P, Lukens, Yang P, Margolese DI, Lettow JS, Ying JY & Stucky GD (2000) Microemulsion Templating of Siliceous Mesoporous Cellular Foams with Well-Defined Ultralarge Mesopores. *Chemistry of Materials* **12**: 686-696
- Schmidt-Winkel P, Lukens, Zhao D, Yang P, Chmelka BF & Stucky GD (1998) Mesocellular Siliceous Foams with Uniformly Sized Cells and Windows. *Journal of the American Chemical Society* **121**: 254-255
- Schramm U, Fricker G, Buscher HP, Gerok W & Kutz G (1993) Fluorescent derivatives of bile salts. III. Uptake of 7 beta-NBD-NCT into isolated hepatocytes by the transport systems for cholytaurine. *Journal of Lipid Research* **34**: 741 -757
- Schrödel A & de Marco A (2005) Characterization of the aggregates formed during recombinant protein expression in bacteria. *BMC Biochemistry* **6**: 10
- Schröder H, Langer T, Hartl FU & Bukau B (1993) DnaK, DnaJ and GrpE form a cellular chaperone machinery capable of repairing heat-induced protein damage. *The EMBO Journal* **12**: 4137-4144
- Shchipunov YA (2003) Sol-gel-derived biomaterials of silica and carrageenans. *Journal of colloid and interface science* **268**: 68-76

- Shchipunov YA (2008) Entrapment of Biopolymers into Sol—Gel-derived Silica Nanocomposites. In *Bio-inorganic Hybrid Nanomaterials*, Ruiz-Hitzky E Ariga K, & Lvov YM (eds) pp 75-112. Weinheim, Germany: Wiley-VCH Verlag GmbH & Co. KGaA
- Shtelzer S, Rappoport S, Avnir D, Ottolenghi M & Braun S (1992) Properties of trypsin and of acid phosphatase immobilized in sol-gel glass matrices. *Biotechnology and Applied Biochemistry* **15**: 227-235
- Sierra L & Guth J-L (1999) Synthesis of mesoporous silica with tunable pore size from sodium silicate solutions and a polyethylene oxide surfactant. *Microporous and Mesoporous Materials* **27**: 243-253
- Simmons LC, Reilly D, Klimowski L, Raju TS, Meng G, Sims P, Hong K, Shields RL, Damico LA, Rancatore P & Yansura DG (2002) Expression of full-length immunoglobulins in *Escherichia coli*: rapid and efficient production of aglycosylated antibodies. *Journal of Immunological Methods* **263**: 133-147
- Sing KSW, Everett DH, Moscou L, Pierrotti R, Roquerol J & Siemieniwska T (1985) Reporting Physisorption Data for Gas/Solid Systems. *Pure and Applied Chemistry* **57**: 603–619
- Skoog DA (1985) Principles of instrumental analysis Philadelphia: Saunders College Publishing
- Slowing II, Trewyn BG, Giri S & Lin VS-. (2007) Mesoporous Silica Nanoparticles for Drug Delivery and Biosensing Applications. *Advanced Functional Materials* **17**: 1225-1236
- Sokolov I, Kievsky YY & Kaszpurenko JM (2007) Self-Assembly of Ultrabright Fluorescent Silica Particles. *Small* **3**: 419-423
- Spector DL, Goldmann RD & Leinwand LA (1998) Preparative methods for scanning electron microscopy. Cells: Cold Spring Harbor Laboratory Press, Cold Spring Harbor, New York
- Stöber W, Fink A & Bohn E (1968) Controlled growth of monodisperse silica spheres in the micron size range. *Journal of colloid and interface science* **26**: 62–69
- Sumper M & Kröger N (2004) Silica formation in diatoms: the function of long-chain polyamines and silaffins. *Journal of Materials Chemistry* **14**: 2059-2065
- Sumper M, Lorenz S & Brunner E (2003) Biomimetic Control of Size in the Polyamine-Directed Formation of Silica Nanospheres. *Angewandte Chemie International Edition* **42**: 5192-5195
- Szabo A (1984) Theory of fluorescence depolarization in macromolecules and membranes. *The Journal of Chemical Physics* **81**: 150
- Takahashi H, Li B, Sasaki T, Miyazaki C, Kajino T & Inagaki S (2000) Catalytic Activity in Organic Solvents and Stability of Immobilized Enzymes Depend on the Pore Size and Surface Characteristics of Mesoporous Silica. *Chemistry of Materials* **12**: 3301-3305
- Tjernberg L, Hosia W, Bark N, Thyberg J & Johansson J (2002) Charge attraction and beta propensity are necessary for amyloid fibril formation from tetrapeptides. *The Journal of Biological Chemistry* **277**: 43243-43246

- Tleugabulova D, Duft AM, Zhang Z, Chen Y, Brook MA & Brennan JD (2004) Evaluating Formation and Growth Mechanisms of Silica Particles Using Fluorescence Anisotropy Decay Analysis. *Langmuir* **20**: 5924-5932
- Toca-Herrera JL, Küpcü S, Diederichs V, Moncayo G, Pum D & Sleytr UB (2006) Fluorescence emission properties of S-Layer enhanced green fluorescent fusion protein as a function of temperature, pH conditions, and guanidine hydrochloride concentration. *Biomacromolecules* **7**: 3298-3301
- Topell, Hennecke J & Glockshuber R (1999) Circularly permuted variants of the green fluorescent protein. *FEBS Letters* **457**: 283-289
- Uedaira H, Kidokoro S, Iwakura M, Honda S & Ohashi S (1990) Thermal stability of dihydrofolate reductase and its fused proteins with oligopeptides. *Annals of the New York Academy of Sciences* **613**: 352-357
- Vamvakaki V & Chaniotakis NA (2007) Immobilization of enzymes into nanocavities for the improvement of biosensor stability. *Biosensors and Bioelectronics* **22**: 2650-2655
- Veinger L, Diamant S, Buchner J & Goloubinoff P (1998) The small heat-shock protein IbpB from *Escherichia coli* stabilizes stress-denatured proteins for subsequent refolding by a multichaperone network. *The Journal of Biological Chemistry* **273**: 11032-11037
- Verkhusha VV, Kuznetsova IM, Stepanenko OV, Zaraisky AG, Shavlovsky MM, Turoverov KK & Uversky VN (2003) High stability of *Discosoma* DsRed as compared to *Aequorea* EGFP. *Biochemistry* **42**: 7879-7884
- Viswanath DS (2007) Viscosity of liquids: theory, estimation, experiment, and data Dordrecht, Netherlands: Springer
- Wang F & Mao C (2009) Nanotubes connected to a micro-tank: hybrid micro-/nano-silica architectures transcribed from living bacteria as bioreactors. *Chemical Communications*: 1222-1224
- Wang G, Wang L, Liu P, Yan Y, Xu X & Tang R (2010) Extracellular Silica Nanocoat Confers Thermotolerance on Individual Cells: A Case Study of Material-Based Functionalization of Living Cells. *ChemBioChem* **11**: 2368-2373
- Wang H, Nakata E & Hamachi I (2009) Recent progress in strategies for the creation of protein-based fluorescent biosensors. *ChemBioChem* **10**: 2560-2577
- Wang Y & Caruso F (2005) Mesoporous Silica Spheres as Supports for Enzyme Immobilization and Encapsulation. *Chemistry of Materials* **17**: 953-961
- Wei Y, Dong H, Xu J & Feng Q (2002) Simultaneous Immobilization of Horseradish Peroxidase and Glucose Oxidase in Mesoporous Sol-Gel Host Materials. *ChemPhysChem* **3**: 802-808
- William LM (1980) Amorphous silica solubilities—I. Behavior in aqueous sodium nitrate solutions; 25–300°C, 0–6 molal. *Geochimica et Cosmochimica Acta* **44**: 907-913
- Wright JD & Sommerdijk NAJM (2001) Sol-gel materials: chemistry and applications Amsterdam, Netherlands: Gordon and Breach Science Publishers
- Yiu HHP, Wright PA & Botting NP (2001) Enzyme immobilisation using siliceous mesoporous molecular sieves. *Microporous and Mesoporous Materials* **44-45**: 763-768



- 
- Young JC, Agashe VR, Siegers K & Hartl FU (2004) Pathways of chaperone-mediated protein folding in the cytosol. *Nature Reviews Molecular Cell Biology* **5**: 781-791
- Yuan JJ & Jin RH (2005) Multiply Shaped Silica Mediated by Aggregates of Linear Poly(ethyleneimine). *Advanced Materials* **17**: 885-888
- Zaborsky O (1972) Immobilised enzymes. Cleveland, Ohio: CRC Press (Chemical Rubber Co.)
- Zhang X & Bremer H (1995) Control of the Escherichia coli rrnB P1 promoter strength by ppGpp. *Journal of Biological Chemistry* **270**: 11181 -11189
- Zhao JY, Ford CF, Glatz CE, Rougvie MA & Gendel SM (1990) Polyelectrolyte precipitation of beta-galactosidase fusions containing poly-aspartic acid tails. *Journal of Biotechnology* **14**: 273-283
- Zhu K, Jutila A, Tuominen EK., Patkar SA, Svendsen A & Kinnunen PK. (2001) Impact of the tryptophan residues of Humicola lanuginosa lipase on its thermal stability. *Biochimica et Biophysica Acta (BBA) - Protein Structure and Molecular Enzymology* **1547**: 329-338
- Zusman R, Beckman DA, Zusman I & Brent RL (1992) Purification of sheep immunoglobulin G using protein A trapped in sol-gel glass. *Analytical Biochemistry* **201**: 103-106
- Zylicz M & Wawrzynow A (2001) Insights into the Function of Hsp70 Chaperones. *IUBMB Life* **51**: 283-287

## Acknowledgements

I would like to express my gratitude to all the people who made this work possible. First of all, I would like to thank Prof. Johannes Buchner for allowing me to work on an interesting, challenging and innovative field of research and for providing me ideas, guidance and encouragement for my research.

My most sincere thanks go to Dr. Martin Haslbeck, for closely supervising my work and always finding time for discussions. His valuable feedback often solved many challenges at once and allowed me to move forward with new drive.

Three years of funding for this PhD were provided by WACKER and are gratefully acknowledged. I would like to express my thanks to the colleagues at WACKER Chemie AG, especially Dr. Manfred Amann, for the regular meetings and feedback to my work.

To all the colleagues in the biotechnology labs, especially to the “Hasi group” and the “Winter early lunch group”: thanks for a great work atmosphere! There is no one from whom I did not learn a lot, discussed great ideas with and/or got kind protein gifts from for my work. I thoroughly enjoyed all casual get-togethers breaks and trips, all of which are very memorable to me. I thank Bettina Richter for her help with SEM measurements. For constant support, patiently managing countless administrative tasks and for always being the good soul of the department, I would like to express my gratitude to Frau Hilber.

My sincere thanks go to Prof. Sevil Weinkauff and her whole group for generously giving me access to and assistance with the electron microscopes. Special thanks go to my good friend Dr. Andreas Kastenmüller for all the great and fun times since our studies.

I would also like to thank the group of Prof. Christian Becker, especially Carolin Lechner, for helpful discussions and collaboration.

Thanks to all the colleagues in the WACKER Silizium-Institut for the time spent together and the many interesting insights into different fields of silicon chemistry. I would like to especially thank Katia Rodewald for performing SEM/STEM measurements for me and for giving me the opportunity to gain experience using the new microscope.

More than I can write here I am grateful for having met you, Kathrin.

Finally, I want to express my love and deepest gratitude to my parents for their constant, unconditional and heartfelt support, my grandparents for all the times they have encouraged me and my brother Patrick who has always been a source of inspiration and motivation to me.